



# Application of hybrid uncertainty-clustering approach in pre-processing well-logs

Pedram Masoudi

## ► To cite this version:

Pedram Masoudi. Application of hybrid uncertainty-clustering approach in pre-processing well-logs. Earth Sciences. Université de Rennes; University of Teheran, 2017. English. NNT : 2017REN1S023 . tel-01625202

**HAL Id: tel-01625202**

**<https://theses.hal.science/tel-01625202>**

Submitted on 27 Oct 2017

**HAL** is a multi-disciplinary open access archive for the deposit and dissemination of scientific research documents, whether they are published or not. The documents may come from teaching and research institutions in France or abroad, or from public or private research centers.

L'archive ouverte pluridisciplinaire **HAL**, est destinée au dépôt et à la diffusion de documents scientifiques de niveau recherche, publiés ou non, émanant des établissements d'enseignement et de recherche français ou étrangers, des laboratoires publics ou privés.

ANNÉE 2017



**THÈSE / UNIVERSITÉ DE RENNES 1**  
*sous le sceau de l'Université Bretagne Loire*

En Cotutelle Internationale avec  
**Université de Téhéran, Iran**

pour le grade de  
**DOCTEUR DE L'UNIVERSITÉ DE RENNES 1**

*Mention : Sciences de la Terre*

**Ecole doctorale Sciences de la Matière**

présentée par

**Pedram MASOUDI**

Préparée à l'unité de recherche Géosciences-Rennes  
CNRS UMR6118, Observatoire des Sciences de l'Univers de Rennes

**Application of hybrid  
uncertainty-clustering  
approach in  
preprocessing well-logs**

---

**Thèse rapportée par**  
**Behzad Tokhmechi**  
Université de North Dakota / *rapporteur*  
**Ali Kadkhodaie**  
Université de Curtin (Perth) / *rapporteur*  
**et soutenue à Téhéran le 16/05/2017**  
*devant le jury composé de :*  
**Ali Moradzadeh**  
Université de Téhéran / *président*  
**Kerry Gallagher**  
Université de Rennes 1 / *examineur*  
**Mohsen Mohammadzadeh**  
Université de Tarbiat Modares / *examineur*  
**Abolghasem Kamkar Rouhani**  
Université Technique Shahrood / *examineur*  
**Omid Asghari**  
Université de Téhéran / *examineur*  
**Dimitri Komatitsch**  
Université d'Aix-Marseille / *examineur*  
**Tahar Aïfa**  
Université de Rennes 1 / *directeur de thèse*  
**Hossein Memarian**  
Université de Téhéran / *co-directeur de thèse*

*To*

*my parents, Marjan and Hossein*

*and*

*Dr. Hooshang Hakimi*

*whom I owe a lot*

*« Faut-il rejeter toutes les probabilités parce qu'elles ne sont pas des certitudes? »*

Jane Austen (1775-1817)

# Acknowledgments

First of all, the warmest thanks to my supervisors, Dr. Tahar Aïfa (University of Rennes 1), Dr. Hossein Memarian (University of Tehran) and my thesis tutor Dr. Behzad Tokhmechi (University of North Dakota) for their scientific advises.

Many thanks to the jury members of the proposal defense (Tehran 31/12/2014): Dr. Gholamhossein Norowzi, Mr. Hassan Madani, Dr. Omid Asghari and Dr. Ali Kadkhodaie-Illchi.

I also appreciate the jury members of the *mi-parcours* defense (Rennes 13/04/2016): Dr. Aline Dia, Dr. Jean-Noël Proust and Dr. Jean-Laurent Monnier.

Many thanks to the jury members of the final defense (Tehran 16/05/2017): Dr. Ali Moradzadeh, Dr. Kerry Gallagher, Dr. Mohsen Mohammadzadeh, Dr. Abolghasem Kamkar Rouhani, Dr. Omid Asghari, Dr. Dimitri Komatitsch, Dr. Behzad Tokhmechi, Dr. Ali Kadkhodaie, Dr. Tahar Aïfa and Dr. Hossein Memarian.

I would like to acknowledge Exploration Directorate of the National Iranian Oil Company for providing data and permitting the publication of scientific achievements. Thanks to the Research Unit of Geosciences-Rennes (CNRS UMR 6188) for the kind hospitality. Warm greetings to my friends in the Laboratory of Geo-engineering of School of Mining Engineering, University of Tehran for their kind help in accessing the computational and technical facilities of the laboratory remotely: Mr. Mohammadkhani, Mr. Amir Mollajan, Mr. Hossein Izadi, Miss Fatemeh Tavanaei, Mrs Atie Mazaheri and Mrs Farzaneh Khorram.

This work has been supported by the Center for International Scientific Studies and Collaboration (CISSC) and French Embassy in Iran through PHC GundiShapur 2016 program no. 35620UL. Kind thanks to other financial supports: The Cultural Institute of the Morality, Dr. Fereydoon Sahabi; Foundation of Dr. Mir-Mohammadi, Dr. Mir Saleh Mir Mohammadi and ZaminNegar Pasargad, Mr. Behzad SaeidBastami.

Pedram MASOUDI  
20 May 2017  
*masoudip@gmail.com*



# Contents

<b>Acknowledgments .....</b>	<b>ii</b>
<b>Contents .....</b>	<b>iii</b>
<i>List of figures .....</i>	<i>vi</i>
<i>List of figures of appendices .....</i>	<i>ix</i>
<i>List of tables .....</i>	<i>x</i>
<b>Abstract .....</b>	<b>1</b>
<b>Résumé étendu.....</b>	<b>3</b>
<b>Graphical abstract.....</b>	<b>6</b>
<b>1 Introduction .....</b>	<b>7</b>
<i>Highlights of the Chapter 1.....</i>	<i>7</i>
1.1 <i>Uncertainty resources in well-logging .....</i>	<i>7</i>
1.2 <i>The thesis questions and objectives .....</i>	<i>9</i>
1.2.1 <i>Question I: vertical resolution of well-logs .....</i>	<i>9</i>
1.2.2 <i>Question II: possibilistic uncertainty range of petrophysical parameters.....</i>	<i>12</i>
1.3 <i>The importance of the thesis .....</i>	<i>13</i>
1.3.1 <i>Fundamental and scientific importance .....</i>	<i>13</i>
1.3.2 <i>Application importance .....</i>	<i>13</i>
1.3.3 <i>Economic and management importance.....</i>	<i>13</i>
1.4 <i>Literature review.....</i>	<i>14</i>
1.4.1 <i>Uncertainty in sciences.....</i>	<i>14</i>
1.4.2 <i>Uncertainty in geosciences and petroleum exploration .....</i>	<i>16</i>
1.5 <i>Introducing datasets .....</i>	<i>21</i>
1.5.1 <i>Basic definitions .....</i>	<i>21</i>
1.5.2 <i>Synthetic data .....</i>	<i>22</i>
1.5.3 <i>Real data .....</i>	<i>22</i>
<b>2 Theories.....</b>	<b>29</b>
<i>Highlights of Chapter 2.....</i>	<i>29</i>
2.1 <i>Dempster-Shafer Theory of evidences.....</i>	<i>29</i>
2.1.1 <i>Body Of Evidences .....</i>	<i>30</i>
2.1.2 <i>Belief and plausibility functions .....</i>	<i>31</i>
2.1.3 <i>Consistency of uncertainty assessment theories .....</i>	<i>31</i>
2.2 <i>Fuzzy arithmetic.....</i>	<i>33</i>
2.2.1 <i>Fuzzy number .....</i>	<i>33</i>
2.2.2 <i>Arithmetic operations on intervals.....</i>	<i>35</i>
2.2.3 <i>Arithmetic operations on fuzzy numbers.....</i>	<i>35</i>
2.3 <i>Cluster analysis .....</i>	<i>36</i>
2.3.1 <i>k-means and fuzzy c-means algorithms.....</i>	<i>37</i>
2.3.2 <i>Gustafson-Kessel clustering technique .....</i>	<i>40</i>
2.3.3 <i>Gath-Geva clustering technique.....</i>	<i>40</i>
2.4 <i>Empirical relations in petrophysics.....</i>	<i>42</i>
2.4.1 <i>Porosity study by well-logs.....</i>	<i>42</i>
2.4.2 <i>Irreducible water saturation .....</i>	<i>44</i>
2.4.3 <i>Wylie-Rose permeability relation.....</i>	<i>45</i>
<b>3 Modelling vertical resolution.....</b>	<b>47</b>
<i>Highlights of Chapter 3.....</i>	<i>47</i>
3.1 <i>Volumetric nature of well-log recordings .....</i>	<i>47</i>
3.1.1 <i>Different types of resolution.....</i>	<i>47</i>

3.1.2	VRmf > spacing > sampling rate .....	49
3.2	<i>Modelling logging mechanism by fuzzy memberships</i> .....	50
3.2.1	Recording configuration and well-log .....	51
3.2.2	Approximating VRmf .....	52
3.2.3	Passive log of GR .....	57
3.2.4	Active logs of RHOB and NPHI .....	57
3.2.5	Complex membership function of compensated sonic log .....	58
3.3	<i>Volumetric Nyquist frequency</i> .....	60
3.4	<i>Conclusions of Chapter 3</i> .....	64
<b>4</b>	<b>Thin-bed characterization, geometric method</b> .....	<b>65</b>
	<i>Highlights of Chapter 4</i> .....	65
4.1	<i>Review of thin-bed studies</i> .....	65
4.1.1	VLSA Method .....	69
4.2	<i>Theory of geometric thin-bed simulator</i> .....	69
4.3	<i>Sensitivity analysis of well-logs to a 30 cm thin-bed</i> .....	73
4.4	<i>Deconvolution relations for thin-bed characterization</i> .....	76
4.5	<i>Thin-bed characterization, the Sarvak Formation case-study</i> .....	78
4.5.1	Multi-well-log thin-bed characterization .....	81
4.6	<i>Conclusions of Chapter 4</i> .....	82
<b>5</b>	<b>Enhancing vertical resolution of well-logs</b> .....	<b>85</b>
	<i>Highlights of Chapter 5</i> .....	85
5.1	<i>Combining adjacent well-log records by Bayesian Theorem</i> .....	85
5.1.1	The importance of volumetric Nyquist frequency in up-scaling .....	87
5.2	<i>Body Of Evidences (BOE) for well-logs</i> .....	88
5.2.1	Focal elements of well-logs .....	88
5.2.2	Mass function of focal element of recording .....	89
5.3	<i>Belief and plausibility functions for focal element of target</i> .....	89
5.3.1	Theoretical functions of belief and plausibility .....	89
5.3.2	Geological constraints as an axiomatic structure .....	89
5.3.3	Practical functions of belief and plausibility .....	91
5.3.4	Compensating shoulder-bed effect by epsilon .....	91
5.4	<i>Log simulators</i> .....	92
5.4.1	Random simulator .....	92
5.4.2	Random-optimization simulator .....	92
5.4.3	Recursive simulator .....	94
5.4.4	Recursive-optimization simulator .....	94
5.4.5	Validation criteria .....	94
5.5	<i>The algorithm</i> .....	95
5.6	<i>Application check on synthetic cases</i> .....	97
5.7	<i>Discussion on results of synthetic cases</i> .....	100
5.7.1	Validating constraint-based error by synthetic cases .....	101
5.8	<i>Application to real data</i> .....	102
5.8.1	Simulator selection .....	102
5.8.2	Optimizing factor of shoulder-bed effect .....	103
5.8.3	Results of resolution improvement of real well-logs .....	103
5.9	<i>Discussions</i> .....	107
5.9.1	Comparing DST and geometry-based results in thin-bed characterization .....	107
5.9.2	Advantages of DST-based algorithm .....	108
5.9.3	Uncertainty conversion using DST .....	109
5.10	<i>Conclusions of Chapter 5</i> .....	110
<b>6</b>	<b>Uncertainty projection on reservoir parameters</b> .....	<b>112</b>
	<i>Highlights of Chapter 6</i> .....	112
6.1	<i>Importance of cluster analysis in well-log interpretation</i> .....	112

6.2	<i>Porosity analysis by cluster-based method</i> .....	114
6.2.1	Methodology of cluster-based porosity analysis.....	114
6.2.2	Results of cluster-based porosity analysis .....	119
6.2.3	Discussion of cluster-based porosity analysis .....	124
6.3	<i>Permeability analysis by fuzzy arithmetic</i> .....	127
6.3.1	Methodology of permeability analysis by fuzzy arithmetic .....	127
6.3.2	Validation with core data.....	129
6.3.3	Results and discussions of analysis by fuzzy arithmetic.....	130
6.4	<i>Conclusions of Chapter 6</i> .....	133
<b>7</b>	<b>Ending</b> .....	<b>139</b>
7.1	<i>Pathway of the thesis</i> .....	139
7.1.1	Outlined achievements of the thesis.....	141
7.2	<i>Recommendations</i> .....	143
7.2.1	Recommendations for industrial applications.....	143
7.2.2	Recommendations for further researches (perspectives) .....	143
	<b>References</b> .....	<b>145</b>
	<b>Appendices</b> .....	<b>150</b>
	<i>Appendix A: Convolution form of Relation 4-2</i> .....	150
	<i>Appendix B: Application check of DST-based simulators on synthetic-logs</i> .....	150
	Case 2: Deepening (fining) upward of GR.....	150
	Case 3: Trough in RHOB.....	152
	Case 4: Increasing upward of NPHI .....	153
	Case 5: Peak in NPHI.....	154
	Case 7: Fractured horizon in DT .....	155
	<i>Appendix C: Application check of random-optimization simulator on real well-logs</i> .....	156
	Well#2: 2766 – 2770 m.....	156
	Well#3: 2809 – 2813 m.....	157
	Well#4: 2662 – 2666 m.....	157
	Well#5: 2840 – 2844 m.....	157
	<i>Appendix D: Publications and presentations of the thesis</i> .....	159
	<i>Appendix E: Publication list</i> .....	165

## List of figures

Figure 1-1. Schematic of basic concepts of logging: a) Vertical resolution of tool, membership function, depth of investigation and assigning horizon. b) Overlap of adjacent records and sampling rate.....	8
Figure 1-2. Using membership functions (right column) in representing a range of heterogeneity (lithology, porosity, etc.) of thin sections. ....	9
Figure 1-3. Conventional well-log interpretation. An example of rock typing (NikTab, 2003). ....	10
Figure 1-4. Comparing proposed and conventional interpretation approaches. Example of GR well-log. ....	11
Figure 1-5. The importance of fuzzy evaluation of well-logs in porosity evaluation. a) Porosity, based on well-log (left) and real values (right). b) VRmf, which is here proposed to be used instead of single value. The height is at 15% and its domain consists of all the possible porosity values. ....	12
Figure 1-6. Location of the field under study within the Abadan Plain, SW Iran. Modified after Sherkati and Letouzey (2004) and Rajabi <i>et al.</i> (2010).....	23
Figure 1-7. Lithostratigraphy of the Sarvak Formation and its neighbours (Dashtban, 2002).....	25
Figure 1-8. a) Underground contour (UGC) map of the top Sarvak Formation in the study area. b) AA' seismic section and its interpretation. c) Root mean square volumetric seismic amplitude attribute map, within 30 ms of the upper Turonian (the top Sarvak Formation, time slice of BCDE). The channelling of the top Sarvak Formation is shown on the FF' seismic section (circle) (Abdollahie Fard <i>et al.</i> , 2006). ....	26
Figure 1-9. Photos of the Sarvak Formation. a) Vugs on the top of Sarvak Formation, Siah-Kuh anticline, near Dehloran city, Ilam province (Masoudi <i>et al.</i> 2017). b) Weathering of the top Sarvak Formation, between Marv-Dasht (plain) and Takht-e Jamshid, Shiraz province. c) The unconformity: contact of the Sarvak and Ilam formations, Siah-Kuh anticline, near Dehloran city, Ilam province. ....	28
Figure 2-1. Comparing uncertainty assessment theories: probability (a) and DST (b). ....	30
Figure 2-2. Schematic examples of fuzzy numbers. ....	34
Figure 2-3. Fuzzy numbers for tidal ranges due to mean sea-level (Demicco and Klir, 2004). ....	34
Figure 2-4. Example of applying fuzzy operators on fuzzy numbers, integrated from Klir and Yuan (1995). ....	36
Figure 2-5. Flowchart of the FCM algorithm.....	39
Figure 2-6. A snapshot of the spreadsheet for porosity estimation by the presented empirical relations. Vsh: shale volume, NPHI <sub>w</sub> , NPHI <sub>h</sub> , NPHI <sub>ma</sub> and NPHI <sub>sh</sub> : NPHI in water, hydrocarbon, matrix and shale, respectively. NPHI <sub>m</sub> and PHI <sub>nc</sub> are outputs (for NPHI) of Relations 2-26 and 2-27, respectively. RHO <sub>Bw</sub> , RHO <sub>Bh</sub> , RHO <sub>Bma</sub> and RHO <sub>Bsh</sub> : RHO <sub>B</sub> in water, hydrocarbon, matrix (2.65 g.cm <sup>-3</sup> for calcite) and shale, respectively. PHI <sub>d</sub> and PHI <sub>dc</sub> : are outputs (for RHO <sub>B</sub> ) of Relations 2-26 and 2-27, respectively. PHI <sub>xdn</sub> , PHI <sub>xdn_Q</sub> and PHI <sub>xdn_CL</sub> are outputs of the methods density-neutron, quick-look and complex lithology, respectively. ....	45
Figure 3-1. Schematic representation of volume of investigation around a sensor in a logging tool. ....	48
Figure 3-2. Depth of investigation and spacing of each well-log (Crain, 2000).....	48
Figure 3-3. The effect of an environment, out of the spacing, on the electrical logging. a) R1<R2: electric flow is getting away from the resistant environment (R2). b) R1=R2: electric flow is symmetrical. c) R1>R2: electric flow is getting closer to the conducting environment (R2). ....	50
Figure 3-4. Fuzzy membership function of contribution of each horizon in recording a passive (a) and an active (b) log.....	51
Figure 3-5. Two possible configurations for detecting a thin-bed. Configuration B results in aliasing. In the well-logging, this phenomenon is called shoulder-bed effect, i.e. the effect of neighbouring beds. ....	52
Figure 3-6. Cross-plots of adjacent recordings of GR (well#2).....	54
Figure 3-7. Measures of similarity (correlation and covariance) and dissimilarity (variance and semivariance) for adjacent recordings of GR in well#2. ....	54
Figure 3-8. Experimental variographs showing linear relation at the first lags. An open-source computer package, named The Stanford Geostatistical Modelling Software (SGeMS) is used to generate variographs. a) GR in well#2, b) RHO <sub>B</sub> in well#2, c) NPHI in well#3 and d) DT in well#5. ....	55
Figure 3-9. Comparison of VRmf with geological beds (Campbell, 1967), log-scale beds (Majid and Worthington, 2012), petrophysical beds (Passey <i>et al.</i> , 2006). Modified after Passey <i>et al.</i> (2006). ....	56

Figure 3-10. Mechanism of measurement of sonic transfer time by Borehole Compensated (BHC) sonic tool. Two transmitters and four receivers, finally fusing them by averaging (Close <i>et al.</i> , 2009). Slowness=DT	58
Figure 3-11. Defined membership function for each half part of compensated sonic tool due to Figure 3-4b and Table 1-4.	59
Figure 3-12. Calculated complex membership function for compensated sonic tool, by averaging membership function of each half: a) theoretical and b) practical.	60
Figure 3-13. Nyquist frequency in three categories. Small balls are centre of recordings. a) Pulse-shapes (VRmf=0) like in telecommunications, domain of time. Volumetric detection b) When $0 < VRmf < SR$ or c) $VRmf > SR$ .	61
Figure 3-14. Comparing probability of detecting a thin-bed without shoulder-bed effect, in three different sensor types. In pulse-shape detections, VRmf=0, common Nyquist frequency is effective, i.e. the minimum thickness of a surely detectable thin-bed is SR. Volumetric detection when a) $0 < VRmf < SR$ , dotted line or b) when $VRmf > SR$ , dashed line.	62
Figure 3-15. Comparing belief function (pessimistic view) of detecting thin-beds without shoulder-bed effect, in three different sensor types. In pulse-shape detections, VRmf=0, common Nyquist frequency is effective, i.e. the minimum thickness of a surely detectable thin-bed is SR. Volumetric detection when a) $0 < VRmf < SR$ , dotted line or b) $VRmf > SR$ , dashed line.	63
Figure 4-1. Flowchart for hydrocarbon pore-thickness evaluation in thin-bed condition (Passey <i>et al.</i> , 2006). LCM stands for Log Convolution Modelling. Volumetric Laminated Sand Analysis (VLSA) is a probabilistic method, developed particularly to petrophysical evaluation of beds thinner than 1 ft (30 cm).	68
Figure 4-2. a) Seven configurations in detecting a thin-bed when membership function is triangular. b) Details of configuration III for calculating synthetic-log.	70
Figure 4-3. Sensitivity analysis and log response of random noise contamination: a) Sensitivity analysis of noisy GR and b) synthetic GR with 0.5, 1, 1.5 and 2% noise. c) Sensitivity analysis of noisy RHOB and d) synthetic RHOB with 1%, 2%, 3% and 4% noise. e) Sensitivity analysis of noisy NPHI and f) synthetic NPHI with 1%, 2%, 5% and 10% noise.	75
Figure 4-4. Deconvolution results on synthetic data. a) Petrophysical values (NPHI) of thin-beds before (x) and after (dot) reducing shoulder-bed effect. b) Thickness of thin-beds before (x) and after (dot) reducing shoulder effect.	78
Figure 4-5. Two examples of thin-bed interpretation on the real data. Thin-bed is firstly interpreted by the well-logs individually. The well-log values are amplified and given on the thin-bed. Final thickness interpretation and its associated uncertainty is provided in the rightmost track. a) Observation#7, well#1 (Table 4-3). b) A case-study in well#3, verified with the core box (yellow circles). The thin-bed interpretation is inclined upward since the well-logs have an upward skewness.	83
Figure 5-1. PDFXn is a combination of n adjacent PDFs. SR=15.24 cm. a) VRmf=61 cm and b) VRmf=76 cm.	86
Figure 5-2. Defined focal elements of recording ( $FE_r$ ) and target ( $FE_t$ ) for a well-log with $VRmf=4 \times SR$ .	88
Figure 5-3. Example of a well-log with vertical resolution of 91 cm (thick line), its average on five adjacent points (dashed line) and the range between belief and plausibility (dotted lines). $\epsilon$ : compensating shoulder-bed effect at peaks and troughs only.	90
Figure 5-4. Scheme of the original well-log (solid line) and simulated-log (dashed line) within the uncertainty range (grey). $\epsilon$ is multiplied by 5 (SE). The R3 should be a weighted average of S1 to S5 (white square) because they are within the $FE_{3r}$ (hatched area). Due to assumptions of the algorithm, the distance should be compensated by S3.	93
Figure 5-5. Scheme of the processing. (a) Random-optimization and recursive-optimization simulators have to pass through an optimization process, while the other more basic simulators only need a free or constraint-based random generation. (b) Flowchart of the DST-based algorithm for resolution enhancement of well-logs.	98
Figure 5-6. a) Ideal-log, synthetic-log, uncertainty range and realizations of case 1. b) Error profiles: Comparison of constraint-based errors vs. depth between the simulators in case 1. c) Total error for 50 iterations.	99
Figure 5-7. Total constraint-based error during optimization in case 1. Convergence is reached at 6 and 12 epochs for random-optimization and recursive-optimization simulators, respectively. The term "epoch" refers to the number of iterations during the optimization process. To avoid confusion, the word "iteration" is specifically used for the number of random generation.	100

Figure 5-8. Confusion matrix of correctness showing cases 1-5 and 7 and percentages. ....	101
Figure 5-9. Ideal-based vs. constraint-based error giving a significant correlation coefficient ( $R^2$ ). ....	102
Figure 5-10. Well-log (solid black line) data for the four tools (GR, RHOB, NPHI and DT), uncertainty range (blue zone), ten realizations (dots) and the best realization (dashed line) as the simulated-log, within the interval a) 3157-3159 m (well#1) and b) 2801.65-2803.45 m (well#3). ....	106
Figure 5-11. Uncertainty conversion by DST. The more depth uncertainty, the less value uncertainty. ....	110
Figure 6-1. Cross-plots of NPHI-RHOB (scaled) within the Sarvak Formation in well#3. RHOB is scaled to the range of NPHI, providing RHOB-based porosity estimation. a) Not clustered and b) clustered into five mass type clusters by FCM with inputs of NPHI, RHOB and DT. ....	113
Figure 6-2. Workflow of the algorithm of cluster-based porosity analysis. ....	115
Figure 6-3. FCM6 is trained on well-logs NPHI, RHOB and DT of well#3 (a). NPHI and core porosity of each cluster are compared through the cross-plot and histograms (b). ....	118
Figure 6-4. NPHI calibration for porosity estimation: removing the extremes of core porosity, then scaling PDF of NPHI to the new core porosity interval. ....	118
Figure 6-5. Results of cluster-based porosity analysis. When the core porosity is between the limits of clusters, the consistency mark is shown on the plot. Cluster limits in non-cored intervals are interpolated by the adjacent data. a) well#1, b) well#2, c) well#3, d) well#4 and e) well#5. fr: fraction. ....	123
Figure 6-6. Comparison of the RMSE of porosity estimation methods. ....	124
Figure 6-7. Generalization check of porosity estimators. ....	125
Figure 6-8. Homogeneous porosity zone within the Sarvak Formation. ....	126
Figure 6-9. Compatibility of core porosity with $\alpha$ -cuts (alfa-cuts). ....	129
Figure 6-10. Porosity analysis by fuzzy number. a) well#1, b) well#2, c) well#3, d) well#4 and e) well#5. fr: fraction. ....	131
Figure 6-11. Comparison of results of clustering-fuzzy arithmetic porosity analyses with VLSA method (based on Monte-Carlo simulation) by criterion 1 (a) and criterion 2 within well#1 (b), well#2 (c), well#3 (d), well#4 (e) and well#5 (f). ....	132
Figure 6-12. Irreducible water analysis of fuzzy number. a) well#1, b) well#2, c) well#3, d) well#4 and e) well#5. fr: fraction. ....	134
Figure 6-13. Comparison of results of fuzzy arithmetic irreducible water analysis (wells #3 and #5) by criterion 1 (a) and criterion 2 (b). ....	135
Figure 6-14. Permeability analysis by fuzzy number: Morris-Biggs (left) and Timur (right) for Well#1 (a,b), well#2 (c,d), well#3 (e,f), well#4 (g,h), well#5 (i,j). ....	138
Figure 6-15. Comparing results of fuzzy arithmetic permeability analysis. ....	138
Figure 7-1. Larger the dimension, smaller the uncertainty range of measurements in petrophysical variables (here porosity). From this viewpoint, the uncertainty (also heterogeneity) has a statistical aspect. ....	140

## List of figures of appendices

Figure A 1. a) Ideal-log, synthetic-log, uncertainty range, simulations (realizations) and the best realization of each simulator in case 2. Error comparison between the simulators: b) error profiles, and c) total error of 50 iterations. ....	151
Figure A 2. Same legend as in Figure A 1, case 3. ....	152
Figure A 3. Same legend as in Figure A 1, case 4. ....	153
Figure A 4. Same legend as in Figure A 1, case 5. ....	154
Figure A 5. Same legend as in Figure A 1, case 7. ....	155
Figure A 6. Well-log (solid line), uncertainty range, simulations (realizations, dots), and best realization (dashed line) in well#2. Correlation of well- and simulated-logs for perforation is marked by solid red and dashed green line, respectively. ....	156
Figure A 7. Well#3. Same descriptions as in Figure A 6. ....	157
Figure A 8. Well#4. Same descriptions as in Figure A 6. ....	158
Figure A 9. Well#5. Same descriptions as in Figure A 6. ....	158

## List of tables

Table 1-1. Sources of uncertainty in well-logs. ....	10
Table 1-2. Specifications of the ideal-logs to generate the synthetic logs. ....	22
Table 1-3. Available data within the Sarvak interval. #: number. GR: gamma ray, CGR: gamma ray of potassium, DT: sonic transfer time, NPHI: neutron porosity, RHOB: bulk density, DRHO: density correction, LLD: deep laterolog, LLS: shallow laterolog, MSFL: microspherically focused log, PEF: photoelectric effect. ....	23
Table 1-4. Details of the available well-logs in the field due to Schlumberger (2015). ....	24
Table 2-1. Consistency of BOEs with uncertainty assessment methodologies. ....	32
Table 2-2. Available axioms for the defined interval operators. Summarized from Klir and Yuan (1995). ....	35
Table 2-3. Suggested constants for Wylie and Rose (1950) permeability relation. ....	46
Table 3-1. Finding VRmf for each well-log, in each well by variography. VRmf is selected as minimum value of all the wells, larger values might be because of homogeneity of rocks. Units are in cm. ....	55
Table 3-2. Summary of designed membership functions of each log. ....	60
Table 3-3. Minimum thickness of beds to be characterized probably or surely. The uncertain interval showing an interval where probability is neither zero nor one. ....	64
Table 4-1. Defining reliable and risky windows for interpreting noisy well-logs, the case of 30 cm thin-bed. ....	75
Table 4-2. Comparing MSE of thin-bed characterization. Interpretations are based on synthetic-logs versus regression models (deconvolved) (Figure 4-4). ....	77
Table 4-3. Thin-bed characterizations of 10 real cases within Sarvak Formation, well#1. The apparent thickness values of the thin-beds are scaled to be closer to real thickness values by the deconvolution models. NAN: thin-bed curve not observed. ....	79
Table 5-1. Properties of constructed PDFs in Figure 5-1. ....	87
Table 5-2. Total errors of simulators for each synthetic case. Minimum errors are highlighted by bold characters. DST-based algorithm cannot detect a single fracture, case 6. ....	101
Table 5-3. Constraint-based total errors for the four simulators. SE=5 and iteration number=200. The reference for $n_{fuse}$ is the vertical resolution (Table 3-1). The parameters of simulation, including $n_{fuse}$ , are summarized in Table 5-5. ....	103
Table 5-4. Optimizing SE by comparing constraint-based total errors, iteration number=50. Larger iteration numbers are also tested, however the outputs were robust. The parameters of the simulation (including SE) are mentioned in Table 5-5. ....	104
Table 5-5. Optimized parameters for random-optimization simulator. Summary of Table 5-3 and 5-4. ....	104
Table 5-6. Comparing the outputs of geometry- and DST-based algorithms in thin-bed characterization, the Sarvak Formation. The most accurate values in each row are given in bold characters. ....	107
Table 6-1. Comparing different algorithms and cluster numbers. The clustering algorithms are: k-means (KM), Fuzzy c-means (FCM), Gustafson-Kessel (GK) and Gath-Geva (GG). *Only one cluster is detected. **Only two clusters are detected. ^The clusters are intervened completely (due to the histogram) so the PM is unreliable. ....	116
Table 6-2. Batch optimization of removing core porosity extremes. The optimization is achieved on the best cases of Table 6-1. The calculated values are RMSE. ....	119
Table 6-3. Sequential optimization of removing core porosity extremes. The calculated numbers are RMSE. In each row, while the percentage of each cluster is changing, the other percentages are fixed. For the first row of each well, all the percentages are chosen based on the best optimization process of Table 6-2, then modified based on the best results of the previous row. ....	120
Table 6-4. Final removal percentages of each cluster for different estimators. ....	120
Table 6-5. Generalization ability of the estimators. ....	126
Table 6-6. Buckles number in each well, calculated from core data. ....	127
Table 7-1. Comparison of different uncertainty approaches. ....	140



# Abstract

In the subsurface geology, characterization of geological beds by well-logs is an uncertain task. The thesis mainly concerns studying vertical resolution of well-logs (*question 1*). In addition, fuzzy arithmetic is applied to experimental petrophysical relations to project the uncertainty range of the inputs to the outputs, here irreducible water saturation and permeability (*question 2*). Regarding the first question, the logging mechanism is modelled by fuzzy membership functions. Vertical resolution of membership function (VRmf) is larger than spacing and sampling rate. Due to volumetric mechanism of logging, volumetric Nyquist frequency is proposed.

Developing a geometric simulator for generating synthetic-logs of a single thin-bed enabled us analysing sensitivity of the well-logs to the presence of a thin-bed. Regression-based relations between ideal-logs (simulator inputs) and synthetic-logs (simulator outputs) are used as deconvolution relations for removing shoulder-bed effect of thin-beds from GR, RHOB and NPHI well-logs. NPHI deconvolution relation is applied to a real case where the core porosity of a thin-bed is 8.4%. The NPHI well-log is 3.8%, and the deconvolved NPHI is 11.7%. Since it is not reasonable that the core porosity (effective porosity) be higher than the NPHI (total porosity), the deconvolved NPHI is more accurate than the NPHI well-log. It reveals that the shoulder-bed effect is reduced in this case. The thickness of the same thin-bed was also estimated to be  $13 \pm 7.5$  cm, which is compatible with the thickness of the thin-bed in the core box ( $< 25$  cm). Usually, *in situ* thickness is less than the thickness of the core boxes, since at the earth surface, there is no overburden pressure, also the cores are crushed.

Dempster-Shafer Theory (DST) was used to create well-log uncertainty range. While the VRmf of the well-logs is more than 60 cm, the VRmf of the belief and plausibility functions (boundaries of the uncertainty range) would be about 15 cm. So, the VRmf is improved, while the certainty of the well-log value is reduced. In comparison with geometric method, DST-based algorithm resulted in a smaller uncertainty range of GR, RHOB and NPHI logs by 100%, 71% and 66%, respectively.

In the next step, cluster analysis is applied to NPHI, RHOB and DT for the purpose of providing cluster-based uncertainty range. Then, NPHI is calibrated by core porosity value in each cluster, showing low RMSE compared to the five conventional porosity estimation models (at least 33% of improvement in RMSE). Then, fuzzy arithmetic is applied to calculate fuzzy numbers of irreducible water saturation and permeability. Fuzzy number of irreducible water saturation provides better (less overestimation) results than the crisp estimation. It is found that when the cluster interval of porosity is not compatible with the core porosity, the permeability fuzzy numbers are not valid, e.g. in well#4. Finally, in the possibilistic approach (the fuzzy theory), by calibrating  $\alpha$ -cut, the right uncertainty interval could be achieved, concerning the scale of the study.

**Keywords:** well-log uncertainty, vertical resolution, volumetric Nyquist frequency, thin-bed characterization, Dempster-Shafer, fuzzy arithmetic

# Résumé étendu

## **Application de l'approche hybride incertitude-partitionnement pour le prétraitement des données de diagraphie**

Dans la géologie de subsurface, la caractérisation des couches minces par les diagraphies est accompagnée d'incertitudes. Les sources de ces incertitudes proviennent des enregistrements discontinus (échantillonnage numérique), de l'acquisition volumétrique des données, des aspects techniques, etc. La thèse est principalement centrée sur l'étude de la résolution verticale des diagraphies (question 1). Dans la deuxième étape, l'arithmétique floue est appliquée aux modèles expérimentaux pétrophysiques en vue de transmettre l'incertitude des données d'entrée aux données de sortie, ici la saturation irréductible en eau et la perméabilité (question 2). Afin de résoudre les questions sus-jacentes, on a appliqué les théories de Dempster-Shafer (DST), d'arithmétique floue, d'analyse de regroupement des données et les expressions empiriques pétrophysiques.

Les diagraphies sont des signaux digitaux dont les données sont des mesures volumétriques. Le mécanisme d'enregistrement de ces données est modélisé par des fonctions d'appartenance floues (*fuzzy membership functions*). On a montré qu'il y avait trois types de résolution verticale pour les diagraphies : (i) le taux d'échantillonnage, (ii) l'espacement et (iii) la Résolution Verticale de la Fonction d'Appartenance (VRmf). Ils sont toujours en ordre descendant : VRmf > espacement > taux d'échantillonnage. Dans l'étape suivante, la fréquence de Nyquist est revue en fonction du mécanisme volumétrique de diagraphie ; de ce fait, la fréquence volumétrique de Nyquist est proposée afin d'analyser la précision des diagraphies.

Basé sur le modèle de résolution verticale développée, un simulateur géométrique est conçu pour générer les registres synthétiques d'une seule couche mince. Le simulateur nous permet d'analyser la sensibilité des diagraphies en présence d'une couche mince. Les relations de régression entre les registres idéaux (données d'entrée de ce simulateur) et les registres synthétiques (données de sortie de ce simulateur) sont utilisées comme relations de déconvolution en vue d'enlever l'effet des épaules de couche (*shoulder-bed effect* ou l'effet des couches voisines) d'une couche mince sur les diagraphies GR, RHOB et NPHI. Les relations

de déconvolution ont bien été appliquées aux diagraphies pour caractériser les couches minces. Par exemple, pour caractériser une couche mince poreuse, on a eu recours aux données de carottage qui étaient disponibles pour la vérification : NPHI mesuré (3.8%) a été remplacé (corrigé) par 11.7%. NPHI corrigé semble être plus précis que NPHI mesuré, car la diagraphie a une valeur plus grande que la porosité de carottage (8.4%). Il convient de rappeler que la porosité totale (NPHI) ne doit pas être inférieure à la porosité effective (carottage). En plus, l'épaisseur de la couche mince a été estimée à  $13 \pm 7.5$  cm, compatible avec l'épaisseur de la couche mince dans la boîte de carottage ( $< 25$  cm). Normalement, l'épaisseur *in situ* est inférieure à l'épaisseur de la boîte de carottage, parce que les carottes obtenues ne sont plus soumises à la pression lithostatique, et s'érodent à la surface du sol.

La Théorie de l'évidence de Dempster-Shafer (DST) est appliquée aux diagraphies. Le Corps Des Evidences (BOE) est défini à partir du mécanisme de diagraphie : si la diagraphie est considérée comme la fonction de masse, les éléments de références (*focal elements*) seraient les volumes d'investigation. Ensuite, les fonctions de croyance (*belief* ou probabilité inférieure) et de plausibilité (probabilité supérieure) sont calculées pour l'intersection de quatre ou cinq enregistrements adjacents de diagraphie. Par conséquent, l'intervalle d'incertitude de DST sera entre les fonctions de croyance et de plausibilité. Tandis que la VRmf des diagraphies GR, RHOB, NPHI et DT est  $\sim 60$  cm, la VRmf des fonctions de croyance et de plausibilité est  $\sim 15$  cm. Or, on a perdu l'incertitude de la valeur de diagraphie, alors que la VRmf est devenue plus précise.

Les diagraphies ont été ensuite corrigées entre l'intervalle d'incertitude de DST avec quatre simulateurs. Les hautes fréquences sont amplifiées dans les diagraphies corrigées, et l'effet des épaules de couche est réduit. La méthode proposée est vérifiée dans les cas synthétiques, la boîte de carottage et la porosité de carotte. Les incertitudes de DST sur les diagraphies GR, RHOB et NPHI sont respectivement de 100%, 71% et 66%, donc inférieures à celles calculées par la méthode géométrique.

L'analyse de partitionnement (*cluster analyses*) est appliquée aux diagraphies NPHI, RHOB et DT en vue de trouver l'intervalle d'incertitude, basé sur les grappes. Puis, le NPHI est calibré par la porosité de carottes dans chaque grappe. Le RMSE de NPHI calibré est plus bas par

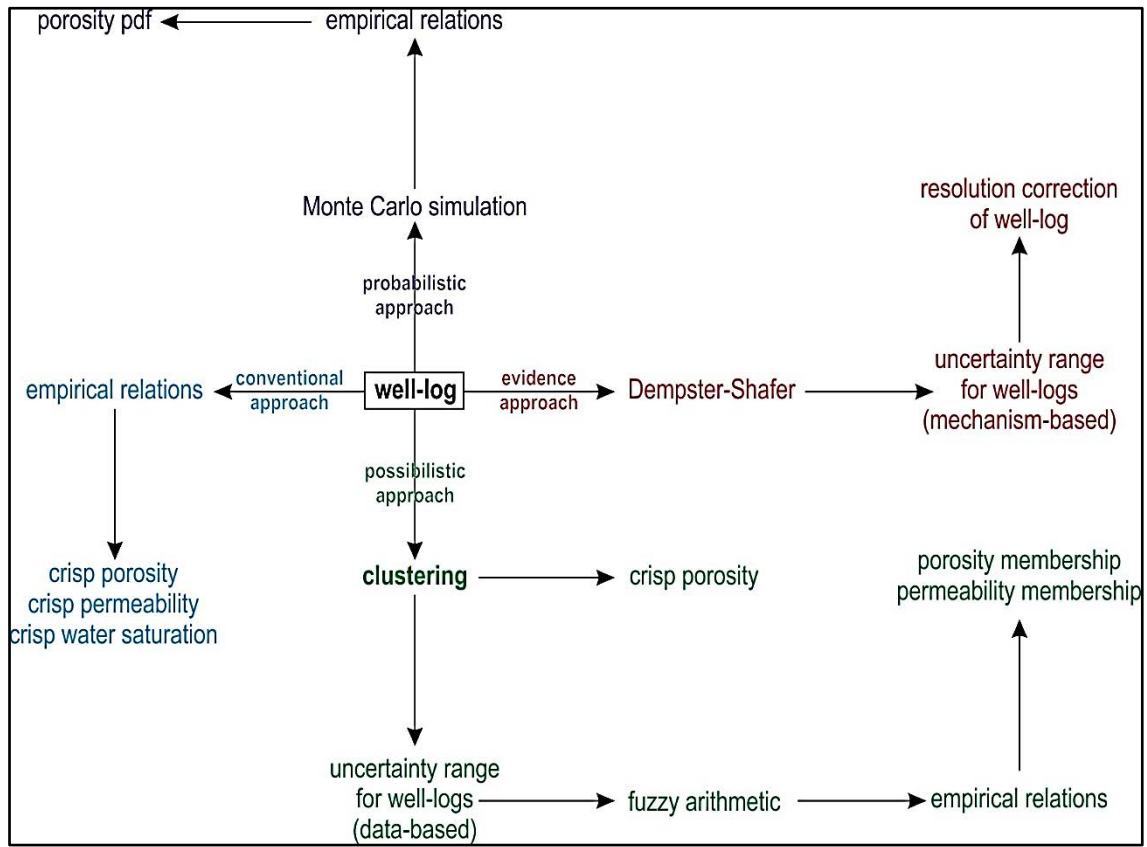
rapport aux cinq modèles conventionnels d'estimation de la porosité (au minimum 33% d'amélioration du RMSE). Le RMSE de généralisation de la méthode proposée entre les puits voisins est augmenté de 42%.

L'intervalle d'incertitude de la porosité est exprimé par les nombres flous (*fuzzy numbers*). L'arithmétique floue (*fuzzy arithmetic*) est ensuite appliquée dans le but de calculer les nombres flous de la saturation irréductible en eau et de la perméabilité. Le nombre flou de la saturation irréductible en eau apporte de meilleurs résultats en termes de moindre sous-estimation par rapport à l'estimation nette (*crisp*). Il est constaté que lorsque les intervalles de grappes de porosité ne sont pas compatibles avec la porosité de carotte, les nombres flous de la perméabilité ne sont pas valables, ex. du puits#4.

Enfin, pour les études géologiques, il est suggéré de considérer « l'échelle de l'étude » à côté d'autres conditions préalables de l'évaluation de l'incertitude, c'est-à-dire le but de l'étude et les sources de l'incertitude. Etant donné les trois conditions préalables, on peut choisir notre approche de l'évaluation de l'incertitude, puis choisir une théorie, donc une méthodologie. Un avantage qu'apporte la théorie possibiliste est que la coupure  $\alpha$  ( $\alpha$ -cut) peut être calibrée pour atteindre un intervalle de l'incertitude approprié, correspondant à l'échelle de l'étude.

**Mots-clés :** incertitude de diagraphie, résolution verticale, fréquence volumétrique de Nyquist, caractérisation de couche mince, Dempster-Shafer, arithmétique floue

# Graphical abstract



# 1 Introduction

## Highlights of the Chapter 1

- Volumetric mechanism of well-logging is one of the uncertainty sources of vertical resolution.
- The first objective of the thesis is to model the vertical resolution of well-logs.
- The second objective is to calculate a possibilistic uncertainty range of petrophysical interpretations, derived from well-logs.
- Due to the literature, the goal of the study and the sources of uncertainty have to be addressed for all the uncertainty assessment studies.

### 1.1 Uncertainty resources in well-logging

Well-log is a digital signal, acquired through a drilled well. It represents some properties (petrophysical, geometrical and sometimes geochemical) of the wellbore. Comparing to the other subsurface data, i.e. cores and well-tests, well-logs are more available, denser and more continuous. The sampling rate in well-logs is about 15 cm, however each sample belongs to a volume of investigation with the dimension of about 7- 160 cm ([Schlumberger, 2015](#)). The larger the dimension of the volume of investigation, the less precise the acquired data. Thin-bed problem arises when the beds are thinner than the vertical dimension of volume of investigation of the tool.

Resolution of well-logs could be discussed vertically or horizontally. Horizontal resolution is equivalent to the depth of investigation, and vertical resolution can be defined by: **(i)** sampling rate, **(ii)** Vertical Resolution of Tool (VRT) or spacing between transmitter and transducer, and **(iii)** domain of Vertical Resolution of membership function (VRmf) ([Figure 1-1](#)).

VRmf shows the degree of membership of the volume of investigation to each property value ([Masoudi \*et al.\*, 2017](#)). When the sample under study is completely homogeneous, VRmf could

be replaced by a single value. However when the heterogeneity rises, wider windows have to be used (Figure 1-2).

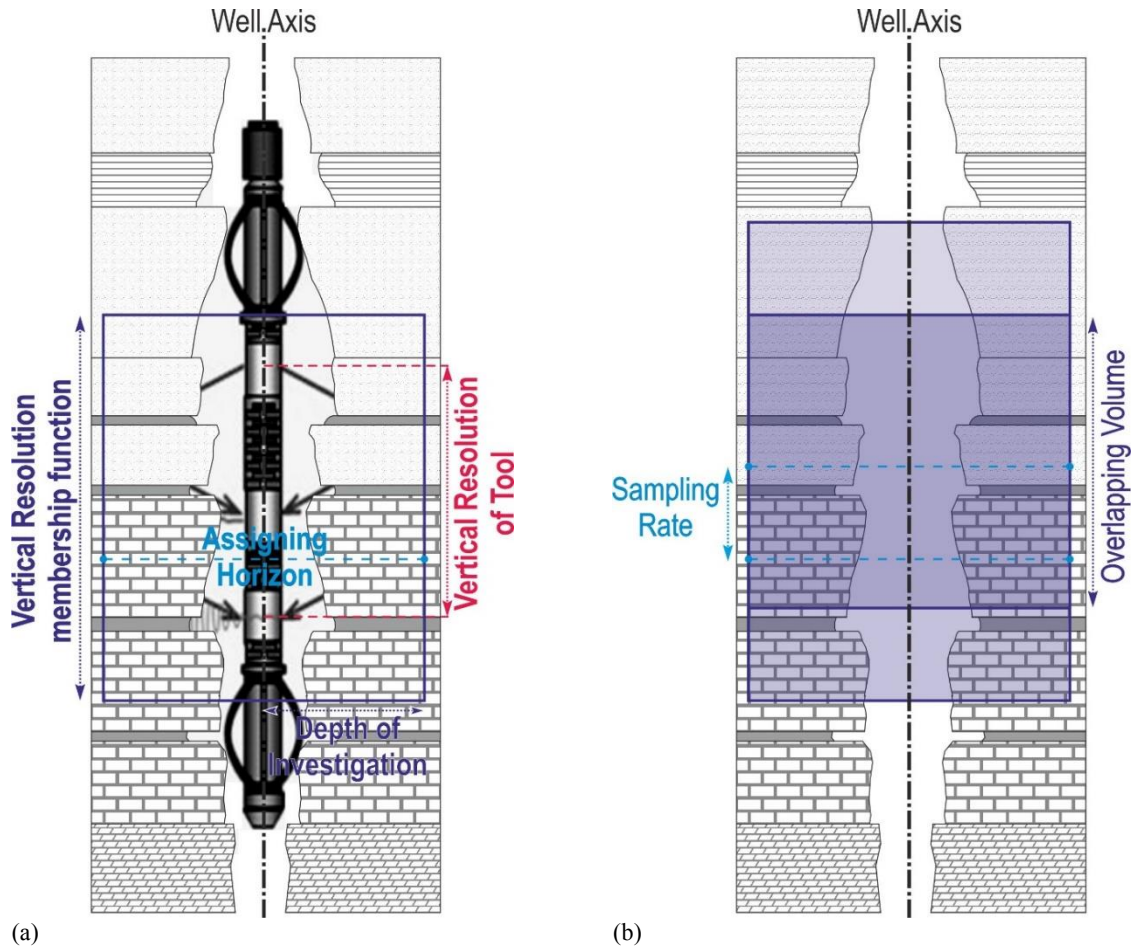


Figure 1-1. Schematic of basic concepts of logging: a) Vertical resolution of tool, membership function, depth of investigation and assigning horizon. b) Overlap of adjacent records and sampling rate.

In addition to the resolution problem, like all the sensory data, well-logs are noise contaminated: white and coloured noises. White noise is a part of a signal (in frequency domain) that is weakly stationary, zero mean and uncorrelated (Gray and Lee, 2007). It contains usually high-frequencies, so resembles random behaviour. The associated white noise of each instrument is provided within the catalogues of the logging tools, like in Schlumberger (2015). Coloured noise is biased, low-frequency, and is related to the environmental changes, like temperature and pressure. Since the coloured noise is not random and its source is known, it is possible to remove (or to reduce) the effect of coloured noises, e.g. correcting gamma well-log



by removing the effect of mud-weight on the measurements. All the explained sources of uncertainty in well-logs, are summarized in [Table 1-1](#).

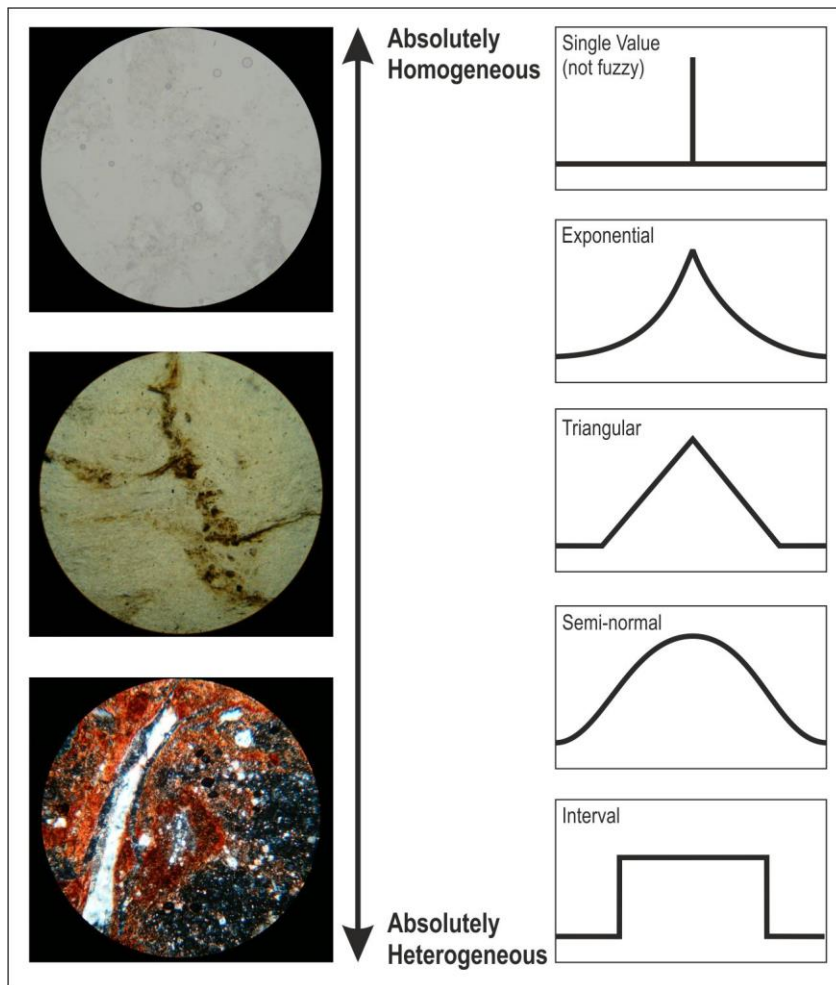


Figure 1-2. Using membership functions (right column) in representing a range of heterogeneity (lithology, porosity, etc.) of thin sections.

## 1.2 The thesis questions and objectives

### 1.2.1 Question I: vertical resolution of well-logs

In conventional well-log interpretations ([Figure 1-3](#)), each depth is interpreted according to the nearest well-log record, could be named distance-based interpretation. The mechanism of well-logging is not taken into account, and we think that this approach is not the most precise way of interpreting well-logs. Instead of assigning each depth to the nearest well-log record,

we try to assign each well-log record to the domain of VRmf (Figure 1-4). Regarding this general idea, two questions are introduced to be discussed within the thesis.

Table 1-1. Sources of uncertainty in well-logs.

Measurement aspect	Source of uncertainty	Studies
Intrinsic randomness of nature	- High complexities and heterogeneities in the nature	<a href="#">Kitts (1976)</a>
Depth of measurement	- Cable stretch - Logging while moving the instrument - Speed of logging	<a href="#">Passey et al. (2006)</a>
Depth of investigation	Volumetric measurement	
Vertical Resolution of Tool (VRT)	Volumetric measurement	<a href="#">Flaum et al. (1989)</a> <a href="#">Galford et al. (1989)</a> <a href="#">Gartner (1989)</a> <a href="#">Flaum (1990)</a>
Vertical Resolution of membership function (VRmf)	Volumetric measurement	<a href="#">Masoudi et al. (2017)</a> <a href="#">Passey et al. (2006)</a> : under the name of absolute resolution
Sampling rate	Digital recording	<a href="#">Passey et al. (2006)</a>
Error of measurement, precision and white noise	Sensors and tools	<a href="#">Gimbe (2015)</a> <a href="#">Bardy (2015)</a>
Coloured noise: environmental effects	- Temperature - Pressure - Mud weight - Borehole breakout - etc.	
Processing, calibration and interpretation	- Imprecise concepts - Incomplete subsurface information, - Human error - etc.	<a href="#">Moore et al. (2011)</a> <a href="#">Passey et al. (2006)</a> <a href="#">Bardy (2015)</a>

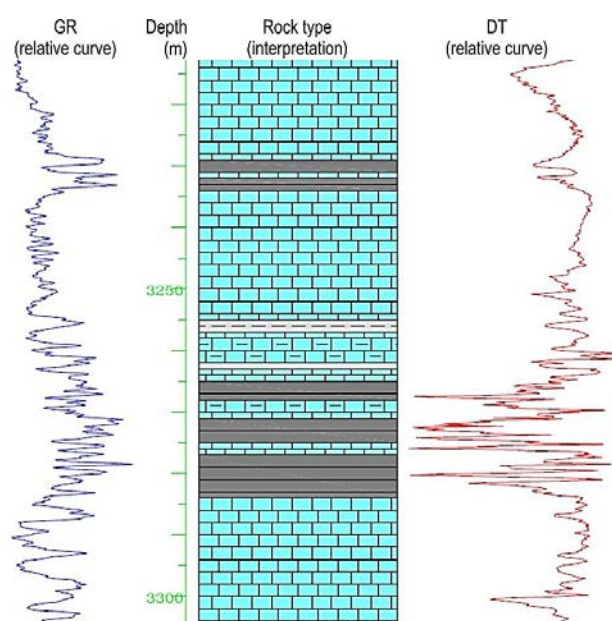


Figure 1-3. Conventional well-log interpretation. An example of rock typing ([NikTab, 2003](#)).

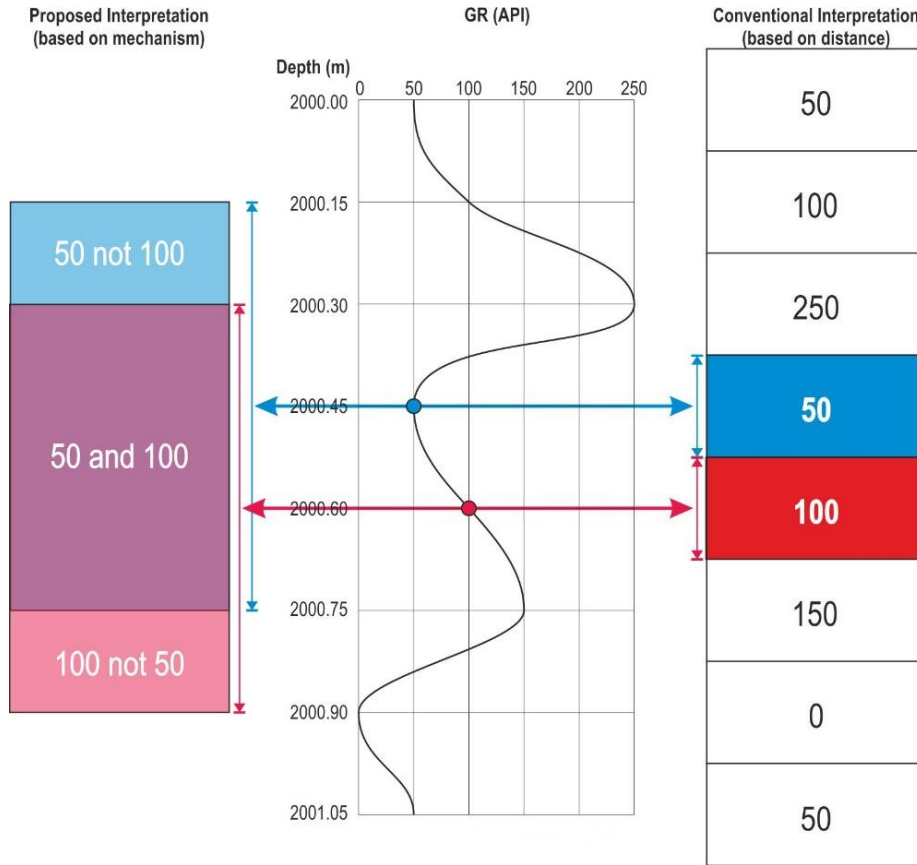


Figure 1-4. Comparing proposed and conventional interpretation approaches. Example of GR well-log.

The sources of uncertainty in well-log data is introduced in the previous part. Each source, [Table 1-1](#), adds its specific uncertainty range to the well-log value. The first question, going to be addressed, is assessing VRmf. The absolute resolution of well-logs is a function of specific tool's intrinsic resolution, sampling rate, logging speed and processing method ([Passey et al., 2006](#)). However in this thesis, this question primarily concerns the uncertainty of unprocessed data. Consider that a porosity well-log, e.g. neutron porosity (NPHI), is acquired over a range of real porosities ([Figure 1-5a](#)). The well-log shows 10% porosity, however the acquisition is taken place over a volume of investigation with the porosity range of [0%, 50%]. Even the height of the membership function is not necessarily equal to the well-log value. In this example, membership degree of the well-log value is higher than 0.9 ([Figure 1-5b](#)). The first objective is thus “**to approximate VRmf of well-logs.**”

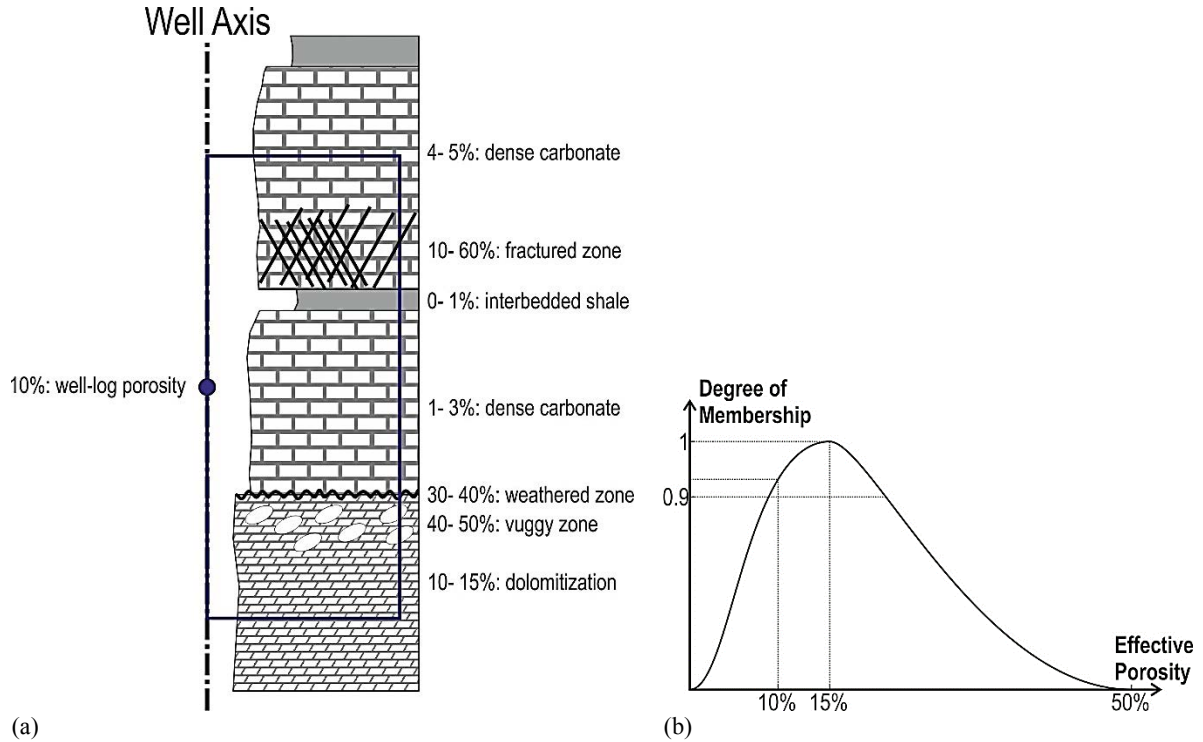


Figure 1-5. The importance of fuzzy evaluation of well-logs in porosity evaluation. a) Porosity, based on well-log (left) and real values (right). b) VRmf, which is here proposed to be used instead of single value. The height is at 15% and its domain consists of all the possible porosity values.

### 1.2.2 Question II: possibilistic uncertainty range of petrophysical parameters

The uncertainty range of acquired data should be propagated to the output of processed data and interpretations. So, the output (porosity, permeability, etc.) will have an uncertainty range, originated from the input well-logs. Therefore, the second objective of the thesis is “**to calculate possibilistic uncertainty range of petrophysical parameters, derived from well-logs.**” The uncertainty range is called “possibilistic” not to be confused with the uncertainty range of Monte-Carlo simulation, which is a “probabilistic” method. Also, from mathematical point of view, the possibilistic uncertainty range is a fuzzy measure, like in the Theory of Possibility, and not a Probability Distribution Function (PDF).

The well-logs gamma ray (GR), bulk density (RHOB), neutron porosity (NPHI) and sonic (DT) are chosen to apply the first objective on. For the second objective, porosity is studied comprehensively, permeability and water saturation are checked as well.

### **1.3 The importance of the thesis**

#### **1.3.1 Fundamental and scientific importance**

Well-logs are subsurface data, acquired from hundreds of meters up to about four kilometres. Therefore, precision and accuracy of the data is under doubt, and it is basically necessary to investigate the uncertainty of these data.

In addition, the volume of investigation is overwhelmed in the common well-log interpretations ([Figure 1-4](#)). In the proposed methodologies, the role of depth uncertainty is also considered in the interpretations.

The proposed methods are based on the theories of Dempster-Shafer, clustering and fuzzy logic, which are specialized for data processing in uncertain situation. Developing these utilities in a new domain, here petroleum geology, is another scientific contribution of the thesis.

#### **1.3.2 Application importance**

The first necessity of studying uncertainty is in identifying the main uncertainty sources, and quantifying their relative importance ([Dromgoole and Speers, 1997](#)). As an example, in [Lia et al. \(1997\)](#), two uncertainty sources associated in modelling reservoir production forecast are introduced: **(i)** heterogeneity uncertainty, caused by geometrical arrangement; **(ii)** model parameter uncertainty because of incomplete knowledge of the whole reservoir properties. In this study, it is shown that heterogeneity uncertainty causes 25% of the total uncertainty, while model parameter uncertainty causes 75% of the whole uncertainty.

The importance of this thesis for the petroleum industry is to improve the vertical resolution of well-logs. The improved well-logs could be used for better characterization of the thin-beds.

#### **1.3.3 Economic and management importance**

The term “exploration” is defined idealistically as “a series of investment decisions made with decreasing uncertainty” ([Rose, 1987](#)). It shows the close relation of both concepts of

“uncertainty” and “decision-making”. Based on [Megill \(1979\)](#), the “Risk” is “an opportunity for loss”, and the “uncertainty” is defined as “the range of probabilities that some condition may exist or occur” ([Rose, 1987](#)).

[Rose \(1987\)](#) also introduced two criteria for continuing an exploration activity: **(i)** consistency with the strategy of investor in dealing with risk and uncertainty; **(ii)** understanding uncertainty accurately, and reducing it if possible. Meanwhile investors must cope with the issue of “risk” to come to reasonable decisions, engineers have to solve the problem of “uncertainty” to provide as clear illustration from the prospect as they can. In an uncertain situation (related to the exploratory activities), there are several biasedness: **(i)** prospect target size, **(ii)** discovery probability, and **(iii)** cost of finding.

From the economical viewpoint, the uncertainty is divided into two parts: risk and immaterial. Immaterial refers to those uncertainties, unimportant to business, whereas risk refers to the uncertainty of which is critical for business. Again, risk is classified into two types: opportunity and threat. The threat reflects risky uncertainties, threatening the enterprise, while the opportunity risk is a risky uncertainty, which might cause opportunities to the business ([Smalley et al., 2008](#)).

“Uncertainty is the only certainty in oil exploration.” It is a famous *cliché* in oil business ([Fang and Chen, 1990](#)). Lack of certainty in exploratory activities associates risk in investments. The terminology of “Responsible Reporting” is discussed in [McLane et al. \(2008\)](#), comprehensively. It discusses that an understanding of uncertainty is necessary for responsible reporting.

## **1.4 Literature review**

### **1.4.1 Uncertainty in sciences**

Philosophical debate on the concept of “uncertainty” backs to “skepticism”. Pyrrho (270-360 BC), who is rendered as being the first skeptic philosopher, reached to this idea that nothing is certain. So, his students and followers did not cry on his death because they did not believe

his death ([Durant, 1953](#)). Empiricism (observation) and rationalism (skepticism included) are two complementary or competing views in the epistemology. The former emphasizes on the importance of sensory data, while the latter concerns reasoning and certainty of human's knowledge.

The debate on certainty of sensory data is not restricted to schools of philosophy. Maybe Thomas Bayes (mathematician and philosopher, lived between 1701 and 1761) is the first scientist who entered the concept of uncertainty in statistics and mathematics by his famous theory of probability. Another historic and well-known measure of uncertainty in mathematics and statistics is “variance”, which shows how data (or simulations) are distributed around a center. Also, error bar is a conventional tool for expressing uncertainty range as in [Wong \(2003\)](#).

Since then, the concept of uncertainty gradually entered in different applications, amongst electronics and telecommunication have benefited the most, by the development of “Information Theory” ([Shannon, 1948](#)). Shannon relation of uncertainty is the development of works of Harry Nyquist and Ralph Hartley in the Bell System Company, with the aim of development of communicating systems. Shannon's formula is so fundamental that nowadays it is a famous measure of uncertainty in different domains of science as geosciences.

Scientists of electronics were pioneer in development of another theory in assessing uncertainty: Theory of Fuzzy, which was a paradigm shift in electronics. Generalizing the Set Theory, [Zadeh \(1965\)](#) introduced a new language for expressing membership of an element to a definite set. Instead of using two values (0 or 1) for indicating membership of an element, he used a membership function that its output could be within the interval of  $[0, 1]$  ([Zadeh, 1965](#)). These days, fuzzy logic is used vastly in various fields of science and engineering, and in geology as well ([Demicco and Klir, 2004](#)). Based on the concept of fuzziness, clustering algorithms were modified to develop fuzzy clustering tools, in order to use membership functions in stating degree of membership of data to clusters. Review of fuzzy clustering methods could be found in [Baraldi and Blonda \(1999\)](#), [Krishnapuram and Keller \(1993\)](#) and [Pal et al. \(2005\)](#). A review of possibilistic, fuzzy and neural models is also presented in [Bezdek \(1993\)](#).

Researchers of statistics and artificial intelligent were able in developing a rival for fuzzy logic. Dempster-Shafer Theory (DST) of evidences is another methodology in evaluating data within uncertain situation. By means of defining “mass function”, researchers were able in further developing Bayes rule to Dempster rule of combination to fuse output of multi-sensory detections under uncertain condition ([Dempster, 1967, 1968; Shafer, 1976, 1990](#)).

#### **1.4.2 Uncertainty in geosciences and petroleum exploration**

Intrinsic randomness of nature is perhaps the first source of uncertainty that is mentioned in geological texts. However, retrodiction is never as uncertain as prediction ([Kitts, 1976](#)). The word “retrodiction” could be of interest of geologists since it is composed of the word “prediction” when the prefix “pre” is replaced by “retro”.

Another pioneer work on uncertainty assessment in core orientation could be found in [Nelson \*et al.\* \(1987\)](#). In quantifying uncertainty in petroleum volume estimation, fuzzy arithmetic (Theory of Possibility) is declared to provide better results, comparing to Monte-Carlo method (Theory of Probability) ([Fang and Chen, 1990](#)). Monte-Carlo simulation is a traditional technique for calculating uncertainty of estimated hydrocarbon volume. For further study about probabilistic Monte-Carlo method, refer to [Hurst \*et al.\* \(2000\)](#) and [Masoudi \*et al.\* \(2011\)](#).

The uncertainty is categorized into two types: vagueness (equivalent to fuzziness, haziness, cloudiness, unclearness and sharplessness) and ambiguity (non-specificity, diversity, divergence, generality, variety and one-to-many). Three sources of uncertainty are introduced: lack of information, intrinsic nature and ignorance ([Fang and Chen, 1990](#)).

In a comprehensive study, fuzzy aggregation is used for reservoir appraisal ([Chen and Fang, 1993](#)). In this work, four trap properties (type, size, closure and timing), five reservoir properties (porosity, permeability, net thickness, depth and saturation), five source rock properties (richness, organic matter, maturity, thickness and area), migration distance and seal integrity, i.e. 16 geologic variables in overall, are fused to assess prospects. In brief, an appraisal method is introduced in this paper, which uses fuzzy aggregation methodology to easily integrate different reservoir properties.



Foley *et al.* (1997) classified uncertainty into three categories: fuzziness, randomness and incompleteness. Incompleteness is equivalent to ignorance, which is one of the sources of uncertainty, introduced in the work. Some authors also classified incompleteness into four categories: **(i)** what we know but have not included in the model; **(ii)** what we know that we do not know; **(iii)** what we do not know that we are unaware of it; and finally **(iv)** what is difficult to understand.

The concept “geoscore” was introduced by Dromgoole and Speers (1997) to measure the complexity of petroleum reserves by quantifying nine categories:

- **Structural complexity:** **(i)** overburden complexity; **(ii)** fault complexity;
- **Reservoir quality and architecture:** **(iii)** reservoir layering; **(iv)** reservoir continuity; **(v)** permeability channels; **(vi)** barrier continuity; **(vii)** fault transmissibility; **(viii)** fractures and **(ix)** diagenesis.

The key achievement of this study is: the higher the geoscore, the less hydrocarbon recovery and the more overestimation of reservoir volume. It was also advised at the end of the paper that for accurate reserve estimation during appraisal, we need to: **(i)** recognize the key uncertainties; **(ii)** quantify the relative importance of uncertainties; and **(iii)** collecting data to reduce uncertainties or being prepared to handle potential problems may arise during development or production. This paper (Dromgoole and Speers, 1997), and the paper of Yeh *et al.* (2014) have well presented the importance of uncertainty assessment in economic evaluation and production forecast, respectively.

Hurst *et al.* (1999) tried to link between the concepts of sequence stratigraphy and the concept of uncertainty. In their paper, there is a discussion about characterizing sandy pinch-out genesis, i.e. infill or onlap types, and correlating sand bodies between wells. Although mathematical basis of this paper is not in-detail, there is a robust geological debate on how to differentiate infill and onlap pinch-outs based on petrophysical and rock sedimentary properties.

Application of probabilistic and fuzzy partitioning on interpreting satellite images is addressed successfully by Matsakis *et al.* (2000). In this paper, image classification is

distributed into classes of lagoon, conglomerate, vegetation, coral rubble, deep water, etc. with the precisions higher than 75%. For mathematical comparison between fuzzy, probabilistic and possibilistic partitioning, refer to [Anderson \*et al.\* \(2010\)](#).

Another application of the concept of uncertainty in production problems is presented in [Zheng \*et al.\* \(2000\)](#). In this paper, the uncertainty of permeability estimation is lowered by combining results of two measurements of permeability: well tests (meso-scale) and core tests (micro-scale). Calibrating both types of data has confined estimation of permeability to smaller range. It seems that this methodology is more certain comparing to conventional approach, since (i) training is constrained to well-test, and (ii) well-test is a measure of permeability of the reservoir, whereas, core permeability is only indicator of permeability of intact rock.

Fuzzy logic is inherently a suitable tool to characterize vague and imperfectly defined situations, like in geological datasets. Therefore, [Saggaf and Nebrija \(2003\)](#) proposed using fuzzy logic in lithological and depositional facies predictions. In their work, accuracy of fuzzy logic in facies prediction is stated to be more than 90% in every run.

For probabilistic hydrocarbon pore-thickness evaluation in intervals (47.6 ft = 14.5 m) with beds thinner than 1 ft (30 cm), Volumetric Laminated Sand Analysis (VLSA) method is developed. The method uses Monte-Carlo simulation for generating realizations, and providing PDF of output, i.e. petrophysical parameters. 400% improvement in accuracy of hydrocarbon pore-thickness estimation is reported by this method ([Passey \*et al.\*, 2004](#)). In this thesis, VLSA is used as a base method for comparing the outputs with.

Geological risk mapping in play level is produced by multivariate and Bayesian methodology ([Chen and Osadetz, 2006](#)). In this work, risk analysis problem is defined as “equivalent to classification with uncertainty in a multivariate space”.

Determination and geostatistical inversion are compared with each other for the purpose of net-pay determination through seismic data ([Sams and Saussus, 2008](#)). Determination method provides higher uncertainties, comparing to geostatistics method. For reservoirs with thinner stratigraphic layers, the magnitude of this difference rises, especially when the beds become thinner than vertical resolution of seismic data.

Grandjean *et al.* (2007, 2009a,b) performed some researches on the application of fuzzy logic in slope stability, hydrogeology and geo-engineering. Their papers present a systematic algorithm for implementing a fuzzy inference system to fuse multi-source geo-data. The systematic algorithm they used contains four stages: **(i)** preparing geo-dataset; **(ii)** creating possibility function (membership function), regarding the purpose; **(iii)** providing technical hypothesis for fusing variables; and **(iv)** checking or discussing hypothesis or outputs of fusion (Grandjean *et al.*, 2007, 2009a,b; Hibert *et al.*, 2012).

In order to handle structural uncertainty in petroleum reserves, Thore *et al.* (2002) considered aggregation of side-effects of all processing and interpreting stages on the final results. Preparation of structural model by seismic studies generally consists of six stages, each one is a source of uncertainty in constructing structural model: acquisition, pre-processing, stacking, migration, time-to-depth conversion and interpretation. In this paper, migration, picking and time-to-depth conversion are introduced as dominant uncertainty resources; and amplitude, direction and correlation length of each are incorporated in calculations. In the article, it is also specified that computation of structural uncertainties has several benefits: **(i)** providing a distribution of gross rock volume; **(ii)** defining optimal well trajectories; and **(iii)** reservoir history matching.

In a recent paper about assessing structural uncertainty, Seiler *et al.* (2009) proposed an elastic grid to be adjustable and trainable due to history of reservoir production. The methodology is approved by synthetic dataset, and is potentially a new frontier for structural uncertainty handling in petroleum appraisal for the next years.

The most comprehensive text book about uncertainty in geosciences is composed by Caers (2011). Five different sources of uncertainty in earth sciences are introduced in the book: **(i)** measurement and processing errors; **(ii)** multiple ways of interpreting processed data; **(iii)** type of geological setting; **(iv)** spatial uncertainty, which is related to heterogeneity and scale of the study; and **(v)** response uncertainty, e.g. solving partial differential equations needs initial and boundary conditions that is sometimes uncertain.

The most important prerequisite to uncertainty assessment is stated to be “purpose of the study”; therefore, fit-for-purpose approach is suggested for quantifying uncertainty in each

study (Caers, 2011). The majority of the book is concerned with geostatistical methodologies, and how to assess uncertainty besides geostatistical modelling. However some simpler uncertainty tools as tornado chart is introduced likewise.

A bootstrap-based methodology for uncertainty analysis when predicting effective porosity by seismic attributes is presented by Ortet *et al.* (2012). The authors have introduced this novel methodology as an alternative to standard geostatistical simulation. They have also stated that in cases the main source of uncertainty is related to the calibration set, bootstrap-based method is well adapted.

For assessing uncertainty of seismic interpretations, picking, four constraints are introduced (Yang *et al.*, 2013): (i) best estimate control point; (ii) best estimate surface; (iii) uncertainty envelope; and (iv) uncertainty envelop surface. Based on this method, more than one realization would be generated that helps interpreters to calculate the probability of each realization.

Uncertainty assessment in pore pressure prediction is carried out by Wessling *et al.* (2013). The paper discusses that the uncertainty, which is associated with the pore pressure, is contributed by geophysical measurements, geological model and manual processing steps. Measurement-related uncertainties could be quantified (and maybe compensated); whereas, it is difficult to handle the uncertainty of descriptive geologic models or manual processing stages. It is suggested in Wessling *et al.* (2013) that, in order to quantify and control uncertainty of a manual processing, we can substitute this part with an automation. This change will result in a more transparent output for interpreters, hence, easier to quantify and assess the uncertainty.

Within a recently defended PhD thesis, the uncertainty of static models is projected to dynamic models. So, the quantiles (P10, P50 and P90) of production prediction curve were calculated, considering a set of geostatistical realizations (Bardy, 2015).

#### ***1.4.2.1 Application points***

Though there are many publications about the concept, definition and categorization of uncertainty in earth-related studies, the application of uncertainty assessment in exploration activities is not well-developed. Two common pragmatic points could be derived from the

literature for all the uncertainty assessment applications: **(i)** what is the aim from uncertainty assessment (Caers, 2011)? **(ii)** What are the sources of uncertainty in the dataset (Chen and Fang, 1993; Dromgoole and Speers, 1997; Lia *et al.*, 1997; Thore *et al.*, 2002; Wessling *et al.*, 2013)?

To rebuild uncertainty bounds of well-logs and propagate it to the petrophysical outputs, Monte-Carlo simulation is used in industrial software applications Techlog- Schlumberger (Gimbe, 2015) and Geolog Datamin Uncertainty Module Paradigm. The algorithm is the same as VLSA, presented for thin-bed studies by researchers of ExxonMobil (Passey *et al.*, 2004).

## 1.5 Introducing datasets

### 1.5.1 Basic definitions

We used four key terms to introduce the datasets: “Well-log”, “real-log”, “synthetic-log” and “ideal-log”. The first two terms describe real data, while the last ones are related to synthetic data.

- A well-log records intrinsic or induced properties of the rocks and their fluids (Gluyas and Swarbrick, 2009). Such records, acquired through a well, are either one dimensional, like gamma ray log, or two dimensional as image logs. Well-log is also known as borehole log since the data are captured through the wellbore.

- A real-log reflects real properties of the well-bore. Well-logs are imprecise (apparent values) in reflecting real properties, especially in thin-bed conditions because well-logs are convolved data (Gartner, 1989). The convolution is applied over an interval of vertical resolution of the logging tool. When this interval approaches zero, the well-log converges to the real-log.

- An ideal-log is equivalent to “real-log” in synthetic datasets. It is defined by the user, while real-log represents rock properties in the nature. Finding the real-log is an open problem, while the ideal-log is definite, so useful in validation.

- A synthetic-log is convolution of an ideal-log over a vertical resolution. It resembles well-log in real data.

### 1.5.2 Synthetic data

The first stage in generating a synthetic-log is defining specifications of its ideal-log (Table 1-2). Ideal-logs (real-logs) are not volumetric signals, i.e. no depth uncertainty.

In Table 1-2, each case represents a petrophysical change in presence of a thin-bed (cases 1-5 and 7) or a single fracture (case 6). Synthetic-log generator for thin-beds (cases 1-5 and 7) convolves the ideal-log (for more details see Chapter 5). For the case 6, simulator generates a synthetic-log based on geological specifications of a single fracture. It calculates the effect of a predetermined fracture on the well-log (Mazaheri *et al.*, 2015).

### 1.5.3 Real data

Well-log data of five exploratory wells were used to check the developed methodology. The wells are located on the axis of an anticlinal oil-field in the Abadan Plain, SW Iran (Figure 1-6). The subsurface data are limited to the Sarvak Formation. Summary of available data and specifications of some well-logs are provided in Table 1-3 and 1-4, respectively.

Table 1-2. Specifications of the ideal-logs to generate the synthetic logs.

Case	Well-log	Description	Lower bed	Thin-bed or fracture	Upper bed	Bed thickness (cm)	Vertical resolution (cm)
1	GR (API)	There is a peak at the horizon of the thin-bed.	20	50	30	30	61
2	GR (API)	Deepening (finning) upward	20	100	120	30	61
3	RHOB (g.cm <sup>-3</sup> )	There is a trough at the horizon of the thin-bed.	2.8	2.4	2.6	15	76
4	NPHI (%)	Increasing upward	5	10	15	30	76
5	NPHI (%)	There is a peak at the horizon of the thin-bed.	5	15	10	30	76
6	DT (μs.m <sup>-1</sup> )	A single fracture with a dip of 60°, aperture of 1 mm, filled up with oil (281 μs/m), within a carbonate formation.	160	281	160	0.1	61
7	DT (μs.m <sup>-1</sup> )	A 1 cm horizontal fractured zone (50% fractured) with a DT of 220 μs/m, within a carbonate formation.	160	220	160	1	61

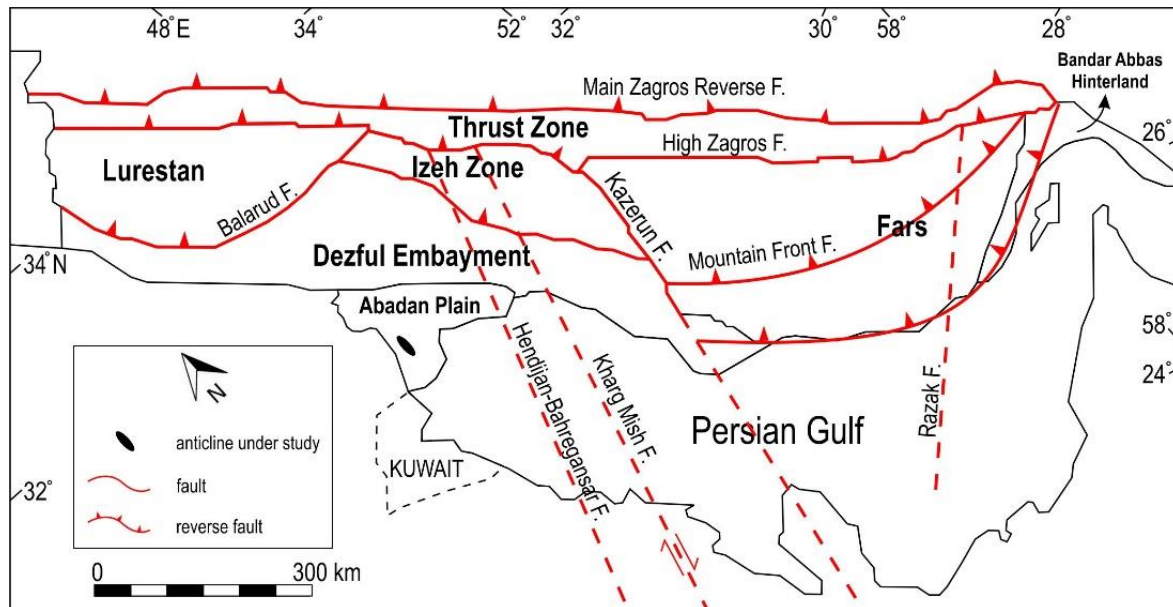


Figure 1-6. Location of the field under study within the Abadan Plain, SW Iran. Modified after [Sherkati and Letouzey \(2004\)](#) and [Rajabi et al. \(2010\)](#).

Table 1-3. Available data within the Sarvak interval. #: number. GR: gamma ray, CGR: gamma ray of potassium, DT: sonic transfer time, NPHI: neutron porosity, RHOB: bulk density, DRHO: density correction, LLD: deep laterolog, LLS: shallow laterolog, MSFL: microspherically focused log, PEF: photoelectric effect.

		W1	W2	W3	W4	W5	W6
Well-logs	Calliper	✓	✓	✗	✓	✓	✓
	GR	✓	✗	✓	✓	✓	✓
	CGR	✓	✓	✓	✓	✓	✓
	DT	✓	✓	✓	✓	✓	✓
	NPHI	✓	✓	✓	✓	✓	✓
	RHOB	✓	✓	✓	✓	✓	✓
	DRHO	✓	✗	✓	✓	✗	✗
	LLD	✓	✓	✓	✓	✓	✓
	LLS	✓	✓	✓	✓	✓	✓
	MSFL	✓	✓	✓	✓	✓	✓
	PEF	✓	✗	✗	✓	✓	✗
Core tests	# of plugs	2	8	5	4	6	0
	# of helium porosity records	38	41	416	228	258	0
	# of gas permeability records	38	41	418	228	250	0
	# of grain density records	0	34	0	244	258	0
	# of irreducible water records	0	0	3	0	9	0
Well tests		6	3	6	3	0	2

Table 1-4. Details of the available well-logs in the field due to [Schlumberger \(2015\)](#).

Well-log	Accuracy	Depth of Investigation (cm)	Vertical Resolution of Tool (spacing) (cm)
GR	±5%	60.96	30.48
RHOB	±0.01 g.cm <sup>-3</sup>	12.70	45.72
NPHI	0-20: ±1% 20-30: ±2% 30-45%: ±6%	~23	30.48
DT	±6.6 μs.m <sup>-1</sup>	7.62	91 152

### 1.5.3.1 Geology of the Sarvak Formation

The type section of the Sarvak Formation (thickness of 832 m) is in the Bangestan Mountain, Khuzestan Province, Iran. It is a hydrocarbon producing formation in many oil fields in the Zagros. The Sarvak Formation is mostly overlaying the Kazhdumi Formation and is overlaid by the Ilam Formation ([Ghazban, 2009](#)). However, in the study area, there is the eight meters-thick Laffan Formation between the Ilam and Sarvak formations ([Figure 1-7](#)).

Sarvak Formation is a homoclinal carbonate ramp, deposited during Albian to Turonian ([Mehrabi \*et al.\*, 2015](#)). In homoclinal carbonate ramps, there is a slight seabed dip toward the sea. This term belongs to a topological classification of carbonate ramps ([Read, 1985](#)). The lithology of Sarvak Formation is wackestone-packstone. The upper Sarvak Formation belongs to a shallower environment, comparing to the pelagic facies of the middle and lower Sarvak Formation ([James and Wynd, 1965](#); [Ghabeishavi \*et al.\*, 2010](#)).

From the viewpoint of sequence stratigraphy, four sequences of the third-order (duration of 1.5-3 Ma and thickness of 50-150 m) are distinguished in the Sarvak Formation. Several sequences of the fourth- and fifth-order are also reported ([Razin \*et al.\*, 2010](#); [Vincent \*et al.\*, 2015](#)).

There is a depositional gap at the top of the Sarvak Formation (Cenomanian unconformity), which has improved reservoir quality of the upper Sarvak Formation ([Figure 1-8](#)). In most



regions, vuggy porosity, karstification and bauxite mineralization are consequences of the depositional gap of the top Sarvak ([Zarasvandi \*et al.\*, 2008](#)) ([Figure 1-9](#)).

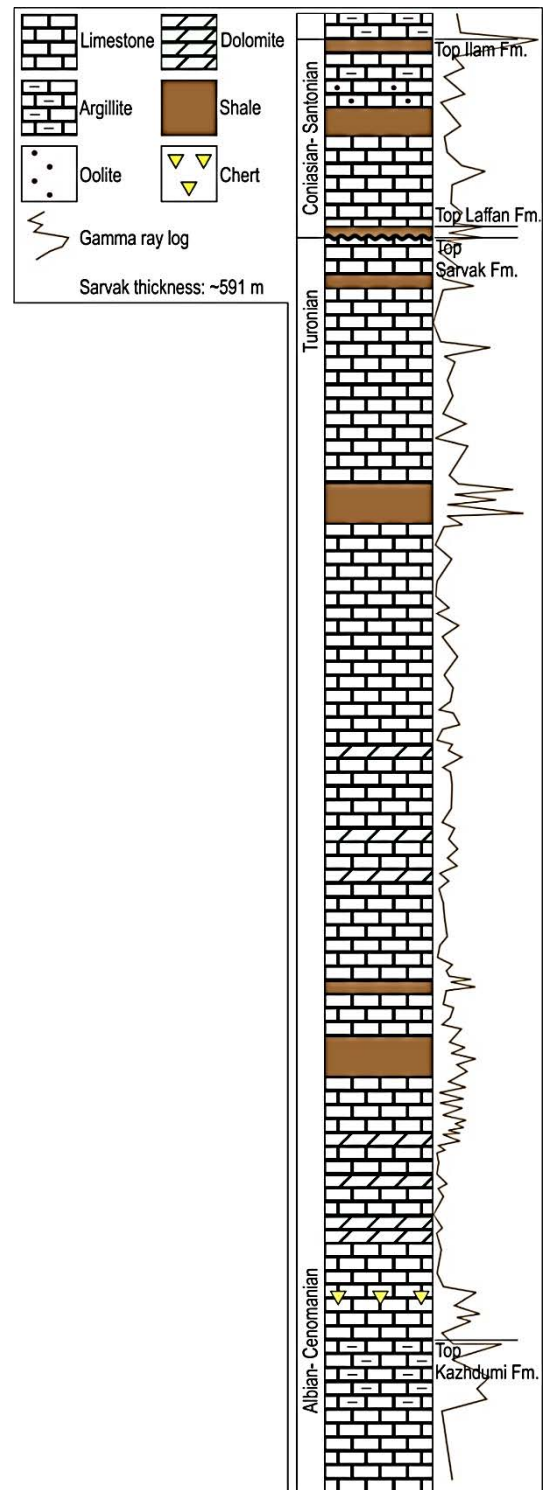
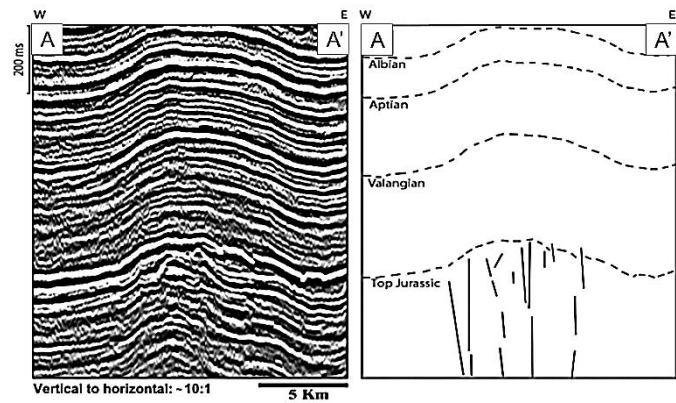
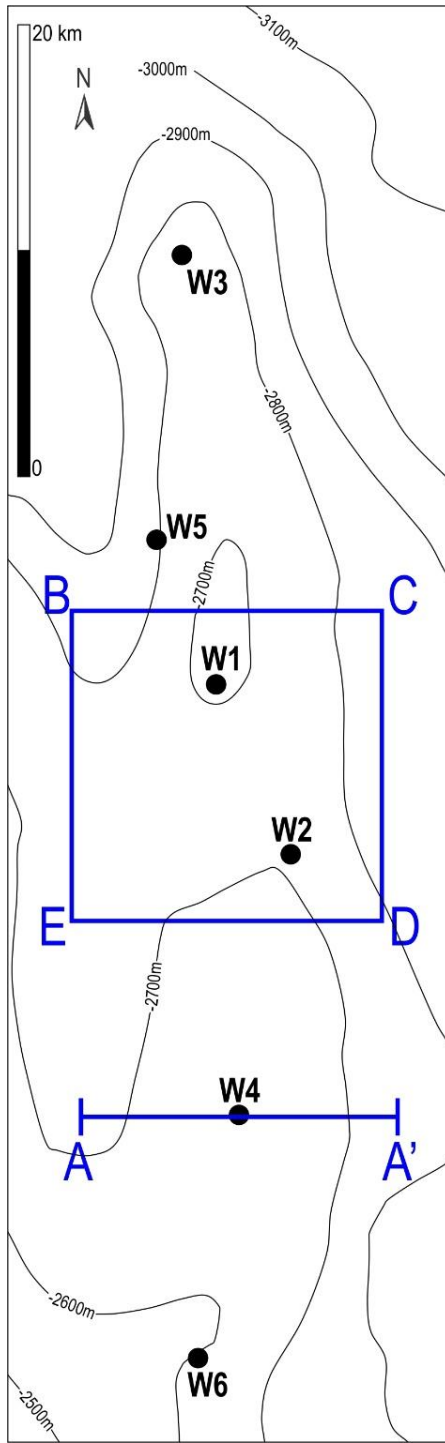
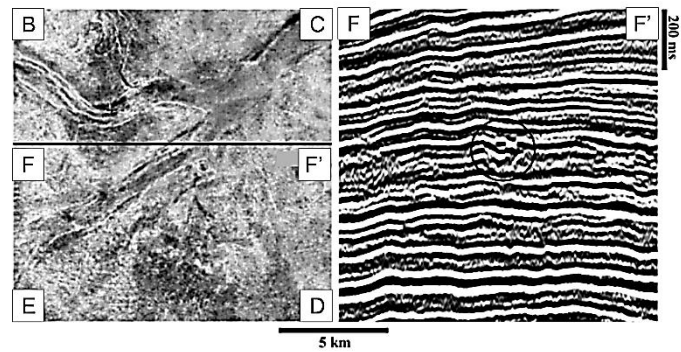


Figure 1-7. Lithostratigraphy of the Sarvak Formation and its neighbours ([Dashtban, 2002](#)).



(b)



(c)

Figure 1-8. a) Underground contour (UGC) map of the top Sarvak Formation in the study area. b) AA' seismic section and its interpretation. c) Root mean square volumetric seismic amplitude attribute map, within 30 ms of the upper Turonian (the top Sarvak Formation, time slice of BCDE). The channelling of the top Sarvak Formation is shown on the FF' seismic section (circle) (Abdollahie Fard *et al.*, 2006).



(a)



(b)





(c)

Figure 1-9. Photos of the Sarvak Formation. a) Yugs on the top of Sarvak Formation, Siyah-Kuh anticline, near Dehloran city, Ilam province ([Masoudi et al. 2017](#)).  
 b) Weathering of the top Sarvak Formation, between Mary-Dasht (plain) and Takht-e Jamsnid, Shiraz province. c) The unconformity: contact of the Sarvak and Ilam formations, Siyah-Kuh anticline, near Dehloran city, Ilam province.

## 2 Theories

### Highlights of Chapter 2

- For the purpose of uncertainty assessment of well-logs, three theories are used, essentially Dempster-Shafer Theory (DST), fuzzy arithmetic and cluster analysis.
- The main theories, in addition to empirical petrophysical relations, are introduced in the chapter.
- The other utilized theories, techniques and concepts; e.g. Nyquist frequency, Bayesian Theory and Monte-Carlo simulation, are also addressed in the thesis.

### 2.1 Dempster-Shafer Theory of evidences

This theory is developed in the domain of subjective probability, useful in evaluating uncertain phenomena. The most basic difference between the Theory of Probability (Bayesian) and DST is that no distribution (PDF or membership function) is considered in DST. So, the mass function (equivalent to PDF) could freely move within its focal element, while satisfying imposed limitations of Body Of Evidence (BOE). In [Figure 2-1b](#), the mass of A can move freely within the set A; while in [Figure 2-1a](#), the probability of A is distributed according to a predefined triangular PDF.

The result of removing the PDF constraint is providing a range of uncertainty for outputs. So, belief function is defined as the least possible (necessity) mass value of a focal element, and plausibility is defined as the highest possible mass value (capacity) of the focal element. Belief and plausibility values have to satisfy the predefined mass functions of each basic focal element. As an example, in [Figure 2-1b](#) plausibility does not exceed mass function within  $A \cup B$ , especially in  $A \cap B$  that honours both focal elements. Belief function within  $A \cap B'$  is also expected to compensate some part of the required mass function of focal element of A, when  $A \cap B$  is completely full.

For studying DST in detail, refer to [Dempster \(1967, 1968\)](#), [Klir and Yuan \(1995\)](#), [Liu and Yager \(2008\)](#) and [Shafer \(1990\)](#). The first stage in applying DST is constructing a BOE.

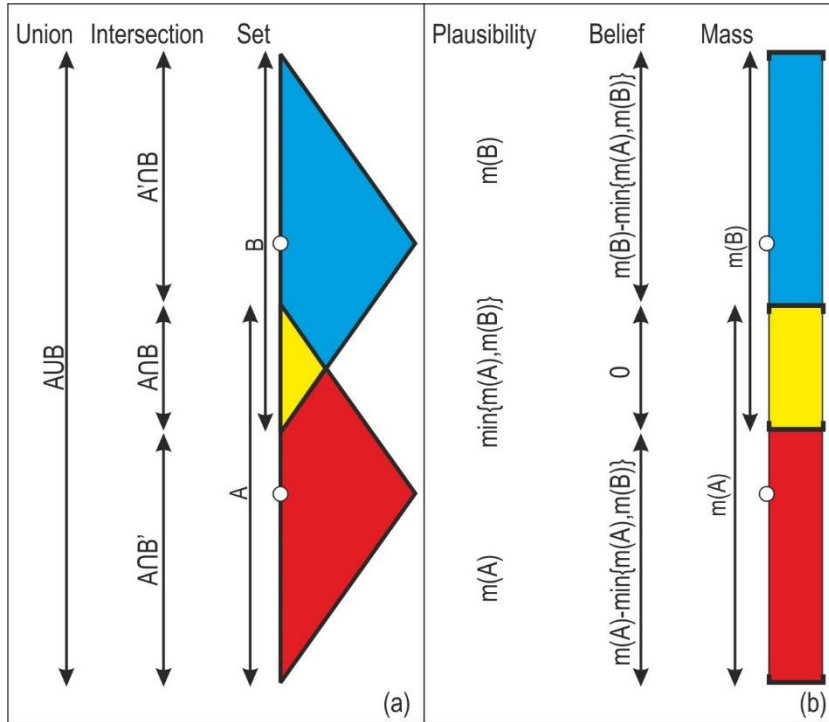


Figure 2-1. Comparing uncertainty assessment theories: probability (a) and DST (b).

## 2.1.1 Body Of Evidences

For constructing a BOE, focal element and corresponding mass function have to be defined. Focal element is a set of elements that a mass function is attributed. The theory does not apply any specific rule on the structure of focal elements, and they are only defined due to the mechanism of data acquisition or gathering. Here, we considered each well-log record as a mass value, corresponding to its volume of investigation, i.e. focal element.

### 2.1.1.1 Mass function

Lack of restrictions on the mass function makes it move freely within its focal element. Mass function is always non-negative, and the summation of mass values over all the focal elements (FE) should be one ([Liu and Yager, 2008](#)). The symbol " $\triangleq$ " in [Relation 2-1](#) means that this equation is defined by user, and is not derived from calculations. This normalization is essential

for combining the results in multisensory situations, as utilized e.g. in [Masoudi et al. \(2014\)](#). In DST, null set ( $\phi$ ) represents unpredicted situations. If it is not important to model the unpredicted situations:  $m(\phi) = 0$ . And if it is important to model the unpredicted situations, the mass function of null set has to be higher than zero.

$$\sum_{i=1}^n m(FE_i) \triangleq 1 \quad (2-1)$$

### 2.1.2 Belief and plausibility functions

Based on BOE, lower (belief) and upper (plausibility) probabilities are defined for each focal element of target. The focal elements of belief and plausibility are not necessarily the same as the focal elements of mass function. They could be defined by the user. Belief (plausibility) function shows the least necessary (most possible) mass value within the focal element of target ([Liu and Yager, 2008](#)).

$$Pls(FE_i) \triangleq \sum_{FE_j \cap FE_i \neq \phi} m(FE_j) \quad (2-2)$$

$$Bel(FE_i) \triangleq \sum_{FE_j \subseteq FE_i} m(FE_j) \quad (2-3)$$

### 2.1.3 Consistency of uncertainty assessment theories

Before applying each uncertainty assessment theory on a defined BOE, we have to analyse whether the theory is compatible with the BOE or not. The analysis of a dice game, using the Probability Theory, leads to a PDF with the probability of  $\frac{1}{6}$  for each of the six sides. In this example, the BOE consists of six focal elements, each containing only one number (one to six). The focal elements do not have any intersection with each other, e.g. when the dice shows number four, it cannot hold any other value simultaneously. So, the Theory of Probability is compatible with dice game.

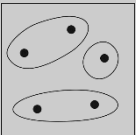
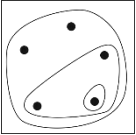
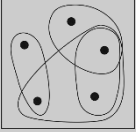
In the other example, consider a person who may eat some eggs (e.g. one to six eggs) at breakfast. The Probability Theory could be used to predict how many eggs he eats every day.

So, due to statistics (*a priori* knowledge), he mostly eats two or three eggs per day, rarely zero, one or four, and never five or six eggs. Thus, the PDF has zero value for cases five and six, and a height at two and three eggs.

Approaching this problem by the possibility theory means that possibility of eating four eggs has the possibility of eating three, two or one egg(s). In the language of the set theory, from each pair of focal elements, one is subset of the other. So, the focal elements are eccentric and the result will be cumulative (a property of fuzzy measure) with the highest possibility for eating one egg, and the lowest possibility for eating five eggs.

Therefore, the Probability Theory is applicable in completely separated focal elements and the Possibility Theory is applicable in eccentric focal elements (Table 2-1). The ability of free movement of the mass function in the DST, has made it powerful in assessing all BOEs (separated, eccentric, etc.). So, wherever the Possibility (or Probability) theory works, DST works too. When theories of Probability (Possibility) and DST are valid, we call that DST and Probability (Possibility) are consistent (Table 2-1).

Table 2-1. Consistency of BOEs with uncertainty assessment methodologies.

Schema of focal elements	Property of focal elements	Theory of probability	Theory of possibility	DST	Consistency
	separated	compatible	incompatible	compatible	consistency of DST and probability
	eccentric	incompatible	compatible	compatible	consistency of DST and possibility
	intersected and not eccentric	incompatible	incompatible	compatible	inconsistency

For checking the consistency, we either can analyse the focal elements or the consistency conditions. The simplest consistency condition is that the probability value, be between the values of belief and plausibility (Klir and Yuan, 1995):



$$Bel(FE_i) \leq Pr(FE_i) \leq Pls(FE_i) \quad (2-4)$$

## 2.2 Fuzzy arithmetic

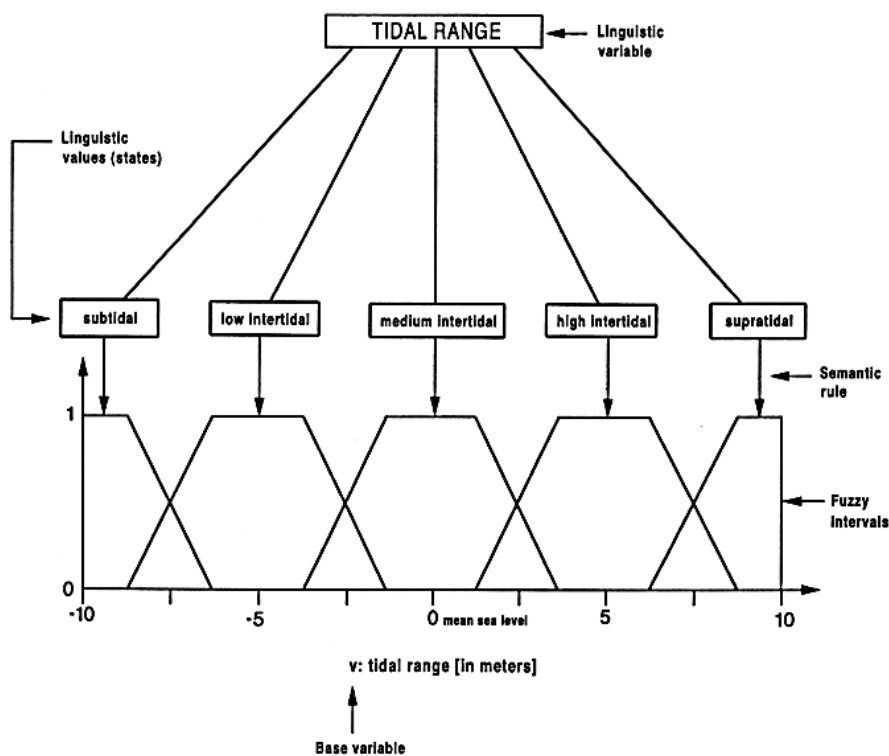
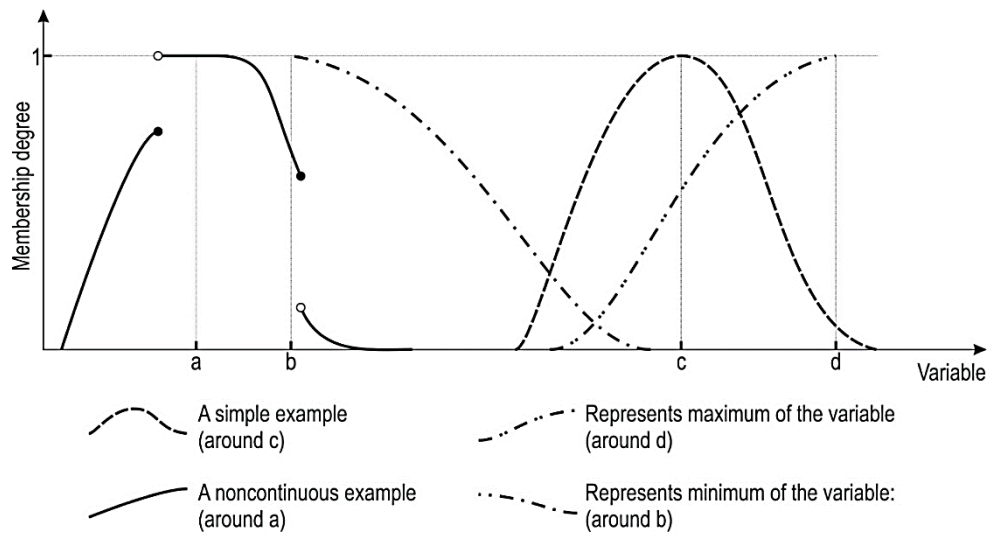
Common arithmetic, applied on the crisp numbers, is still the dominant arithmetic, being used in the science. However, it is some decades that interval arithmetic and fuzzy arithmetic are playing role of complementary tools, when there are uncertainties or impreciseness about the numbers. Interval arithmetic is applied on the intervals, instead of numbers; and fuzzy arithmetic is a generalization of the interval arithmetic when a fuzzy membership, called fuzzy number, is defined on the intervals.

The first time, fuzzy arithmetic was developed for calculating linguistic variables. For example, “age” is a linguistic variable that can obtain different values: child, teenager, young and old. The basics of a fuzzy variable, fuzzy operations (complement, union, intersection, product, convex combination, Cartesian product and fuzzification) and relations between the variables are discussed in [Zadeh \(1975a\)](#). Successively, mathematical introduction of a fuzzy variable and Boolean operators for applying on the fuzzy variables are extended ([Zadeh, 1975b](#)). In the next step, the Theory of Probability and approximate reasoning for fusing multiple fuzzy variables are developed ([Zadeh, 1975c](#)). Later, the concept of fuzzy variable is called fuzzy number, and is used for two major imperatives: **(i)** the available information is too imprecise to justify the use of the common numbers, and **(ii)** there is a tolerance for imprecision ([Zadeh, 1996](#)).

### 2.2.1 Fuzzy number

We use fuzzy number when ordinary number is not justifiable in representing the data. Fuzzy number is a fuzzy membership function possessing three properties: **(i)** It should be a normal (unimodal) fuzzy number. **(ii)** Each  $\alpha$ -cut of the fuzzy number should be a closed interval for every  $\alpha \in (0,1]$ . The consequence is that the height of the fuzzy number have to be one. **(iii)** The support of the fuzzy number should be bounded, i.e. does not support  $\infty$  ([Klir and Yuan, 1995](#)).

As examples, extensions of ordinary numbers  $a$ ,  $b$ ,  $c$  and  $d$  to fuzzy numbers are presented in Figure 2-2 to show different possibilities of fuzzy numbers. In the domain of sedimentology, trapezoidal fuzzy numbers are used for representing tidal ranges by mean sea-level (Figure 2-3).



### 2.2.2 Arithmetic operations on intervals

Based on [Relation 2-5](#), arithmetic operators on intervals ([Relations 2-6 to 2-8](#)) are derived. Considering four intervals A, B, C and D, seven famous arithmetic axioms are valid for the defined operators, [Table 2-2](#).

$$[a, b] * [c, d] = \{f * g \mid a \leq f \leq b; c \leq g \leq d\} \quad (2-5)$$

$$[a, b] \pm [c, d] = [a \pm c, b \pm d] \quad (2-6)$$

$$[a, b]. [c, d] = [\min(ac, ad, bc, bd), \max(ac, ad, bc, bd)] \quad (2-7)$$

$$[a, b] / [c, d] = [a, b]. \left[ \frac{1}{c}, \frac{1}{d} \right] \quad (2-8)$$

Table 2-2. Available axioms for the defined interval operators. Summarized from [Klir and Yuan \(1995\)](#).

	Axiom	Definition
1	Community	$A + B = B + A$ $A . B = B . A$
2	Associativity	$A + (B + C) = (A + B) + A$ $A . (B . C) = (A . B) . A$
3	Identity	$A = A + 0$ $A = A . 1$
4	Subdistributivity	$A . (B + C) \subseteq A . B + A . C$
5	Distributivity	If: $b . c > 0$ , for every $b \in B$ and $c \in C$ , then: $A . (B + C) = A . B + A . C$ So if $A = [a, a]$ , then $a . (B + C) = a . B + a . C$
6	Inverse of identity	$0 \in A - A$ $1 \in A / A$
7	Inclusion monotonicity	If: $A \subseteq C$ and $B \subseteq D$ , then: $A * B \subseteq C * D$

### 2.2.3 Arithmetic operations on fuzzy numbers

There are two approaches in developing arithmetic operations on fuzzy numbers: based on **(i)** interval arithmetic or **(ii)** extension of operations on real numbers. The interval operators could be extended to fuzzy operators, using the theorem of resolution identity, [Relations 2-9](#) and [2-10](#) ([Zadeh, 1971](#)). The other name of this relation is first decomposition theorem.

$$A = \bigcup_{\alpha \in [0,1]} \alpha . {}^{\alpha}A \quad (2-9)$$

$$A * B = \bigcup_{\alpha \in [0,1]} \alpha. {}^{\alpha}(A * B) = \bigcup_{\alpha \in [0,1]} \alpha. ({}^{\alpha}A * {}^{\alpha}B) \quad (2-10)$$

where A and B are two fuzzy numbers, and \* represents a fuzzy operator, going to be applied on them. An example of applying fuzzy operators on two fuzzy numbers is given in [Figure 2-4](#).

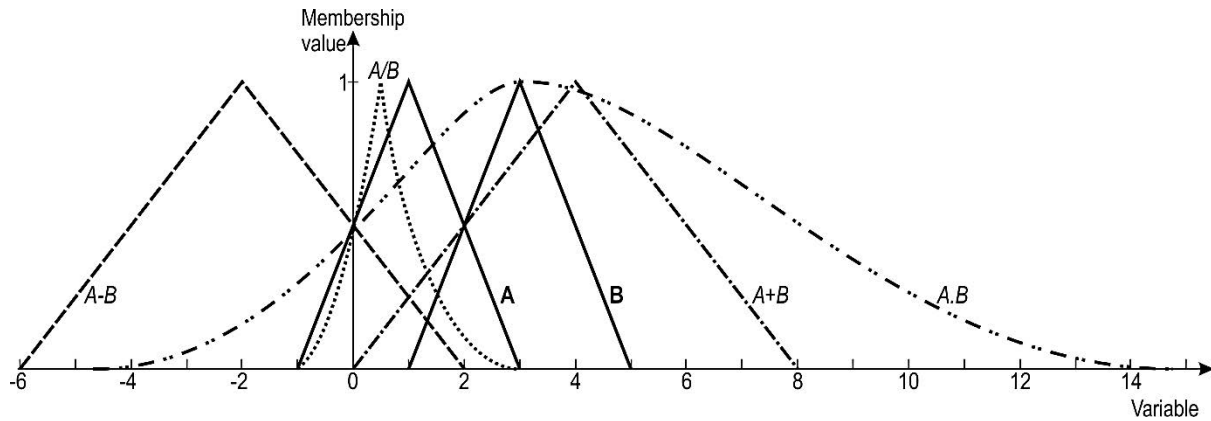


Figure 2-4. Example of applying fuzzy operators on fuzzy numbers, integrated from [Klir and Yuan \(1995\)](#).

Extension of operations on real numbers to fuzzy numbers could be defined by applying an axiomatic structure. The axioms indicate our expectations from fuzzy operators, inspired from common operators ([Klir and Yuan, 1995](#)). Some researchers believe that current standard fuzzy operators need to be revised. The reason is that the output of standard operators does not resemble the output of operators of real numbers in some cases; e.g.  $A - A \neq 0$  ([Klir, 1997](#)).

### 2.3 Cluster analysis

Cluster analysis is an unsupervised learning method to decompose a dataset into some sets of objects, i.e. clusters, based on a similarity index. Labelling data by clustering methods helps primarily in understanding the structure of data, in data reduction as well ([De Oliveira and Pedrycz, 2007](#)).

Among different domains in the earth sciences, geochemistry benefitted the most from clustering in separating the anomalous area from the background ([Templ et al., 2008](#); [Meshkani et al., 2011](#)). In lithofacies prediction by fuzzy partitioning, clustering is used to detect structure of multidimensional well-log data. Each cluster is considered as a potential

fuzzy classification rule, i.e. a fuzzy if-then rule (Finol *et al.*, 2001). Similarly in reservoir zonation, statistical and intelligent clustering methods are tested. Self-organizing map neural network is the most successful clustering tool for lithofacies categorization (Sfidari *et al.*, 2014). In reservoir characterization, clustering is used for studying productive zones, saturation or permeability variations (Moradi *et al.*, 2015; Masoudi *et al.*, 2016).

For a finite dataset, clustering algorithm searches for  $c$  prototypes, cluster centers, representative of  $c$  clusters. The data points are grouped with the nearest prototype, based on a measure of distance (Klir and Yuan, 1995). Four clustering algorithms are used in this thesis: k-means (KM), Fuzzy C-Means (FCM), Gustafson-Kessel (GK) and Gath-Geva (GG) algorithms.

### 2.3.1 k-means and fuzzy c-means algorithms

“The aim of the k-means algorithm is to divide  $m$  points in  $n$  dimensions into  $k$  clusters so that the within-cluster sum of squares is minimized” (Hartigan and Wong, 1979). In a simple language, the algorithm of k-means starts with selecting  $k$  data points randomly (primary clusters) from the dataset. In the next step, each point will be added to its nearest cluster, and the means of clusters should be readjusted (the reason why this method is called k-means) (MacQueen, 1967).

Using fuzzy partitioning (Relation 2-11) instead of crisp cluster labels, resulted in fuzzy c-means (FCM) algorithm. It means that summation of degrees of membership ( $A_i$ ) of each data point  $x_k$  to each of  $c$  clusters is one.

$$\sum_{i=1}^c A_i(x_k) = 1 \quad (2-11)$$

The algorithm of FCM consists of four steps below, illustrated in Figure 2-5 (Klir and Yuan, 1995):

(i) Primary definitions:

(i-i) Put the counter of iteration:  $t=0$

**(i-ii)** Define number of clusters,  $c$ .

**(i-iii)** Randomize an initial fuzzy partition:  $\mathcal{P}^{(0)} = \{A_1, A_2, \dots, A_c\}$

**(i-iv)** Choose a fuzzifier:  $m \in (1, +\infty)$ . Actually, there is no theoretical way for optimizing  $m$  but trial and error by [Relation 2-16](#). We suggest an easy number of 2.

**(i-v)** Define the convergence limit:  $\varepsilon$

**(ii)** Calculate the cluster centres  $v_i^{(t)}$  in [Relation 2-12](#): It is a weighted average of data points. The weights are due to the defined membership function  $A_i^{(t)}$ . This relation is driven from descent-based optimization of [Relation 2-16](#), i.e.  $\frac{\partial J}{\partial v} = 0$  ([Gustafson and Kessel, 1978](#)).

$$v_i^{(t)} = \frac{\sum_{k=1}^n [A_i^{(t)}(x_k)]^m \cdot x_k}{\sum_{k=1}^n [A_i^{(t)}(x_k)]^m} \quad (2-12)$$

**(iii)** Update the fuzzy pseudopartition  $\mathcal{P}^{(t+1)}$  by [Relation 2-13](#). This relation is also driven from descent-based optimization of [Relations 2-16](#) and [2-11](#) ([Gustafson and Kessel, 1978](#)).

$$A_i^{(t+1)}(x_k) = \left[ \sum_{j=1}^c \left( \frac{\|x_k - v_i^{(t)}\|^2}{\|x_k - v_j^{(t)}\|^2} \right)^{\frac{1}{m-1}} \right]^{-1} \quad (2-13)$$

The term  $\|x_k - v_i^{(t)}\|$  is Euclidian distance between the data point  $x_k$  and the cluster center  $v_i^{(t)}$ . If for some clusters ( $i \in I \subseteq \mathbb{N}_c$ ):  $\|x_k - v_i^{(t)}\| = 0$ ; then define  $A_i^{(t+1)}(x_k)$  for  $i \in I$  by any non-negative real numbers that satisfies [Relation 2-14](#), and zero for the other membership functions:  $A_i^{(t+1)}(x_k) = 0$ ;  $i \in \mathbb{N}_c - I$ .

$$\sum_{i \in I} A_i^{(t+1)}(x_k) = 1 \quad (2-14)$$

(iv) Check the stopping condition:  $|\mathcal{P}^{(t)} - \mathcal{P}^{(t+1)}| \leq \varepsilon$ ; otherwise increase  $t$  and return to step (ii).

The distance could be defined by the user, e.g. the maximum change of membership function in [Relation 2-15](#). Performance index,  $J_m(\mathcal{P}^{(t)})$ , could be used also as a cluster validity. The lower  $J_m(\mathcal{P}^{(t)})$  is the more acceptable ([Relation 2-16](#)).

$$|\mathcal{P}^{(t)} - \mathcal{P}^{(t+1)}| = \max_{i \in \mathbb{N}_c, k \in \mathbb{N}_n} |A_i^{(t+1)}(x_k) - A_i^{(t)}(x_k)| \quad (2-15)$$

$$J_m(\mathcal{P}^{(t)}) = \sum_{k=1}^n \sum_{i=1}^c [A_i^{(t)}(x_k)]^m \cdot \|x_k - v_i^{(t)}\|^2 \quad (2-16)$$

Where  $\mathbb{N}_c$  and  $\mathbb{N}_n$  are sets of cluster numbers and numbers of data points, respectively.

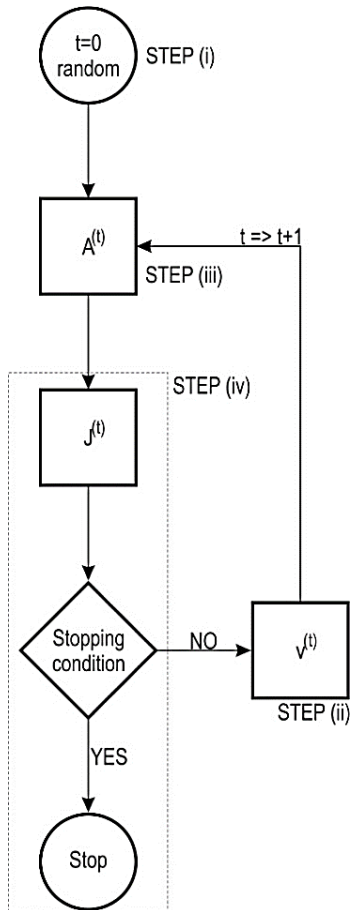


Figure 2-5. Flowchart of the FCM algorithm.

### 2.3.2 Gustafson-Kessel clustering technique

Neither KM nor FCM are suitable algorithms for oriented or multi-sized clusters. In the FCM algorithm, if the Euclidian distance (Relation 2-17) is replaced by the Mahalanobis distance (Relation 2-18) the new algorithm, Gustafson-Kessel (GK), would be capable of detecting uni-sized (in terms of number of data) but oriented (linear at extreme mode) clusters too (Gustafson and Kessel, 1978; Babuka *et al.*, 2002).

$$\|x_k - v_i\|^2 = (x_k - v_i)(x_k - v_i) = \sum_{j=1}^f (x_{k,j} - v_{i,j})^2 \quad \text{Euclidian distance} \quad (2-17)$$

$$\|x_k - v_i\|^2 = (x_k - v_i)^T C_i (x_k - v_i) \quad \text{Mahalanobis distance} \quad (2-18)$$

where:

$x_k = \{x_{k,1}, x_{k,2}, \dots, x_{k,f}\}$ : Vector of  $k$ th data point.

$v_i = \{v_{i,1}, v_{i,2}, \dots, v_{i,f}\}$ : Vector of center of  $i$ th cluster.

$C_i$ : Covariance matrix of  $i$ th cluster. A square matrix with the size of number of clusters.

### 2.3.3 Gath-Geva clustering technique

Gath-Geva (GG) algorithm solved clustering problems of (i) multi-sized clusters, and (ii) number of clusters. Fuzzy Maximum Likelihood Estimation (FMLE) or GG is a development on the FCM algorithm (Gath and Geva, 1989):

(i) Primary definitions and cluster centers calculation ( $v_i^{(t)}$  in Relation 2-12): the same as steps (i) and (ii) in FCM but  $c$  is the maximum number of clusters.

(ii) Cluster with the fuzzy modification of the maximum likelihood estimation:

(ii-i) Calculating fuzzy covariance matrix for  $i$ th cluster:



$$F_i = \frac{\sum_{k=1}^n A_i(x_k)(x_k - v_i)(x_k - v_i)^T}{\sum_{k=1}^n A_i(x_k)} \quad (2-19)$$

**(ii-ii)** Calculating exponential distance measure:

$$\|x_k - v_i\|^2 = \frac{\sqrt{\det(F_i)}}{\frac{1}{n} \sum_{k=1}^n A_i(x_k)} \exp \left[ \frac{1}{2} (x_k - v_i)^T F_i^{-1} (x_k - v_i) \right] \quad (2-20)$$

**(ii-iii)** Updating fuzzy partitioning:

$$A_i(x_k) = \frac{\frac{1}{\|x_k - v_i\|^2}}{\sum_{i=1}^c \frac{1}{\|x_k - v_i\|^2}} \quad (2-21)$$

**(iii)** Compute performance measures that is based on three criteria: **(iii-i)** Separation of clusters (low fuzzy hypervolume, [Relation 2-22](#)), **(iii-ii)** Minimal volume of the clusters, but **(iii-iii)** Maximal number of data points, concentrated in the vicinity of the cluster centroid (high average density partition, [Relation 2-23](#) or high density partition, [Relation 2-24](#)).

$$F_{HV} = \sum_{i=1}^c \sqrt{\det(F_i)} \quad (2-22)$$

$$D_{PA} = \frac{1}{c} \sum_{i=1}^c \frac{\sum_{k=1}^n u_{i,k}}{\sqrt{\det(F_i)}} \quad (2-23)$$

$$P_D = \frac{\sum_{i=1}^c \sum_{k=1}^n u_{i,k}}{F_{HV}} \quad (2-24)$$

If the  $k$ th data point is within a hyperellipsoid, centered at the cluster prototype of the  $i$ th cluster with radii of one standard deviation of each feature, then  $u_{i,k}$  is the distance between the  $k$ th data point and the  $i$ th cluster. Otherwise, it is zero to exclude far data points from calculations of (average) density partition.

**(iv)** If number of clusters is lower than the predefined maximum, increase the number of clusters, and go to (iii). Otherwise stop the algorithm, then choose the best cluster number due to performance measures.

## 2.4 Empirical relations in petrophysics

Using empirical relations in reservoir characterization is very common. All the well-log interpretation software applications contain some of these relations for estimating reservoir properties: porosity, permeability, saturation, rock typing, etc. The focus of the thesis is on the porosity, then permeability. In the next step, results of irreducible water are provided in some cases. Since there is not a measurement for evaluating saturation results, it is not discussed as porosity and permeability properties.

### 2.4.1 Porosity study by well-logs

Porosity could be studied by three well-logs: neutron porosity (NPHI), bulk density (RHOB) and sonic (DT). NPHI is a measure of hydrogen content. Since this element exists in the water and hydrocarbons (not in solid phase of formations), so NPHI is a measure of whole the porous media, i.e. total porosity either effective or non-effective (Johnson and Pile, 2002). RHOB has negative correlation with NPHI since higher the porosity, lower the density. Despite the former logs, DT represents only secondary porosity, like fractures or vuggy porosity. In fact, DT is sensitive to the discontinuities that result in dispersion of sonic waves (Johnson and Pile, 2002). Therefore peaks in DT could be interpreted as fractured or porous zones.

#### 2.4.1.1 One-log porosity methods: neutron- or density-based

The response of NPHI and RHOB could be modelled by Relation 2-25. The acquired log value is summation of matrix, shale, hydrocarbon and water parts.

$$\begin{aligned} \log &= \varphi_e \cdot S_{XO} \cdot \log_w + && \text{Water term} && (2-25) \\ \varphi_e \cdot (1 - S_{XO}) \cdot \log_h + && \text{Hydrocarbon term} && \\ V_{sh} \cdot \log_{sh} + && \text{Shale term} && \\ (1 - V_{sh} - \varphi_e) \cdot \sum v_i \cdot \log_i && \text{Matrix term} && \end{aligned}$$

where  $\varphi_e$  and  $V_{sh}$  are effective porosity and volume of shale, both in fraction.  $\log_w$ ,  $\log_h$ ,  $\log_{sh}$  and  $\log_i$  are log readings (either NPHI or RHOB) in 100% water, hydrocarbon, shale and

the  $i$ th component of matrix rock, respectively.  $S_{XO}$  is water saturation in invaded zone (fractional). Finally,  $v_i$  is the volume of  $i$ th component of matrix rock.

In this thesis, since the dataset belongs to a gas-free reservoir, the difference between the log reading in water and hydrocarbon horizons is neglected,  $\log_w = \log_h$ . Also, the invaded zone is considered completely full of drilling water  $S_{XO} = 1$  (Crain, 2000). It means that water and hydrocarbon terms are integrated into a single term.

$$\log^{(s)} = \frac{\log - \log_{ma}}{\log_w - \log_{ma}} \quad \text{Lithology correction} \quad (2-26)$$

$$\varphi_{log} = \log^{(s)} - V_{sh} \cdot \log_{sh} \quad \text{Shale correction} \quad (2-27)$$

where  $\log^{(s)}$  is scaled log value.  $\log_w$  and  $\log_{ma}$  are log responses in 100% water saturation and rock matrix, respectively (lithology correction).  $\varphi_{log}$  is the final porosity value from NPHI or RHOB logs. In case of occurrence of gas, applying neutron gas correction factor is necessary (Crain, 2000).

### 2.4.1.2 Two-log porosity methods

#### 2.4.1.2.1 Density-neutron (shaly sand) cross-plot

Although this method is widely used, it is not recommended. It is used here since still is found in log analysis software applications. Complex lithology models are recommended instead of shaly sand models, because most of sandy reservoirs contain other minerals than quartz and clay minerals. The output of Relation 2-26 for the logs NPHI and RHOB, i.e.  $NPHI^{(s)}$  and  $RHOB^{(s)}$ , are inputs of this method. The shale correction will be applied through the algorithm (Crain, 2000):

If  $NPHI^{(s)} \geq RHOB^{(s)}$ , i.e. there is no gas crossover, so:

$$\varphi_{DN} = \frac{RHOB^{(s)} \cdot NPHI_{sh}^{(s)} - NPHI^{(s)} \cdot RHOB_{sh}^{(s)}}{NPHI_{sh}^{(s)} - RHOB_{sh}^{(s)}} \quad (2-28)$$

Otherwise:

$$\varphi_{DN} = \sqrt{\frac{1}{2} \left( RHOB^{(s)^2} - NPHI^{(s)^2} \right)} \quad (2-29)$$

There is a quick-look (Relation 2-30) for density-neutron porosity method which uses the output of Relation 2-27. In the version of quick-look, the gas crossover is not accounted since shale corrections result in apparent gas crossover, which is an artifact. In addition, in the shale zones, there are some recommendations: **(i)** for  $RHOB_{sh}^{(s)}$ , replace zero for the range of -0.03 to 0.12; and **(ii)** for  $NPHI_{sh}^{(s)}$ , replace 0.30 for the range of 0.10 to 0.40 (Crain, 2000).

$$\varphi_{DN}^{(q)} = \varphi_{NPHI} + \frac{1}{3}(\varphi_{NPHI} - \varphi_{RHOB}) \quad (2-30)$$

#### 2.4.1.2.2 Complex lithology

This model is developed to be used in complex lithological situations, and it is the best available empirical relation for the porosity estimation. If  $\varphi_{NPHI} \geq \varphi_{RHOB}$ , i.e. no gas crossover, and really the gas does not exist (Crain, 2000):

$$\varphi_{LC} = \frac{1}{2}(\varphi_{NPHI} + \varphi_{RHOB}) \quad (2-31)$$

But if there is gas crossover after shale correction and we are sure that gas is present:

$$\varphi_{LC} = \sqrt{\frac{1}{2}(\varphi_{NPHI}^2 + \varphi_{RHOB}^2)} \quad (2-32)$$

Finally, if there is no gas crossover after shale correction but we are sure about the presence of gas, a correction based on the photoelectric log is necessary (Crain, 2000), which is out of the scope here. All the above-mentioned relations are applied through a spreadsheet (Figure 2-6) to the five wells, under study.

### 2.4.2 Irreducible water saturation

Calculating irreducible water is a prerequisite for permeability modelling by well-logs and estimating water-cut. In core testing, it is measurable by increasing capillary pressure. Before perturbing the initial equilibrium of the reservoir fluids by production, above the water contact,

the irreducible water is equal to the actual (initial) water saturation ( $S_{wir} = S_w$ ). But in transition, water and depleted zones, it is not:  $S_{wir} \leq S_w$ . So we need to calculate it. The difference between  $S_w$  and  $S_{wir}$ , and relative permeability are controlling factors of water-cut. The used algorithm for irreducible water calculation has two steps (Crain, 2000):

(i) Finding Buckles number in a clean pay zone, where there is no water-cut ( $S_{wir} = S_w$ ), using Relation 2-33 (Buckles, 1965):

$$k_{Buckles} = \min(\varphi_e \cdot S_w) \quad (2-33)$$

(ii) If the zone is hydrocarbon bearing:  $S_{wir} = S_w$  otherwise:

$$S_{wir} = \min\left(\frac{k_{Buckles}}{\varphi_e \cdot (1 - V_{sh}^m)}, 1, S_w\right) \quad (2-34)$$

The component  $m$  is defined by the user. It is usually set as 1, however other values, like 2, are possible for being sure that  $S_{wir} \leq S_w$ . The effective porosity,  $\varphi_e$ , could be either measured or estimated by one of porosity modelling methods.

Depth, m	KNOWN			ASSUMPTIONS				CALCULATIONS				ASSUMPTIONS				CALCULATIONS			
	Vsh, fr	NPHI, fr	RHOB, gr/cc	NPHIw	NPHIh	NPHIma	NPHIsh	KN, fr	NPHIm	PHInc	RHOBw	RHOBh	RHOBma	RHOBsh	PHId	PHIdc	PHIxdn	PHIxdn_Q	PHIxdn_CL
2885,5	0,49	0,21	2,31	1	1	0	0,1537	1	0,21	0,135	1	1	2,65	0,14	0,21	0,138	0,16	0,03	0,14
2886,1	0,49	0,17	2,37	1	1	0	0,1537	1	0,17	0,093	1	1	2,65	0,14	0,17	0,100	0,16	0,03	0,10
2887,74	0,49	0,09	2,54	1	1	0	0,1537	1	0,09	0,009	1	1	2,65	0,14	0,07	0,000	0,00	0,04	0,00
2888,15	0,48	0,07	2,57	1	1	0	0,1537	1	0,07	0,000	1	1	2,65	0,14	0,05	0,000	0,00	0,05	0,00
2888,7	0,45	0,08	2,67	1	1	0	0,1537	1	0,08	0,011	1	1	2,65	0,14	-0,01	0,000	0,00	0,05	0,01
2896,67	0,44	0,08	2,55	1	1	0	0,1537	1	0,08	0,016	1	1	2,65	0,14	0,06	0,000	0,00	0,06	0,01
2898,15	0,43	0,12	2,49	1	1	0	0,1537	1	0,12	0,052	1	1	2,65	0,14	0,09	0,034	0,00	0,06	0,04
2898,22	0,42	0,12	2,49	1	1	0	0,1537	1	0,12	0,056	1	1	2,65	0,14	0,09	0,036	0,00	0,06	0,05
2898,56	0,40	0,09	2,48	1	1	0	0,1537	1	0,09	0,032	1	1	2,65	0,14	0,10	0,046	0,00	0,07	0,04
2898,78	0,39	0,08	2,51	1	1	0	0,1537	1	0,08	0,023	1	1	2,65	0,14	0,08	0,029	0,00	0,08	0,03
2899	0,31	0,09	2,55	1	1	0	0,1537	1	0,09	0,044	1	1	2,65	0,14	0,06	0,015	0,00	0,08	0,03

Figure 2-6. A snapshot of the spreadsheet for porosity estimation by the presented empirical relations. Vsh: shale volume, NPHIw, NPHIh, NPHIma and NPHIsh: NPHI in water, hydrocarbon, matrix and shale, respectively. NPHIm and PHInc are outputs (for NPHI) of Relations 2-26 and 2-27, respectively. RHOBw, RHOBh, RHOBma and RHOBsh: RHOB in water, hydrocarbon, matrix (2.65 g.cm<sup>-3</sup> for calcite) and shale, respectively. PHId and PHIdc: are outputs (for RHOB) of Relations 2-26 and 2-27, respectively. PHIxdn, PHIxdn\_Q and PHIxdn\_CL are outputs of the methods density-neutron, quick-look and complex lithology, respectively.

## 2.4.3 Wylie-Rose permeability relation

Wylie and Rose (1950) proposed a well-known empirical relation for permeability estimation (Relation 2-35). It is reliable when we have core tests for calibration.

$$k_{WR} = C_k \frac{\varphi_e^m}{S_{wir}^n} \quad (2-35)$$

where  $C_k$ , m and n are constants to be chosen (Table 2-3). Effective porosity and irreducible water saturation are in fraction.

Table 2-3. Suggested constants for Wylie and Rose (1950) permeability relation.

Reference	$C_k$	m	n
Morris and Biggs (1967)	Oil: 65000 Gas: 6500	6.0	2.0
Timur (1968)	Oil: 3400 Gas: 340	4.4	2.2

Other empirical relations for permeability modelling were also checked, however they were not used since:

- Permeability from porosity (power of ten): at the moment, fuzzy arithmetic is not practical on the power of ten because of (i) RAM limitation, and (ii) too wide domains of resulting fuzzy memberships. A possible solution is to define a suitable power fuzzy operator.

- Permeability from formation factor: needs at least five stages of fuzzy calculations for achieving the final result. So, not practical at the moment.

- Coates and Dumanoir (1974): completely impractical due to several fuzzy calculations, containing logarithmic calculations. By the progress of calculators and toolboxes, it would be applicable later.

- Lucia (1983 and 1995): impractical at the moment because of several fuzzy power calculations and hardware limitation.

- Kozeny-Carman relation (Tiab and Donaldson, 2004): needs pore radii evaluation, unavailable here.

## 3 Modelling vertical resolution

### Highlights of Chapter 3

- Well-log data are volumetric records.
- Three types of vertical resolution are introduced for the well-logs: **(i)** vertical resolution of sampling rate, **(ii)** vertical resolution of tool (VRT) or spacing, and **(iii)** vertical resolution of membership function (VRmf).
- $VRmf > \text{spacing} > \text{sampling rate}$
- The vertical resolutions of GR, RHOB and NPHI are modelled by triangular fuzzy memberships.
- The vertical resolution of DT is modelled by a complex fuzzy membership function.
- Volumetric Nyquist frequency is developed. It is suitable for the volumetric recordings like well-logs.

### 3.1 Volumetric nature of well-log recordings

Conventionally, petrophysicists assign the depth of recorded well-log value to a single horizon; i.e. at the depth of recorder or exactly in the middle of transmitter and recorder. Although a volumetric response is acquired ([Figure 3-1](#)), the recorded value is only assigned to the centre of volume of investigation. Therefore the volumetric nature of recording is ignored! Here, the goal is to model the vertical dimension of volume of investigation using fuzzy membership function. The function shows the contribution of each horizon in the recorded value. Designing the membership function should be based on the structure of each instrument, individually.

#### 3.1.1 Different types of resolution

Resolution of well-logs could be discussed vertically and horizontally. Horizontal resolution is equivalent to the “depth of investigation”, while vertical resolution can be categorized into three types: **(i)** vertical resolution of sampling rate, **(ii)** vertical resolution of tool (VRT) or

spacing, and **(iii)** vertical resolution of membership function (VRmf) which is introduced in this work for the first time. VRmf is representative of whole the effective depth interval on the recording. Inherit of the logging measurement and geological conditions control VRmf. The smaller VRmf, the more concentrated (or focused) measurement.

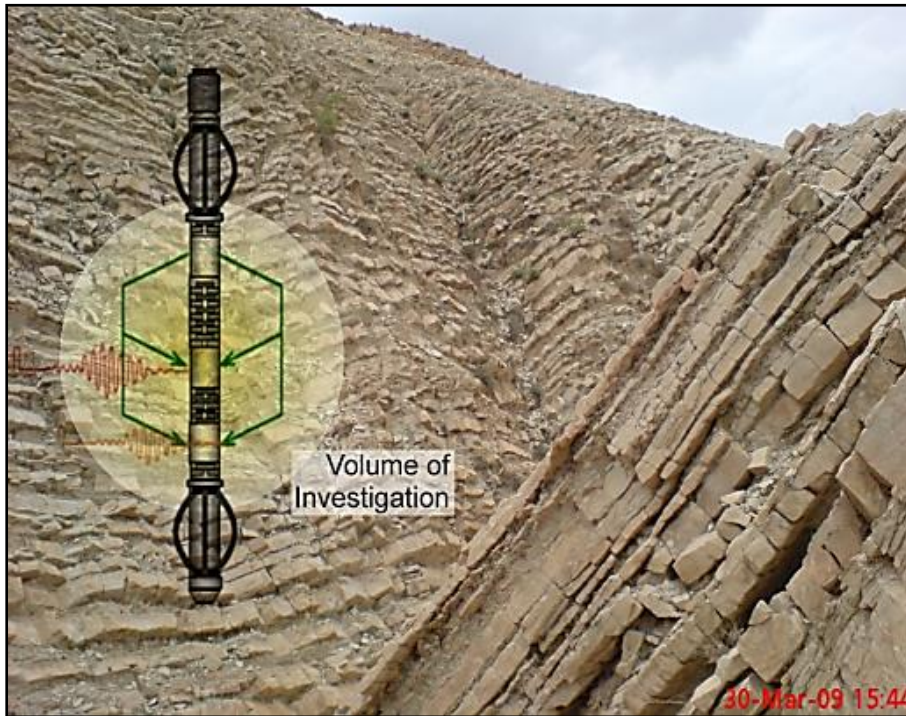


Figure 3-1. Schematic representation of volume of investigation around a sensor in a logging tool.

Combination of these three vertical resolutions defines the overall precision of acquired logs in characterizing the reservoirs. Depth of investigation and vertical resolution of some tools are presented on [Figure 3-2](#) and [Table 3-2](#).

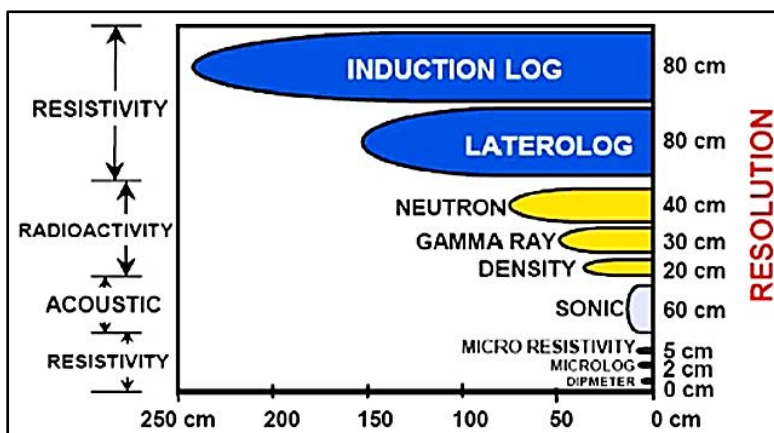


Figure 3-2. Depth of investigation and spacing of each well-log ([Crain, 2000](#)).



Due to [Figure 3-2](#), no guarantee to identify geologic phenomena (mostly sedimentary beds) smaller than 30 cm by gamma log. As an example, if a porous bed with the thickness of 10 cm is surrounded by thick beds of marl, never the influence of this porous bed exceeds 33%, while marls have an effect of 67% on the recording. It is called shoulder-bed effect or the effect of neighbouring beds.

Another limitation on vertical resolution is imposed by the sampling rate. After data acquisition, all sampling rates are up-scaled on about 15 cm. Application of Nyquist frequency in well-logging says: no guarantee to detect a bed thinner than sampling rate. We believe, applying Nyquist frequency in the geophysical domains is not precise; since, it is primarily developed and suitable in the domain of telecommunication, where the data (pulses) are not volumetric.

In summary, there are two limitations in studying thin-beds: tools configuration (spacing and VRmf) and sampling rate. In this chapter, we are going to modify the conventional Nyquist frequency to be more effective in petrophysical investigations. As a prerequisite, we need to have a more comprehensive understanding of the mechanisms and principles of logging, which are addressed in this chapter.

### **3.1.2 VRmf > spacing > sampling rate**

Among the three introduced types of vertical resolution, sampling rate is usually the most precise resolution (resistivity logs are exceptions). It could be set by the logger through the speed of logging. So, the sampling rate does not impose an important resolution limitation on the readings.

It is declared here that VRmf is larger than the spacing (compare the oval of volume of investigation with the spacing in [Figure 3-1](#)). It means that the effective interval on the well-log recordings is not limited to the spacing. There are four reasons for this phenomenon. The two first reasons concern recording stage, and the two last concern preprocessing algorithms.

- (i) The recording is taking place while the recording tool is moving upward.

(ii) The effect of geological phenomena, which are out of the spacing, on the formation factor, is presented in [Figure 3-3](#).

(iii) Up-scaling the acquired data to the standard sampling rate of 15.24 cm.

(iv) Other noise reduction algorithms, applied in the stage of pre-processing.

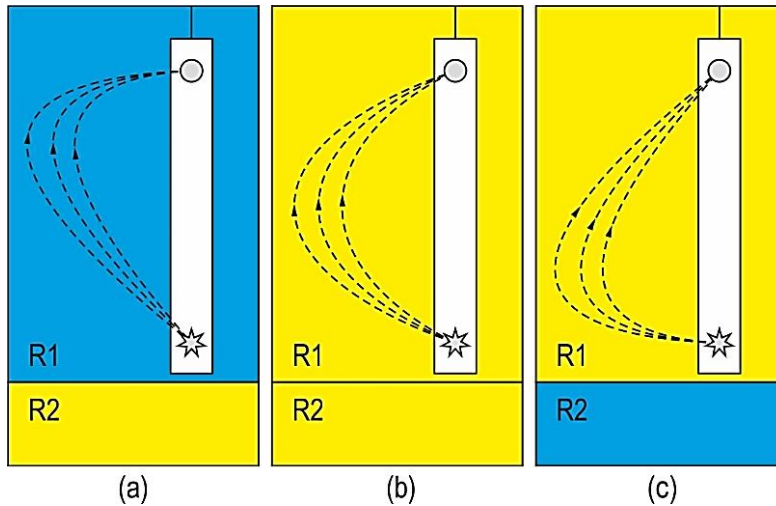


Figure 3-3. The effect of an environment, out of the spacing, on the electrical logging. a)  $R1 < R2$ : electric flow is getting away from the resistant environment (R2). b)  $R1 = R2$ : electric flow is symmetrical. c)  $R1 > R2$ : electric flow is getting closer to the conducting environment (R2).

### 3.2 Modelling logging mechanism by fuzzy memberships

Well-logs could be categorized into two types: passive and active. Passive logs are simple recordings of a physical property (formation radiation) or a geometric property (diameter) within the wellbore, and could be registered only by a recorder. However, active logs require a transmitter or source, for transmitting energy (electro-magnetic, sonic, beam, etc.) towards the wellbore, and recording the response of the stimulated formation by a recorder ([Figure 3-4](#)).

In the passive logs, the closer distances to the recorder are more effective on the sensor. Therefore, a membership function has to have two properties: (i) being symmetric and (ii) the height is exactly at the horizon of detector. In [Figure 3-4a](#), the simplest possible fuzzy membership function, triangular, is presented; however, the function could be non-linear.

Membership function is more complex in the active logs. [Figure 3-4b](#) shows two triangular membership functions. Height of one of them is at the horizon of transmitter (mfT) and the

other is at the horizon of receiver ( $mfR$ ). The act of recording takes place at receiver but both  $mfT$  and  $mfR$  are required for the logging. Therefore, an intersection operator, “and” or “minimum”, is necessary for fusing  $mfT$  and  $mfR$  to reach the final membership. The only unknown parameter of triangular membership functions (Figure 3-4) is the domain of triangles (or  $VRmf$ ), because the height is one, and the functions are symmetric.

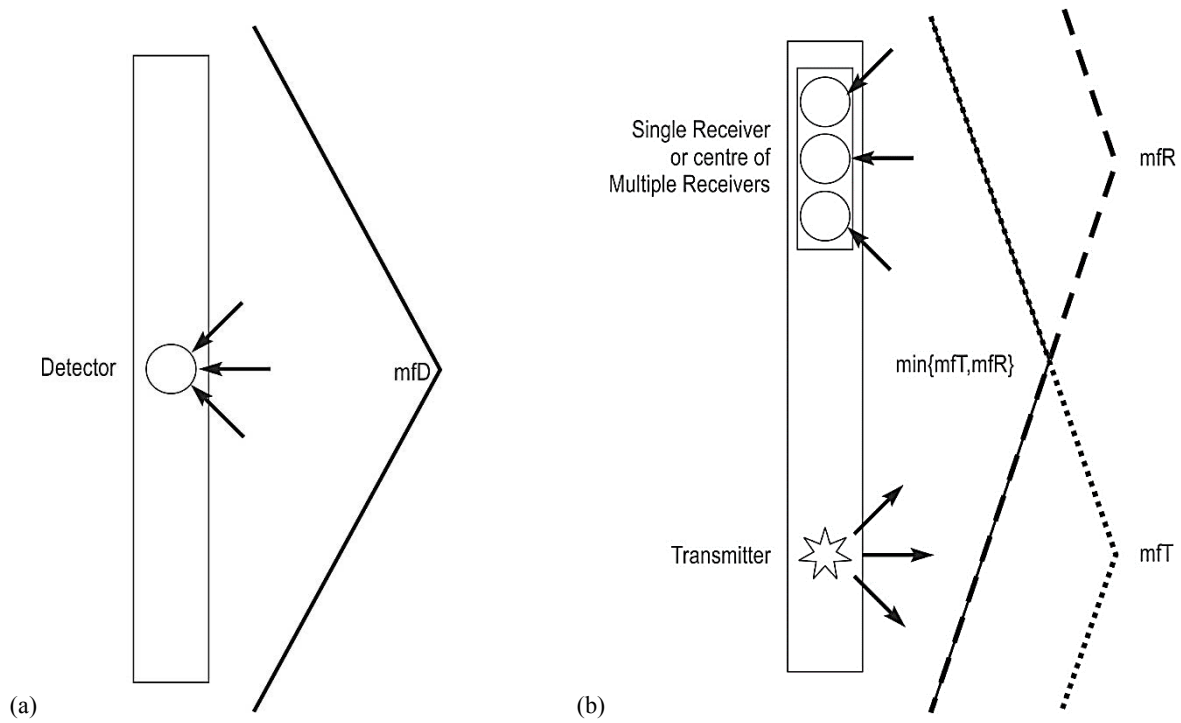


Figure 3-4. Fuzzy membership function of contribution of each horizon in recording a passive (a) and an active (b) log.

### 3.2.1 Recording configuration and well-log

In detecting a specific thin-bed, the well-log shape is controlled by volume of investigation, sampling rate and coordination (depths) of recording points, relative to the thin-bed position. The effect of misplacement of recordings, aliasing, is shown by configuration B (Figure 3-5). In this figure, two different configurations have resulted in two different well-log shapes. In configuration A, only one point has detected the thin-bed, however the thin-bed contributes effectively in this record. In configuration B, dashed line, there is no detection within the thin-bed, and the bed has only minor contributions in the volumes of investigation of two adjacent recording points.

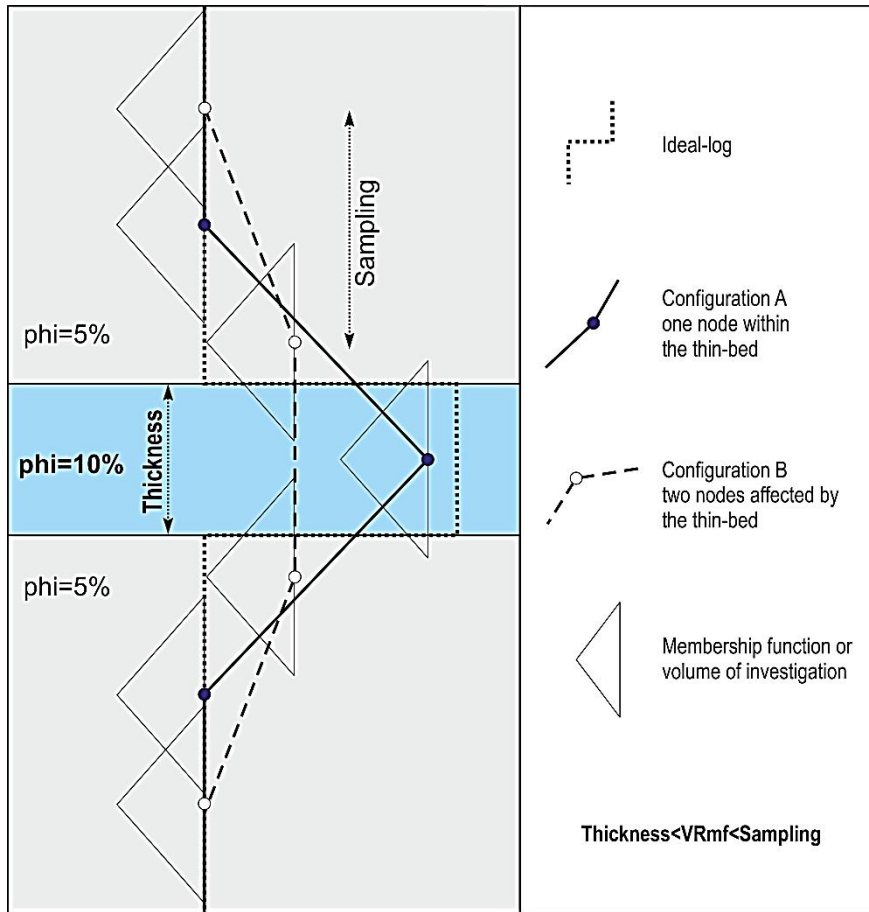


Figure 3-5. Two possible configurations for detecting a thin-bed. Configuration B results in aliasing. In the well-logging, this phenomenon is called shoulder-bed effect, i.e. the effect of neighbouring beds.

### 3.2.2 Approximating VRmf

#### 3.2.2.1 Variography analysis

VRmf is tried to be approximated practically. In fact, sometimes VRmf varies through the same reservoir. “The net result is that one can visualize at any instant a neutron cloud surrounding the source, extending a maximum of about 2 ft [ $\sim 67$  cm]. As the hydrogen content of the formation varies, the size of the cloud expands and shrinks. The greater the hydrogen content, the smaller the cloud and vice versa (Dewan, 1983).” These lines show that VRmf of NPHI could vary about 67 cm, depending on formation conditions.

To gain a primary guess about VRmf, the well-logs were observed precisely. It was found that in a homogeneous environment, the thinnest bell-shape trace consists of 5, 8 or 12 data

points on the well-logs GR, RHOB and NPHI. It means that the beds thinner than five records, i.e.  $4 \times 15 \text{ cm} = 60 \text{ cm}$ , are not detectable by the well-logs. So:  $\text{VRmf} > 60 \text{ cm}$ .

Larger the intersection of volume of investigation, higher the similarity of neighbouring records. When the similarity increases, the well-log becomes smoother and more continuous. To study the similarity of neighbouring records, correlation coefficient is firstly checked between pairs of neighbouring records ( $R_i, R_{i+j}$ ).  $R_i$  is the  $i$ th record, and  $R_{i+j}$  is the  $j$ th neighbour of  $R_i$ . As an example, for GR log in well#2, the correlation coefficients between the neighbours ( $j=0, 1, 2, 3, 4$  and  $5$ ) were 1, 0.93, 0.81, 0.70, 0.62 and 0.57, respectively (Figure 3-6). So, due to statistics, similarity between the neighbouring records reduces as the distance increases between the pairs of records. Correlation coefficient of more than 0.9 could be considered as very high and 0.70-0.90 as high (Mukaka, 2012). Considering cut-off of high correlation ( $>0.7$ ), corresponding to high similarity, three neighbours ( $j=3$ ) will be highly similar to each other. So, for GR in well#2, VRmf contains three adjacent records ( $j=1, 2$  and  $3$ ), but not the fourth, i.e.  $3 \times 15.24 \text{ cm} < \text{VRmf} < 4 \times 15.24 \text{ cm}$  or  $46 \text{ cm} < \text{VRmf} < 61 \text{ cm}$ . Even though correlation coefficient provides an approximation for VRmf, variography analysis is preferred. In fact, variography is a specialized tool to quantify variability (including continuity) of spatial data (Gringarten and Deutsch, 2001) (Figure 3-7).

Experimental variographs of well-logs were checked within Sarvak reservoir of the five available wells, SW Iran. There is an exact linear relation at small lags in all the wells, but the continuity of the data exists up to about six meters (Figure 3-8). There is no nugget effect, i.e. all the variographs start from about the centre of coordination (0,0). Nugget effect and initiation of variographs are measures of discontinuity (Gringarten and Deutsch, 2001).

The gradient of variographs at the linear part is higher than the nonlinear part. It shows that the continuity of the data decreases more rapidly at the linear part. The decrease of the continuity of the data has two reasons: (i) geological continuity, which lasts up to 6 meters (linear and nonlinear parts), and (ii) the intersection of volumes of investigation of adjacent data (only in the linear part). So the decrease of continuity has two reasons in the linear part, but in the nonlinear part, there is only one reason: geological continuity.

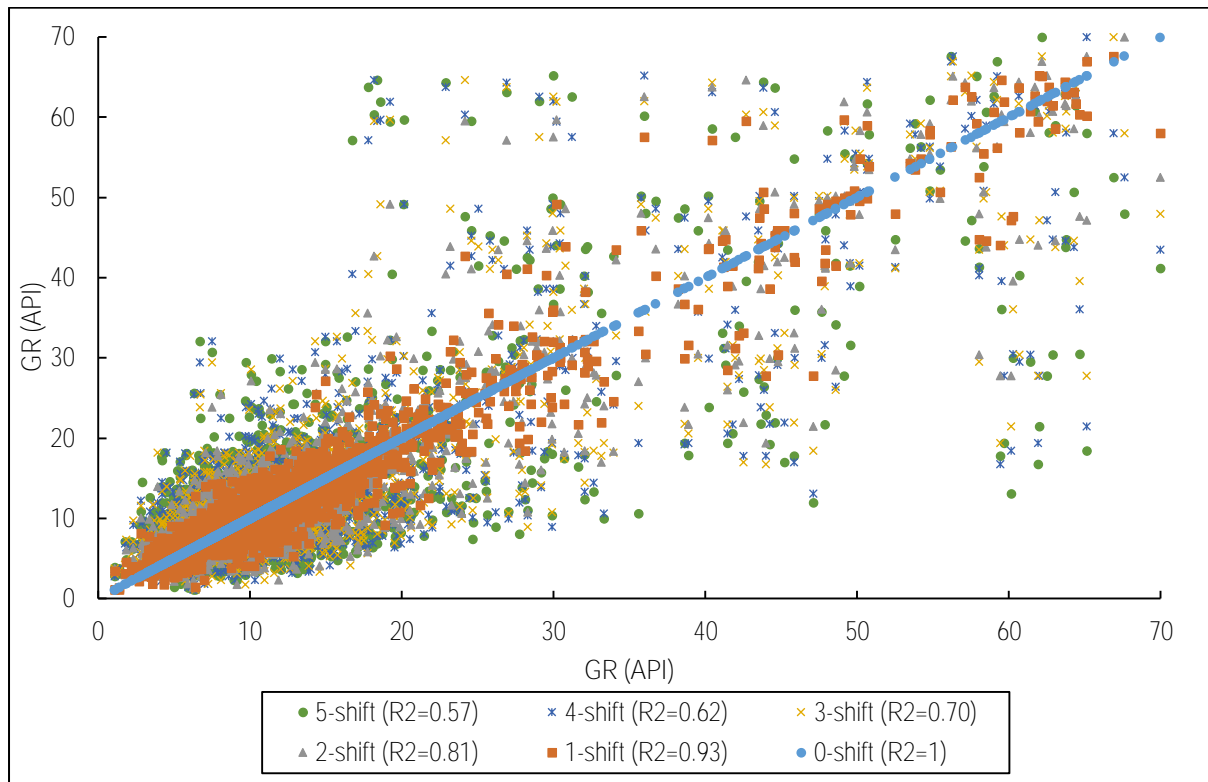


Figure 3-6. Cross-plots of adjacent recordings of GR (well#2).

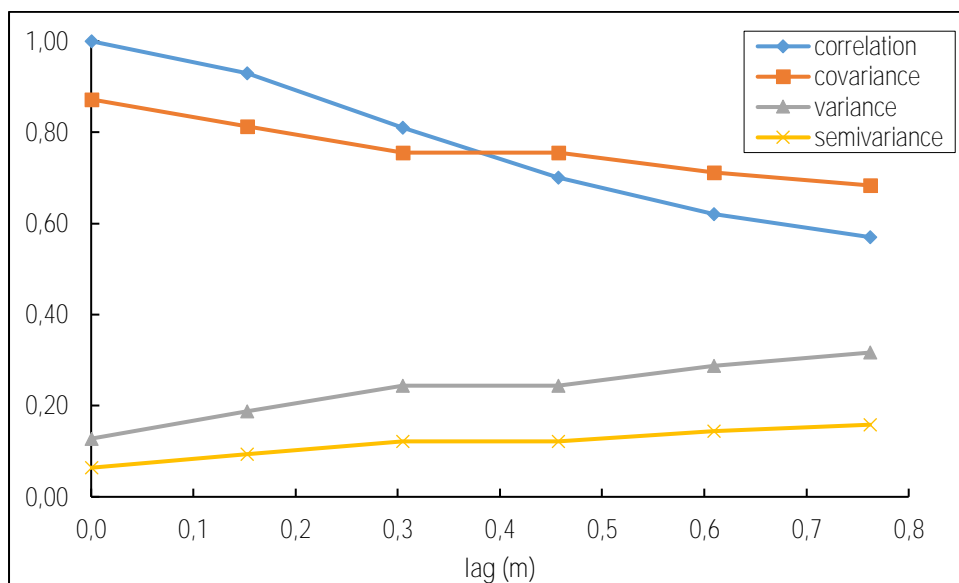


Figure 3-7. Measures of similarity (correlation and covariance) and dissimilarity (variance and semivariance) for adjacent recordings of GR in well#2.

So, the second structure, i.e. linear part of variography, is considered as cut-off of high similarity between neighbouring records. Interpreting the variograph of GR in well#2 (Figure

3-8) reveals that four adjacent records are very similar to each other, leading to VRmf=61 cm, which is about the approximation of correlation coefficient. VRmf for the well-logs under study in all the wells is presented in Table 3-1 and 3-2, and it is compared to the geological bed classifications (Figure 3-9).

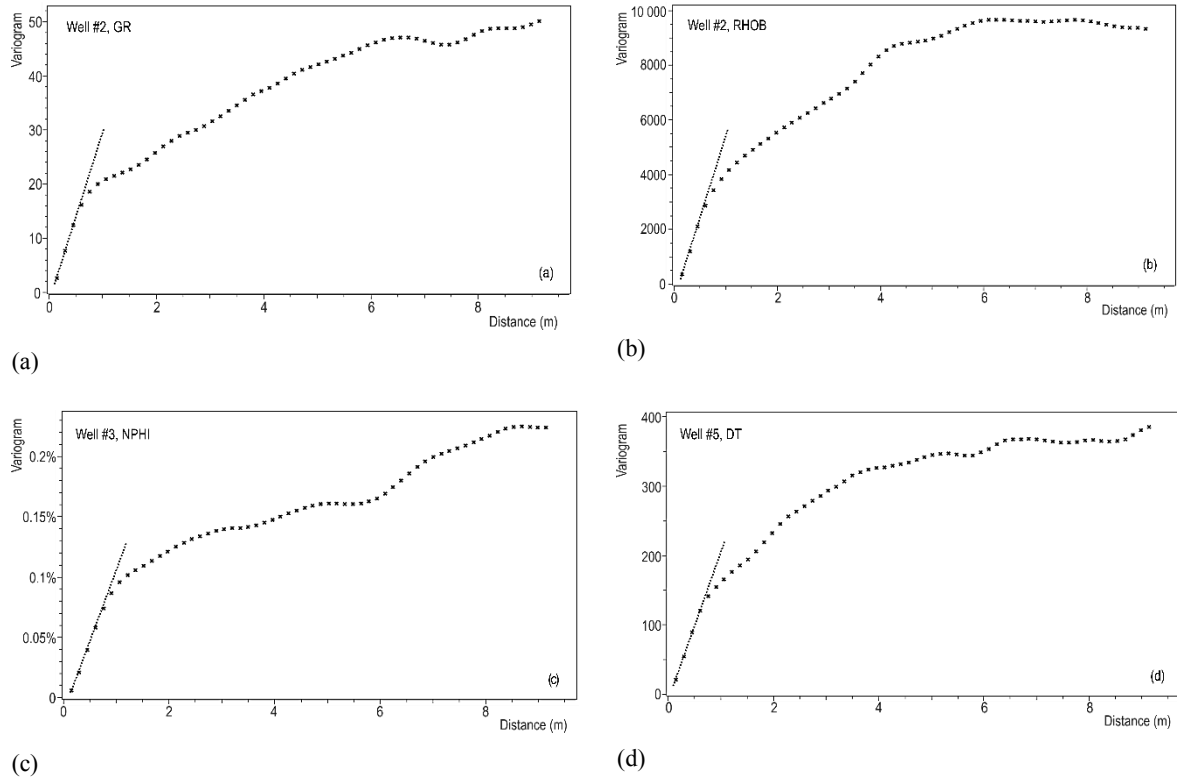


Figure 3-8. Experimental variographs showing linear relation at the first lags. An open-source computer package, named The Stanford Geostatistical Modelling Software (SGeMS) is used to generate variographs. a) GR in well#2, b) RHOB in well#2, c) NPHI in well#3 and d) DT in well#5.

Table 3-1. Finding VRmf for each well-log, in each well by variography. VRmf is selected as minimum value of all the wells, larger values might be because of homogeneity of rocks. Units are in cm.

Well-log	Well #1	Well #2	Well #3	Well #4	Well #5	VRmf
GR	61	61	61	61	61	61
RHOB	76	76	91	76	76	76
NPHI	76	76	91	76	76	76
DT	61	61	61	61	61	61

### 3.2.2.2 Analytics

When the adjacent records have a common volume of investigation, a linear relation exists between recorded values. To proof this hypothesis, recorded well-log value at the depth of  $d_i$ ,

i.e.  $R(d_i)$ , is expressed as a weighted average of petrophysical value ( $v$ ) over a VRmf. The weights are provided by membership function  $f_d$  (Relation 3-1). By this relation, recorded well-log of one depth ( $d_i$ ) is expressed by an adjacent recording ( $d_{i+1}$ ) (Relation 3-2). Its discrete form is given by Relation 3-3.

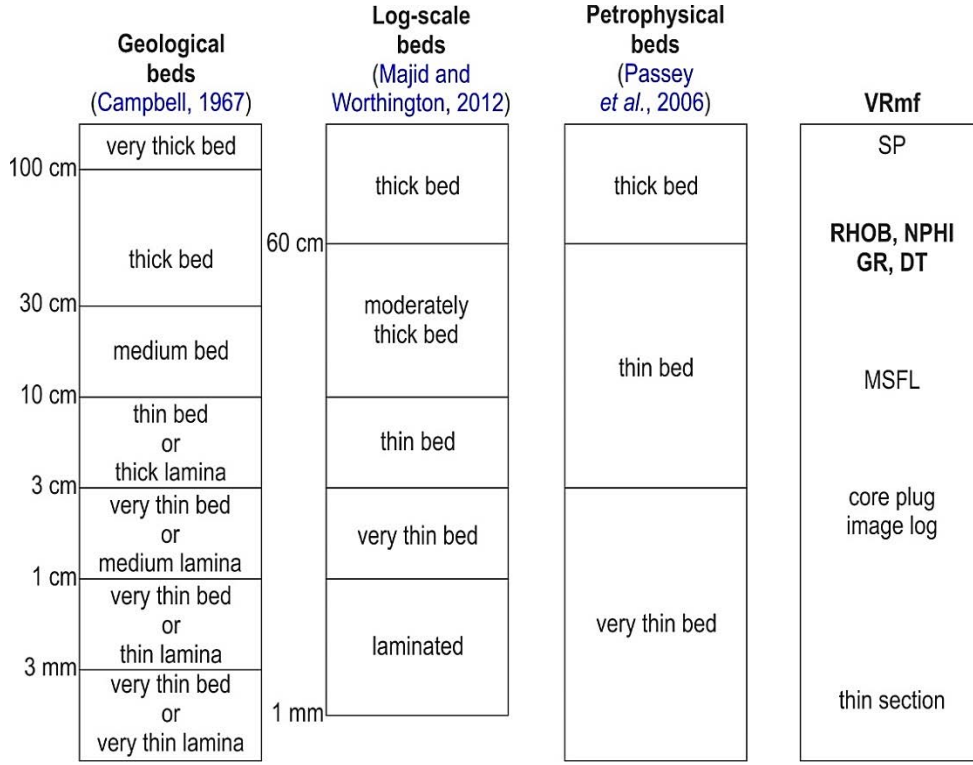


Figure 3-9. Comparison of VRmf with geological beds (Campbell, 1967), log-scale beds (Majid and Worthington, 2012), petrophysical beds (Passey *et al.*, 2006). Modified after Passey *et al.* (2006).

$$R(d) = \int_{VRmf} f_d(z) \times v(z) \times dz \quad (3-1)$$

$$\begin{aligned} R(d_{i+1}) - R(d_i) &= \int_{VRmf} f_{d_{i+1}}(z)v(z)dz - \int_{VRmf} f_{d_i}(z)v(z)dz \\ &= \int_{VRmf} ([f_{d_{i+1}}(z) - f_{d_i}(z)]v(z)dz) \end{aligned} \quad (3-2)$$

$$R(d_{i+1}) = R(d_i) + \sum_{VRmf} ([f_{d_{i+1}}(z) - f_{d_i}(z)]v(z)) \quad (3-3)$$



Here,  $f_d$  is defined to be linear (triangular membership functions). So, if  $v(z)$  is a linear or constant variable, the relation between the two adjacent records would be linear. The assumption of  $v(\bar{z}) \cong v(z)$  is true in homogeneous conditions. In heterogeneous conditions, like when there is a thin-bed between shoulder-beds, the assumption is true if and only if the volumes of investigations are well intervened. Therefore,  $v(z)$  could be considered as a constant value. So, [Relation 3-3](#) could be rewritten by [Relation 3-4](#):

$$R(d_{i+1}) = R(d_i) + v(\bar{z}) \times \sum_{gross} [f_{d_i}(z) - f_{d_{i+1}}(z)] \quad (3-4)$$

So, when the ratio of the thickness of sandwiched bed to the vertical resolution is small enough,  $R(d_{i+1})$  has a linear relation with  $R(d_i)$ . As a result of accepting linearity of [Relation 3-4](#), variograph of recordings has to show a linear behaviour for small lags without a nugget effect in ideal situation. This behaviour could be seen on [Figure 3-8](#). Linear behaviour of variographs shows linear relationship between records, i.e. validity of  $v(\bar{z}) \cong v(z)$ , subsequently commonness of volume of investigations during the first lags. Hence, it is mathematically acceptable to use the linear part of variographs for estimating VRmf.

### 3.2.3 Passive log of GR

Detector of Gamma Ray (GR) log belongs to the category of passive logs, since it only records emitting energy of radioactive elements uranium, thorium and potassium. Though previous tools could not distinguish such elements, newer instruments can distinguish level of energy of each of mentioned elements individually. Therefore, triangular membership function of [Figure 3-4a](#) is selected for showing the contribution of each horizon to the recorded value. Vertical resolution of tool is 30.48 cm, while VRmf is 61 cm ([Table 3-2](#)).

### 3.2.4 Active logs of RHOB and NPHI

Bulk density log (RHOB) is of active logs, having transmitter and receiver simultaneously. It transmits gamma ray toward the wellbore, and records its attenuation: difference of energy of transmitted and recorded gamma ray ([Dewan, 1983](#)). Therefore, membership function of

Figure 3-4b is selected for showing the contribution of each horizon to the recorded value. Vertical resolution of tool is 45.72 cm, and VRmf is 76 cm (Table 3-2).

Like RHOB, neutron porosity log (NPHI) is of active logs. It transmits fast neutrons (~5 MeV) toward the wellbore in all directions, and records very low, thermal energies (~0.025 eV) (Dewan, 1983). Therefore, membership function of Figure 3-4b is suitable for showing contribution of each horizon to the recorded value. Spacing of transmitter and receiver is 30.48 cm, and VRmf is 76 cm (Table 3-2).

### 3.2.5 Complex membership function of compensated sonic log

Defined membership function of compensated sonic log (DT) is not as simple as previous logs. Since Borehole Compensated (BHC) sonic tool has two transmitters on each ending part and four detectors. BHC measures transmitting time twice. One is related to the top transmitter, the other to the bottom transmitter. Each transmitter is linked to a pair of detectors, for removing the effect of mud filtrate. Finally, the two transmitting times are aggregated by an averaging operator. It helps increasing the signal to noise ratio, and making the final log less asymmetric when the tool is not well-aligned (Figure 3-10).

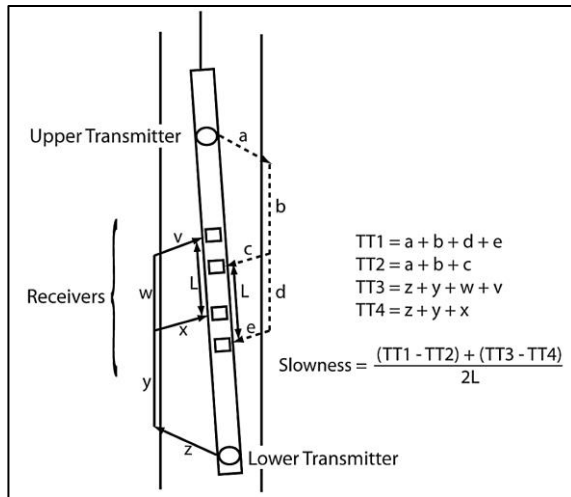


Figure 3-10. Mechanism of measurement of sonic transfer time by Borehole Compensated (BHC) sonic tool. Two transmitters and four receivers, finally fusing them by averaging (Close *et al.*, 2009). Slowness=DT

Membership function of each transmitter/ detector is set to be linear. Minimum operator is used for creating four membership functions (two for each half) between each transmitter and linked detectors (mfDT1 and mfDT2 in Figure 3-11). Each pair of membership functions,

related to the single transmitter, are aggregated by averaging, resulting in the final membership function (mfDT in Figure 3-12a). Finally, the domain of the membership function is scaled to the estimated VRmf (Table 3-1), which is 61 cm for DT (Figure 3-12b). Noteworthy that VRT of DT is 152 cm.

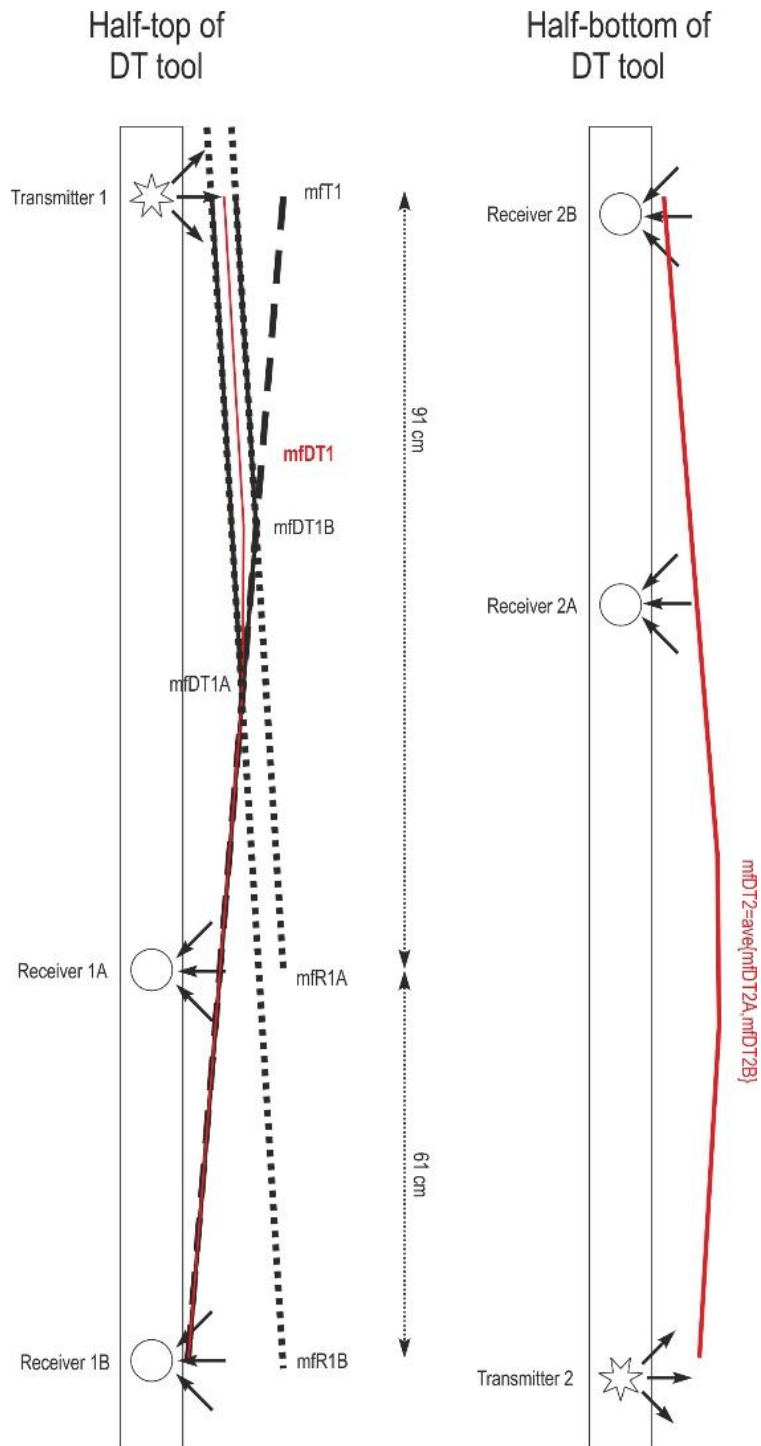


Figure 3-11. Defined membership function for each half part of compensated sonic tool due to Figure 3-4b and Table 1-4.

Following defining membership functions, properties of membership functions of well-logs GR, RHOB, NPHI and DT are specified and presented in Table 3-2. This table is set as the basis of creating synthetic well-logs for thin-bed characterization in Chapter 4.

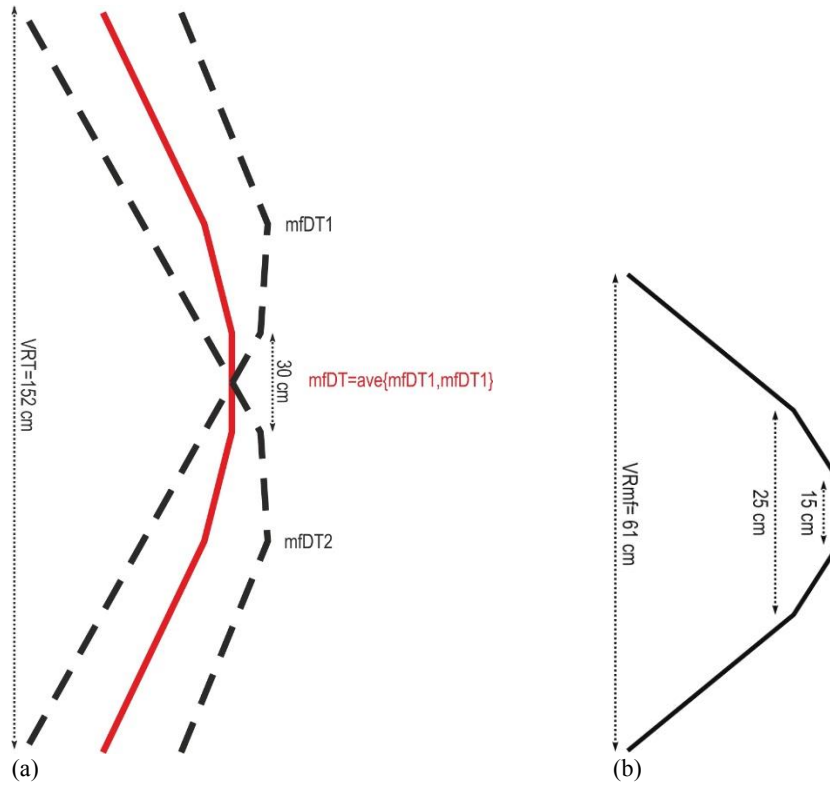


Figure 3-12. Calculated complex membership function for compensated sonic tool, by averaging membership function of each half: a) theoretical and b) practical.

Table 3-2. Summary of designed membership functions of each log.

Well-log	Vertical resolution of tool	Depth of investigation	Type of membership function	Vertical Resolution of Membership Function (VRmf)	Height of membership function
GR	30.48 cm	60.96 cm	triangular	61 cm	middle
RHOB	45.72 cm	12.7 cm	triangular	76 cm	middle
NPHI	30.48 cm	23 cm	triangular	76 cm	middle
DT	152.00 cm	7.62 cm	trapezoidal	61 cm	25 cm in the middle

### 3.3 Volumetric Nyquist frequency

In digital recordings, like well-logs, the relationship between Sampling Rate (SR) and VRmf could be categorized into three types: **(i)**  $VRmf=0$ , **(ii)**  $0 < VRmf < SR$  and **(iii)**  $VRmf > SR$ . The concept of Nyquist frequency is developed in telecommunication systems (Nyquist, 1924),

Figure 3-13a, where the Nyquist frequency and related inferences are effective. Well-log recordings have volumetric nature (Figure 3-13b and c). Here, we present a modification on the common concept of the Nyquist frequency, which is more adequate for being used in interpreting well-log data.

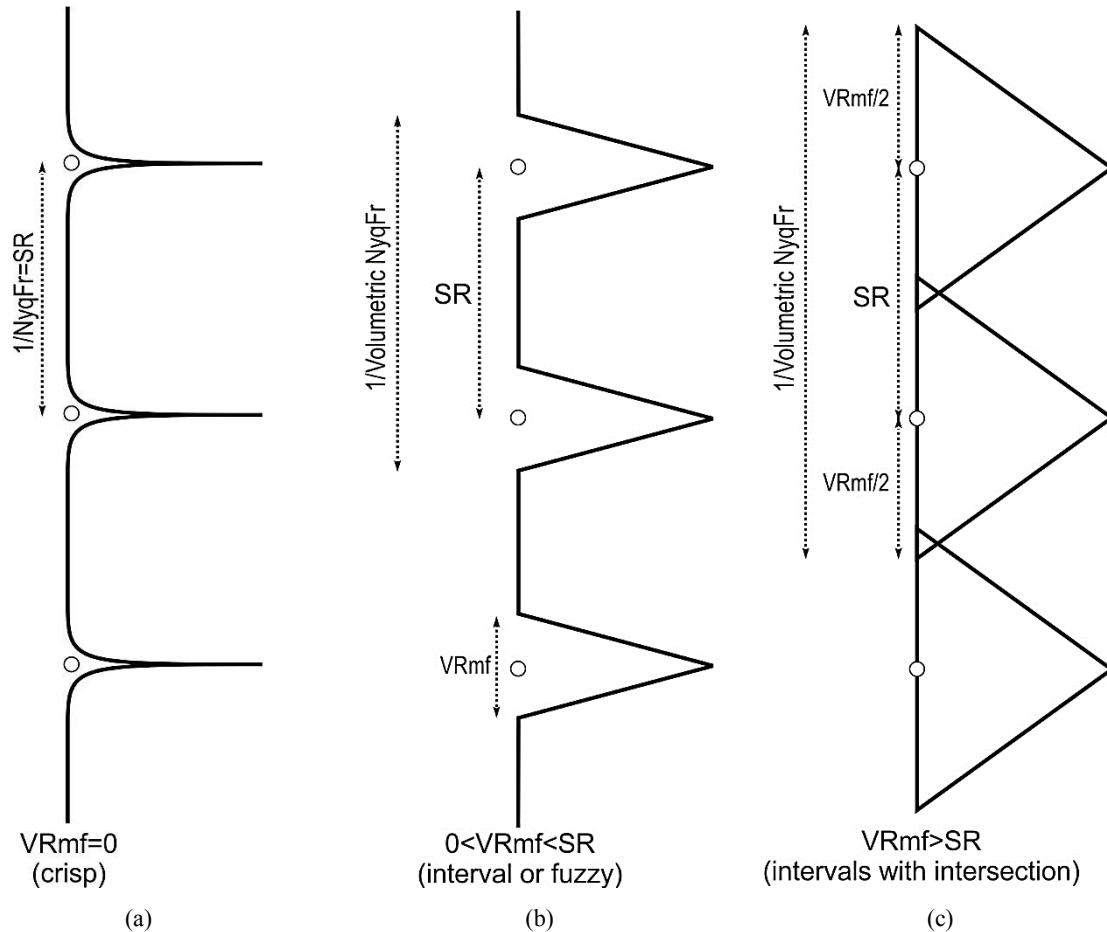


Figure 3-13. Nyquist frequency in three categories. Small balls are centre of recordings. a) Pulse-shapes ( $VRmf=0$ ) like in telecommunications, domain of time. Volumetric detection b) When  $0 < VRmf < SR$  or c)  $VRmf > SR$ .

It is obvious that in the category of  $VRmf=0$ , when thickness of a geologic bed is thicker than  $SR$ , we are sure that at least one record will detect it completely (probability of 1 in solid-lines, Figure 3-14). The chance of detecting this bed decreases linearly as its thickness decreases down to zero (linear part in solid-line, Figure 3-14).

When  $VRmf$  is not zero, the thickness of bed must be thicker than  $VRmf$  and  $SR$  simultaneously to be detectable at least by one record. Its thickness must be larger than the summation of  $SR+VRmf$  to be sure that volume of investigation of at least one record be

completely occupied by the thin-bed (probability of 1 in dotted and dashed lines, Figure 3-14). As before, the thinner the bed, the less probability of detection (linear parts in dotted and dashed lines, Figure 3-14). The probability in Figure 3-14, is very the same as Cumulative Distribution Function (CDF), since a thick bed has a cumulative behaviour of thinner beds.

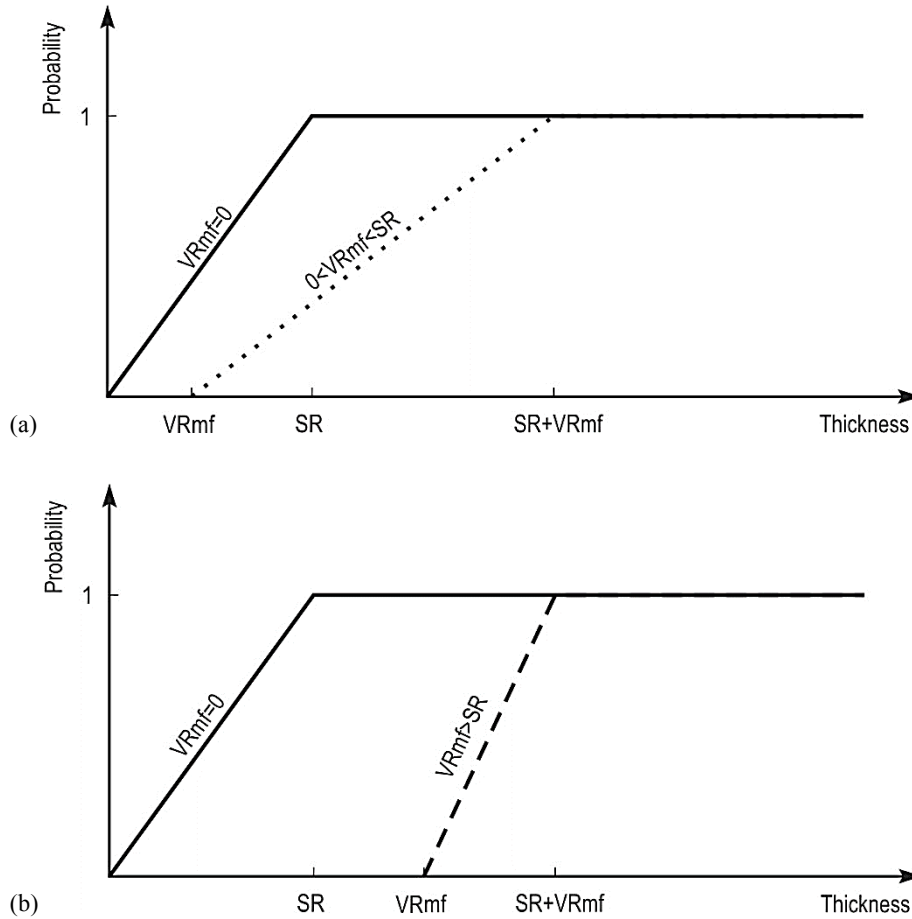


Figure 3-14. Comparing probability of detecting a thin-bed without shoulder-bed effect, in three different sensor types. In pulse-shape detections,  $VRmf=0$ , common Nyquist frequency is effective, i.e. the minimum thickness of a surely detectable thin-bed is SR. Volumetric detection when a)  $0 < VRmf < SR$ , dotted line or b) when  $VRmf > SR$ , dashed line.

“Belief function” has the meaning of “lower probability” in the literature. It is a fuzzy measure, which is less than probability measure, and presents a pessimistic view towards the chance of happening (Dempster, 1967, 1968). In non-volumetric recordings ( $VRmf=0$ ), probability of detecting a bed, thinner than SR is linear (Figure 3-14), while this part is absolutely zero due to belief function (solid-line in Figure 3-15). In volumetric recordings with  $0 < VRmf < SR$ , when the bed is thicker than the summation of SR+VRmf, we are sure that at least one record will be fully affected from the bed. Finally, it is obvious that when the bed is

thinner than VRmf, volume of investigation of no detection is completely occupied by the bed. The mentioned interpretations could be adjusted using [Figure 3-13](#).

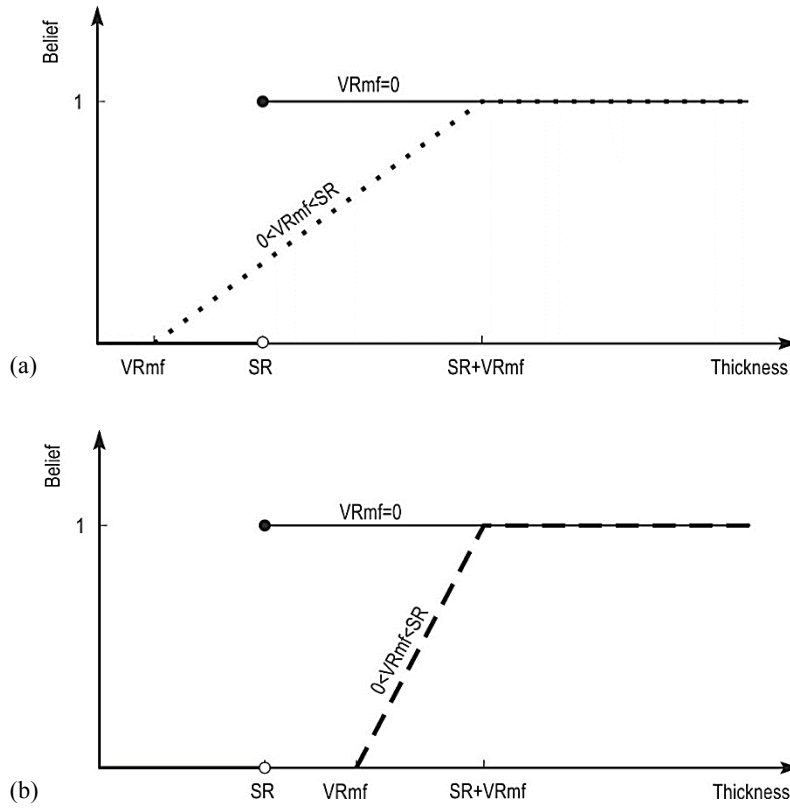


Figure 3-15. Comparing belief function (pessimistic view) of detecting thin-beds without shoulder-bed effect, in three different sensor types. In pulse-shape detections, VRmf=0, common Nyquist frequency is effective, i.e. the minimum thickness of a surely detectable thin-bed is SR. Volumetric detection when a)  $0 < VRmf < SR$ , dotted line or b)  $VRmf > SR$ , dashed line.

Volumetric Nyquist frequency is defined in [Relation 3-5](#). The minimum thickness of beds to be detected (probably or surely) are presented in [Table 3-3](#). The difference between these two thicknesses is an uncertain interval, i.e. the thin-bed will probably be detected but no guarantee to be characterized. Interestingly, the uncertain interval remains constant for all the three categories ([Table 3-3](#)).

$$fr_{Nq,vol} = \frac{1}{SR + VRmf} \quad (3-5)$$

Table 3-3. Minimum thickness of beds to be characterized probably or surely. The uncertain interval showing an interval where probability is neither zero nor one.

	VRmf=0	0<VRmf<SR	VRmf>SR
Minimum required thickness of a bed, to be probably characterized without shoulder-bed effect	0	VRmf	VRmf
Minimum required thickness of a bed to be surely characterized without shoulder-bed effect	SR	SR+VRmf	SR+VRmf
Uncertain interval	SR	SR	SR

### 3.4 Conclusions of Chapter 3

The Vertical Resolution of membership function (VRmf), introduced here, is a useful parameter for well-log simulation and modelling. It could be estimated using variography analysis. In five wells, VRmf of well-logs GR, RHOB, NPHI and DT were estimated to be 61, 76, 76 and 61 cm, respectively. Following the development of membership functions to study the volume of investigation of each well-log, it was found that the triangular function is suitable for studying GR, RHOB and NPHI well-logs, while a trapezoidal shape function is more suitable for studying DT.

Considering the relative values of Sampling Rate (SR) and VRmf, the application of Nyquist frequency in well-logs is reviewed, and volumetric Nyquist frequency is developed for volumetric recordings (VRmf>0). It was shown that when VRmf>0, the minimum identifiable thin-bed should be thicker than SR+VRmf.



## 4 Thin-bed characterization, geometric method

### Highlights of Chapter 4

- A literature review is presented on the thin-bed study by well-logs.
- Based on the developed model of vertical resolution, introduced in [Chapter 3](#), a geometric simulator is developed for generating synthetic-logs of a single thin-bed.
- A probabilistic method of thin-bed study, VLSA, is extracted from the literature and introduced.
- This chapter provides a better understanding toward thin-bed study by well-logs, which is a foundation for [Chapter 5](#).
- Geometric simulator enables us analysing the sensitivity of well-logs to a thin-bed.
- Deconvolution relations for removing shoulder-bed effect of thin-beds are developed for GR, RHOB and NPHI well-logs.
- Deconvolution relations are successfully applied to well-logs to characterize thin-beds.

### 4.1 Review of thin-bed studies

The importance of studying thin-bed reservoirs is two-fold and could be summarized as: **(i)** “future exploration targets are likely to be thinner” in petroleum discoveries ([Sengupta, 1987](#); [Sengupta \*et al.\*, 1989](#)). **(ii)** A near wellbore thin-bed could be pinch out of larger sandy lenses, or related to other stratigraphic traps, e.g. channel filling, lateral variation, etc. ([Qi and Carr, 2006](#)). Vertical resolution of logging tools varies from 2 to 10 inches (5.08-25.4 cm), so characterizing geological beds thinner than the vertical resolution is imprecise even if the sampling rate is precise enough ([McCall \*et al.\*, 1987](#)).

In the first publications, only signal-processing theories, Weiner and Kalman filter, were developed for the purpose of increasing frequency of well-logs ([Foster \*et al.\*, 1962](#); [Bayless and Brigham, 1970](#)). The other practical issue of signal processing algorithms is the lack of knowledge about the theoretical parameters since there was no confidence about the used parameters ([Lyle and Williams, 1987](#)).

Until 1987, the studies were totally theoretical. Practical improvement of vertical resolution of well-logs was basically accomplished within the years 1989-1990, when industrial researchers of Schlumberger, Halliburton and British Petroleum played part. They used geometrical and numerical analysis for developing easy-to-apply procedures to improve well-log resolution.

The beds thinner than 2 feet (60.96 cm) cannot be properly evaluated by density log. Based on geometry, a wise correction to enhance density log for characterizing thin-beds (less than 6 inches or 15.24 cm) is developed. The main idea was inferring the high-frequencies from short-interval density measurements (applying a low-cut filter), and adding the remained high-frequencies to the long-interval density measurements (Flaum *et al.*, 1989). This methodology was used in Schlumberger's 'alpha' processing for resolution improvement of density and neutron well-logs (Passey *et al.*, 2006).

Inspired from the former work, resolution of compensated neutron log is enhanced too (Galford *et al.*, 1989). In addition, the contact of two beds with different porosities is identified with less uncertainty:  $\pm 2$  inches (5.08 cm) rather than  $\pm 6$  inches (15.24 cm) (Gartner, 1989). In another similar work, it is assumed that the attenuation log of Electromagnetic Propagation Tool (EPT) and clay volume (derived from geochemical logging) are strongly correlated linearly. Hence, high-frequencies are inferred from high-resolution EPT log, and coherent small changes are recreated for geochemical logs (Flaum, 1990).

True understanding of mechanism and spatial response of well-logs is important in a successful well-log interpretation. This necessity becomes more rigorous in heterogeneous media. Monte-Carlo simulation is used to study spatial response (mostly horizontal resolution) of density log. It is found that in carbonate formations, 75% of density log response captures the distance of 8 cm from the borehole wall and 90% captures till 12 cm (Petler, 1990).

Based on the previously developed logical relation for vertical resolution correction (Flaum *et al.*, 1989), a three dimensional sensitivity analysis is addressed by Monte-Carlo simulation. Using density and neutron logs in high-angle (near horizontal) wells, the uncertainty of identifying depth of bed boundaries is about  $\pm 2.5$  inches (6.35 cm). This uncertainty rises under shoulder-bed effect to about  $\pm 10$  inches (25.4 cm) and  $\pm 15$  inches (38.1 cm) by density and

neutron logs, respectively. This uncertainty in highly deviated wells is justifiable by the fact that neutron and density tools are designed and calibrated for vertical wells. So, standard interpretations will result in incorrect results (Mendoza *et al.*, 2006).

Depending on bed thickness average, geoscientists in ExxonMobil Upstream Research Company proposed two methodologies for hydrocarbon evaluation in thin-bed condition. When the average thickness of beds is thinner than 1 ft (30 cm), the individual beds are no more detectable directly by the well-logs (aliasing effect). So, high-frequency geological features, like thin-beds, will not be tractable on well-logs, and the resulting well-log will contain lower frequencies. Therefore, the method for studying beds, thinner (thicker) than 30 cm is called low-resolution (high-resolution) method. In high-resolution modelling, well-known iterative inverse solution is introduced, and in low-resolution modelling, Volumetric Laminated Sand Analysis (VLSA) is developed (Figure 4-1) (Passey *et al.*, 2004).

VLSA modelling is a probabilistic approach, based on the volumetric recording mechanism of well-logs. It is considered that each record is an average of petrophysical parameters of thin-beds, weighted by corresponding thicknesses. Then, the evaluation is realized by Monte-Carlo (MC) simulation on the intervals of 47.6 ft (14.5 m). Compared to conventional method, estimation of hydrocarbon pore-thickness in thin-bed condition is improved by 400%, using VLSA method. In the current thesis, VLSA is a base for comparing the proposed methodology with.

Researchers of ExxonMobil further published their thin-bed evaluation experiences in a comprehensive book (Passey *et al.*, 2006):

- Conventional well-log analysis methods underestimate hydrocarbon pore-thickness in shaly sand thin-beds: in tidal and submarine environments, respectively 80% and 30% of reservoir volume occurs in beds, below standard core-plug diameter (1 inch = 2.5 cm). In most of the time, errors of hydrocarbon pore-thickness evaluation is more than 20%. When net to gross ratio exceeds 90%, the error of conventional method becomes acceptable.
- Resistivity is a key log for reservoir characterization, therefore vertical resolution of LLD (2 ft = 60 cm) is suggested as thickness limit of thin-bed characterization.

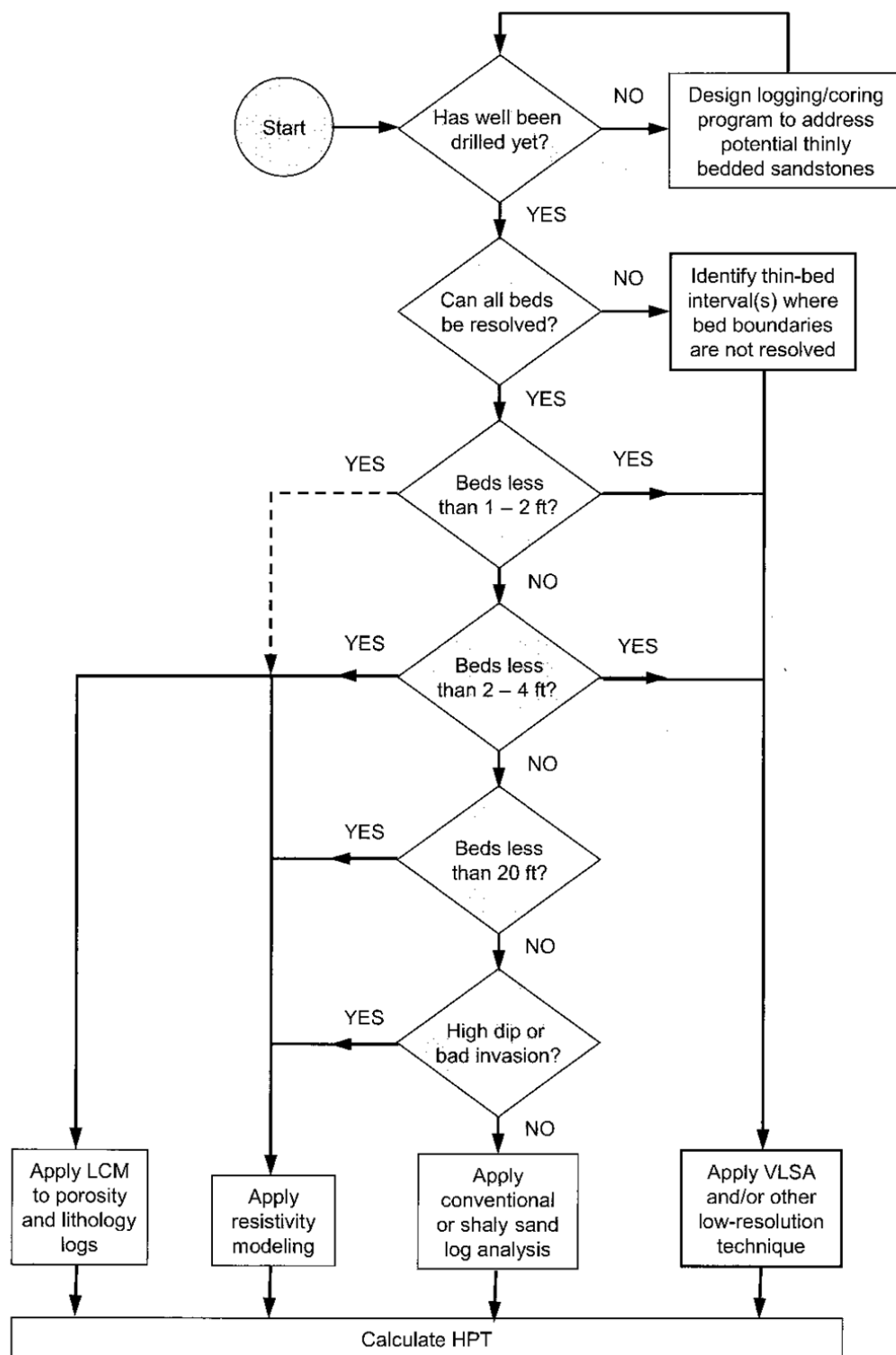


Figure 4-1. Flowchart for hydrocarbon pore-thickness evaluation in thin-bed condition (Passey *et al.*, 2006). LCM stands for Log Convolution Modelling. Volumetric Laminated Sand Analysis (VLSA) is a probabilistic method, developed particularly to petrophysical evaluation of beds thinner than 1 ft (30 cm).

### 4.1.1 VLSA Method

Since this method is a reference for comparing the results of the proposed thin-bed methods in coming chapters, the algorithm is introduced briefly. For detailed studies, refer to [Passey \*et al.\* \(2004\)](#).

(i) For each well-log, a parametric PDF is created. The PDF could have rectangular, normal, or other distribution. The average and standard deviation of the PDF are driven from well-log data, and the uncertainty of each well-log is defined as the ratio of standard deviation to the average data.

(ii) For estimating each petrophysical parameter, porosity, permeability, hydrocarbon content, etc., the input parameters, from well-logs, are generated randomly from the corresponding PDF.

(iii) After each random generation, the output is calculated and saved.

(iv) PDF of the output is updated and plotted.

(v) The second stage is iterated for several times to reach a convergence condition.

## 4.2 Theory of geometric thin-bed simulator

A simulator is designed here to better understand the mechanism of logging in presence of a single thin-bed. The simulator generates synthetic-logs, which are developed for GR, RHOB and NPHI. A more complex simulator, with much more rules (configurations), is required for DT. The reason is that the membership function of GR, RHOB and NPHI is triangular, but it is trapezoidal for DT. In order to have only seven configurations ([Figure 4-2a](#)), the thin-bed is considered thinner than the half of VRmf ([Relation 4-1](#)).

$$bed\ thickness \leq \frac{1}{2}VRmf \quad (4-1)$$

Consider a thin-bed with petrophysical value of  $q_2$ , between two thick beds (Figure 4-2a). The synthetic-log would be an average of  $q_1$ ,  $q_2$  and  $q_3$ , weighted by the membership function, over a VRmf (Relation 4-2). Reminding that the membership function shows contribution of each horizon to the recording. For example, in the configuration III, Figure 4-2b, it is expected to have a larger weight for  $q_1$  because it occupies larger volume of investigation. The convolution form of Relation 4-2 is previously developed for calculating susceptibility log (Desvignes *et al.*, 1992) (Appendix A).

The synthetic-log could be solved in a discrete space. The volume of investigation in Figure 4-2b is subdivided into four parts:  $S_1$ ,  $S_2$ ,  $S_3$  and  $S_4$ , and simply the ratio of  $S_i$  to  $\sum S_i$  is defined as the weight of each n parts in the averaging (Relation 4-3).

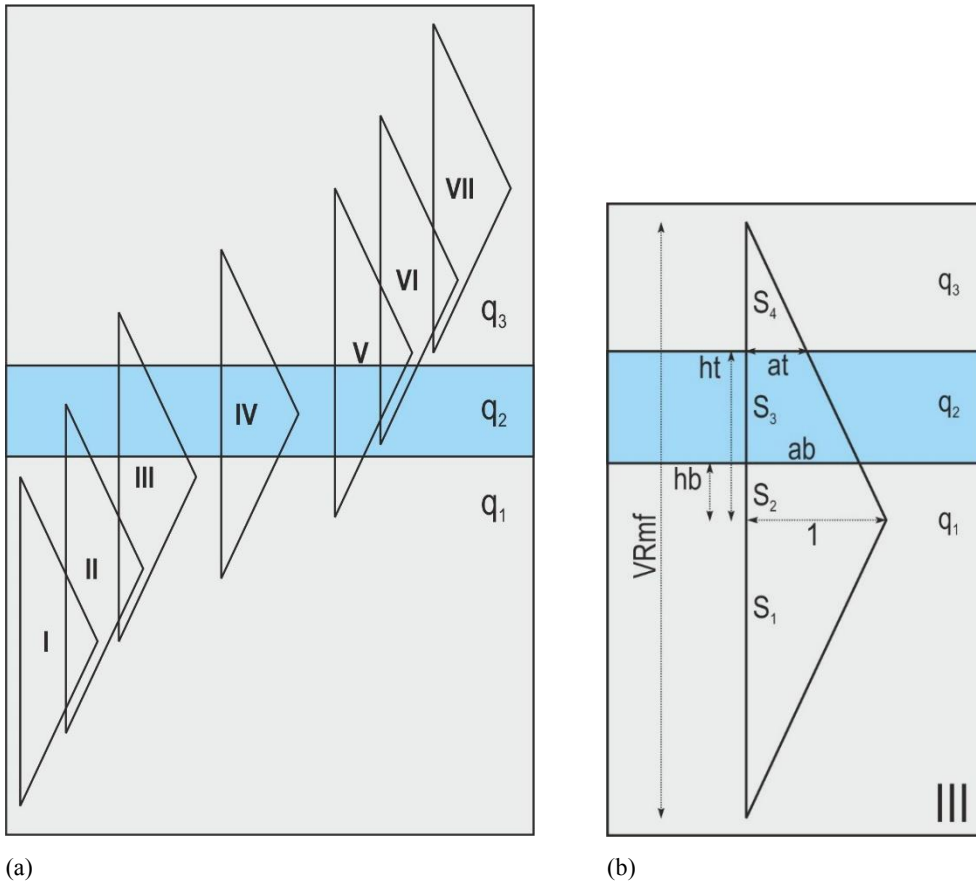


Figure 4-2. a) Seven configurations in detecting a thin-bed when membership function is triangular. b) Details of configuration III for calculating synthetic-log.

$$slog = \int_{x=0}^{VRmf} q(x) \times MF(x) \times dx \quad (4-2)$$

$$slog = \frac{\sum_{i=1}^n q_i \times S_i}{\sum_{i=1}^n S_i} \quad (4-3)$$

The limiting conditions for geometric thin-bed simulator are: **(i)** the existence of a thin-bed between two thick beds; **(ii)** the wellbore is drilled perpendicular to the geological beds; **(iii)**  $q_1 = q_3$ ; **(iv)** triangular membership function; **(v)** thin-bed thickness  $\leq \frac{1}{2}VRmf$ .

In [Figure 4-2b](#),  $S_1$  and  $S_4$  are triangles, and  $S_2$  and  $S_3$  are trapezoids.  $hb$  ( $ht$ ) is the distance from the centre of  $VRmf$  to the bottom (top) of the thin-bed. Because all the depths are known,  $hb$  and  $ht$  are known variables too.  $at$  and  $ab$ , introduced in [Figure 4-2b](#), could be calculated by  $hb$ ,  $ht$  and  $DI$ , using the Intercept Theorem of Thales. So, the weights are calculated for all the configurations.

$$at = DI - \frac{2 \times ht \times DI}{VRmf} \quad (4-4)$$

$$ab = DI - \frac{2 \times hb \times DI}{VRmf} \quad (4-5)$$

$$slog_I = q_1$$

Configuration I

$$slog_{II} = \frac{S_1 \times q_1 + S_2 \times q_1 + S_3 \times q_2}{S_1 + S_2 + S_3}$$

$$S_1 = \frac{1}{2} \times \frac{VRmf}{2} \times DI$$

$$S_2 = \frac{1}{2} \times hb \times (ab + DI)$$

$$S_3 = \frac{1}{2} \times at \times \left( \frac{VRmf}{2} - hb \right)$$

Configuration II

$$slog_{III} = \frac{S_1 \times q_1 + S_2 \times q_1 + S_3 \times q_2 + S_4 \times q_3}{S_1 + S_2 + S_3 + S_4}$$

$$S_1 = \frac{1}{2} \times \frac{VRmf}{2} \times DI$$

$$S_2 = \frac{1}{2} \times hb \times (ab + DI)$$

$$S_3 = \frac{ha - hb}{2} \times (at + ab)$$

$$S_4 = \frac{1}{2} \times \left( \frac{VRmf}{2} - ht \right) \times at$$

Configuration III

$$slog_{IV} = \frac{S_1 \times q_1 + S_2 \times q_2 + S_3 \times q_2 + S_4 \times q_3}{S_1 + S_2 + S_3 + S_4}$$

$$S_1 = \frac{1}{2} \times ab \times \left( \frac{VRmf}{2} + hb^- \right)$$

$$S_2 = \frac{1}{2} \times (-hb^-) \times (ab + DI)$$

$$S_3 = \frac{1}{2} \times ht \times (at + DI)$$

$$S_4 = \frac{1}{2} \times \left( \frac{VRmf}{2} - ht \right) \times at$$

Configuration IV

$$slog_V = \frac{S_1 \times q_1 + S_2 \times q_2 + S_3 \times q_3 + S_4 \times q_3}{S_1 + S_2 + S_3 + S_4}$$

$$S_1 = \frac{1}{2} \times ab \times \left( \frac{VRmf}{2} + hb^- \right)$$

$$S_2 = \frac{1}{2} \times (ht^- - hb^-) \times (ab + at)$$

$$S_3 = \frac{1}{2} \times (-ht^-) \times (at + DI)$$

$$S_4 = \frac{1}{2} \times DI \times \frac{VRmf}{2}$$

Configuration V



$$slog_{VI} = \frac{S_1 \times q_2 + S_2 \times q_3 + S_3 \times q_3}{S_1 + S_2 + S_3}$$

$$S_1 = \frac{1}{2} \times at \times \left( \frac{VRmf}{2} + ht^- \right)$$

$$S_2 = \frac{1}{2} \times (-ht^-) \times (DI + at)$$

$$S_3 = \frac{1}{2} \times DI \times \frac{VRmf}{2}$$

Configuration VI

$$slog_{VII} = q_3$$

Configuration VII

In the all above calculations, the height of the membership function, i.e. the centre of VRfm, is considered as the zero point of one-dimensional (vertical) coordinate system, positive upward. Therefore, when the top (bottom) bed line is located above the zero point, the value of  $ht$  ( $hb$ ) is positive. And when the top (bottom) bed is below the zero point, the value of  $ht^-$  ( $hb^-$ ) is negative. The negative superscript indicates the relative location to the zero point, and the sign of  $ht$ .

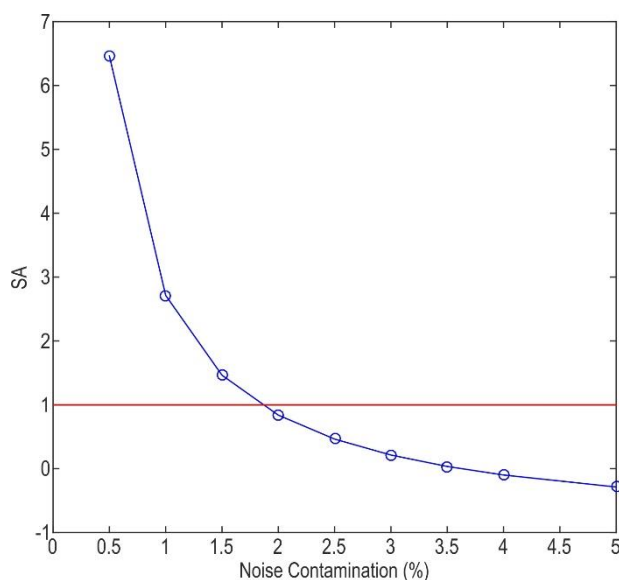
### 4.3 Sensitivity analysis of well-logs to a 30 cm thin-bed

The geometric simulator regenerates several realizations of well-logs, detecting a single thin-bed. It provides us the opportunity of analysing the sensitivity of well-logs in thin-bed detection. The presumed geological conditions for the sensitivity analysis are: **(i)** Thin-bed thickness of 30 cm; **(ii)** GR, RHOB and NPHI of host rock 200 API, 2.5 g.cm<sup>-3</sup> and 10%, respectively; **(iii)** GR, RHOB and NPHI of the thin-bed is 215 API, 3 g.cm<sup>-3</sup> and 15%, respectively; **(iv)** VRmf is considered 70 cm; **(v)** SR is 15.24 cm.

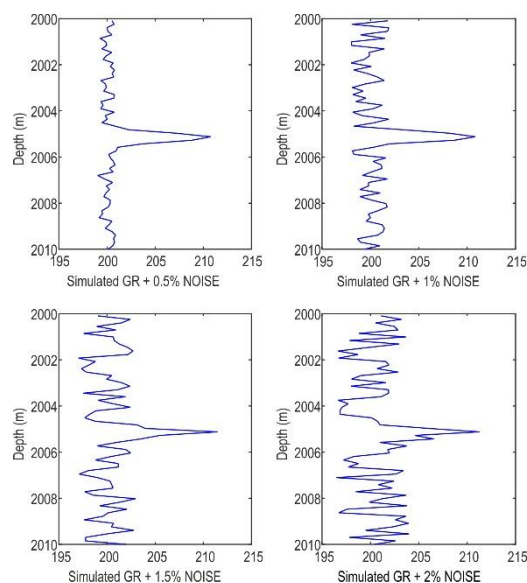
By increasing noise contamination, thin-bed trace (peak) is going to be diminished (Figure 4-3). Noise contamination is a random variable, between zero and one, with the uniform distribution. The index of the sensitivity analysis is considered as the ratio of the destruction at

the depth of the thin-bed to the highest generated peak at the other depths, [Relation 4-6](#). If the destructive effect of noise covers the thin-bed trace, so  $SA < 1$ .

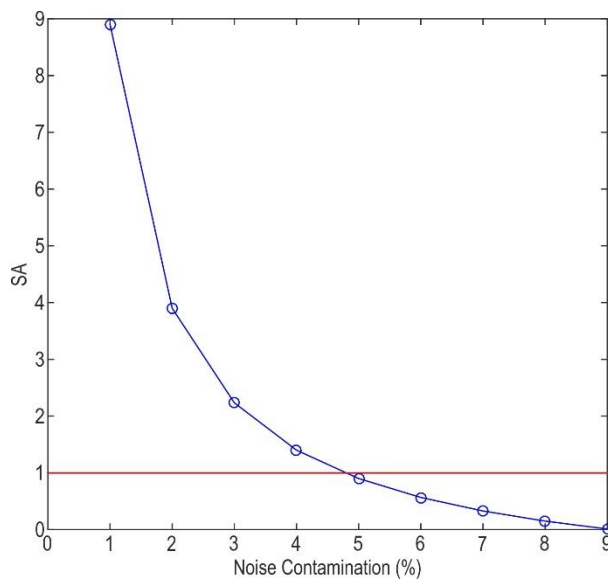
$$SA = \frac{peak - peak \times noise}{host + host \times noise} \quad (4-6)$$



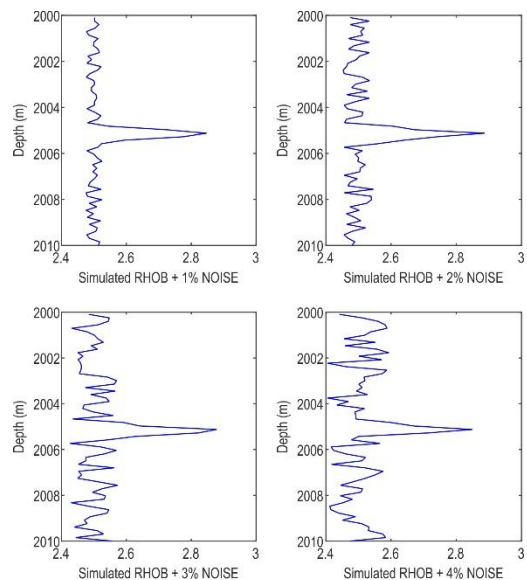
(a)



(b)



(c)



(d)

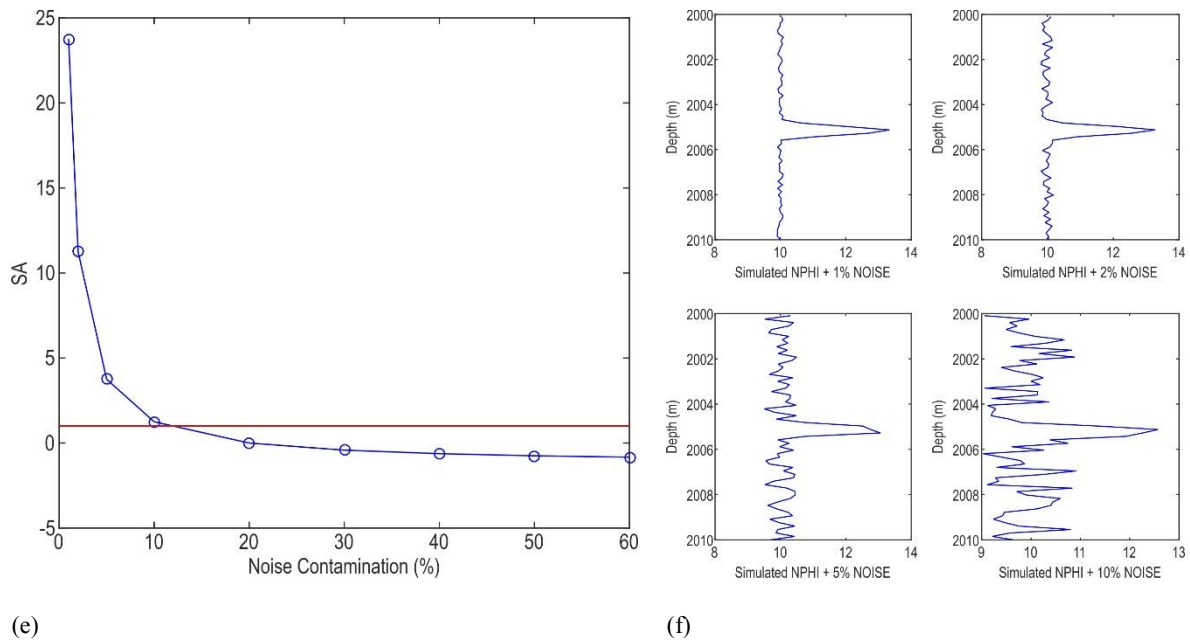


Figure 4-3. Sensitivity analysis and log response of random noise contamination: a) Sensitivity analysis of noisy GR and b) synthetic GR with 0.5, 1, 1.5 and 2% noise. c) Sensitivity analysis of noisy RHOB and d) synthetic RHOB with 1%, 2%, 3% and 4% noise. e) Sensitivity analysis of noisy NPHI and f) synthetic NPHI with 1%, 2%, 5% and 10% noise.

In Figure 4-3a,c,e, dots around the line  $y=1$  are risky points, and above (below) the line  $y=1$  is (un)reliable window. Comparing this categorization with reported noise of well-logs (Table 1-4) provides us reliability of well-log detection for thin-beds (30 cm). Therefore, GR well-log is not a reliable well-log for thin-beds thinner than 30 cm and 15 API difference in GR. This problem could be solved either by increasing thickness of the target for GR or increasing GR difference of the bed and the neighbouring beds.

Table 4-1. Defining reliable and risky windows for interpreting noisy well-logs, the case of 30 cm thin-bed.

Well-log	GR	RHOB	NPHI
Reported Noise (see Table 1-4)	$\pm 5\%$	$\pm 0.01 \text{ g.cm}^{-3}$ $\cong$ $\pm 0.33\%$	0-20: $\pm 1\%$ 20-30: $\pm 2\%$ 30-45: $\pm 6\%$
Reliable	$< 1.5\%$	$< 4\%$	$< 10\%$
Risky	1.5-2%	4-5%	10-20%
Unreliable	$> 2\%$	$> 5\%$	$> 20\%$

#### 4.4 Deconvolution relations for thin-bed characterization

Deconvolving well-logs (here GR, RHOB and NPHI) is necessary to characterize a thin-bed accurately, i.e. decreasing the shoulder-bed effect to approximate the real thickness and the real petrophysical value of a thin-bed. Here, thin-bed deconvolution is based on the balance between amplitude and apparent thickness of well-log (Figure 3-5). Thus a statistical analysis is used to find a relation between synthetic- and ideal-logs.

For developing deconvolution relations, a set of ideal-logs is first generated. That means petrophysical specifications of thin-beds (thickness of the thin-bed and values of  $q_1$ ,  $q_2$  and  $q_3$ ) have to be defined. Five thicknesses are assumed: 5, 10, 15, 20 and 30 cm. Due to limitation of the simulator, it is assumed to have the same petrophysical values above and below the thin-bed, i.e.  $q_1 = q_3$ . Without loss of generality, assume  $q_1 = q_3 = 0$ , because the goal is rescaling or deconvolving the shape of the well-log, i.e. reducing the shoulder-bed effect. Therefore, only the difference of the  $q_2$  to  $q_1$  (or  $q_3$ ), before and after adding shoulder effect are important. The petrophysical value of  $q_2$  is set to be 1, 3, 5, 7, 10, 12, 15, 17, 20, 22, 25, 27 or 30 for GR (API) and NPHI (%), whereas it is considered to be 0.01, 0.02, 0.05, 0.07, 0.10, 0.12, 0.13 or 0.15 for RHOB ( $\text{g.cm}^{-3}$ ). Reminding that these values are not absolute petrophysical values. They are relative differences of thin-bed petrophysical values, according to the surrounding beds. Combining the thickness and petrophysical values of synthetic thin-beds, 65 ideal-logs for GR and NPHI, and 40 ideal-logs for RHOB were generated.

In the second stage, synthetic-log simulator is run over the ideal-logs. Synthetic-logs are the outputs of convolution (Relation 4-3) hence contaminated by shoulder-bed effect (Figure 4-4). The crosses on Figure 4-4a are synthetic-log values, plotted against ideal-log values. All the values are below the line  $y=x$ , i.e. underestimated by synthetic-log. The thickness of the thin-bed read from the synthetic-log is plotted against the thickness read from the ideal-log, crosses on Figure 4-4b. The crosses above the line  $y=x$  are thickness overestimations. Underestimation of petrophysical value and overestimation of thickness were expected because of the nature of shoulder-bed effect.

For Figure 4-4a,b, the regression lines are calculated for GR, RHOB and NPHI for correlating synthetic-logs to ideal-logs (Relations 4-7 to 4-12). The inputs of regression models

are thickness and relative synthetic-log (or well-log) values of thin-bed, and the outputs are regression models, representing ideal thickness (or real thickness) and relative ideal-log (or real-log).

$$\Delta GR_{reg} = 1.0356 \Delta GR_{log} + 0.0669 TH_{log GR} \quad (4-7)$$

$$TH_{reg} = -0.1663 \Delta GR_{log} + 0.2926 TH_{log GR} \quad (4-8)$$

$$\Delta RHOB_{reg} = 0.9127 \Delta RHOB_{log} + 0.0007 TH_{log RHOB} \quad (4-9)$$

$$TH_{reg} = 115.591 \Delta RHOB_{log} + 0.1860 TH_{log RHOB} \quad (4-10)$$

$$\Delta NPHI_{reg} = 1.0262 \Delta NPHI_{log} + 0.1124 TH_{log NPHI} \quad (4-11)$$

$$TH_{reg} = 0.7417 \Delta NPHI_{log} + 0.1499 TH_{log NPHI} \quad (4-12)$$

where  $TH$  stands for thickness. For GR model, the thickness, read from the well-log has to be thinner than 100 cm, and the difference of well-log value of thin-bed, relative to upper and lower beds, should be lower than 30 API. The acceptable domain of thickness for RHOB is up to 110 cm, and the maximum relative well-log value is  $0.15 \text{ g.cm}^{-3}$ . NPHI of thin-bed could vary as much as 30% (Figure 4-4a) and its well-log-based thickness should be thinner than 110 cm (Figure 4-4b).

Finally, the developed relations are applied on the outputs of simulators (i.e. synthetic-logs) to move the crosses closer to  $y=x$ , i.e. for better matching the ideal-logs (dots on Figure 4-4a,b). Based on MSE of synthetic data, the error is reduced two to three times in characterizing petrophysical values, and from 40 to about 80 times in thickness estimation (Table 4-2).

Table 4-2. Comparing MSE of thin-bed characterization. Interpretations are based on synthetic-logs versus regression models (deconvolved) (Figure 4-4).

	MSE of synthetic-logs			MSE of deconvolved synthetic-log		
	GR	RHOB	NPHI	GR	RHOB	NPHI
Petrophysical value	42.25	0.003	139.61	20.20	0.001	39.99
Thickness	2249.41	3202.01	4134.78	50.75	67.31	53.29

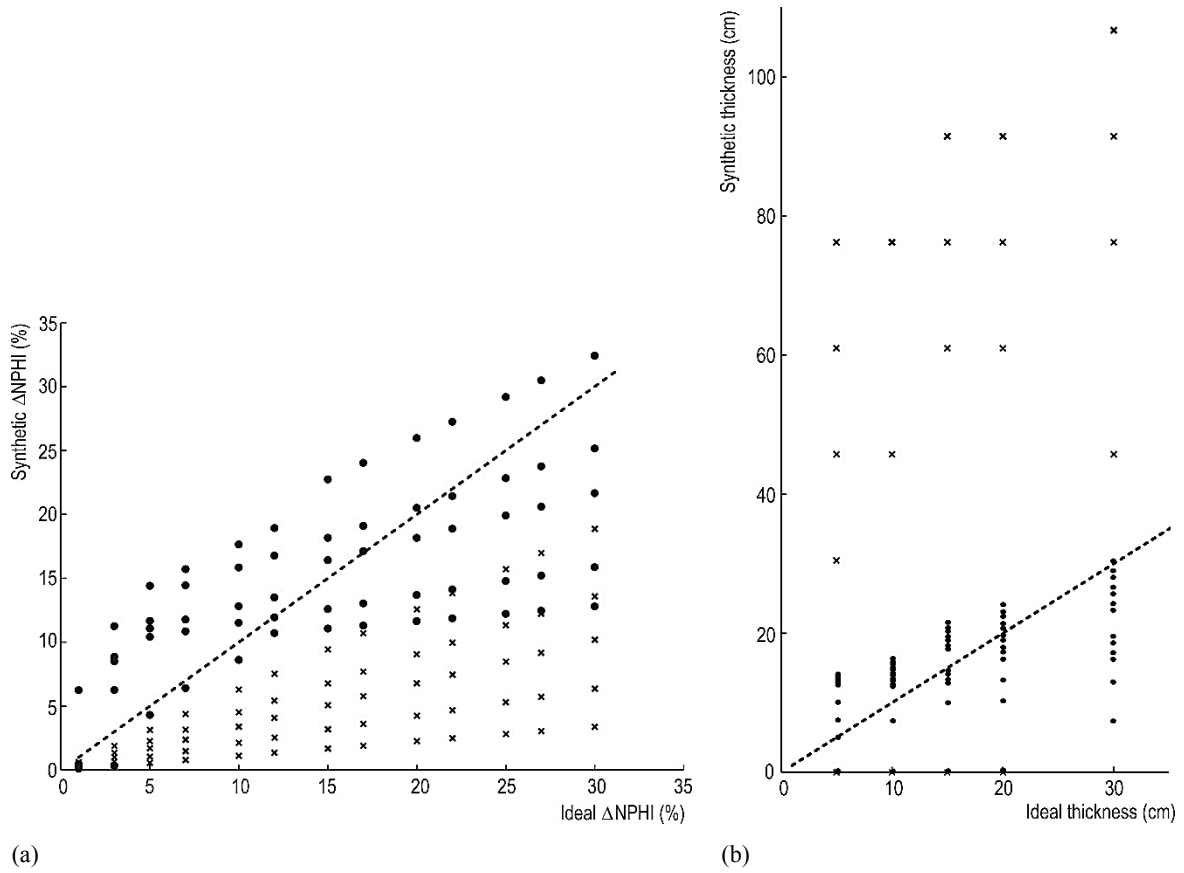


Figure 4-4. Deconvolution results on synthetic data. a) Petrophysical values (NPHI) of thin-beds before (x) and after (dot) reducing shoulder-bed effect. b) Thickness of thin-beds before (x) and after (dot) reducing shoulder effect.

#### 4.5 Thin-bed characterization, the Sarvak Formation case-study

In order to characterize thin-beds within Sarvak Formation, deconvolution relations (4-7 to 4-12) are applied to the well-logs. Ten depths are selected, which show thin-bed behaviour, i.e. there are small peaks in two or three of well-logs: GR, RHOB and NPHI (Table 4-3).

It is worthy to mention why the observations of Table 4-3 and Figure 4-5 are interpreted as thin-beds. The very thin-beds that do not have any effect on the well-logs are of course undetectable in the well-scale. When the beds have some effects on two or three well-logs, there are two possibilities: either the bed is (i) thick enough to let the receivers detect its real petrophysical value, i.e. the shape of the well-log is stable, not a peak or a through; or (ii) too thin that only a few records could reflect it (configurations A or B, Figure 3-5). In this case, the

well-log shows a peak or a trough shape, and cannot fully represent the real petrophysical value. So, when there are peaks or troughs at the same depth within well-logs, it is interpreted as thin-beds. They could also be interpreted as a thin phenomenon, like vuggy or fractured interval. The former interpretation is true since in the petroleum geology, well-logs are acquired through sedimentary layers, and geological phenomena are often related to these strata.

Table 4-3. Thin-bed characterizations of 10 real cases within Sarvak Formation, well#1. The apparent thickness values of the thin-beds are scaled to be closer to real thickness values by the deconvolution models. NAN: thin-bed curve not observed.

	RMSE	1	2	3	4	5	6	7	8	9	10
depth (m)		2727.96	2803.40	2831.13	2850.49	3150.87	3156.00	3158.19	3165.20	3184.55	3186.38
$\Delta$ GR log (API)	6.50	22.10	10.17	25.72	12.79	10.40	30.67	23.00	41.32	7.41	8.80
$\Delta$ GR model (API)	4.49	32.06	17.67	32.75	19.36	14.85	34.82	27.90	47.89	12.77	14.21
GR log thickness (cm)	47.43	137.16	106.68	91.44	91.44	60.96	45.72	60.96	76.20	76.20	76.20
GR model thickness (cm)	7.12	36.46	29.52	22.48	24.63	16.11	8.28	14.01	15.42	21.06	20.83
$\Delta$ RHOB log (g.cm <sup>-3</sup> )	0.06	0.07	0.09	0.07	0.03	NAN	0.07	0.04	0.15	NAN	0.06
$\Delta$ RHOB model (g.cm <sup>-3</sup> )	0.03	0.10	0.17	0.13	0.08	NAN	0.13	0.09	0.18	NAN	0.14
RHOB log thickness (cm)	56.59	45.72	121.92	91.44	76.20	NAN	91.44	76.20	60.96	NAN	121.92
RHOB model thickness (cm)	8.20	16.60	33.08	25.10	17.64	NAN	25.10	18.80	28.68	NAN	29.42
$\Delta$ NPHI log (%)	11.82	9.00	14.00	4.00	5.00	9.00	14.00	4.00	11.00	4.00	1.00
$\Delta$ NPHI model (%)	6.32	24.16	29.29	15.30	14.46	20.43	29.29	11.57	22.48	17.16	12.22
NPHI log thickness (cm)	64.30	121.92	121.92	91.44	76.20	91.44	121.92	60.96	91.44	106.68	91.44
NPHI model thickness (cm)	7.30	24.95	28.66	16.67	15.13	20.38	28.66	12.10	21.87	18.96	14.45
Final Thickness (cm)		26.05	30.42	21.42	19.16	18.23	20.62	14.97	21.96	20.02	21.57
Standard deviation of thickness (cm)		8.14	1.91	3.52	4.02	2.14	8.89	2.81	5.41	1.05	6.13

Then, the apparent thicknesses and apparent variation of petrophysical values are read through the well-logs, and added to the table. These values are not the real thickness and real petrophysical values. The petrophysical value is affected by the neighbouring beds, and the well-log thickness is an overestimation of real thickness due to shoulder-bed effect. Now, using the deconvolution relations, shoulder-bed effect is reduced to get closer to the real values, and the outputs are added to [Table 4-3](#).

In practice, thin-beds have to be studied by different logs individually; then, comparing multiple results (approaches) to come to the final decision. The main reason is that a thin-bed might inherently show a specific change in a petrophysical feature; e.g. GR, while not a clear trace on other well-logs. Therefore, using various well-logs simultaneously will not necessarily end-up to a successful thin-bed characterization. The second reason for studying thin-beds separately is that well-logs have different volume of investigation and sampling rate. So, some logs might not detect some thicknesses, while others may detect. The third reason is designing thin-bed characterization algorithms by individual well-logs, mentioned in the literature ([Gallet and Courtilot, 1989](#); [Desvignes \*et al.\*, 1992](#); [Heidari \*et al.\*, 2012](#)).

The application of deconvolution relations amplifies all petrophysical values. In eight observations (#1-4, #6-8 and #10), three thickness models can be given, and in two observations (#5 and #9), only two thickness models can be obtained. The final thickness is calculated by a weighted average of thickness models, regarding RMSE of each model ([Table 4-2](#)). Low standard deviation of the thickness estimations show high confidence-level and similarity of the thickness models.

In observation#3, e.g. the thickness according to GR model is  $22.48 \pm 7.12$  cm ([Table 4-3](#)). The thickness derived from RHOB model is  $25.10 \pm 8.20$  cm, which is just a little thicker, however GR model is more precise. The third thickness estimation ( $16.67 \pm 7.30$  cm), given by NPHI model, is lower than the others. The final thickness value is a weighted average of the three values provided from thickness models. The final thickness for observation#3 is  $21.42 \pm 7.57$  cm. White noise could be reduced through fusing multiple outputs. The standard deviation of the three thickness values (22.48, 25.10 and 16.67 cm) is small (3.52 cm), compared to the final error of estimation deduced from RMSE (7.57 cm) ([Table 4-3](#)).

Based on the concept of volumetric Nyquist frequency, there is no guarantee to have a direct measurement of a geologic bed thinner than  $SR + VR_{mf}$  ([Relation 3-5](#)). But the deconvolution procedure estimates petrophysical and thickness values of a bed thinner than  $SR + VR_{mf}$ , after reducing the shoulder-bed effect. The thin-bed characterization after deconvolution is much more accurate ([Table 4-2](#)). The characterization results of ten thin-beds (thickness values from 14 to 30 cm, [Table 4-3](#)) are promising for developing the methodology on the well-logs.



#### 4.5.1 Multi-well-log thin-bed characterization

The well-logs of the thinnest characterized bed, observation#7 of Table 4-3, are provided and interpreted (Figure 4-5a). At a depth of about 3158.19 m, there are positive peaks in GR and NPHI logs and a negative peak in RHOB. The GR increase is due to shale content (GR is here only the response of the potassium content). The increase of NPHI at this depth is the sign of increase of total porosity. The decrease of RHOB could be related to increase of porosity and shale content, simultaneously. RHOB log around this horizon fluctuates between 2.71 and 2.65 g.cm<sup>-3</sup>, which are equivalents to the densities of calcite and shale average, respectively (Ellis, 2007). So, this thin-bed can be interpreted as a shale inter-layer with the thickness of 15.0±7.5 cm (Figure 4-5a). The error (±7.5 cm) is calculated by error propagation methodology, which is about the expected error of ±7.75 cm, derived from RMSE (Table 4-3).

From the viewpoint of sedimentology, the horizon at 3158.19 m depth, located at the lower Sarvak Formation, belongs to outer shelf sedimentary environment. Previous studies on this interval confirms deep water facies and marine conditions (Ghabeishavi *et al.*, 2010). Stratigraphic sequences of the third, fourth and fifth order are previously reported within the Sarvak Formation. Its lower part consists of about three sequences of the third order (Razin *et al.*, 2010; Vincent *et al.*, 2015). It has the potential for lithological variation, especially increase of shale volume. Therefore, the thin-bed characterization is acceptable (Figure 4-5a).

Thin-bed characterization method is also applied to a cored interval of the upper Sarvak Formation, within well#3 to verify thin-bed detection with the cores (Figure 4-5b). The lithology belongs to the shallow carbonates. The petrophysical behaviour of the black porous thin-bed differs from the neighbouring beds, since there is a core porosity anomaly (8.4% core porosity, Figure 4-5b). Therefore, it might be detectable by the well-logs.

At the depth of about 2802.85 m, within well#3, the deconvolution relations are applied on NPHI and RHOB logs. GR does not show thin-bed behaviour. The result is a thin-bed, with a thickness of 13±7.5 cm, compatible with the black thin-bed thickness in the core box (<25 cm). Worthy to mention that the real subsurface thickness of the black thin-bed is less than the core box because of core crushing at the surface and the overburden removal. In addition, corrected NPHI (11.7%) which is higher than the core porosity (8.4%) is compatible with the fact that the

effective porosity (core porosity) is never higher than the total porosity (NPHI). While non-corrected NPHI (3.8%) is lower than the core porosity, which is clearly far from the reality.

#### 4.6 Conclusions of Chapter 4

A thin-bed simulator was designed using geometric relations. The simulator was used to generate numerous synthetic-logs for different geological situations. Ideal-logs (without shoulder-bed effect) and synthetic-logs (contaminated by shoulder-bed effect) were compared to build regression models to deconvolve well-logs GR, RHOB and NPHI. They estimate the thickness of thin-beds, 40 to 80 times more accurately, compared to the apparent thickness, read from the well-logs. Petrophysical characterization could be carried out more precisely: RMSE of GR, RHOB and NPHI values were reduced from 42.25 to 20.20, 0.003 to 0.001 and 139.61 to 39.99, respectively. Such methodology could be developed for all well-log data in various conditions.

Finally, the application of deconvolution relations was checked in characterizing ten real thin-beds within the Sarvak Formation. All petrophysical values (GR, RHOB and NPHI) were increased and all the thickness values were reduced due to the decrease of shoulder-bed effect. The resulting thickness values of observations were calculated by an averaging (weighted by RMSE) over thickness values of the individual well-logs. The average of standard deviation of the thickness values was 4.4 cm, which is a precise value, considering the vertical resolution of more than 60 cm.

In well#3 (Figure 4-5b), NPHI and thickness of a porous thin-bed were estimated (corrected) by the proposed method, and the results were compared to the core data. The measured NPHI was 3.8%. The proposed method corrected the NPHI value to 11.7%. The corrected NPHI seems to be more accurate than the measured NPHI, since it is higher than the core porosity (8.4%). Reminding that the total porosity (NPHI) should not be less than the effective porosity (core). The thickness of the thin-bed was estimated to be  $13 \pm 7.5$  cm, which is compatible with the thickness of the thin-bed in the core box ( $< 25$  cm). Usually the *in situ* thickness is less than the thickness of the core boxes, since the lithostatic pressure is removed at the surface, and the cores are crushed.

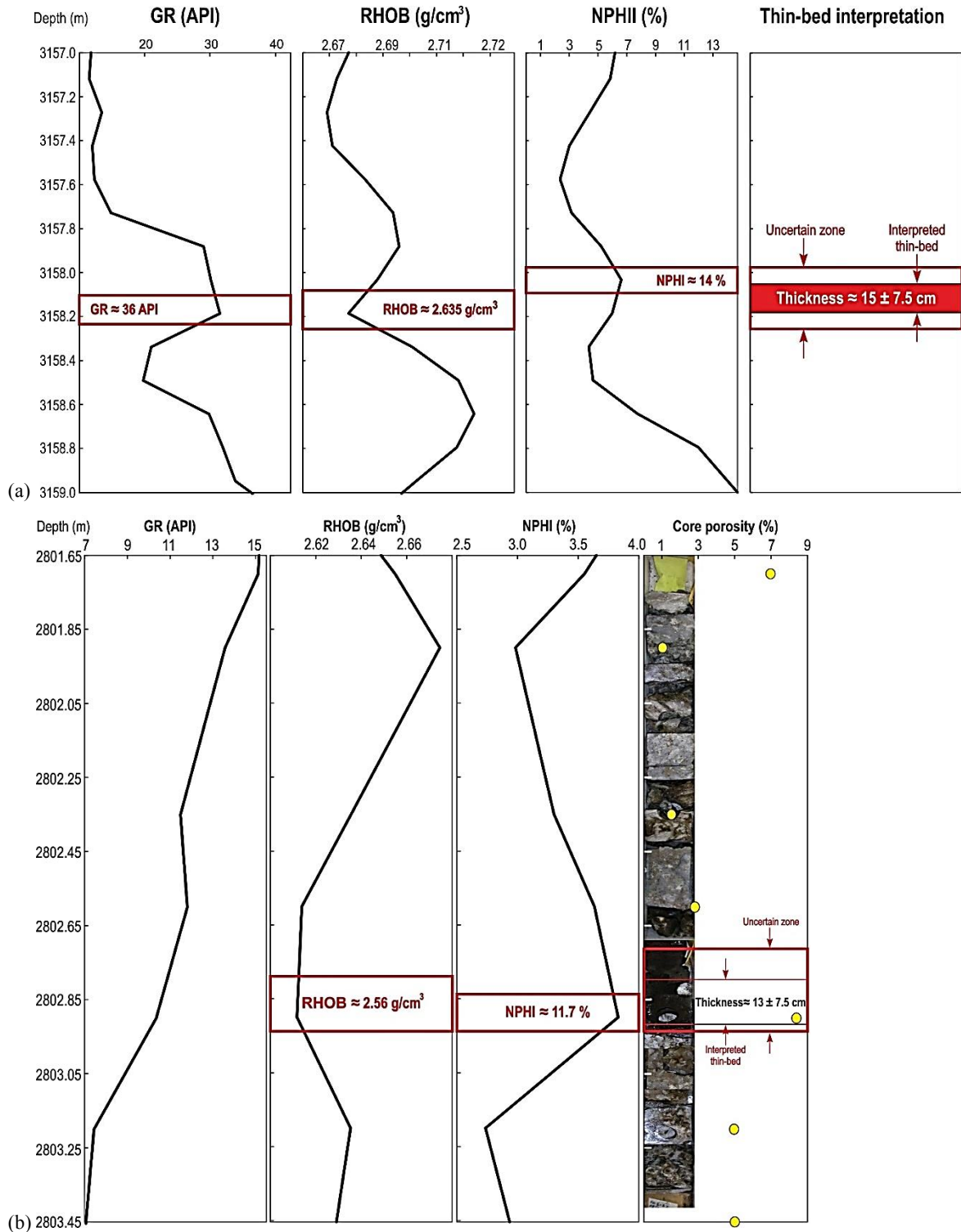


Figure 4-5. Two examples of thin-bed interpretation on the real data. Thin-bed is firstly interpreted by the well-logs individually. The well-log values are amplified and given on the thin-bed. Final thickness interpretation and its associated uncertainty is provided in the rightmost track. a) Observation#7, well#1 (Table 4-3). b) A case-study in well#3, verified with the core box (yellow circles). The thin-bed interpretation is inclined upward since the well-logs have an upward skewness.

Geometry-based algorithm has the following advantages: it **(i)** estimates the thickness of thin-bed, **(ii)** corrects (deconvolves) the petrophysical value of a well-log at the depth of thin-bed, **(iii)** is easy to understand the methodology basis. Whereas the disadvantages are: the algorithm **(i)** does not provide a complete curve, i.e. the estimation belongs only to a single point, and **(ii)** is time consuming and not automated.

## 5 Enhancing vertical resolution of well-logs

### Highlights of Chapter 5

- Bayes Theorem and Dempster-Shafer Theory (DST) of evidences are used to combine adjacent well-log records.
- The importance of volumetric Nyquist frequency in up-scaling is shown.
- Application of DST is developed for assessing intersections of well-log recordings.
- Vertical resolutions of GR, RHOB, NPHI and DT are improved from ~60 cm to the sampling rate (~15 cm).
- The well-logs are corrected by amplifying the attenuated high frequencies.
- Shoulder-bed effect, i.e. effect of neighbouring beds, is reduced.
- The proposed method is verified by synthetic cases, core box and core porosity.
- The depth uncertainty of well-logs is converted into the value uncertainty of well-logs.

### 5.1 Combining adjacent well-log records by Bayesian Theorem

Bayesian Theorem is the oldest mathematical tool for uncertainty assessment (Figure 2-1a). The newer tools are developed within the domain of subjective probability: Fuzzy Theory and Dempster-Shafer Theory (DST) of evidences (Figure 2-1b). The basic concepts for each of these theories are: PDF, membership function and mass function for Bayesian, fuzzy and DST, respectively.

By the means of Bayes rule, the uncertainty of intersections (Figure 2-1a) are going to be assessed. So, previously defined membership functions (Table 3-2) are converted into PDFs. VRmf remaining constant (61 and 76 cm), only the height of membership functions are reduced so that the surface area becomes 1 (PDFs, Figure 5-1) to satisfy the famous law of probability within the universal set (Relation 5-1). When VRmf is 61cm (76 cm), a maximum of four (five) adjacent distribution functions can have a non-empty intersection (Figure 5-1).

$$\int_{\text{universal set}} P(A_i) \times dA = 1; A_i \cap A_j = \emptyset; i \neq j \quad (5-1)$$

Considering  $PDF_i$  as distribution function of the  $i$ th recording point, therefore  $PDF_{i-1}$  and  $PDF_{i+1}$  will be adjacent distribution functions, having an intersection with  $PDF_i$ . So, [Relation 5-2](#) would be valid.

$$PDF_i + PDF_{i+1} = PDF_i \cup PDF_{i+1} + PDF_i \cap PDF_{i+1} \quad (5-2)$$

For satisfying [Relation 5-1](#), the left-hand side of [Relation 5-2](#) is divided by the number of PDFs, i.e. averaging PDFs. The result is a new probability function, PDFX, are given in [Figure 5-1](#). For each of new PDFs, Shannon entropy and VRmf are calculated, and due to [Table 3-3](#), the thinnest surely detectable bed is provided in [Table 5-1](#).

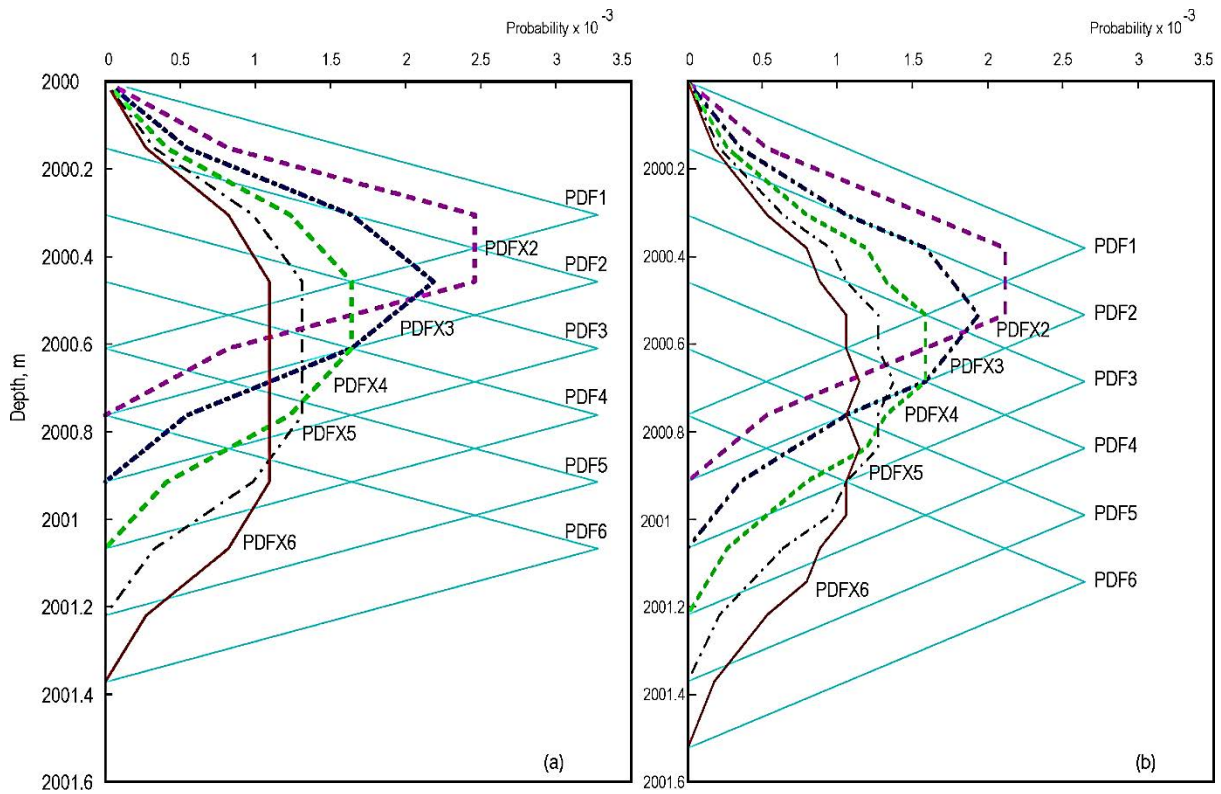


Figure 5-1. PDFXn is a combination of n adjacent PDFs. SR=15.24 cm. a) VRmf=61 cm and b) VRmf=76 cm.

Table 5-1. Properties of constructed PDFs in Figure 5-1.

VRmf of PDF	PDF(Xn)	Shannon entropy	VRmf (cm)	SR+ VRmf (cm)
61 cm	PDF1	6.22	61	76
	PDFX2	6.39	76	91
	PDFX3	6.58	91	106
	PDFX4	6.75	107	122
	PDFX5	6.91	122	137
	PDFX6	7.04	137	152
76 cm	PDF1	6.44	76	91
	PDFX2	6.56	91	106
	PDFX3	6.70	106	121
	PDFX4	6.85	122	137
	PDFX5	6.98	137	152
	PDFX6	7.11	152	167

As  $n$  increases, the entropy and VRmf of PDFX $n$  increases too. Table 5-1 provides us the opportunity of choosing our PDF, regarding the thickness of the prospect under study. It means that when our target is exploring reservoir beds thicker than 150 cm, it is reasonable to use PDFX6 (or PDFX5), instead of PDF1. The other advantage of this table is in suggesting a sequential well-log interpretation, i.e. as a quick-log interpretation we can do the interpretations by PDFX6, which overwhelms beds thinner than about 150 cm. In the next stage, detailed interpretation could be given by PDF1.

Based on Table 5-1, the most important fact is that conventional thin-bed studies does not characterize the beds, thinner than 76 cm, even if SR is much less, i.e. 15.24 cm. This deficiency of well-logs is addressed in this chapter by DST.

### 5.1.1 The importance of volumetric Nyquist frequency in up-scaling

The other important inference is regarding up-scaling issue. The goal in the up-scaling is to reduce the data volume, i.e. increase of SR while integrating the adjacent data. Due to the volumetric Nyquist frequency, if we increase the SR while averaging the adjacent recordings, considerable amount of data would be lost. As an example, by up-scaling five neighbouring data, corresponding VRmf would be 137 cm (61cm for PDF1). Now, if the SR be kept at 15.24 cm, i.e. the fused data are not deleted, the thinnest detectable bed would be  $VRmf+SR=152$  cm (Table 5-1). But if the SR is increased five times (by deleting the fused data) from 15.24 to 76.20, so the thinnest identifiable bed would be 213.2 cm! Deleting the fused data while

upscaling is usual in the petroleum industry, since the goal of upscaling is to decrease the volume of data.

## 5.2 Body Of Evidences (BOE) for well-logs

### 5.2.1 Focal elements of well-logs

In a series of observations (measurements, tests, etc.), each evidence is assigned to a space, named focal element. Here, focal elements are defined as depth intervals, i.e. focal elements are one-dimensional. We have defined two types of focal elements: **(i)** recording (r) that represents vertical resolution of the logging tool, and **(ii)** target (t) which is the target resolution, defined by the user. [Figure 5-2](#) shows focal elements of recording and target when vertical resolution is four times larger than sampling rate. In fact, the aim is to improve the vertical resolution of well-logs from the focal element of recording ( $FE^r$ ) to a smaller focal element, named target ( $FE^t$ ).

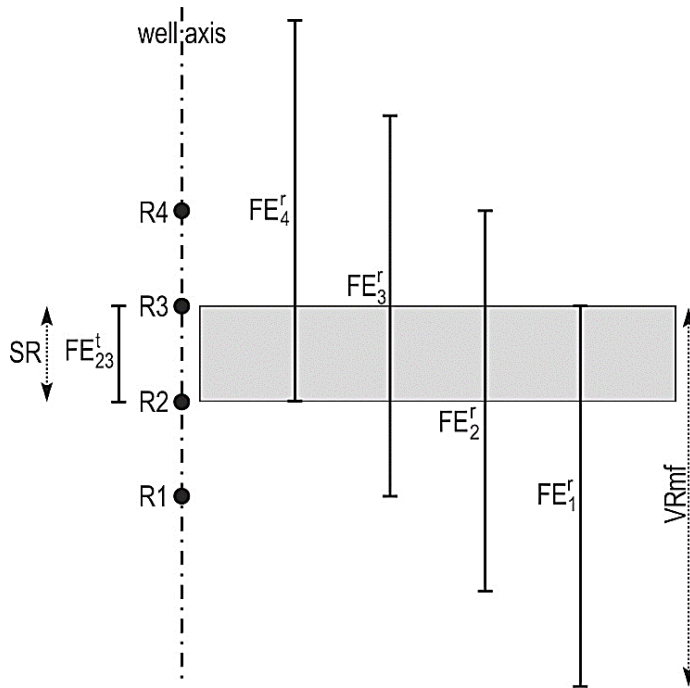


Figure 5-2. Defined focal elements of recording ( $FE^r$ ) and target ( $FE^t$ ) for a well-log with  $VRmf=4 \times SR$ .



### 5.2.2 Mass function of focal element of recording

Corresponding to each  $FE^r$ , a mass value is defined, which is free to move inside it. In addition to the BOE, redistribution of the mass has to obey the constraints of the problem, here geological and technical conditions. Mass function is always non-negative, and the summation of mass values over all the focal elements should be one ([Relation 2-1](#)).

Petrophysical well-logging is a volumetric measurement, i.e. assigns a single value to a volume of investigation. So, these recordings satisfy the requirements of designing a BOE: well-log as mass function, corresponding to the volume of investigation (focal element). Hence, uncertainty of well-logs could be modelled by DST, and the ignored geological heterogeneity could be rebuilt. In order to satisfy [Relation 2-1](#), mass function is defined as normalized value of well-log. Modelling unpredicted situations is not the concern of this study, therefore the mass function of null set ( $\phi$ ), does not take part in the calculations, i.e.  $m(\phi) = 0$ . The null function in DST corresponds to a situation that the defined BOE is not valid, e.g. well-logging under abnormal situations: high-noise, logging tool not working properly, turbulences, etc.

## 5.3 Belief and plausibility functions for focal element of target

### 5.3.1 Theoretical functions of belief and plausibility

Due to [Figure 5-2](#), the recorded well-log consists of four subset focal elements of target. The petrophysical value of each focal element of target affects the four adjacent well-log recordings. In the language of BOE, mass values of the four adjacent focal elements of recording could freely pass through a common focal element of target ( $FE_{23}^t$ , [Figure 5-2](#)). DST-based structure helps us to find lower (belief) and upper (plausibility) probabilities for each focal element of target ([Relations 2-2](#) and [2-3](#)).

### 5.3.2 Geological constraints as an axiomatic structure

Whereas [Relations 2-2](#) and [2-3](#) are valuable theoretically for defining belief and plausibility, they are not practically useful because the uncertainty range will be too large due to: (i) belief

function that is absolutely zero since the condition  $FE_j^r \subseteq FE_i^t$  of [Relation 2-3](#) is never valid in the defined BOE. The focal element of recording is always larger than the focal element of target. **(ii)** Plausibility value is always a too large value, i.e. a summation of adjacent recordings. Plausibility values, much larger than well-log values, lead to unrealistic situation since it is only a result of calculation. So, the uncertainty range would be too large. In addition, when an interval of a VRmf is homogeneous petrophysically, i.e. with constant well-log values, it is obvious not to have any uncertainty in the middle of the interval, while the theoretical functions of belief and plausibility will create an excessive uncertainty boundary.

An axiomatic structure is then designed to impose geological facts and BOE constraints on belief and plausibility functions. Applying three axioms results in a reasonable uncertainty range: **(i)** volumetric nature of the well-logs ([Section 3.1](#)): for each horizon, belief (plausibility) is the minimum (maximum) well-log value within the interval of a vertical resolution, centred at the depth of recording. We cannot generate or remove the mass, but the mass can move within its corresponding focal element of recording. **(ii)** No uncertainty in homogeneous conditions: if the well-log values remain constant within an interval of at least one vertical resolution, i.e. a focal element of record, there is no uncertainty range in the middle of the horizon. Thus belief, plausibility and mass functions will be equal. **(iii)** Shoulder-bed effect: at peaks and troughs the destructive shoulder-bed effect occurs. It has to be compensated, i.e. at peaks (troughs), belief (plausibility) has to be equal to the mass function. Belief (plausibility) at troughs (peaks) should be compensated by  $\epsilon$  as well ([Figure 5-3](#)).

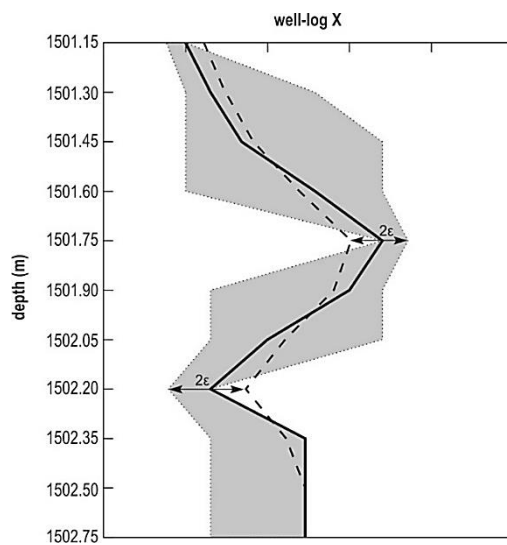


Figure 5-3. Example of a well-log with vertical resolution of 91 cm (thick line), its average on five adjacent points (dashed line) and the range between belief and plausibility (dotted lines).  $\epsilon$ : compensating shoulder-bed effect at peaks and troughs only.

### 5.3.3 Practical functions of belief and plausibility

Based on the axiomatic structure and defined mass function on the  $FE^r$ , belief and plausibility for  $FE^t$  is formulated:

$$Pls(FE_i^t) = \begin{cases} \max_{Fl_j^r \cap Fl_i^t \neq \emptyset} m(FE_j^r) + \varepsilon; & m(FE_{i-1}^r) \leq m(FE_i^r) \text{ and } m(FE_{i+1}^r) \leq m(FE_i^r) \text{ (peak)} \\ m(FE_i^r); & m(FE_i^r) \leq m(FE_{i-1}^r) \text{ and } m(FE_i^r) \leq m(FE_{i+1}^r) \text{ (trough)} \\ \max_{Fl_j^r \cap Fl_i^t \neq \emptyset} m(FE_j^r); & m(FE_{i-1}^r) \leq m(FE_i^r) \leq m(FE_{i+1}^r) \text{ (otherwise)} \end{cases} \quad (5-3)$$

$$Bel(FE_i^t) = \begin{cases} m(FE_i^r); & m(FE_{i-1}^r) \leq m(FE_i^r) \text{ and } m(FE_{i+1}^r) \leq m(FE_i^r) \text{ (peak)} \\ \min_{Fl_j^r \cap Fl_i^t \neq \emptyset} m(FE_j^r) - \varepsilon; & m(FE_i^r) \leq m(FE_{i-1}^r) \text{ and } m(FE_i^r) \leq m(FE_{i+1}^r) \text{ (trough)} \\ \min_{Fl_j^r \cap Fl_i^t \neq \emptyset} m(FE_j^r); & m(FE_{i-1}^r) \leq m(FE_i^r) \leq m(FE_{i+1}^r) \text{ (otherwise)} \end{cases} \quad (5-4)$$

If  $m(FE_i^r)$  is neither at peak nor at trough, then the minimum (maximum) of mass functions of intersecting  $FE_j^r$  is defined as the belief (plausibility) value. If  $m(FE_i^r)$  is at the peak (trough), the belief (plausibility) is defined to be the exact amount of the well-log value, and the plausibility (belief) will be the maximum (minimum) of intersecting  $FE_j^r$  plus (minus) an epsilon. The epsilon is a positive value to compensate the shoulder-bed effect, and will be optimized in the next section. Finally, both belief and plausibility values are rescaled to well-log range. From the application viewpoint, normalization ([Relation 2-1](#)) and rescaling could be ignored, since here we do not fuse multi-sensory data.

### 5.3.4 Compensating shoulder-bed effect by epsilon

For compensating shoulder-bed effect, epsilon ( $\varepsilon$ ) is defined by comparing the well-log to its weighted averaging filter. Reminding that a well-log is a weighted averaging of real-log, over a VRmf. So, we applied another smoothing (averaging) on the well-log. Then, the distance between the well-log and its smoothed curve,  $\varepsilon$ , is used to compensate the shoulder-bed effect at peaks and troughs ([Figure 5-4](#)). In the validation part, the well-log is known to be too much smoothed that  $\varepsilon$  could not fully compensate the shoulder effect. A multiplier, named factor of Shoulder-bed Effect (SE), is necessary to amplify  $\varepsilon$ . The concept of  $\varepsilon$  is comparable with the resolution enhancement relation of [Flaum et al. \(1989\)](#).

## 5.4 Log simulators

The uncertainty range provides an interval in which the real-log probably occurs. In this section, four DST-based simulators are developed in order to modify the well-log to a simulated-log with improved vertical resolution.

### 5.4.1 Random simulator

This is the simplest designed simulator that only produces uniform random values between belief and plausibility values. Heterogeneity is the highest in the uniform distribution, so the simulator generates the most heterogeneous realizations, which is usually desired in unknown geological conditions. In fact, this is a base simulator, and it is expected that other simulators provide more accurate results in general.

### 5.4.2 Random-optimization simulator

Second simulator starts by random simulation again, followed by a sequential optimization process, based on the volumetric constraint of well-logs. It means that each record should be a weighted average of simulated values within an interval of a vertical resolution ([Relation 5-5](#) and [Figure 5-4](#)). Within the interval, the distance is defined as an extraction of well-log from the weighted average of the corresponding simulations ([Relation 5-6](#) and [Figure 5-4](#)).

$$wl_s(i) \triangleq \sum_{j=i-\lfloor \frac{n_{fuse}}{2} \rfloor}^{i+\lfloor \frac{n_{fuse}}{2} \rfloor} \left[ sim(j) \times w \left( j - i + \left\lfloor \frac{n_{fuse}}{2} \right\rfloor + 1 \right) \right] \quad (5-5)$$

$$dist(i) \triangleq |wl(i) - wl_s(i)| \quad (5-6)$$

where  $wl_s(i)$  is the weighted average of simulated-log,  $sim(j)$ , over a vertical resolution. Vertical resolutions of  $wl_s(i)$  and  $sim(j)$  correspond to  $FE_i^r$  and  $FE_i^t$ , respectively.  $dist(i)$  is distance of the well-log,  $wl(i)$ , from  $wl_s(i)$ , both have the same vertical resolution, so they are comparable.  $wl_s(i)$ ,  $sim(j)$  and  $dist(i)$  are functions of depth.  $n_{fuse}$  is the number of adjacent simulations, within a vertical resolution, e.g.  $n_{fuse} = 5$  in [Figure 5-4](#).

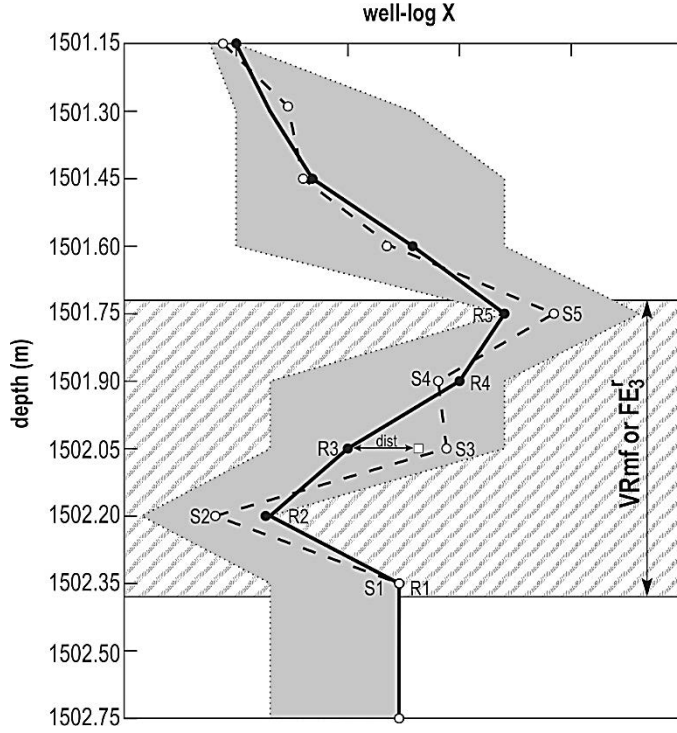


Figure 5-4. Scheme of the original well-log (solid line) and simulated-log (dashed line) within the uncertainty range (grey).  $\epsilon$  is multiplied by 5 (SE). The R3 should be a weighted average of S1 to S5 (white square) because they are within the  $FE_3^r$  (hatched area). Due to assumptions of the algorithm, the distance should be compensated by S3.

Note that the methodology could be applied to all the possible combinations of sampling rate and vertical resolution if an appropriate  $n_{fuse}$  is found.  $w$  is a linear weight for prioritizing closer simulations to recording depth. To calculate the weights, the natural values 1, 2, 3, etc. are primarily attributed to the parameter  $w$ , in function of distance. Then, the weights are normalized by the summation of  $w$ .

After a random generation, the corresponding distance of the first  $n_{fuse}$  simulations is calculated (Relation 5-6). For simplicity, and to avoid re-modification of the former optimized points, the distance is compensated only by one simulation point, which is the closest to the well-log record, e.g. S3 in Figure 5-4. The optimization continues through the well till the end. After each round of simulation, the summation of new distances is stored as the error of the modified simulated-log. Modification could be iterated up to convergence of the error. The convergence cut-off is a stop condition of the optimization process. It is recommended to set the convergence cut-off at 0.001 for the summation of all distances. The stages of the optimization algorithm are introduced in section “5.5 The algorithm/v-ii”.

### 5.4.3 Recursive simulator

This simulator consists of two stages. In the first stage, uniform random values between belief and plausibility values will be generated for the first  $(n_{fuse} - 1)$  value. In the second stage, simulated-log for the remaining depths will be calculated recursively. The recursive [Relation 5-7](#) is derived from the volumetric constraint of well-logs.

$$\text{sim}\left(i + \left\lfloor \frac{n_{fuse}}{2} \right\rfloor\right) = \frac{1}{w\left(i + \left\lfloor \frac{n_{fuse}}{2} \right\rfloor\right)} \sum_{j=i-\left\lfloor \frac{n_{fuse}}{2} \right\rfloor}^{i+\left\lfloor \frac{n_{fuse}}{2} \right\rfloor-1} \left[ \text{wl}(i) - \text{sim}(j) \times w\left(j - i + \left\lfloor \frac{n_{fuse}}{2} \right\rfloor + 1\right) \right] \quad (5-7)$$

### 5.4.4 Recursive-optimization simulator

The final simulator consists of three stages. The two first stages of recursive simulator are followed by the optimization process of random-optimization simulator. The interrelations and brief of the stages of the four developed simulators are provided in [Figure 5-5a](#). Two of the simulators (random and random-optimization) start with free random generation, and two others (recursive and recursive-optimization) start with constraint-based random generation.

### 5.4.5 Validation criteria

Different realizations could be generated by the introduced simulators. It is necessary to have a measure to validate and prioritize realizations, and finally choose the most accurate realization. An ideal criterion is to compare the simulated-log with the ideal-log ([Relation 5-8](#)).

$$e_{t\_id} = \sum_{\forall i} |\text{wl}_{id}(i) - \text{sim}_{int}(i)| \quad (5-8)$$

where  $\text{wl}_{id}(i)$  and  $\text{sim}_{int}(i)$  are ideal- and simulated-log, respectively. The subscript “int” shows that the simulated-log is interpolated at the depths of the ideal-log. Both are functions of depth but due to possible depth mismatch between the simulated- and ideal-log, the simulations have to be interpolated to the exact depths of the ideal-log.  $e_{t\_id}$  stands for total ideal-based error.

Evidently in subsurface geology, we do not have ideal-logs, so [Relation 5-8](#) is practical only in synthetic cases. In real data, instead of ideal error, summation of distances ([Relation 5-6](#)) is used as a validation criterion. Since the distance is based on the volumetric constraint of well-logs, the criterion is named “constraint-based error”. Both ideal- and constraint-based errors are applied on synthetic data, showing a high correlation coefficient ( $R^2=0.89$ , [Figure 5-9](#)). The advantages of using constraint-based error is fourfold: it **(i)** provides an error for each horizon (error profile), **(ii)** calculates the total error (integral of error profile), **(iii)** validates the well-log, such as other measurements like core, well-tests or ideal-log are not needed, and **(iv)** correlates highly with ideal-based error.

## 5.5 The algorithm

The algorithm consists of two parts: **(i)** DST uncertainty assessment and **(ii)** simulation (dashed rectangles, [Figure 5-5b](#)). In the first part, the uncertainty range of each record is defined and in the second part, the simulation is applied within the uncertainty range. The details of stages of the algorithm are provided below, and the background of each part was previously discussed.

**(i) Input:** the algorithm assesses well-logs individually, i.e. the algorithm has to be applied on a single selected well-log. The well-logs without volume of investigation, like geochemical logs or calliper log, could not be chosen. Both synthetic- and real well-logs could be used in the algorithm.

**(ii) Vertical resolution:** corresponding to the vertical dimension of volume of investigation of the selected well-log, the vertical resolution should be defined. The catalogue of the logging instrument could be used for this purpose. In case no catalogue is available, vertical resolution could be approximated by a measure of continuity, like variograph. To find out the number of adjacent records correlated with each other, three steps are addressed ([3.2.2.1 Variography analysis](#)):

**(ii-i)** Experimental variography analysis.

**(ii-ii)** Selection of its linear part.

(ii-iii) Considering vertical resolution as its length.

(iii) **Mass function:** vertical dimension of volume of investigation of each well-log record is considered as a linear focal element ( $FE^r$ ). The recorded well-log value is considered as the mass value within its corresponding  $FE^r$ . The  $FE^r$  and its mass function construct a BOE, which should be honoured in the next step.

(iv) **Belief and plausibility functions:** goal of DST part of the algorithm is to provide an evidence-based reasoning for intersection of the adjacent  $FE^r$ . Based on the ratio of vertical resolution to sampling rate, the number of adjacent intersecting records (Figure 5-2) is calculated. The intersecting interval is called focal element of target ( $FE^t$ ). The mass function, which moves within different  $FE^r$ , provides a range of mass values for  $FE^t$ . Mass value of  $FE^t$  cannot exceed the maximum mass value of intersecting  $FE^r$  (Figure 5-2). Therefore, to honour the records, which are our evidences, the belief (plausibility) is limited to the minimum (maximum) of intersecting mass functions (Relations 5-3 and 5-4). Belief and plausibility functions are the limits of the created uncertainty range. This process contains two steps:

$$(iv-i) n_{fuse} = \left\lfloor \frac{VR}{SR} \right\rfloor.$$

(iv-ii) Calculating belief and plausibility functions.

(v) **Simulation:** simulation could be realized using one of the four designed simulators (Figure 5-5a). The simulator could be chosen according to a validation criterion (Relation 5-6 or 5-8). All the simulators start by a random generation stage. In recursive simulator, the random generation is limited to a few numbers of focal elements. However, in random simulator, all the elements are guessed randomly. If the designed optimization process is applied to the outputs of random or recursive simulators, the outputs might converge.

(v-i) If recursive simulator is used, Relation 5-7 will be used to calculate the simulated-log for the rest of the depths.

(v-ii) If the optimization process is used:

(v-ii-i) The distance (Relation 5-6) is computed for the  $i$ th well-log data.



(v-ii-ii) The distance is compensated by the  $i$ th simulated-log data.

(v-ii-iii)  $i=i+1$ , then go to line (v-ii-i).

**(vi) Validation:** the validation is implemented either regarding ideal-log (ideal-based error, [Relation 5-8](#)) or well-log (constraint-based error, [Relation 5-6](#)). Ideal-based error is only applicable in synthetic cases, and constraint-based error could be calculated for both synthetic and real data. In a homogenous formation, the order of the errors is indicated in [Figure 5-6c](#). This general order could be violated in heterogeneous formations. So, precision of all the simulators have to be always checked to find the most accurate simulated-log.

**(vii) Simulated-log:** the simulated-log with the least error is selected as an alternative for the original well-log. The advantage of the simulated-log is that its vertical resolution is equal to the  $FE^t$  which is more accurate than the original well-log resolution.

## 5.6 Application check on synthetic cases

Worthy to remind that the aim of the developed methodology is to correct the well-log (synthetic-log) to get closer to its real-log (ideal-log). Four simulated-logs can be generated by the designed simulators. All the simulators are applied on all the cases of [Table 1-2](#). The predefined ideal-log (stars) and corresponding synthetic-log (black dots) of case 1 are presented in [Figure 5-6a](#), and the other cases are interpreted in [Appendix B](#). To calculate ideal-based error, the realizations are first interpolated to the depths of the predefined ideal-log, if necessary. Then, the mismatch of the realization with the ideal-log is calculated for each depth, called error profile ([Figure 5-6b](#)). Successively, the summation of the error profile through the well-log is named total ideal-error ([Figure 5-6c](#)).

Random simulator never satisfies the goal. In this case, it has neither recreated the shape of the ideal-log, nor its real value. Compared to other simulators, it has the highest profile and total errors ([Figure 5-6b,c](#)). The best realization of random-optimization simulator is exactly the realization of recursive-optimization simulator. Both random-optimization and recursive-optimization simulators provided the same result for 48 iterations out of 50. They pass through

the same optimization procedure (Figure 5-7); so convergence of the realizations is anticipated. The same reasoning is valid for the other cases (Appendix B).

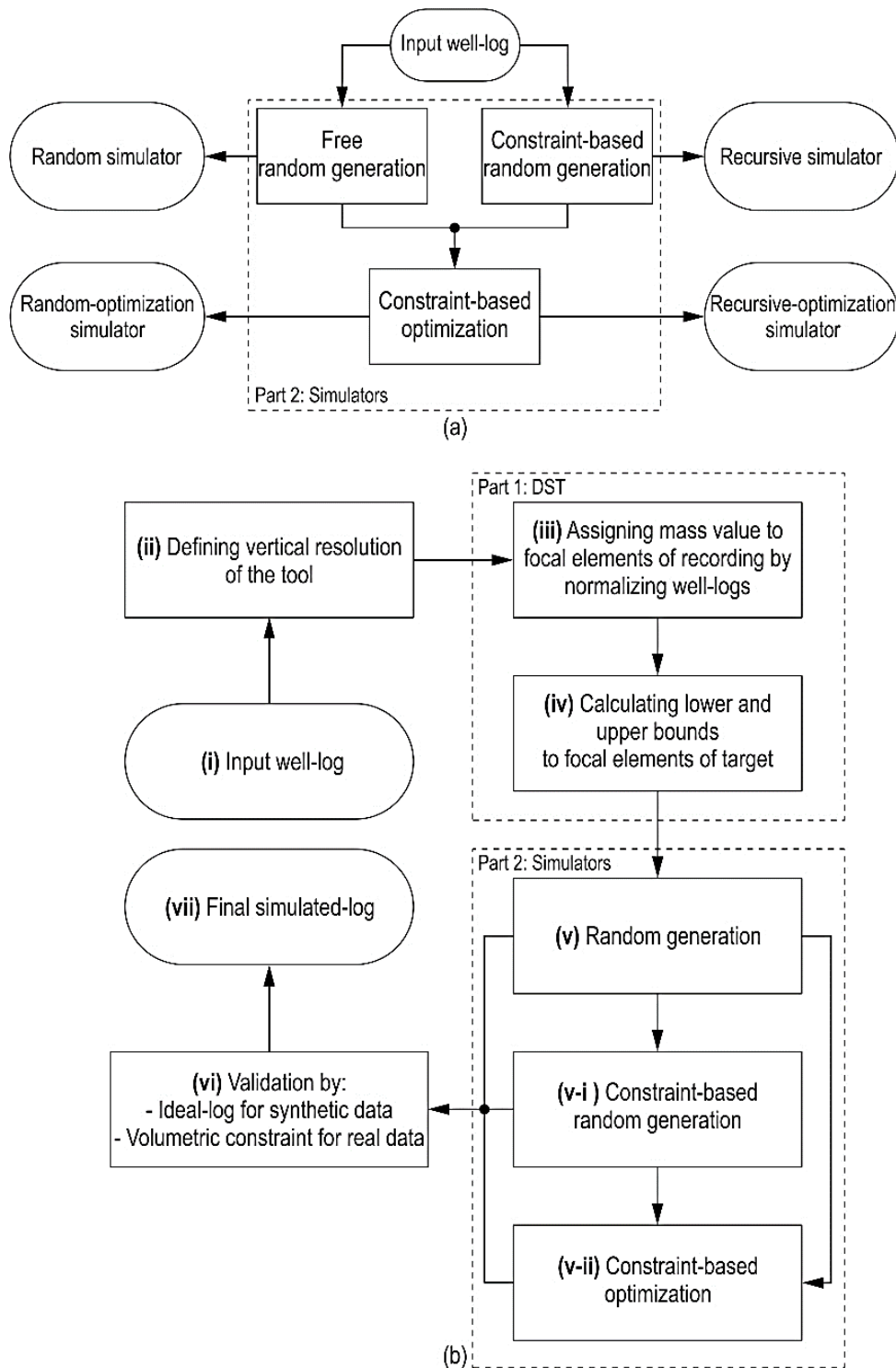


Figure 5-5. Scheme of the processing. (a) Random-optimization and recursive-optimization simulators have to pass through an optimization process, while the other more basic simulators only need a free or constraint-based random generation. (b) Flowchart of the DST-based algorithm for resolution enhancement of well-logs.

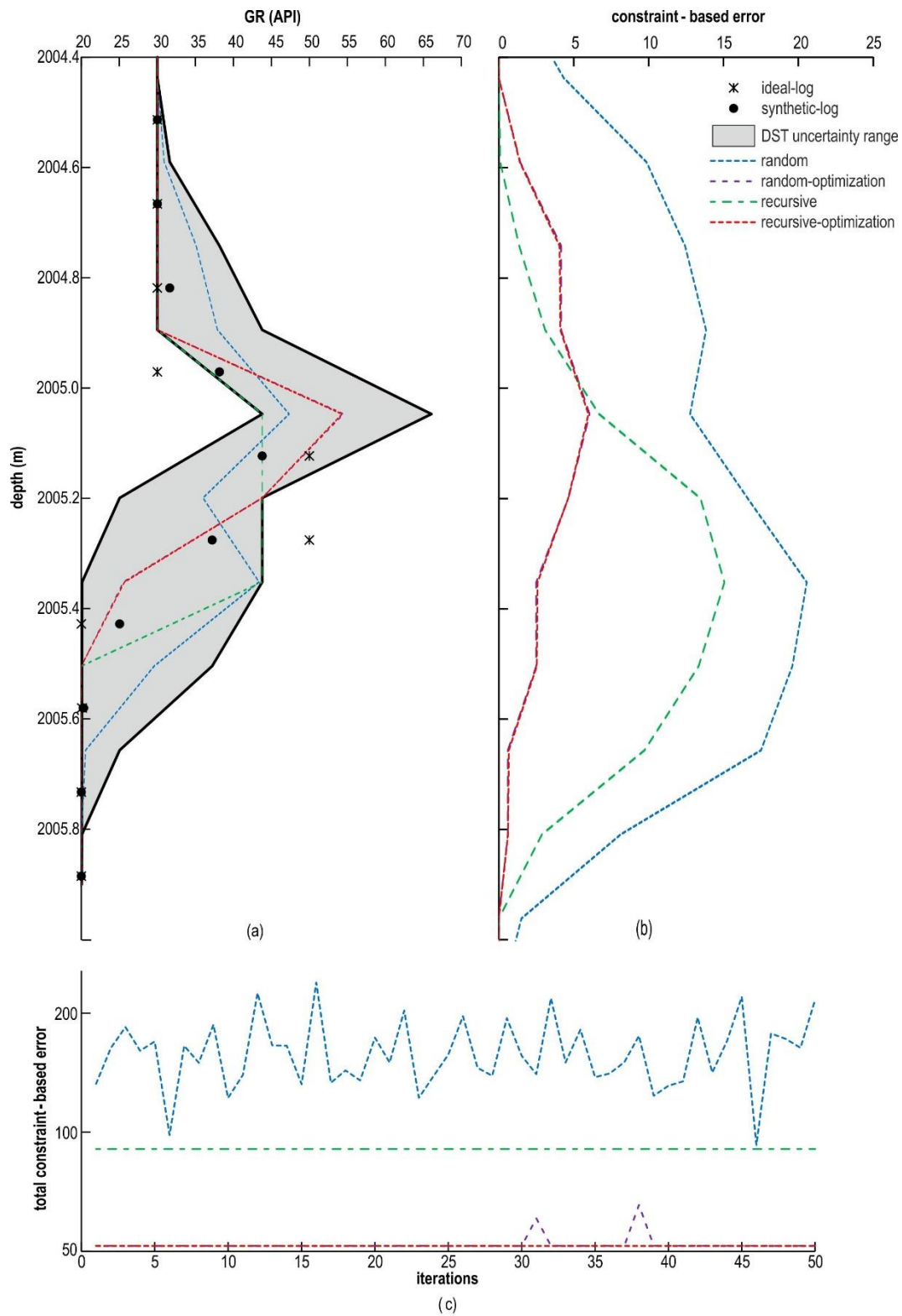


Figure 5-6. a) Ideal-log, synthetic-log, uncertainty range and realizations of case 1. b) Error profiles: Comparison of constraint-based errors vs. depth between the simulators in case 1. c) Total error for 50 iterations.

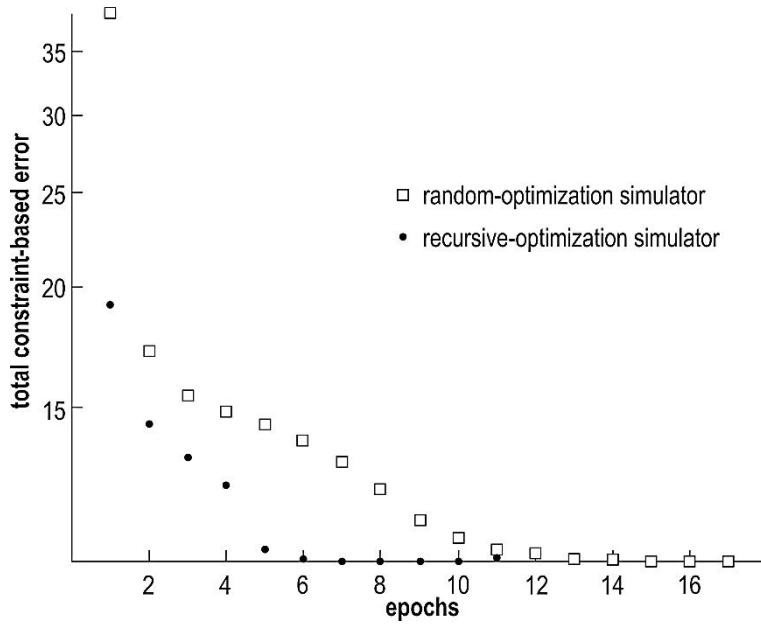


Figure 5-7. Total constraint-based error during optimization in case 1. Convergence is reached at 6 and 12 epochs for random-optimization and recursive-optimization simulators, respectively. The term “epoch” refers to the number of iterations during the optimization process. To avoid confusion, the word “iteration” is specifically used for the number of random generation.

## 5.7 Discussion on results of synthetic cases

Since none of the simulators were able to detect a single fracture in case 6, further evaluation is thus exempted for this case. In cases 1, 3 and 5 (Table 5-2), both ideal- and constraint-based errors have the least values in recursive-optimization simulator. In case 2, random-optimization simulator is the best. However, recursive-optimization simulator is a competing simulator, and it is only 0.6% less accurate than random-optimization simulator. The same for case 7. As for case 4, constraint-based error votes for recursive-optimization simulator; though ideal-based error selects random simulator. The descriptions are summarized in Figure 5-8. From viewpoint of ideal-based error, in 50% (8%+42%) of the cases, the recursive-optimization simulator provides the best output. The random-optimization simulator is the most accurate simulator only in 33% (8%+25%) of the cases. On the other hand, from the standpoint of constraint-based error, recursive-optimization simulator is also the best, since it is valid in 67% (8%+42%+17%) of the cases.

There is another advantage for recursive-optimization simulator: the optimization starts from a lower error value, compared to random-optimization simulator, subsequently, convergence is

reached within only 6 epochs (Figure 5-7). Therefore, less time is required for recursive-optimization simulator to reach a local optimum point (a terminology in machine learning that means a local minimum error of a complex objective function). In the synthetic cases, recursive-optimization simulator is the best. Recursive simulator is never successful, compared to the others, but random simulator provides the best result only in case 4 whereas the other simulators are not satisfactory (Table 5-2 and Figure 5-8).

Table 5-2. Total errors of simulators for each synthetic case. Minimum errors are highlighted by bold characters. DST-based algorithm cannot detect a single fracture, case 6.

Case	Log	Random simulator		Random-optimization simulator		Recursive simulator		Recursive-optimization simulator	
		Constraint-based bulk error	Ideal-based bulk error	Constraint-based bulk error	Ideal-based bulk error	Constraint-based bulk error	Ideal-based bulk error	Constraint-based bulk error	Ideal-based bulk error
1	GR	163.4	63.1	51.6	31.2	90.7	31.2	51.6	31.2
2	GR	348.8	117.6	81.6	50.0	149.0	73.5	90.0	50.3
3	RHOB	2.4	0.43	1.6	0.37	2.3	0.39	1.6	0.37
4	NPHI	59.8	4.7	43.8	13.9	62.3	17.3	42.1	13.4
5	NPHI	125.5	16.6	77.6	15.2	16.2	10.8	8.8	8.9
6	DT	-	-	-	-	-	-	-	-
7	DT	112.6	33.0	77.8	22.0	81.7	28.0	70.9	22.8

total constraint-based error	recursive-opt	17% ④	8% ⑦	0%	① ③ 42% ⑤ ⑦
	recursive	0%	0%	0%	0%
	random-opt	0%	① ② ③ 25%	0%	② 8%
	random	0%	0%	0%	0%
		random	random-opt	recursive	recursive-opt
		total ideal-based error			

Figure 5-8. Confusion matrix of correctness showing cases 1-5 and 7 and percentages.

### 5.7.1 Validating constraint-based error by synthetic cases

It is impossible to calculate ideal-based error in the real well-log data, because it needs an ideal-log that does not exist in real cases. Instead, it is suggested to use developed constraint-based error, i.e. summation of distances in Relation 5-6. To verify constraint-based error, the

synthetic data are used. The 24 pairs of errors (Table 5-2) are plotted (Figure 5-9). Cross plot of errors shows high positive correlation ( $R^2=0.89$ ) between the two errors, however constraint-based error is an overestimation of ideal-based error. Therefore, the behaviours of both the errors are similar, and constraint-based error could be used as a validation criterion in real datasets.

## 5.8 Application to real data

### 5.8.1 Simulator selection

The four developed simulators are applied on four well-logs of the five wells under study. Due to total constraint-based error, random-optimization simulator is the most accurate simulator in all the situations (Table 5-3). However, the error of recursive-optimization simulator is not much higher than that of random-optimization simulator. This may be interpreted such as random-optimization simulator searches the minimum points more effectively, hence it can get closer to the global optimum point. However, the recursive-optimization method does not check the variety of possibilities for each depth. Further studies are applied using random-optimization simulator.

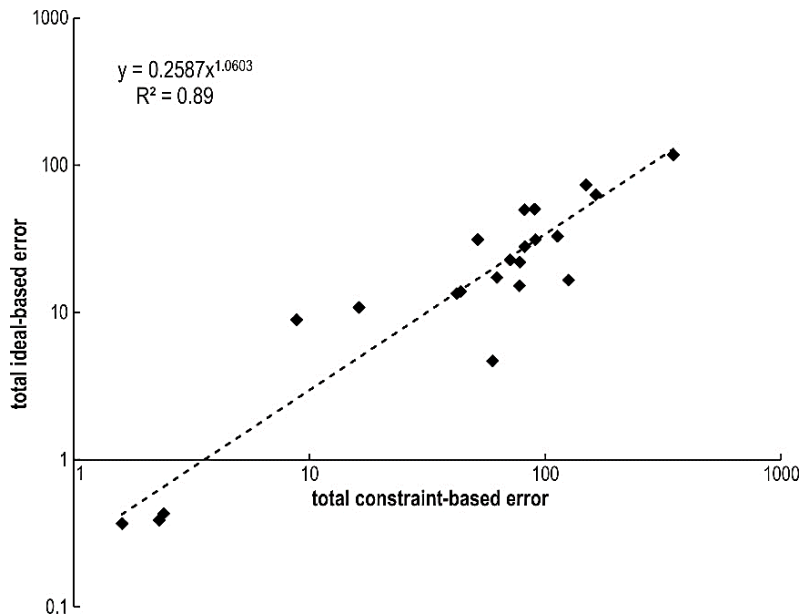


Figure 5-9. Ideal-based vs. constraint-based error giving a significant correlation coefficient ( $R^2$ ).

Table 5-3. Constraint-based total errors for the four simulators. SE=5 and iteration number=200. The reference for  $n_{fuse}$  is the vertical resolution (Table 3-1). The parameters of simulation, including  $n_{fuse}$ , are summarized in Table 5-5.

Well#	Well-log	Random simulator	Random-optimization simulator	Recursive simulator	Recursive-optimization simulator
1	GR	20'750	<b>9'495</b>	18'527	11'479
	RHOB	261'880	<b>79'619</b>	215'370	107'450
	NPHI	156	41	110	51
	DT	42'008	<b>20'155</b>	28'653	23'160
2	GR	14'237	<b>6'773</b>	9'932	7'538
	RHOB	305'260	<b>89'164</b>	222'610	109'250
	NPHI	228	65	162	79
	DT	37'223	<b>15'548</b>	22'689	17'696
3	GR	16'522	<b>9'259</b>	12'493	10'221
	RHOB	194'260	<b>64'285</b>	142'460	85'612
	NPHI	133	44	102	60
	DT	42'448	<b>22'140</b>	29'704	24'463
4	GR	14'789	<b>8'137</b>	11'109	9'052
	RHOB	300'230	<b>84'143</b>	208'900	103'490
	NPHI	173	45	120	55
	DT	45'304	<b>20'958</b>	30'256	24'423
5	GR	9'273	<b>3'802</b>	6'012	4'245
	RHOB	199'110	<b>50'851</b>	146'620	68'958
	NPHI	109	28	75	35
	DT	38'457	<b>17'246</b>	23'444	18'865

### 5.8.2 Optimizing factor of shoulder-bed effect

The factor of Shoulder-bed Effect (SE) is the only parameter in the simulators that requires manual optimization. Using random-optimization simulator, SE is checked from 2 to 7 (Table 5-4). The optimum SE for GR and DT is 3 (exception: the optimum SE for GR in well#2 is 4). For RHOB and NPHI, the optimum SE varies between 5 and 7.

### 5.8.3 Results of resolution improvement of real well-logs

To apply random-optimization simulator on real well-logs, the optimized parameters (Table 5-5) are used. Here, the results of resolution improvement are illustrated for the intervals of 3157-3159 m (well#1) and 2801.65-2803.45 m (well#3) (Figure 5-10). The outputs of the other intervals are provided in the Appendix C. Each well-log track in Figure 5-10a,b contains: (i) the original well-log (solid black line) with the vertical resolution of 61-91 cm (Table 3-1); (ii)

the uncertainty range (blue zone) which is between the belief and plausibility; (iii) ten realizations from random-optimization simulator (dots), and (iv) the best one is marked by dashed line (simulated-log). The vertical resolution of the realizations is 15 cm ( $FE^t$  in Figure 5-2). In the rightmost tracks, geometry-based thin-bed characterizations are provided. The results of core porosity test are also shown in Figure 5-10b.

Table 5-4. Optimizing SE by comparing constraint-based total errors, iteration number=50. Larger iteration numbers are also tested, however the outputs were robust. The parameters of the simulation (including SE) are mentioned in Table 5-5.

Well#	Well-log	SE=2	SE=3	SE=4	SE=5	SE=6	SE=7
1	GR	8'231	<b>8'161</b>	8'170	8'304	8'496	8'762
	RHOB	104'350	88'664	82'795	79'619	<b>79'079</b>	79'864
	NPHI	51	45	42	41	40	41
	DT	19'617	<b>19'504</b>	19'509	20'199	20'923	21'281
2	GR	6'650	6'624	<b>6'558</b>	6'789	68'921	7'164
	RHOB	107'100	95'427	90'604	89'164	87'467	<b>87'346</b>
	NPHI	77.0	69.0	66.0	65.1	65.0	64.8
	DT	15'338	<b>15'237</b>	15'376	15'548	16'117	16'735
3	GR	9'069	<b>8'955</b>	9'030	9'259	9'385	9'659
	RHOB	73'707	68'040	65'537	64'285	64'650	<b>64'196</b>
	NPHI	50.0	48.0	45.0	44.0	44.3	43.0
	DT	21'809	<b>21'376</b>	21'658	22'140	22'868	23'730
4	GR	7'998	<b>7'894</b>	7'978	8'137	8'296	8'482
	RHOB	106'380	91'714	85'826	84'143	84'258	<b>83'560</b>
	NPHI	55.0	48.0	44.6	44.4	43.2	43.3
	DT	<b>20'255</b>	20'237	20'609	20'958	21'928	22'507
5	GR	3'934	<b>3'773</b>	3'786	3'802	3'968	4'096
	RHOB	67'105	57'344	52'542	<b>50'851</b>	51'133	51'953
	NPHI	34.0	30.0	28.1	27.6	28.2	28.0
	DT	16'870	<b>16'649</b>	16'941	17'246	17'708	19'181

Table 5-5. Optimized parameters for random-optimization simulator. Summary of Table 5-3 and 5-4.

Well#	Interval	Well-log	n <sub>fuse</sub>	SE	Well#	Interval	Well-log	n <sub>fuse</sub>	SE
W1	3157 - 3159 m lower Sarvak	GR	4	3	W2	2766 - 2770 m upper Sarvak	GR	4	4
		RHOB	5	6			RHOB	5	7
		NPHI	5	6			NPHI	5	7
		DT	4	3			DT	4	3
W3	2802 - 2804 m 2809 - 2813 m upper Sarvak	GR	4	3	W4	2662 - 2666 m upper Sarvak	GR	4	3
		RHOB	6	7			RHOB	5	7
		NPHI	6	7			NPHI	5	6
		DT	4	3			DT	4	2
W5	2840 - 2844 m upper Sarvak	GR	4	3					
		RHOB	5	5					
		NPHI	5	5					
		DT	4	3					



The uncertainty range honours the predefined axiomatic structure ([Relations 5-3](#) and [5-4](#)).

(i) The lower (upper) bound is the minimum (maximum) value over the  $n_{fuse}$  neighbouring values. (ii) The uncertainty in the top half metre (3157-3157.5 m) is about the zero due to the constant value of the original well-log for some neighbouring records. (iii) The SE is compensated (to some degree) by the sparks at peaks and troughs; i.e. high-frequency variations are amplified ([Figure 5-10a](#)).

All the well-logs show less uncertainty range in the half top metre (3157-3157.5 m, [Figure 5-10a](#)), compared to the other parts. It means that the top part is more homogeneous, while the heterogeneity arises downward. Therefore, any interpretation (estimation of porosity, permeability, etc.) within the homogeneous part is more certain than the heterogeneous part. In fact, heterogeneity of rocks is quantified by DST-uncertainty range.

In [Figure 5-10b](#), the available core box is provided to evaluate core porosity vs. NPHI and thin-bed thickness. The target is here to characterize a black porous thin-bed, ~2802.9 m. GR shows a finning (deepening) upward pattern, and there is no sign of a thin-bed. RHOB shows a trough, however there is a depth mismatch. NPHI shows a peak, with the plausibility of just below 8%, which is comparable with the core porosity, 8.4%, of the black thin-bed. However, the best simulated NPHI (dashed-line) is about 5%. Hence, NPHI is corrected from 3.8% to about 5%, even if the plausibility is very close to the core porosity. At about the same depth, DT shows a positive anomaly too.

Therefore, if a thin-bed (>15 cm) shows a petrophysical anomaly, DST-based method identifies it. When comparing NPHI and core porosity ([Figure 5-10b](#)), the vertical resolution is improved in the corrected well-log (dashed-line). However, depth mismatch (half of SR: ~7.5 cm) and lack of thickness estimation are its weaknesses. For the depth mismatch, an error bar of  $\pm 7.5$  cm should be considered.

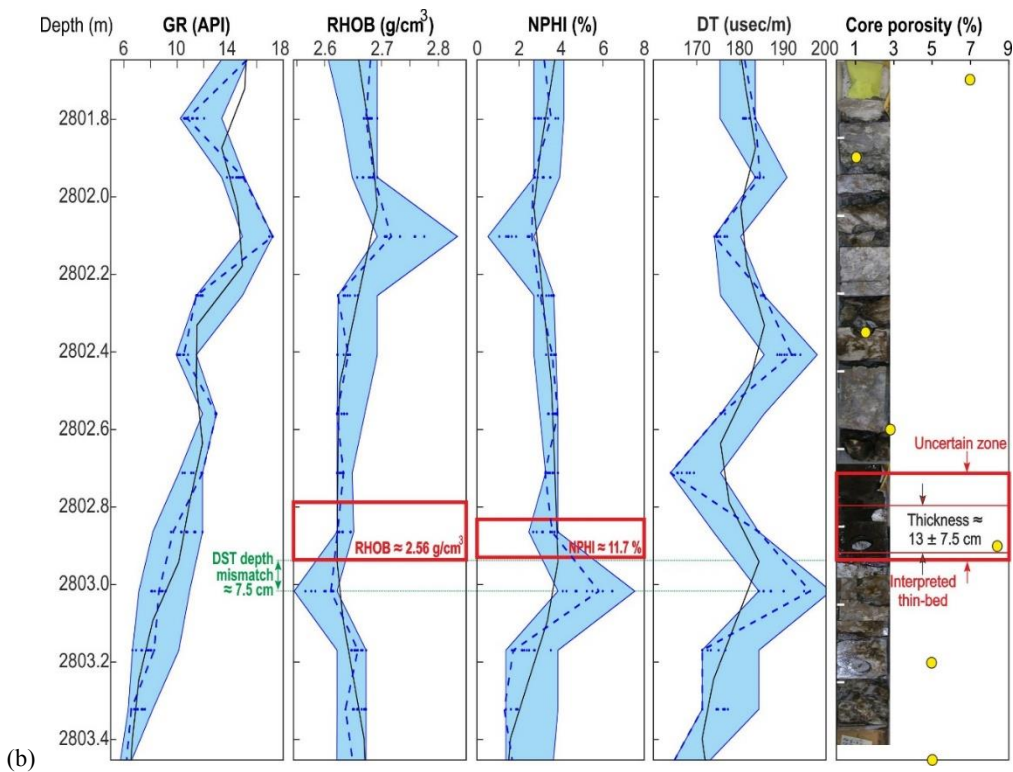
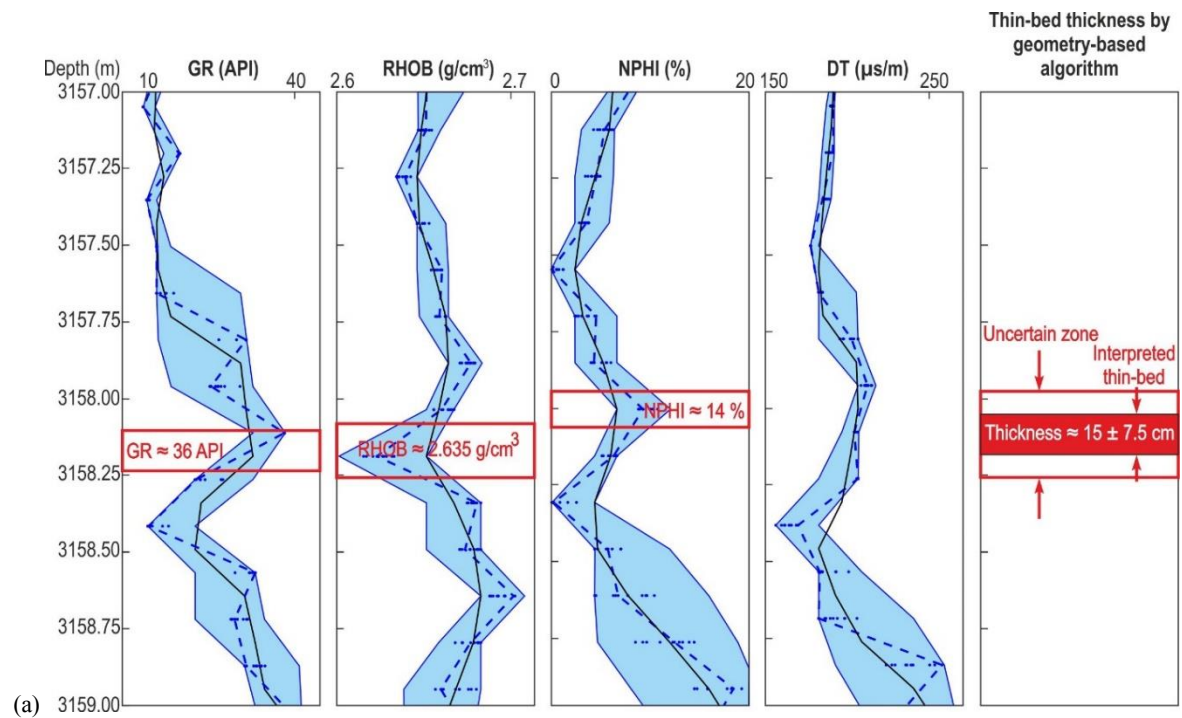


Figure 5-10. Well-log (solid black line) data for the four tools (GR, RHOB, NPHI and DT), uncertainty range (blue zone), ten realizations (dots) and the best realization (dashed line) as the simulated-log, within the interval a) 3157-3159 m (well#1) and b) 2801.65-2803.45 m (well#3).

## 5.9 Discussions

### 5.9.1 Comparing DST and geometry-based results in thin-bed characterization

A thin-bed at the depth of 3158.19 m (2802.9 m) within well#1 (well#3) is characterized by both the developed thin-bed characterization algorithms (Table 5-6). Noteworthy that DST-based algorithm is more precise than geometry-based algorithm when the uncertainty measures (column of DST-based algorithm) are smaller than the Root Mean Square Error (RMSE) (column of geometry-based algorithm) (Table 5-6). On the other hand, if the RMSE is smaller than the uncertainty measures, it does not necessarily mean that geometry-based algorithm is more precise than DST-based algorithm.

Table 5-6. Comparing the outputs of geometry- and DST-based algorithms in thin-bed characterization, the Sarvak Formation. The most accurate values in each row are given in bold characters.

			Well-log		Geometry-based algorithm		DST-based algorithm		
	Thin-bed characterization		RMSE	Value	RMSE	Value	DST Uncertainty	Simulator uncertainty	Value
Well#1 Depth of 3158.19 m	GR	Log value (API)	--	31.5	±6.50	<b>≈36</b>	±6.02	±0	37.52
		Thickness (cm)	±47.43	60.96	±7.12	14.01	--	--	--
	RHOB	Log value (g.cm <sup>-3</sup> )	±0.06	2.677	±0.031	<b>≈2.635</b>	±0.053	±0.028	2.624
		Thickness (cm)	±56.59	76.20	±8.20	18.80	--	--	--
	NPHI	Log value (%)	±11.82	4.00	±6.32	<b>≈14</b>	±5.44	±2.17	9.96
		Thickness (cm)	±64.30	60.96	±7.30	12.10	--	--	--
	DT	Log value (μs/m)	--	206.5	--	--	±10.8	±6.4	211.1
		Thickness (cm)	--	--	--	--	--	--	--
	Final thickness (cm)					14.97 ±7.5			
Well#3 Depth of 2802.85 m	GR	Log value (API)	--	--	--	--	±3.64	±2.70	8.70
		Thickness (cm)	±47.43	--	--	--	--	--	--
	RHOB	Log value (g.cm <sup>-3</sup> )	±0.06	2.62	±0.031	<b>≈2.56</b>	±0.073	±0.051	2.603
		Thickness (cm)	±56.59	85	±8.20	15.74	--	--	--
	NPHI	Log value (%)	±11.82	3.80	±6.32	<b>≈11.7</b>	±5.44	±2.78	5.8
		Thickness (cm)	±64.30	70	±7.30	10.88	--	--	--
	DT	Log value (μs/m)	--	--	--	--	±17	±12	202
		Thickness (cm)	--	--	--	--	--	--	--
	Final thickness (cm)					13.17 ±7.5			

The process of Relations 5-9 to 5-12 proves mathematically that RMSE is smaller than the uncertainty range. There are n estimations,  $x_i$ , corresponding to the true values,  $z_i$ . The uncertainty range (right-hand in Relation 5-9) is always larger than the error (left-hand) because it considers all the possible situations, i.e. the maximum possible distance (error) from the real

value but RMSE is the error of the most probable case. When  $Pls - Bel \geq 1$ , it is evident that [Relation 5-12](#) is true. But in case  $Pls - Bel < 1$ , the inequality changes twice. The first change occurs when squaring (generating [Relation 5-10](#) from [Relation 5-9](#)), because both parts are considered as positive values, smaller than one. The second change happens when rooting both sides ([Relation 5-12](#)). The reason for the second change is that when  $Pls - Bel < 1$ , necessarily error, square of errors and MSE are smaller than one too. So, rooting results in change of inequality in [Relation 5-12](#).

$$|x_i - z_i| \leq Pls - Bel \quad (5-9)$$

$$\Rightarrow \begin{cases} (x_i - z_i)^2 \leq (Pls - Bel)^2; & \text{if } Pls - Bel \geq 1 \\ (x_i - z_i)^2 > (Pls - Bel)^2; & \text{if } Pls - Bel < 1 \end{cases} \quad (5-10)$$

$$\Rightarrow \begin{cases} MSE = \frac{1}{n} \sum_{i=1}^n (x_i - z_i)^2 \leq (Pls - Bel)^2; & \text{if } Pls - Bel \geq 1 \\ MSE = \frac{1}{n} \sum_{i=1}^n (x_i - z_i)^2 > (Pls - Bel)^2; & \text{if } Pls - Bel < 1 \end{cases} \quad (5-11)$$

$$\Rightarrow \begin{cases} RMSE = \sqrt{\frac{1}{n} \sum_{i=1}^n (z_i - t_i)^2} \leq Pls - Bel; & \text{if } Pls - Bel \geq 1 \\ RMSE = \sqrt{\frac{1}{n} \sum_{i=1}^n (z_i - t_i)^2} < Pls - Bel; & \text{if } Pls - Bel < 1 \end{cases} \quad (5-12)$$

### 5.9.2 Advantages of DST-based algorithm

The principle goal of DST-based algorithm is “uncertainty assessment of the well-logs”. Two uncertainty boundaries are created at each depth. The broader boundary, DST uncertainty, is provided by belief and plausibility functions. A narrower boundary, simulator uncertainty, is created by realizations within the larger uncertainty range. The simulator uncertainty depends on the simulator mechanism. For instance, the simulator uncertainty of random simulator is exactly equal to DST uncertainty, but narrower for the other simulators. At depth of about 3157.2 m in DT well-log ([Figure 5-10a](#)) both the uncertainty ranges are narrow. At the same

depth, the uncertainty ranges of the other well-logs are relatively narrow too, so the interpretations in this interval, which is homogeneous, are relatively certain.

Another advantage is the reduction of the focal element ( $FE^r > FE^t$ ). It means that an alternative log with a smaller vertical resolution can be regenerated: the dashed-line (Figure 5-10) is the correction of well-logs after scanning within DST uncertainty range, i.e. simulation. By scanning, different petrophysical values are checked and the best one, according to the volumetric constraint of well-logs, is selected. The corrected well-log contains higher frequencies. The regenerated frequencies are one realization of many possible high-frequency variations which honour the volumetric nature of well-logs.

In addition, the proposed algorithm is automated and applicable by usual computers, i.e. it does not require specific hardware or facilities. RMSE of DST-based algorithm could be considered a little higher than the RMSE of geometry-based algorithms (Table 5-6). For thin-bed characterization (well#1): RMSE of GR in geometry-based algorithm, i.e.  $\pm 6.50$ , is reduced to  $\pm 0$  (column of simulator uncertainty), i.e. 100% error reduction. RMSE of RHOB,  $\pm 0.031$ , is reduced to  $\pm 0.028$ , i.e. 71% reduction in the uncertainty of the output. Similarly, error of NPHI is reduced by 66%. For well#3, RMSE of RHOB is increased in DST-based algorithm by 65%, while its NPHI is reduced by 56%. But DST-based algorithm does not estimate the thickness of thin-beds.

### 5.9.3 Uncertainty conversion using DST

In this chapter, we were able to reduce the vertical resolution of well-logs from SR+VRmf to SR. But, simultaneous with the depth uncertainty reduction, we have an increase of the well-log uncertainty value: from zero to the interval between belief and plausibility. In fact, the DST does not provide any uncertainty removal methodology. Instead, it converts the state of uncertainty, i.e. from depth uncertainty to value uncertainty.

Figure 5-11 shows how the DST converts depth uncertainty (point I) to value uncertainty (point II). At (I), there is no value uncertainty, while depth uncertainty is maximum, i.e. SR+VRmf. But at (II), depth uncertainty is reduced to SR, while value uncertainty is maximized to the interval between belief and plausibility.

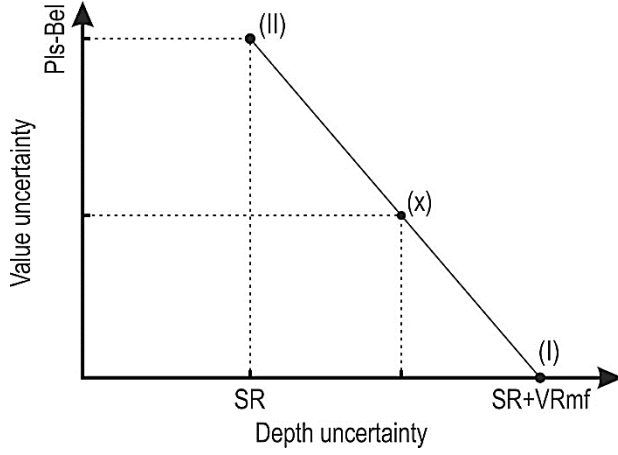


Figure 5-11. Uncertainty conversion by DST. The more depth uncertainty, the less value uncertainty.

By means of the DST, the overall uncertainty is not reduced. In fact, the depth uncertainty ( $UNC_d$ ) is converted to the value uncertainty ( $UNC_v$ ). Heisenberg's uncertainty principle (Busch *et al.*, 2007) is still valid in this context. So, multiplication of value uncertainty by depth uncertainty is always higher than a certain value of delta (Relation 5-13).

$$UNC_d \times UNC_v \geq \delta \quad (5-13)$$

## 5.10 Conclusions of Chapter 5

The very first application of volumetric Nyquist frequency is in the up-scaling. The goal in the up-scaling is to reduce the data volume, i.e. increase of SR while integrating the adjacent data. Hence, the destructive effects of VRmf and SR have to be considered simultaneously in the final resolution of up-scaling.

Volumetric nature of the well-logs imposes resolution limitation on the recordings, i.e. the measurements are not well-representative of high-frequency petrophysical variations, and only provide an average value over the interval of measurement (between the transmitter and the receivers). For coping with this resolution problem, a DST-based algorithm using four simulators is devised to modify well-logs and improve the vertical resolution (Figure 5-5b). Comparing the consistency of the theories of probability, possibility and DST analytically proved that the DST is capable in uncertainty assessment of well-logs.

The application of the proposed DST-based algorithm was checked on synthetic and real data. Recursive-optimization simulator was the best simulator for uncertainty assessment in the synthetic cases, and random-optimization simulator provided the most precise realizations in the real well-logs. The reason is that getting close to the global optimum point is much more difficult in the well-log data, because of heterogeneity, and the vast random generation process helps more effectively in searching for the optimum point in real data.

Realization selection is achieved through two errors: constraint- and ideal-based errors. Ideal-based error is only practical in synthetic cases, where ideal-log is predefined. While constraint-based error does not need any reference, i.e. ideal-log, for assessing simulated-log. Constraint-based error validates the simulated-log by comparing it to the original well-log, considering its volumetric nature. Constraint-based error for selecting the best realization is validated by the synthetic cases, and shows high positive correlation ( $R^2=0.89$ , [Figure 5-9](#)) with ideal-based error. So, constraint-based error is a practical measure in prioritizing and validating realizations, i.e. outputs of simulations.

The advantages of developed DST-based algorithm could be summarized in: **(i)** providing uncertainty assessment measures for well-logs. **(ii)** Simulating an alternative well-log with the vertical resolution of about 15 cm, i.e. sampling rate, from the original well-log with the vertical resolution of 61-91 cm. **(iii)** Regenerating and amplifying high-frequency petrophysical variations, within the well-logs that were filtered during logging measurements. **(iv)** Using common processors of the market through an automated algorithm, without significant manual interference. **(v)** Providing more precise petrophysical values for thin-beds, compared to the previously developed geometry-based algorithm. DST-based algorithm reduced the uncertainty of GR, RHOB and NPHI logs by 100%, 71% and 66%, respectively. It shows a high performance in reducing the destructive shoulder-bed effect. However, it cannot estimate the thickness of thin-beds, compared to geometry-based algorithm.

## 6 Uncertainty projection on reservoir parameters

### Highlights of Chapter 6

- Cluster analysis on NPHI, RHOB and DT well-logs is used for the purpose of porosity analysis.
- Fuzzy numbers are used to interpret porosity value, and providing uncertainty range.
- Fuzzy arithmetic is applied to calculate fuzzy numbers of irreducible water saturation and permeability.
- Fuzzy number of irreducible water saturation provides better (less overestimation) results than crisp assessment.
- Fuzzy number of permeability was very much successful in well#5, not successful in wells #1 and #4.
- When the porosity interval (clusters) is incompatible with the core porosity, the permeability fuzzy numbers are not valid, e.g. in well#4.

### 6.1 Importance of cluster analysis in well-log interpretation

Red circle on the cross-plot of NPHI-RHOB contains several neighbouring data ([Figure 6-1a](#)). How much these neighbouring data points vary from each other? If we reacquire RHOB or NPHI well-logs, will the data remain exactly at their current coordinates? Of course there is a big possibility of displacement of data points in the second run of logging instruments. The coordinate's variation results in an uncertainty for each data, sourced from the measurement. So, we propose to group (cluster) the neighbouring data for which their coordinates differences is meaningless.

In the clustering of [Figure 6-1b](#), the data are not correlated within each cluster, while the whole data is highly correlated. It means that the logging instruments are unable to regenerate the general correlation, i.e. the correlation of the whole data, within each cluster. Cluster analysis is used in this chapter to reconstruct the uncertainty range of the well-logs. The uncertainty range of the data within each cluster is the same. Idealistically, this range should



contain all the well-log values of all the geological formations, within the volume of investigation.

Cluster analysis does unsupervised grouping of data, based on a measure of similarity. Unsupervised categorization means no predefined label is available for each group. Therefore the algorithm has to find the number of clusters and the cluster limits. As an example in [Figure 6-1b](#), the dataset is clustered into five clusters due to the distance in a three-dimensional space for NPHI, RHOB and DT.

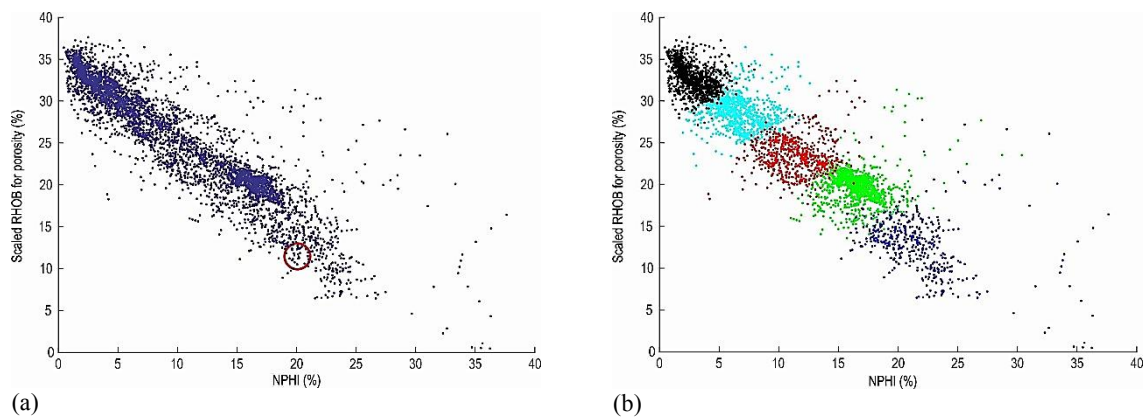


Figure 6-1. Cross-plots of NPHI-RHOB (scaled) within the Sarvak Formation in well#3. RHOB is scaled to the range of NPHI, providing RHOB-based porosity estimation. a) Not clustered and b) clustered into five mass type clusters by FCM with inputs of NPHI, RHOB and DT.

Considering the limits of the clusters as uncertainty boundaries of NPHI and scaled RHOB ([Figure 6-1b](#)), there are two uncertainty boundaries for porosity. It would be ideal if the core porosity remains within the uncertainty boundaries of well-log porosities at the corresponding depth.

The other advantage of clustering is that further processing steps could be addressed for each cluster, individually. For instance, in the porosity estimation, the calibration of results will be checked in each cluster, individually. Furthermore, cluster-based manipulation of data helps modelling the local variations.

## 6.2 Porosity analysis by cluster-based method

### 6.2.1 Methodology of cluster-based porosity analysis

There are three common well-logs for porosity studies: **(i)** NPHI measures hydrogen content, which is present in the water and hydrocarbon molecules. It represents the total porosity. The effective porosity represents the situation where the pores are connected to each other, leading to stored fluids flow through the formation, so the porosity can be effective for production. In none-effective porosity, e.g. in shaly formations, reservoir fluid is captured in unconnected pores or trapped by pore pressure in the pore throats. **(ii)** RHOB: The density of the solid phase of the formations is always much higher than the liquid or gas phase occurring within the pores. Therefore, higher the porosity, lower the RHOB. **(iii)** DT log is sensitive to dispersions of sonic waves at the place of discontinuities, fractures, vuggy zones, etc. So, it is used for studying secondary porosity ([Dewan, 1983](#)).

There is a negative correlation in the cross-plots of RHOB-DT and NPHI-RHOB ([Figure 6-1](#)). But, between NPHI and DT, positive correlation is observed. In the first step of the developed method, cluster-based porosity analysis, a clustering algorithm is going to be applied on the well-logs (NPHI, RHOB and DT) of the Sarvak Formation, within a selected well ([Figure 6-2](#)). Each well-log value would be associated with a cluster label, representative of a porosity range. This range is chosen from NPHI, and it depends on the inputs (NPHI, RHOB and DT), number of clusters and clustering algorithm. As an example, larger the number of clusters, larger the uncertainty range. The input is chosen based on the literature ([Masoudi \*et al.\*, 2015](#)). For the number of clusters and clustering algorithm, the criterion of Precision Measure (PM) is used ([Relation 6-1](#)).

#### 6.2.1.1 Clustering algorithm, compatible with cluster shapes

The clustering algorithm has to be chosen regarding the desired cluster shape: mass type, shell type, linear, same-size, multi-size, etc. For instance, if we are searching for a road in an aerial photo, the pixels of the road create a curve line. So, the clustering algorithm have to be capable in finding the curves on the photo.

The shape of the clusters is highly dependent on the combination of distance and objective functions of the clustering algorithm. In KM and FCM algorithms, the clusters are spherical with the same size. While in GK, they are elongated, still with the same size. The clusters of GG vary in size, besides being elongated.

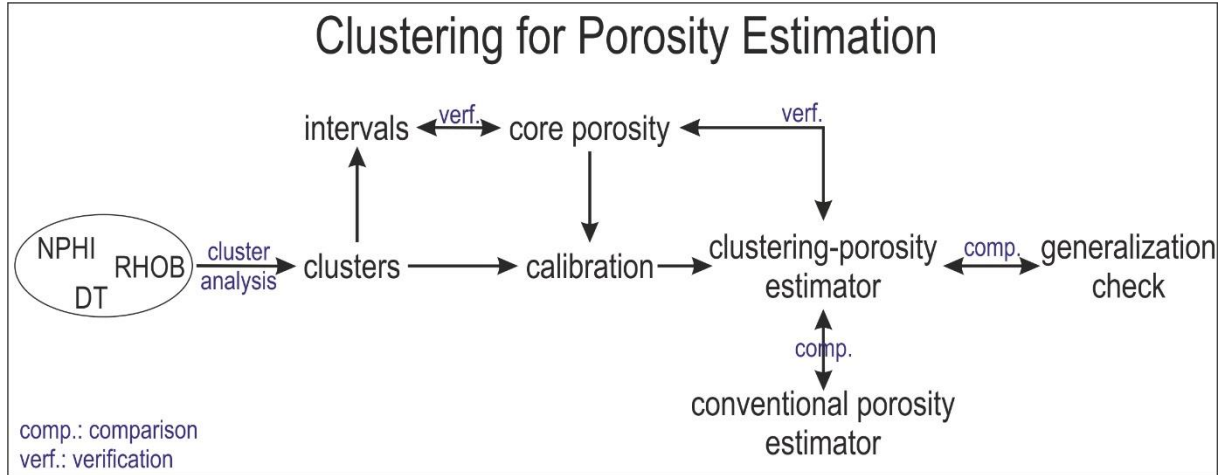


Figure 6-2. Workflow of the algorithm of cluster-based porosity analysis.

#### 6.2.1.2 Precision measure for choosing the algorithm and optimizing cluster number

The Precision Measure (PM) is the ratio of Consistency Measure (CM) to the average of cluster intervals ( $Int_{ave}$ ) (Relation 6-1). Consistency between porosity intervals (derived from well-logs) and core porosity is represented by CM. When core porosity is within NPHI-range of each cluster, it is counted as a correct case. In each cluster, the ratio of the number of correct cases to cluster size, i.e. number of data within the cluster, is calculated. The average of the ratios in all the clusters is named CM. A good cluster analysis has high CM with a narrow interval of clusters. CM and  $Int_{ave}$  are both in percentage, so they are comparable and their ratio, PM, is taken as the choice criterion of the cluster algorithm and the number of clusters for porosity analysis.

$$PM = \frac{CM}{Int_{ave}} \quad (6-1)$$

Different algorithms and cluster numbers are checked in each well. Then, based on the PM, the best-fit algorithm for porosity analysis is selected, and the cluster number is optimized

(Table 6-1). For instance, in well#3, the FCM with six clusters (FCM6) has the highest PM, whereas in well#4, the FCM with five clusters (FCM5) is the best choice.

Applying FCM6 on well#3 results in six same-size mass-type clusters (Figure 6-3a). The data of the cross-plot of NPHI and core porosity are coloured according to the cluster labels. The histograms of clusters on NPHI and core porosity axis show that the core porosity is discriminated too, however not as well as NPHI (Figure 6-3b). The porosity range of each data point is assigned by core porosity range of its cluster, e.g. the porosity range of all red data varies from about 5% to about 25%.

Table 6-1. Comparing different algorithms and cluster numbers. The clustering algorithms are: k-means (KM), Fuzzy c-means (FCM), Gustafson-Kessel (GK) and Gath-Geva (GG). \*Only one cluster is detected. \*\*Only two clusters are detected. ^The clusters are intervened completely (due to the histogram) so the PM is unreliable.

	Algorithm	3 clusters	4 clusters	5 clusters	6 clusters
Well 1	KM	CM=100% <i>Int<sub>ave</sub></i> =23% PM=4.4**^	CM=100% <i>Int<sub>ave</sub></i> =19% PM=5.3**^	CM=95% <i>Int<sub>ave</sub></i> =17% PM=5.7**	CM=95% <i>Int<sub>ave</sub></i> =15% PM=6.4**
	FCM	CM=100% <i>Int<sub>ave</sub></i> =23% PM=4.4**^	CM=100% <i>Int<sub>ave</sub></i> =20% PM=5.0**	CM=100% <i>Int<sub>ave</sub></i> =19% PM=5.3**	CM=100% <i>Int<sub>ave</sub></i> =16% PM=6.1
	GK	CM=100% <i>Int<sub>ave</sub></i> =30% PM=3.3**^	CM=100% <i>Int<sub>ave</sub></i> =24% PM=4.2**^	CM=100% <i>Int<sub>ave</sub></i> =25% PM=4.0**	CM=100% <i>Int<sub>ave</sub></i> =21% PM=4.8**
	GG	CM=100% <i>Int<sub>ave</sub></i> =19% PM=5.1*	CM=100% <i>Int<sub>ave</sub></i> =27% PM=3.7**^	CM=100% <i>Int<sub>ave</sub></i> =22% PM=4.5*	Nan
Well 2	KM	CM=96% <i>Int<sub>ave</sub></i> =29% PM=3.4	CM=97% <i>Int<sub>ave</sub></i> =28% PM=3.5	CM=97% <i>Int<sub>ave</sub></i> =27% PM=3.6	CM=86% <i>Int<sub>ave</sub></i> =25% PM=3.5
	FCM	CM=96% <i>Int<sub>ave</sub></i> =29% PM=3.4	CM=98% <i>Int<sub>ave</sub></i> =26% PM=3.7	CM=97% <i>Int<sub>ave</sub></i> =26% PM=3.7	CM=97% <i>Int<sub>ave</sub></i> =24% PM=4.1
	GK	CM=100% <i>Int<sub>ave</sub></i> =41% PM=2.5	CM=87% <i>Int<sub>ave</sub></i> =36% PM=2.4	CM=97% <i>Int<sub>ave</sub></i> =27% PM=3.6	CM=73% <i>Int<sub>ave</sub></i> =23% PM=3.1
	GG	CM=100% <i>Int<sub>ave</sub></i> =29% PM=3.4*	CM=100% <i>Int<sub>ave</sub></i> =31% PM=3.2*	CM=100% <i>Int<sub>ave</sub></i> =21% PM=4.9**	CM=100% <i>Int<sub>ave</sub></i> =31% PM=3.2*
Well 3	KM	CM=93% <i>Int<sub>ave</sub></i> =19% PM=4.9	CM=87% <i>Int<sub>ave</sub></i> =16% PM=5.4	CM=84% <i>Int<sub>ave</sub></i> =15% PM=5.6	CM=78% <i>Int<sub>ave</sub></i> =14% PM=5.6
	FCM	CM=92% <i>Int<sub>ave</sub></i> =19% PM=4.8	CM=86% <i>Int<sub>ave</sub></i> =16% PM=5.3	CM=79% <i>Int<sub>ave</sub></i> =15% PM=5.4	CM=82% <i>Int<sub>ave</sub></i> =14% PM=5.8
	GK	CM=89% <i>Int<sub>ave</sub></i> =24% PM=3.7	CM=89% <i>Int<sub>ave</sub></i> =23% PM=3.8	CM=91% <i>Int<sub>ave</sub></i> =23% PM=3.9	CM=91% <i>Int<sub>ave</sub></i> =22% PM=4.2
	GG	CM=92% <i>Int<sub>ave</sub></i> =25% PM=3.7	CM=70% <i>Int<sub>ave</sub></i> =19% PM=3.7	CM=84% <i>Int<sub>ave</sub></i> =16% PM=5.2	CM=89% <i>Int<sub>ave</sub></i> =21% PM=4.2

Well 4	KM	CM=75% <i>Int<sub>ave</sub></i> =33% PM=2.2	CM=59% <i>Int<sub>ave</sub></i> =27% PM=2.2	CM=51% <i>Int<sub>ave</sub></i> =22% PM=2.3	CM=48% <i>Int<sub>ave</sub></i> =20% PM=2.5
	FCM	CM=71% <i>Int<sub>ave</sub></i> =27% PM=2.7	CM=78% <i>Int<sub>ave</sub></i> =29% PM=2.7	CM=73% <i>Int<sub>ave</sub></i> =24% PM=3.1	CM=71% <i>Int<sub>ave</sub></i> =24% PM=2.9
	GK	CM=82% <i>Int<sub>ave</sub></i> =47% PM=1.8	CM=77% <i>Int<sub>ave</sub></i> =46% PM=1.7	CM=75% <i>Int<sub>ave</sub></i> =40% PM=1.9	CM=64% <i>Int<sub>ave</sub></i> =38% PM=1.7
	GG	CM=100% <i>Int<sub>ave</sub></i> =29% PM=3.5^	CM=96% <i>Int<sub>ave</sub></i> =31% PM=3.1^	Nan	Nan
Well 5	KM	CM=96% <i>Int<sub>ave</sub></i> =25% PM=3.9	CM=93% <i>Int<sub>ave</sub></i> =21% PM=4.4	CM=90% <i>Int<sub>ave</sub></i> =16% PM=5.5	CM=89% <i>Int<sub>ave</sub></i> =15% PM=5.8
	FCM	CM=91% <i>Int<sub>ave</sub></i> =23% PM=4.0	CM=94% <i>Int<sub>ave</sub></i> =22% PM=4.4	CM=92% <i>Int<sub>ave</sub></i> =19% PM=4.8	CM=92% <i>Int<sub>ave</sub></i> =18% PM=5.3
	GK	CM=100% <i>Int<sub>ave</sub></i> =42% PM=2.4	CM=93% <i>Int<sub>ave</sub></i> =32% PM=2.9	CM=93% <i>Int<sub>ave</sub></i> =26% PM=3.6	CM=86% <i>Int<sub>ave</sub></i> =19% PM=4.4
	GG	CM=99% <i>Int<sub>ave</sub></i> =24% PM=4.1	CM=100% <i>Int<sub>ave</sub></i> =21% PM=4.7	CM=84% <i>Int<sub>ave</sub></i> =18% PM=4.7	CM=81% <i>Int<sub>ave</sub></i> =22% PM=3.7

### 6.2.1.3 Calibrating NPHI in each cluster

The core porosity is estimated by calibrating NPHI individually in each cluster. The clusters are narrower on the NPHI axis, compared to the axis of core porosity (Figure 6-3b). NPHI is an average over the formation porosity (Relation 3-1) so it cannot present the extreme core porosity values. For example, the lowest core porosity within the green cluster is about 7%, while its NPHI is more than 18%. The calibration is done in two stages. Since the majority of the data are located near the centre of each cluster, the extremes (outliers) are removed firstly (Figure 6-4). Then, the remained data are scaled to the range of core porosity in each cluster, individually. The percentages of removed extremes are found by the trial-and-error process. For instance, the lowest RMSE in rescaling NPHI of core porosity is associated with removing 30% of extreme core porosity values of each cluster (Table 6-2).

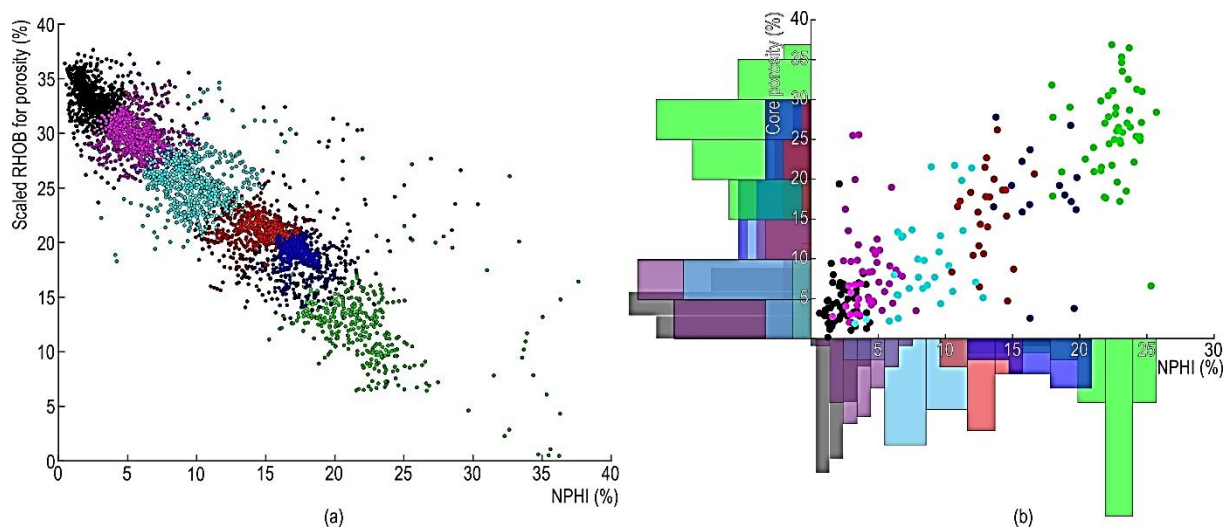


Figure 6-3. FCM6 is trained on well-logs NPHI, RHOB and DT of well#3 (a). NPHI and core porosity of each cluster are compared through the cross-plot and histograms (b).

In Table 6-2, the extreme removal is applied in batch for all the clusters, i.e. the percentage of the extreme removal is constant within all the clusters. In the next step, extreme removal is addressed sequentially, i.e. within each cluster (Table 6-3 and 6-4).

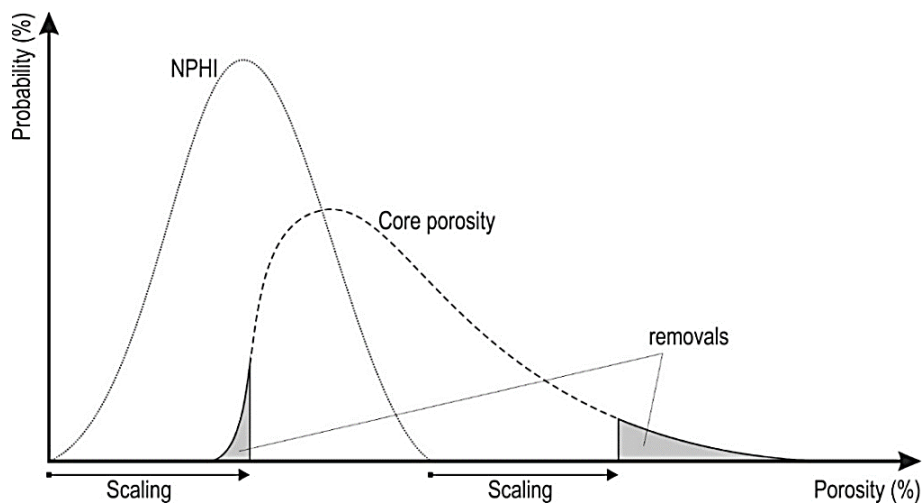


Figure 6-4. NPHI calibration for porosity estimation: removing the extremes of core porosity, then scaling PDF of NPHI to the new core porosity interval.

Table 6-2. Batch optimization of removing core porosity extremes. The optimization is achieved on the best cases of Table 6-1. The calculated values are RMSE.

Extreme removal (%) → Estimator ↓	10	20	30	40	50	60	70
W1-FCM6	6.12	5.07	5.22	5.37	5.47	5.35	5.45
W2-FCM6	3.75	3.72	3.79	3.46	3.37	3.32	3.52
W3-FCM6	6.79	6.75	6.17	6.19	6.34	6.27	6.27
W4-FCM5	6.87	6.79	6.73	6.70	6.85	6.78	6.77
W5-KM6	5.45	5.24	5.32	5.09	5.05	5.12	5.40

## 6.2.2 Results of cluster-based porosity analysis

In well#1, there is a limited number of core data with only two clusters, and the core porosity is always consistent with the clustering ranges (Figure 6-5a). In well#2, only two core porosities are not consistent, however very close to the minimum of clusters (Figure 6-5b). Whereas there is a high CM (82%) in well#3 (Table 6-1).

In well#4, the core porosity is not as compatible with uncertainty range as in the other wells. The frequency of variation of core data is higher than the well-logs (Figure 6-5d). Noteworthy that well#4 is drilled in a complex tectonic location, where the trend of the anticline changes from NS (Arabian trend) to NW-SE (Zagros trend). The most probable interpretation is that there is high tectonic activity due to dual stress regime, hence resulting in faults and fractures. So, the core porosity is lower than the overall formation porosity. The NPHI (total porosity) which is higher than core porosity, i.e. effective porosity, is an evidence for this interpretation (Figure 6-5d). Therefore, in the intervals where core porosity is lower than the minimum of cluster, e.g. in the interval of 2665- 2680 m of well#4 (Figure 6-5d), a fracture study could be applied. In the mentioned interval, the GR value reaches the clean reservoir line, about 10 API, so the shale content is negligible, which makes the formation elastic and easy to be fractured.

In contrast to well#4, core and well-log data are compatible in well#5 for which high porosity variation, with a CM of 89% higher than in wells#3 and #4 (Figure 6-5e). In wells #1, #2, #3 and #5, the calibrated NPHI is very close to the core porosity (Figure 6-5a,b,e).

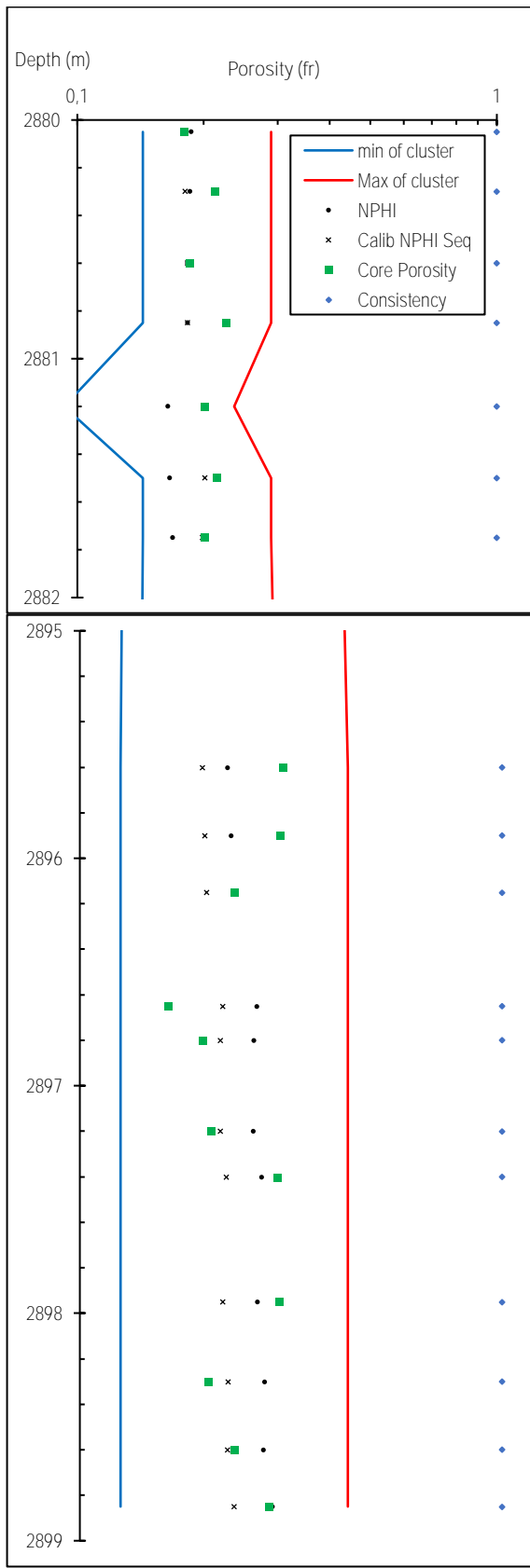
Table 6-3. Sequential optimization of removing core porosity extremes. The calculated numbers are RMSE. In each row, while the percentage of each cluster is changing, the other percentages are fixed. For the first row of each well, all the percentages are chosen based on the best optimization process of Table 6-2, then modified based on the best results of the previous row.

	Extreme removal (%) → Cluster number ↓	10	20	30	40	50	60	70
W1-FCM6	1	6.12	5.07	5.52	5.35	5.44	5.32	5.46
	2	5.07	5.07	5.07	5.07	5.07	5.07	5.07
	3	5.07	5.07	5.07	5.07	5.07	5.07	5.07
	4	5.07	5.07	5.07	5.07	5.07	5.07	5.07
	5	5.07	5.07	5.07	5.09	5.09	5.09	5.06
	6	5.06	5.06	5.06	5.06	5.06	5.06	5.06
W2-FCM6	1	3.36	3.36	3.37	3.37	3.46	3.35	3.35
	2	3.76	3.71	3.79	3.44	3.26	3.35	3.55
	3	3.26	3.26	3.26	3.26	3.26	3.26	3.26
	4	3.23	3.25	3.24	3.26	3.26	3.26	3.23
	5	3.23	3.23	3.23	3.23	3.23	3.23	3.23
	6	3.23	3.23	3.23	3.23	3.23	3.23	3.23
W3-FCM6	1	6.31	6.32	6.17	6.20	6.34	6.28	6.27
	2	6.24	6.16	6.17	6.19	6.22	6.19	6.16
	3	6.18	6.18	6.16	6.17	6.15	6.16	6.15
	4	6.11	6.15	6.15	6.11	6.09	6.10	6.10
	5	6.55	6.49	6.09	6.10	6.09	6.09	6.09
	6	6.08	6.14	6.09	6.10	6.11	6.12	6.17
W4-FCM5	1	6.67	6.72	6.75	6.70	6.87	6.81	6.93
	2	6.69	6.69	6.67	6.67	6.67	6.67	6.67
	3	6.74	6.71	6.67	6.67	6.68	6.68	6.69
	4	6.72	6.65	6.64	6.67	6.66	6.67	6.59
	5	6.66	6.64	6.61	6.59	6.58	6.57	6.50
W5-KM6	1	5.16	5.14	5.15	5.09	5.05	5.08	5.12
	2	5.09	5.03	5.03	5.04	5.05	5.05	5.05
	3	5.03	5.03	5.03	5.03	5.03	5.03	5.03
	4	5.29	5.20	5.25	5.06	5.03	5.07	5.30
	5	5.02	4.99	5.00	5.02	5.03	5.04	5.05
	6	4.99	4.99	4.99	4.99	4.99	4.99	4.99

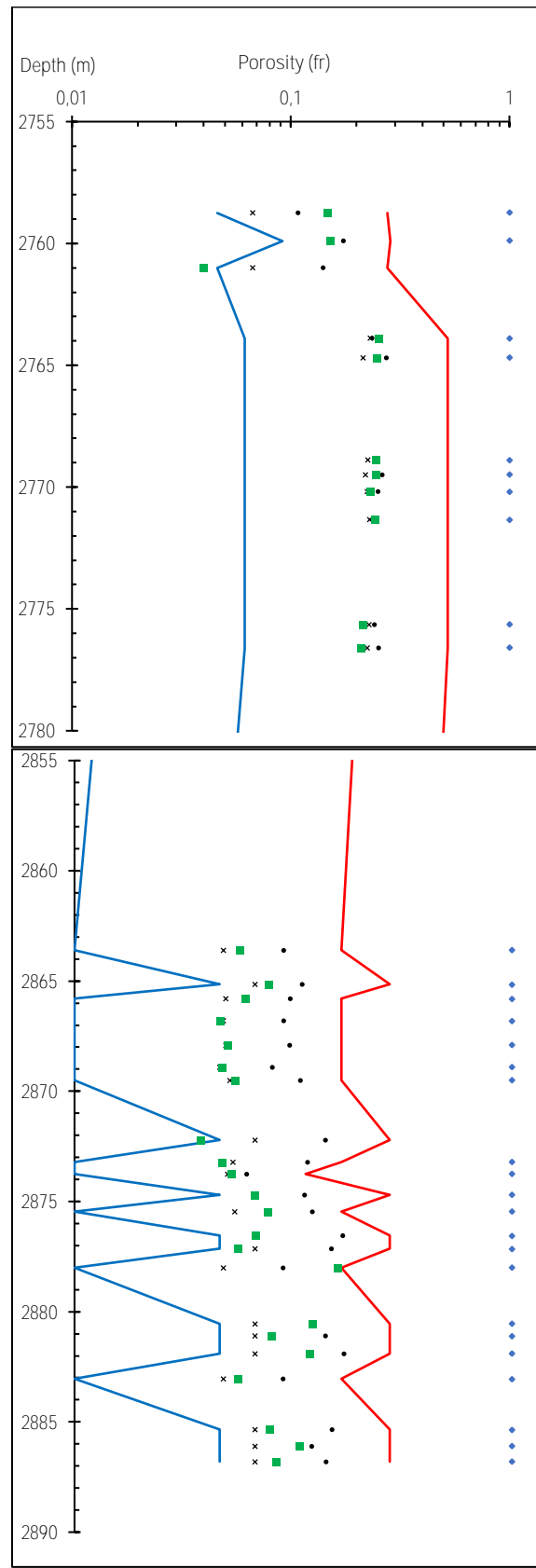
Table 6-4. Final removal percentages of each cluster for different estimators.

Cluster number → Estimator ↓	1	2	3	4	5	6
W1-FCM6	20	10	10	10	70	10
W2-FCM6	60	50	10	10	10	10
W3-FCM6	30	20	50	50	30	10
W4-FCM5	10	30	30	70	70	-
W5-KM6	50	20	10	50	20	10

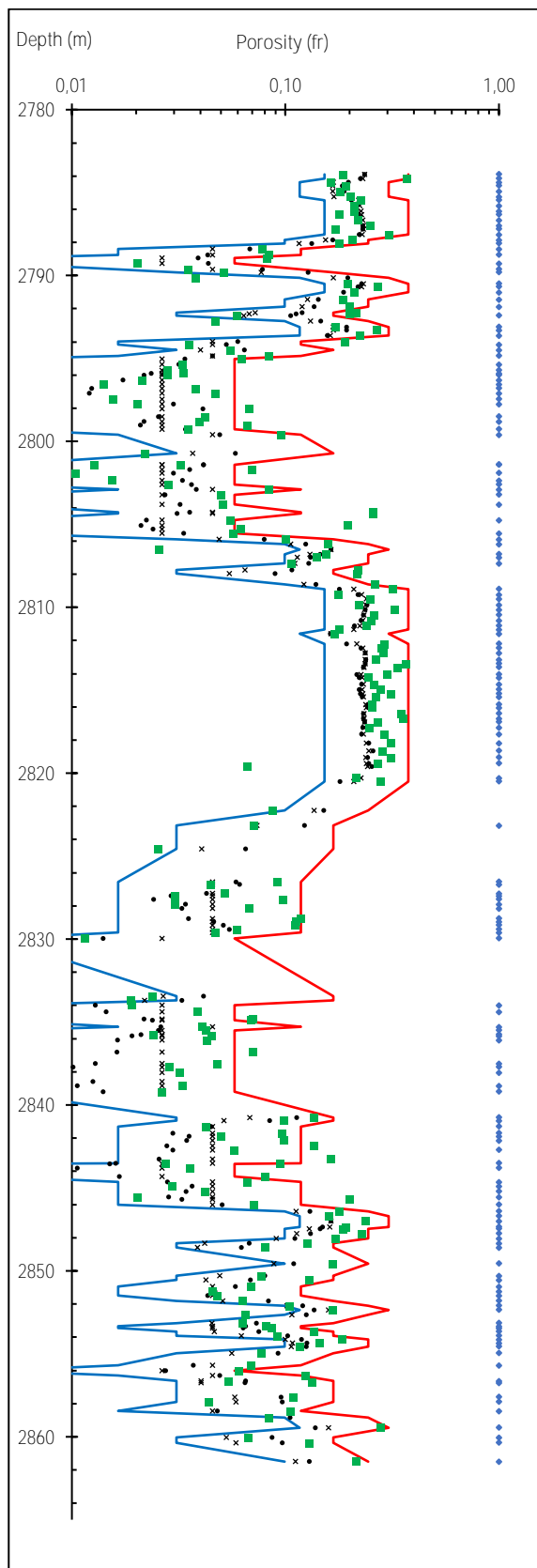




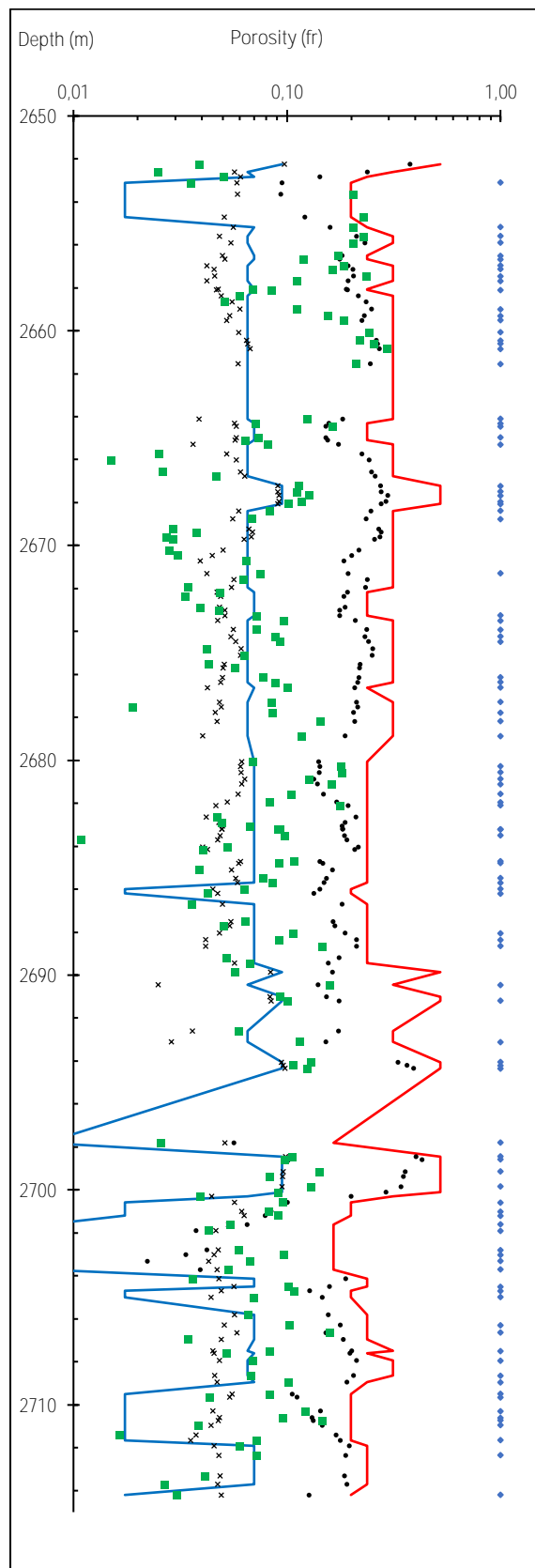
(a)



(b)



(c)



(d)

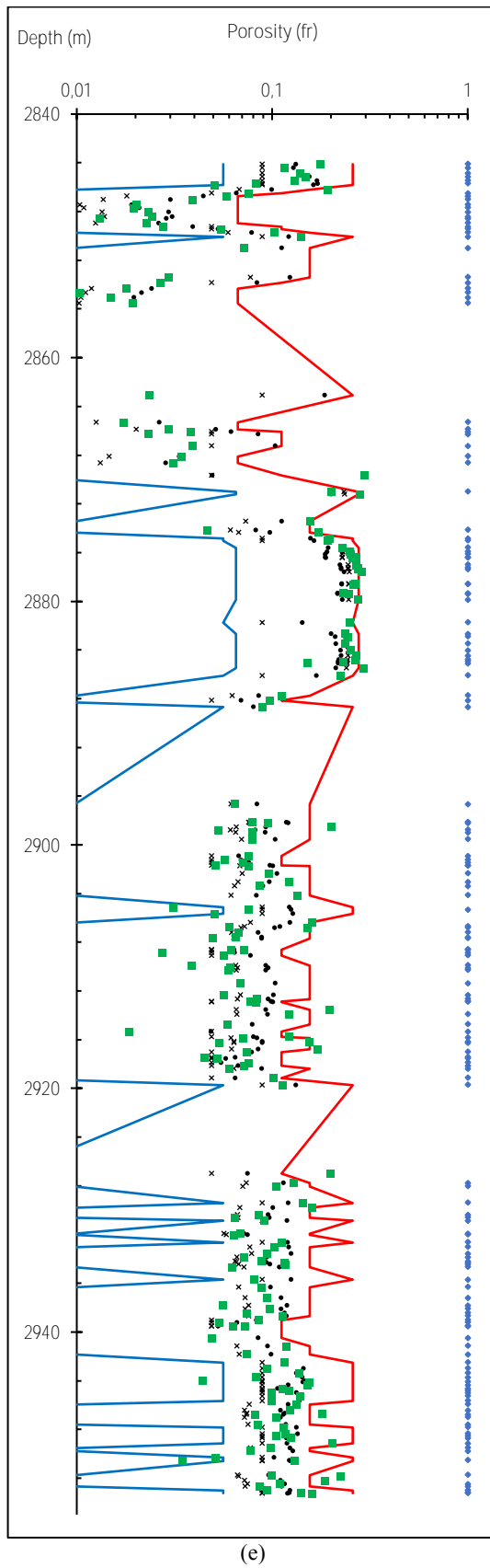


Figure 6-5. Results of cluster-based porosity analysis. When the core porosity is between the limits of clusters, the consistency mark is shown on the plot. Cluster limits in non-cored intervals are interpolated by the adjacent data. a) well#1, b) well#2, c) well#3, d) well#4 and e) well#5. fr: fraction.

### 6.2.3 Discussion of cluster-based porosity analysis

#### 6.2.3.1 Comparing the results with conventional methods

The clustering-based porosity analysis estimates the core porosity and is more precise than nearly all conventional methods. It is only NPHI that is more precise than clustering-based method in wells #1, #3 and #5. However the difference of RMSE is less than 0.1%, i.e. negligible (Figure 6-6).

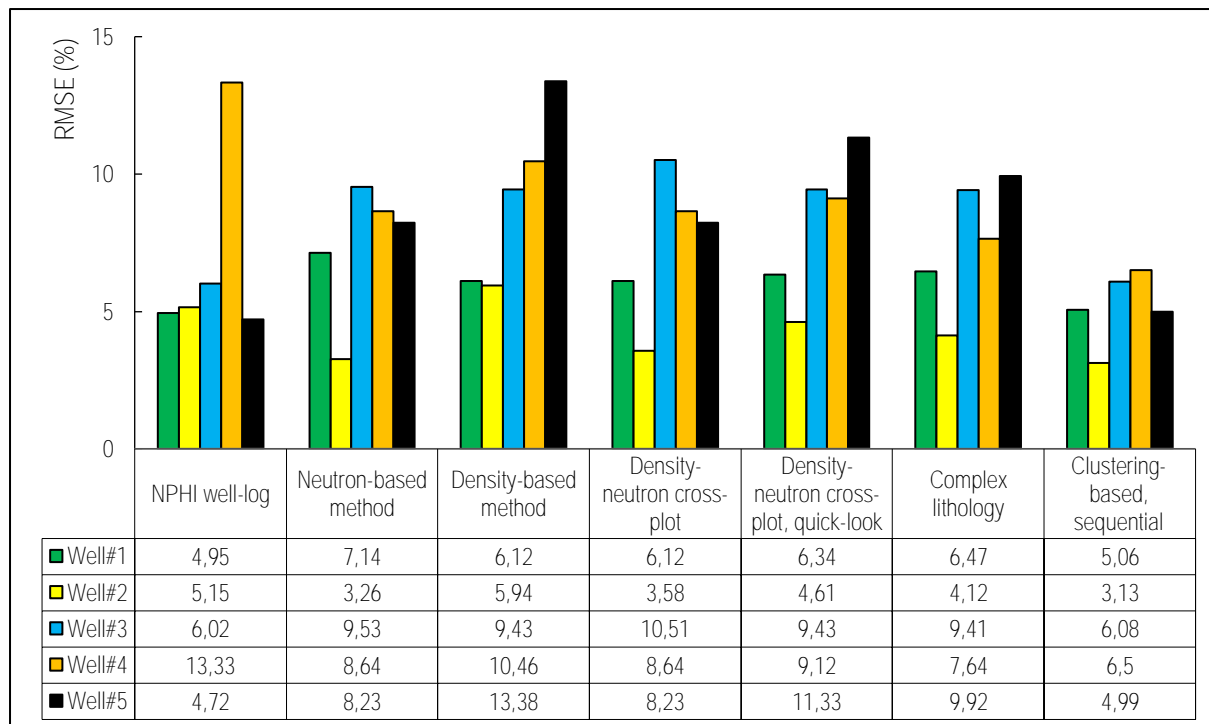


Figure 6-6. Comparison of the RMSE of porosity estimation methods.

There are two reasons why conventional methods are less precise than NPHI in estimating core porosity. **(i)** Conventional methods are developed in the clastic rocks, while the Sarvak Formation consists of carbonate, contaminated by shale (increasing downward). **(ii)** An important functionality of conventional methods is to correct the shale effect, so in clean formations, like the upper Sarvak Formation, they lose this functionality. Therefore, in the upper Sarvak Formation, NPHI is closer to core porosity, comparing to the conventional methods. The cored intervals are from the cleanest parts of the reservoirs, here the upper Sarvak Formation, where the total porosity (NPHI) is close to the effective porosity (core porosity).

### 6.2.3.2 Generalization ability and homogeneous zone of porosity

The estimators W1-FCM6, W3-FCM6 and W5-KM6 have about the same RMSE in wells #1, #3 and #5 (Figure 6-7). Well#4 (the southernmost) is incompatible with the other wells, i.e. the other estimators do not estimate porosity precisely in well#4. In addition, the estimator, trained and calibrated in well#4, i.e. W4-FCM5, is neither accurate in the other wells. To check the reason of isolation of well#4, all the wells were ordered due to the RMSE of each estimator (Table 6-5).

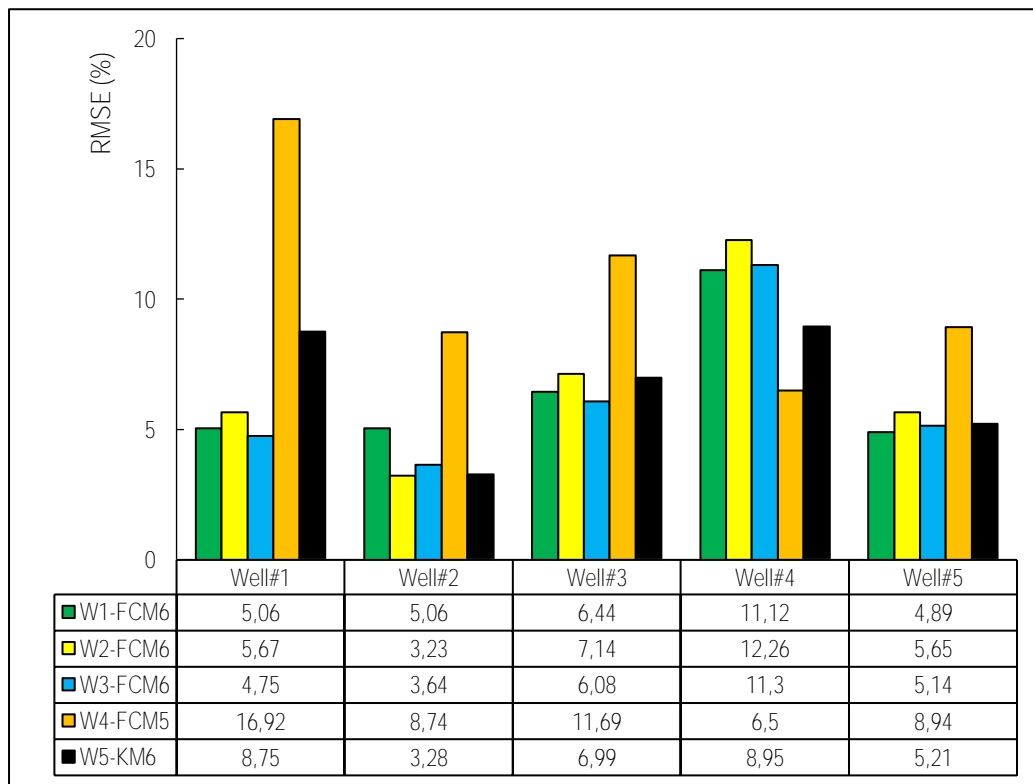


Figure 6-7. Generalization check of porosity estimators.

The estimator W1-FCM6 is more accurate in wells #2 and #5 than in well#1 (Table 6-5). So, the generalization ability of this estimator is about 10 km from the north (distance between wells #1 and #5) and 10 km from the south (distance between wells #1 and #2) (Figure 6-8). Based on the same logic, the estimators W3-FCM6 and W5-KM5 could be generalized up-to about 30 km (toward south) and 20 km (toward south and north), respectively (Table 6-5). The estimators W2-FCM6 and W4-FCM5 are the best local estimators, while they show high errors in the other wells. Hence, they could be interpreted, especially in well#4, as located within another porosity zones. Finally, a homogeneous porosity zone is considered for wells #1, #3

and #5. Around well #2 a transition zone is defined, and well#4 is far from the homogeneous porosity zone (Figure 6-8).

Table 6-5. Generalization ability of the estimators.

Estimator	Wells in the order of RMSE	Distance of generalizability
W1-FCM6	$\underline{W5 < W2 < W1} < W3 < W4$	~10 km toward north and south
W2-FCM6	$\underline{W2 < W5 < W1} < W3 < W4$	0 km
W3-FCM6	$\underline{W2 < W1 < W5 < W3} < W4$	~30 km toward south
W4-FCM6	$\underline{W4 < W2 < W5 < W3 < W1}$	0 km
W5-KM5	$\underline{W2 < W5 < W3 < W1 < W4}$	~20 km toward south and north

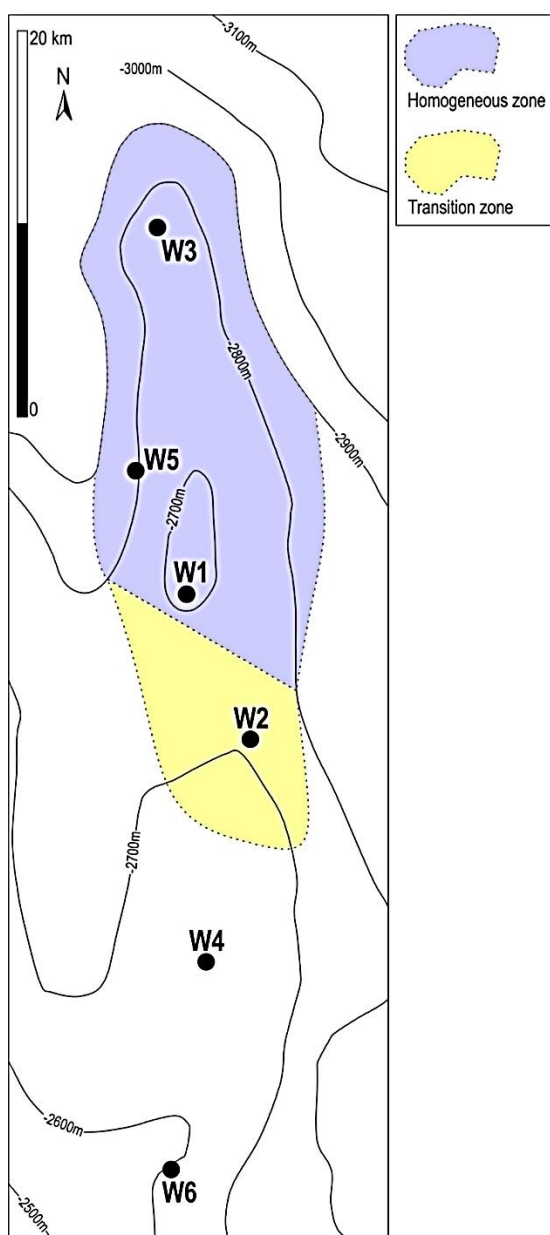


Figure 6-8. Homogeneous porosity zone within the Sarvak Formation.

### 6.3 Permeability analysis by fuzzy arithmetic

#### 6.3.1 Methodology of permeability analysis by fuzzy arithmetic

We applied fuzzy arithmetic on empirical relations of irreducible water ([Relation 2-34](#)) and Wylie-Rose ([Relation 2-35](#)). For the relation of irreducible water, shale percentage is estimated by normalizing GR, and its power is set to be one,  $m=1$ . Buckles number is calculated from the core data in each well ([Table 6-6](#)).

Table 6-6. Buckles number in each well, calculated from core data.

	Well#1	Well#2	Well#3	Well#4	Well#5
Buckles number (%)	1.7	1.6	2.7	1.5	4.6

The porosity is included in the calculations as a triangular fuzzy number. The fuzzy number is defined by clustering-based method of porosity analysis. Its minimum and maximum are derived from the cluster limits of NPHI, and its height is the calibrated NPHI value. When the calibrated NPHI is out of range of the NPHI cluster, a rectangular fuzzy number is defined between the limits of the cluster.

In the next step, permeability ([Relation 2-35](#)) is calculated twice with the constants of Morris-Biggs and Timur ([Table 2-3](#)). The precision of domain of digitized fuzzy numbers of porosity, irreducible water saturation and permeability are 1%, 1% and 0.01 mD, respectively. The domains of permeability fuzzy numbers could vary from zero to 1000 mD. The precisions of domains and the size of domains of fuzzy numbers are effective factors to save calculation time and memory. The proposed values are optimum for a computer with a RAM of 16 gigabytes. If we decrease the precisions, the small permeability values could not be calculated. On the other hand, if we decrease the domain, large fuzzy numbers could not be completely created.

Calculations in fuzzy arithmetic should be done in separate steps. In each step, only one fuzzy operator could be applied. Calculating irreducible water ([Relation 2-34](#)) is addressed in two steps. In the first step, the ratio of buckles number to the  $1 - V_{sh}$  is computed with normal operators ([Relation 6-2](#)). Then,  $a$  is converted to a fuzzy number,  $A$ , with height at  $a$  and zero

for other values of the domain. In the second step, irreducible water is calculated by a fuzzy division ([Relation 6-3](#) and [Figure 6-12](#)).

$$a = \frac{k_{Buckles}}{1 - V_{sh}} \quad \text{Normal operators} \quad (6-2)$$

$$S_{wir} = \frac{A}{\varphi_e} \quad \text{Fuzzy operator of division} \quad (6-3)$$

Calculating Wylie-Rose permeability ([Relation 2-35](#)) is realized in five steps: **(i)** the ratio of porosity to irreducible water is calculated ([Relation 6-4](#)). **(ii)** This ratio,  $A_1$ , to the power of  $n$  is calculated ([Relation 6-5](#)). **(iii)** The effective porosity to the power of  $m - n$  is calculated ([Relation 6-6](#)). **(iv)** Fuzzy multiplication of the fuzzy number of constant  $C_k$ , and  $A_2$  ([Relation 6-7](#)). **(v)** Finally, fuzzy number of permeability is calculated ([Relation 6-8](#) and [Figure 6-14](#)).

$$A_1 = \frac{\varphi_e}{S_{wir}} \quad \text{Fuzzy operator of division} \quad (6-4)$$

$$A_2 = A_1^n \quad \text{Fuzzy operator of power} \quad (6-5)$$

$$B = \varphi_e^{m-n} \quad \text{Fuzzy operator of power} \quad (6-6)$$

$$A_3 = C_k \cdot A_2 \quad \text{Fuzzy operator of product} \quad (6-7)$$

$$k_{WR} = A_3 \cdot B \quad \text{Fuzzy operator of product} \quad (6-8)$$

In the ordinary arithmetic, firstly powers of  $\varphi_e^m$  and  $S_{wir}^n$  are calculated, then their ratio, i.e.  $\frac{\varphi_e^m}{S_{wir}^n}$ . The above order ([Relations 6-4](#) to [6-8](#)) is designed in a way not to produce fuzzy numbers out of the range of [0.01, 1000], since the precision and domain of permeability are set to be 0.01 mD and 1000 mD, respectively. In addition, before calculating [Relation 6-4](#), porosity and irreducible water are converted into the unit of ten%, e.g. the porosity value of 32% is converted to 3.2 ten%. The unit of ten% helps not to produce too small numbers. The conversion is realized by fuzzy product operator of the variables using a triangular fuzzy number of ten, i.e.



its domain is [9.99, 10.01] and its height is at 10. Successively, the constant  $C_k$ , is updated to 6.5 and 21.45 for Morris-Biggs and Timur formulas, respectively.

### 6.3.2 Validation with core data

The core porosity values, irreducible water and permeability have to be within the domains of their corresponding fuzzy numbers. For example, the core porosity is 7.5%; and for  $\alpha=25\%$ , and 50%,  $\alpha$ -cuts are [6.5%, 8%] and [6.7%, 7%], respectively. Therefore, the core porosity is compatible with the  $\alpha$ -cut of 25% but incompatible with the  $\alpha$ -cut of 50% (Figure 6-9). Two validation criteria are designed for compatibility check of the fuzzy numbers with core data. The first one is the average of  $n$  core  $\alpha$  values (Relation 6-9). Closer the core value to the height of the fuzzy number, higher the value of Crit1. Crit1 is a positive criterion lower than one. The second criterion, Crit2, is defined on reference  $\alpha$ -cuts,  $\alpha_{ref}$ : 0.1, 0.2, 0.3, 0.4, 0.5, 0.6, 0.7, 0.8, 0.9 and 0.95 (Relation 6-10).

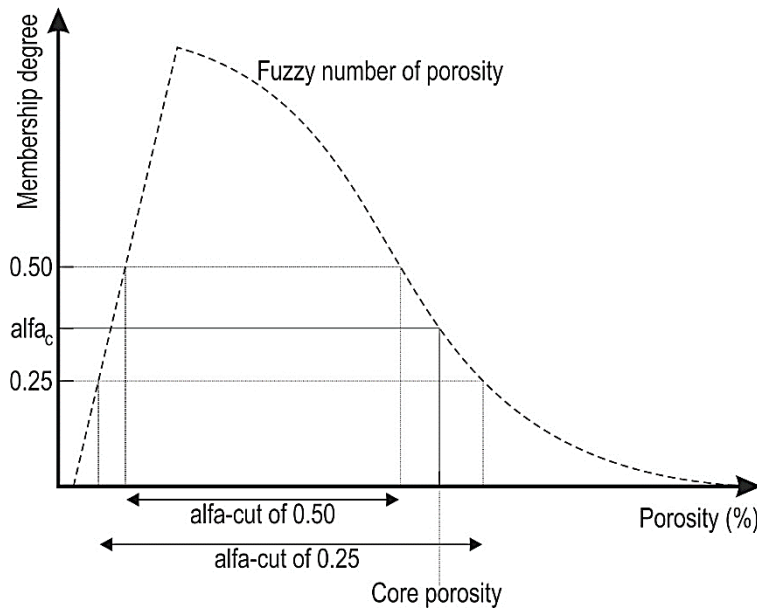


Figure 6-9. Compatibility of core porosity with  $\alpha$ -cuts (alfa-cuts).

$$Crit1 = \frac{1}{n} \sum_{i=1}^n \alpha_c(i) \quad (6-9)$$

$$Crit2_{ref} = \frac{\sum_{i=1}^n [\alpha_c(i) - \alpha_{ref}]}{\sum_{i=1}^n \alpha_{ref} FN(i)} \alpha_{ref} \quad (6-10)$$

where  $\alpha_c(i)$  is the  $\alpha$  value, corresponding to the  $i$ th core value.  ${}^{\alpha_{ref}}FN(i)$  is the  $\alpha$ -cut of fuzzy number (FN) for the  $i$ th core according to  $\alpha_{ref}$ .  ${}^{\alpha_{ref}}FN(i)$  is a domain of uncertainty, so it is desired to be minimum. But higher  $\alpha_{ref}$  and  $\sum_{i=1}^n [\alpha_c(i) - \alpha_{ref}]$  are desired.

### 6.3.3 Results and discussions of analysis by fuzzy arithmetic

The advantage of a fuzzy number to an interval is in providing membership degrees to the interval domain. The fuzzy numbers of porosity (Figure 6-10), irreducible water saturation (Figure 6-12) and permeability (Figure 6-14) are shown. The  $\alpha$ -cuts of 0.7, 0.9 and 0.95 are marked by blue colour tones.

#### 6.3.3.1 Porosity fuzzy numbers

In well#4, the porosity fuzzy number is not well-supported by core porosity (Figure 6-10d, same as in Figure 6-5d). However, for the other wells, the core data is compatible with the porosity fuzzy number.

Fuzzy number of porosity value is compared with the output of the porosity evaluation by the VLSA method. The Monte-Carlo simulation is applied on two porosity estimators: NPHI and output of complex lithology. For each estimator, the simulation is run twice (two different PDFs). The PDF for simulation is first created by 95 adjacent data, i.e. equal to the interval of 14.5 m (Passey *et al.*, 2004). Then, the interval is reduced to about the VRmf (~76 cm), i.e. 5 adjacent data are considered. The VLSA method with the input of NPHI and the interval of VRmf provides the best porosity analyses among the VLSA outputs, red line in Figure 6-11. However, the proposed method is the most accurate (dotted-line).

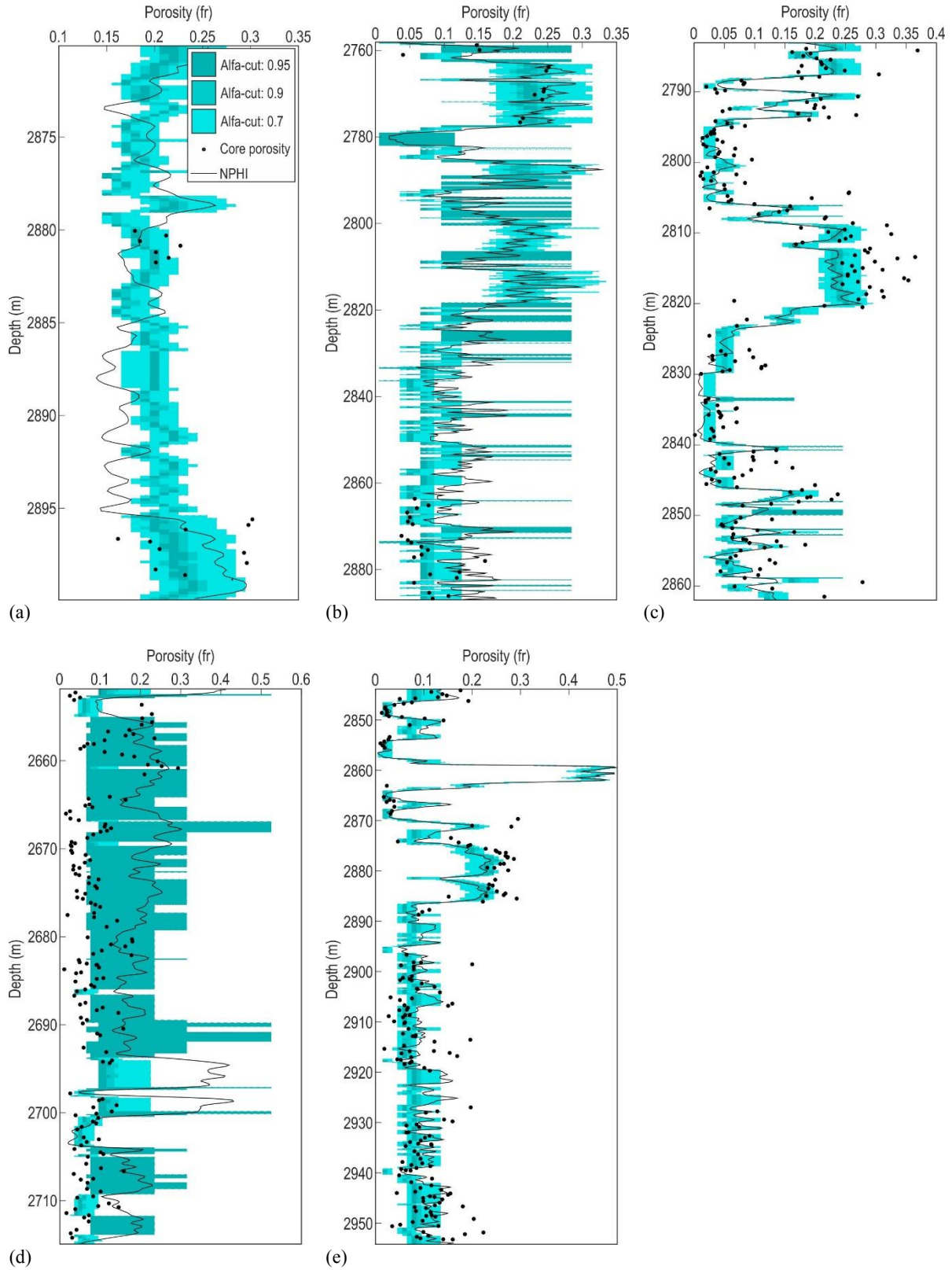


Figure 6-10. Porosity analysis by fuzzy number. a) well#1, b) well#2, c) well#3, d) well#4 and e) well#5. fr: fraction.

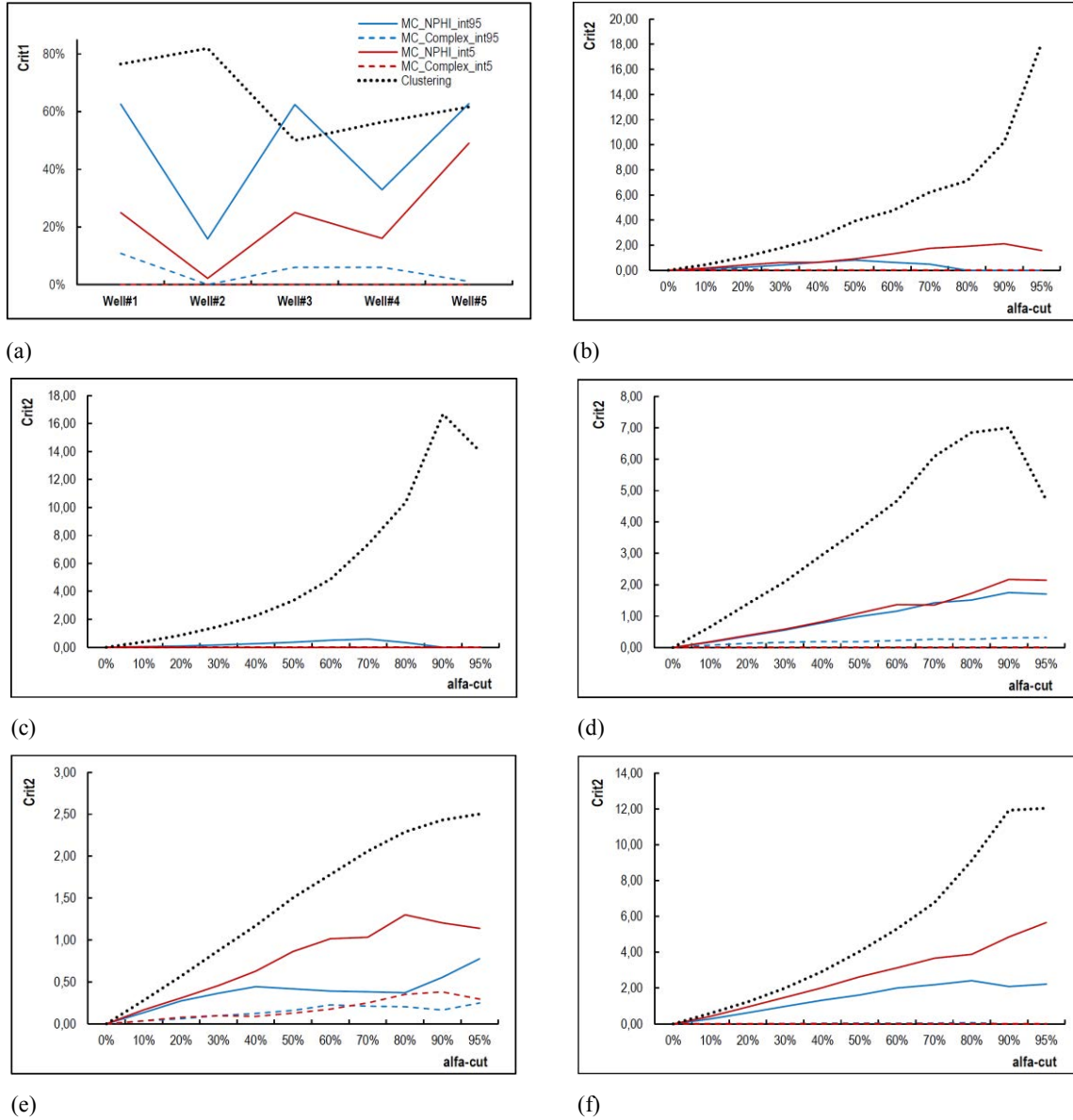


Figure 6-11. Comparison of results of clustering-fuzzy arithmetic porosity analyses with VLSA method (based on Monte-Carlo simulation) by criterion 1 (a) and criterion 2 within well#1 (b), well#2 (c), well#3 (d), well#4 (e) and well#5 (f).

### 6.3.3.2 Irreducible water fuzzy numbers

The irreducible water saturation values of cores are available only in wells #3 and #5. In both cases, crisp evaluation of irreducible water saturation is overestimated. The advantage of fuzzy number of irreducible water is in extending the uncertainty range toward the core values. Especially in well#3, even the height of the fuzzy number is closer to the core values, compared to the crisp evaluation of the irreducible water (Figure 6-12c). The evaluation criteria also show that the proposed method is more successful in well#3 than in well#5 (Figure 6-13).

In well#4, the crisp and fuzzy evaluation of irreducible water saturation values are not compatible. The reason is that the porosity clusters (and fuzzy numbers of porosity) are not compatible with NPHI, so the input porosity for the fuzzy irreducible water is lower than in the crisp value, resulting in lower irreducible water in the fuzzy state (Figure 6-12d).

### 6.3.3.3 Permeability fuzzy numbers

In well#1, fuzzy numbers do not match core permeability (Figure 6-14a,b). In wells #2 and #3, both the fuzzy and crisp approaches have well identified a very low permeability ( $\sim 0$  mD), however a big overestimation occurred in the nonzero values (Figure 6-14c-f). In well#4, the incompatibility of the porosity clusters resulted in big uncertainty intervals ( $\alpha$ -cuts), Figure 6-14g,h, so the method is unsuccessful when there is incompatibility of core porosity and corresponding fuzzy number. In well#5, the permeability fuzzy number matches very well with the core permeability (Figure 6-14i,j).

The outputs of Morris-Biggs and Timur methods are very close to each other, however Timur method could be a little prioritized (Figure 6-15). Wylie-Rose model for permeability estimation (Morris-Biggs and Timur) is not an accurate model in the current oil-field (Figure 6-14). The uncertainty interval, produced by fuzzy arithmetic, is not capable in containing the core permeability values. So, it is suggested to apply fuzzy arithmetic to more complicated permeability models, which are more accurate in the available dataset.

## 6.4 Conclusions of Chapter 6

Cluster-based calibration of NPHI provides accurate estimation of core porosity. The average RMSE of the proposed porosity estimation method is 5.15, which is less than the conventional methods (at least 33%, Figure 6-6). The generalization of the proposed method is 42% less accurate, i.e. RMSE=7.3. In addition, the NPHI range in each cluster provides an uncertainty interval for the porosity. Fuzzy number of porosity is defined within the interval of uncertainty.

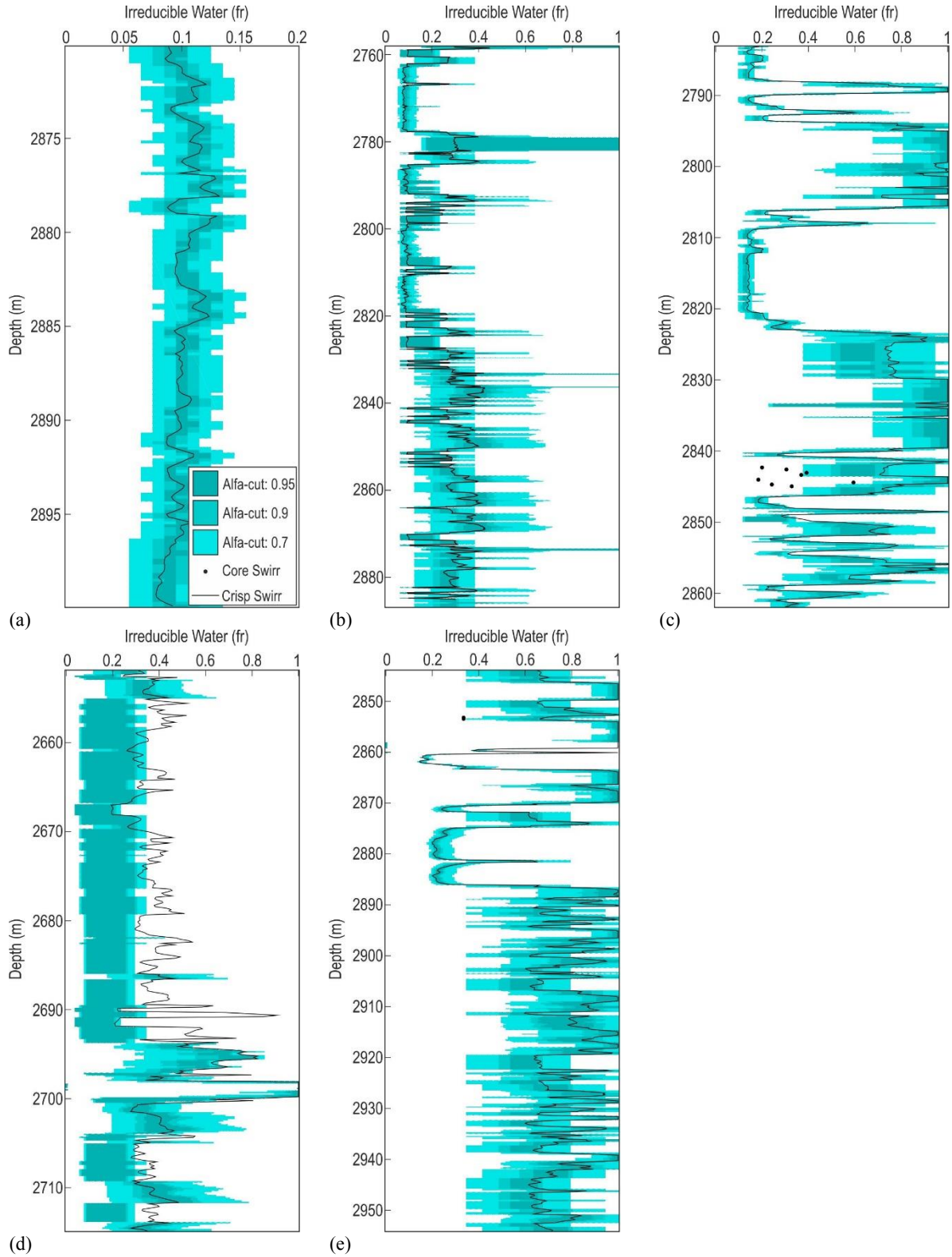


Figure 6-12. Irreducible water analysis of fuzzy number. a) well#1, b) well#2, c) well#3, d) well#4 and e) well#5. fr: fraction.



By the means of  $\alpha$ -cut, the uncertainty range could be optimized. Due to Crit2, the  $\alpha$ -cut of  $>0.90$  is proposed for porperm assessment (Figure 6-11 and 6-15). Porosity fuzzy number is more compatible with core tests than porosity PDF (VLSA method).

Applying fuzzy arithmetic to the fuzzy numbers enabled converting porosity uncertainty to the outputs, here irreducible water saturation and permeability. Fuzzy numbers of irreducible water saturation are less overestimated, compared to the crisp calculations.

Checking generalization ability of porosity estimators resulted in a zonation of the anticline: wells #1, #3 and #5 are in the same homogeneous porosity zone. But the porosity of well#4 is not predictable by the estimators of the other wells. Well#2 is drilled in a transition zone between the homogeneous porosity zone and well#4.

However, for permeability, fuzzy numbers were not fully successful but only in well#5. The basic permeability formula, i.e. Wylie-Rose formula, is basically inaccurate in the available data. So, to improve accuracy, it is recommended to further apply fuzzy arithmetic to the other experimental permeability models.

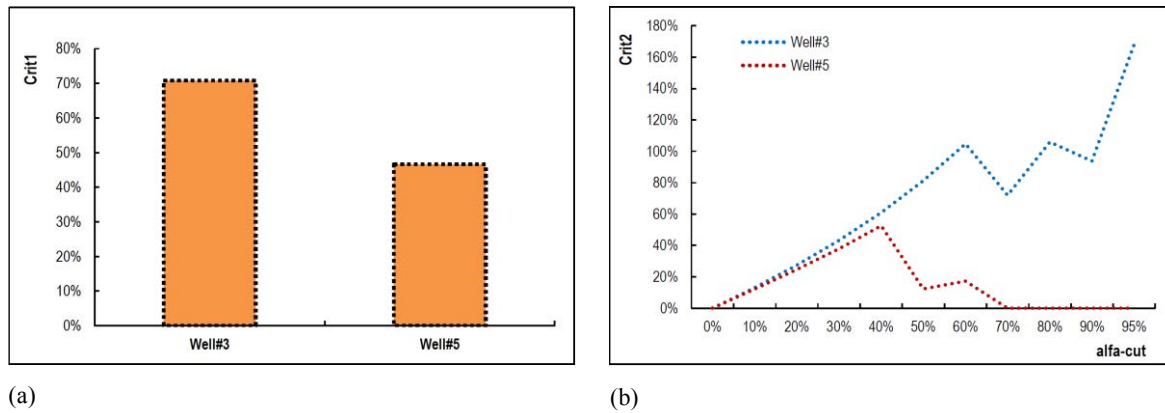
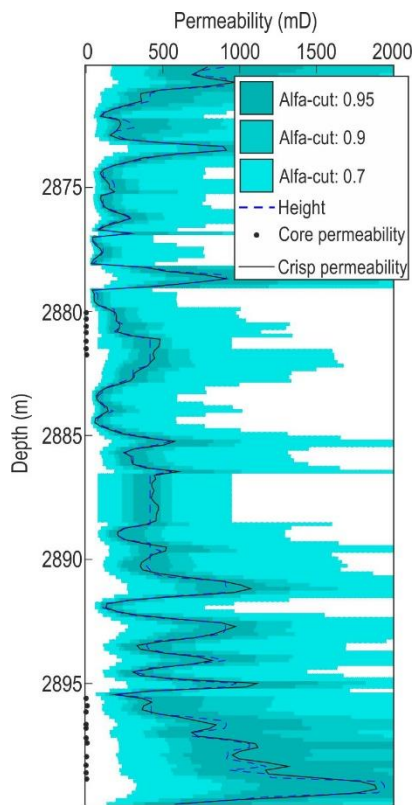
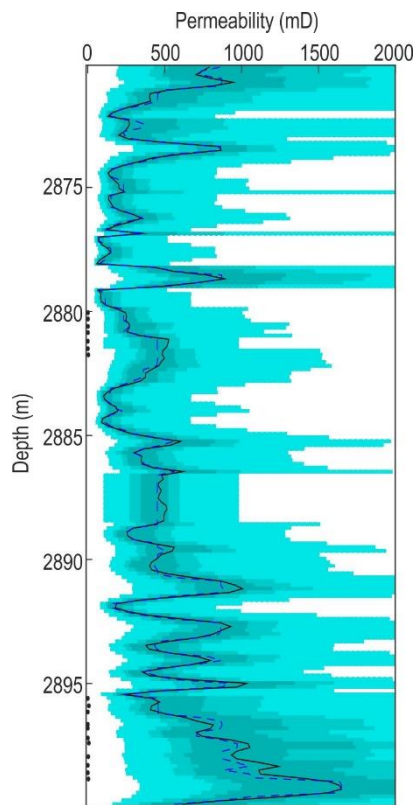


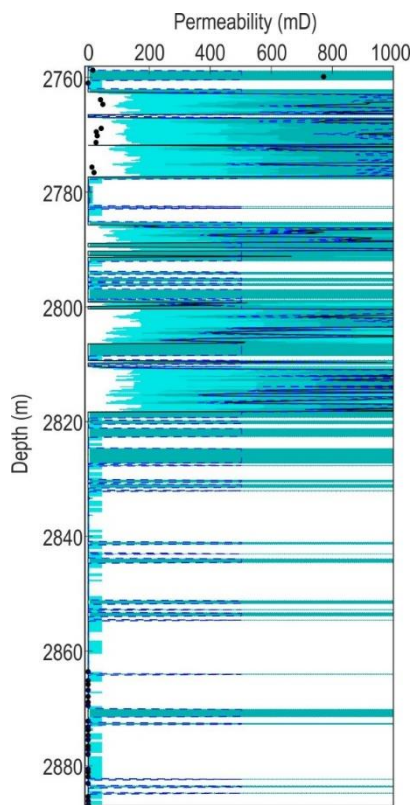
Figure 6-13. Comparison of results of fuzzy arithmetic irreducible water analysis (wells #3 and #5) by criterion 1 (a) and criterion 2 (b).



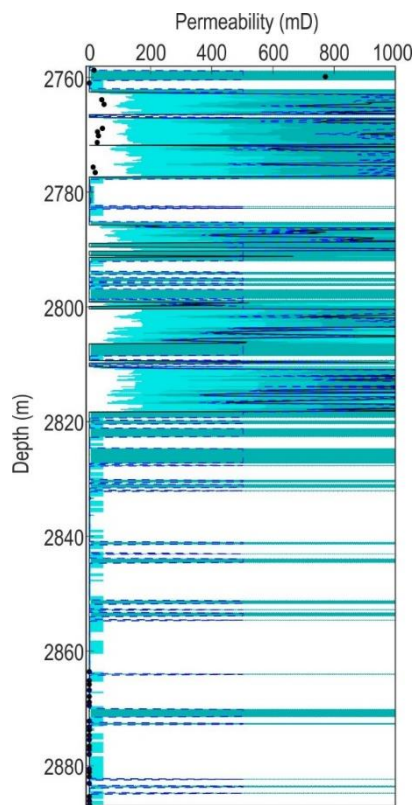
(a)



(b)

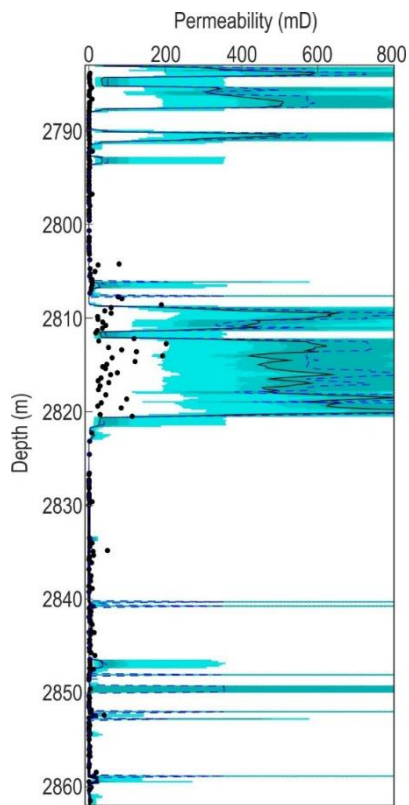


(c)

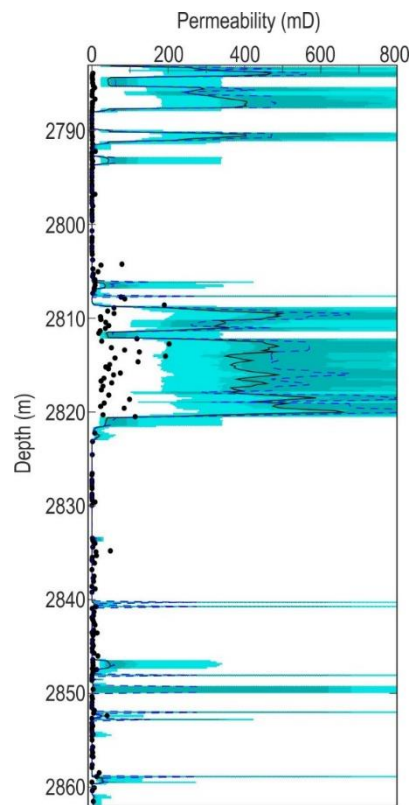


(d)

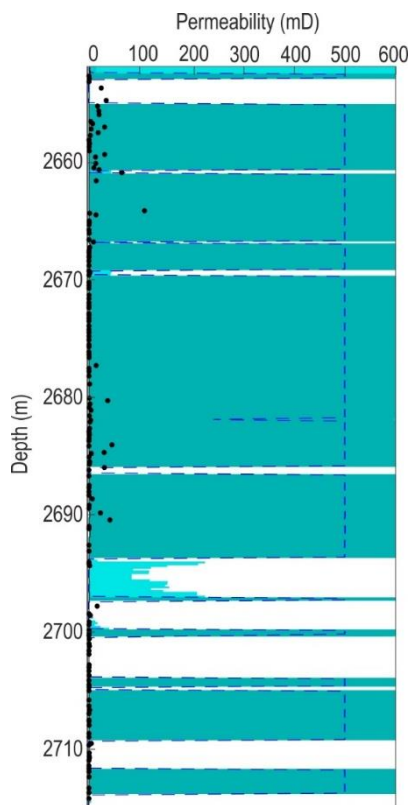




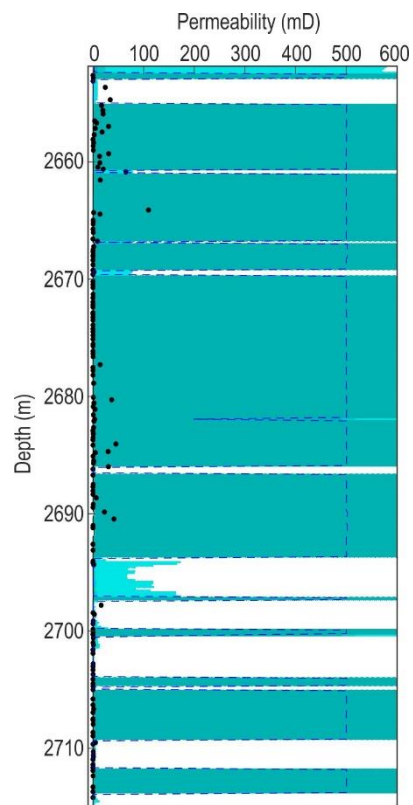
(e)



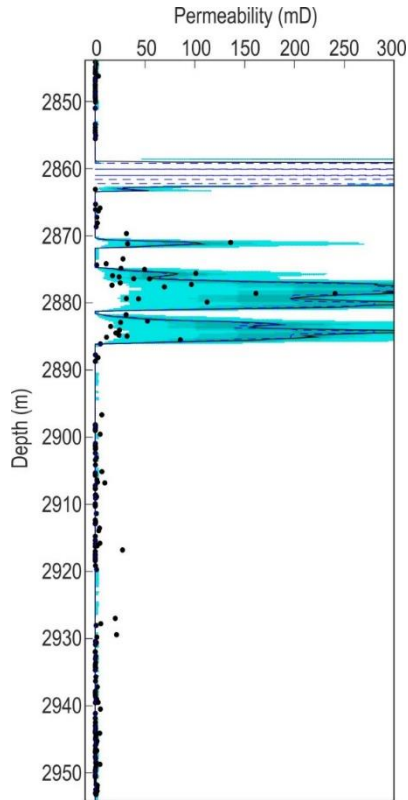
(f)



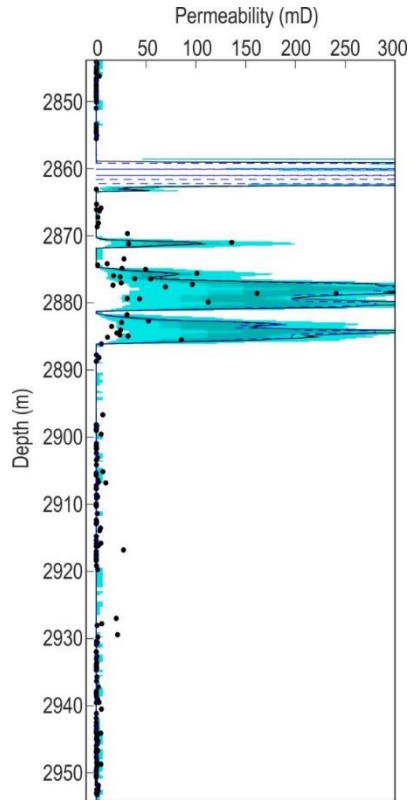
(g)



(h)

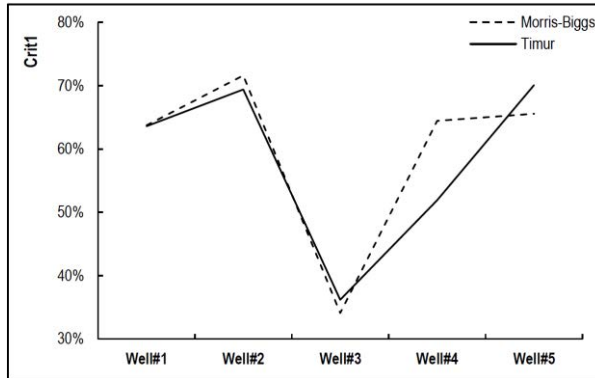


(i)

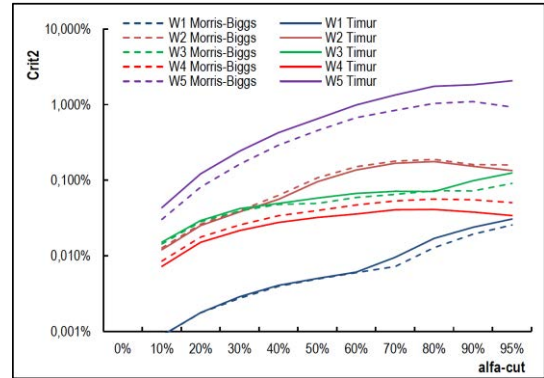


(j)

Figure 6-14. Permeability analysis by fuzzy number: Morris-Biggs (left) and Timur (right) for Well#1 (a,b), well#2 (c,d), well#3 (e,f), well#4 (g,h), well#5 (i,j).



(a)



(b)

Figure 6-15. Comparing results of fuzzy arithmetic permeability analysis.

## 7 Ending

### 7.1 Pathway of the thesis

The thesis started with two questions. The first one concerns the vertical resolution of well-logs, which is addressed in [Chapters 3 to 5](#): logging mechanism was modelled, synthetic-logs were generated ([Chapter 3](#)), and geometric-based thin-bed characterization was developed for thickness estimation and well-log correction ([Chapter 4](#)). Then, DST-based method is elaborated for well-log uncertainty assessment and automated well-log correction, i.e. to enhance the vertical resolution ([Chapter 5](#)).

The second question of the thesis is to find a possibilistic uncertainty boundary of petrophysical interpretations: fuzzy arithmetic was applied to project the uncertainty interval of inputs to the estimations of porosity, irreducible water saturation and permeability ([Chapter 6](#)).

The developed methodologies are applied to the well-logs (meso-scale), and the outputs were verified by core data (micro-scale), which are direct measurements. In fact, some micro-scale characteristics were inferred from the available meso-scale information. The scale change results in the change of data uncertainty. The concept of the scale has always been considered and reviewed in geosciences ([Masoudi \*et al.\*, 2013, 2014](#)).

For the petrophysical variables, when the scale of the study increases (smaller dimensions), the standard deviation of measurements increases; so, higher heterogeneity and uncertainty occur ([Figure 7-1](#)). In the possibilistic approach,  $\alpha$ -cut could be calibrated to achieve the right uncertainty interval, corresponding to the scale of study.

The scale of study determines the specifications and expectations of the project. Therefore, the approach of uncertainty assessment could be selected ([Table 7-1](#)). In the next stage, the uncertainty theory and methodology (Bayesian, DST, fuzzy, Shannon, etc.) should be selected based on our approach.

In addition to both the before-mentioned necessities of uncertainty assessment, “the scale of study” has to be taken into consideration in geosciences. So, the items to be addressed in

uncertainty assessment of the geological projects are summarized by **(i)** clear definition of the aim of study, **(ii)** distinguished uncertainty sources and **(iii)** definition of the scale(s) of study.

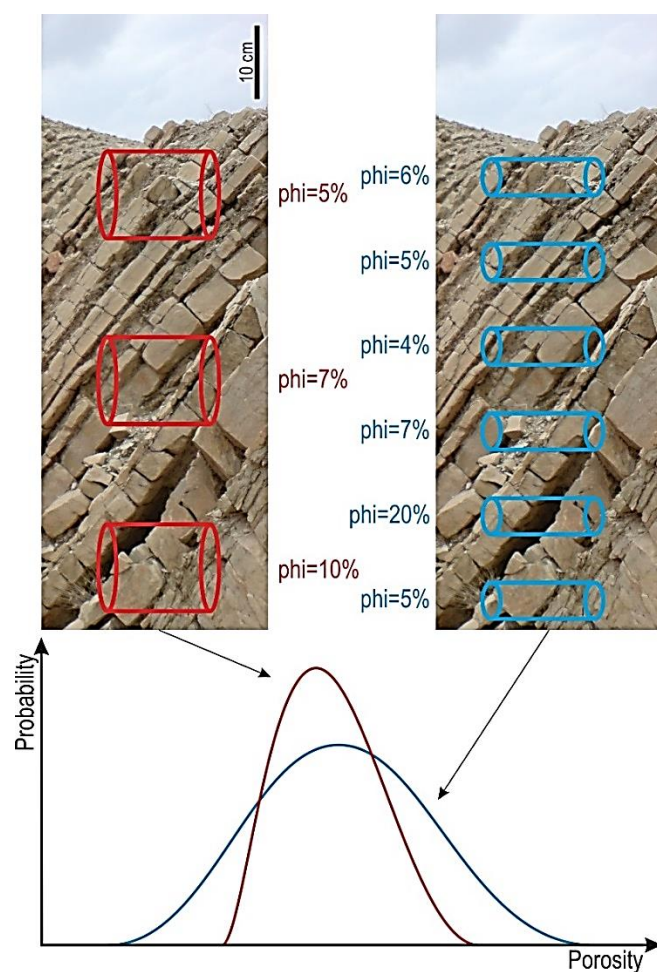


Figure 7-1. Larger the dimension, smaller the uncertainty range of measurements in petrophysical variables (here porosity). From this viewpoint, the uncertainty (also heterogeneity) has a statistical aspect.

Table 7-1. Comparison of different uncertainty approaches.

	Deterministic	Probabilistic	Possibilistic
Inputs and outputs	Fixed numbers	PDF No constraint of fixed numbers.	Fuzzy membership functions. The constraint of PDF is removed: the integral of PDF equal to one
The basic of defining inputs	Measurements and analysis	Measurements and their uncertainty ranges	Evidences: measurements and the mechanisms of measurement
Considered scenarios	Only the most probable case is taken into consideration	The unnecessary (unimportant) values are removed	All the possibilities are considered. Sometimes too much realistic to be applied.
Application	Primary reconnaissance stages	An optimum approach in decision-making	For precise studies and a successful operation

### 7.1.1 Outlined achievements of the thesis

- Despite of the commonly accepted belief, the vertical dimension of volume of investigation of well-logs is larger than the tool spacing (distance between the transmitter and receiver). By the aides of variographs, the vertical dimensions of volume of investigation of GR, RHOB, NPHI and DT are approximated to be 61, 76, 76 and 61 cm, respectively.
- For analysing the volumetric signals, like well-logs, volumetric Nyquist frequency is proposed. Hence, in order to characterize a geologic bed, its thickness have to be more than the summation of sampling rate and vertical dimension of volume of investigation. The application of volumetric Nyquist frequency is useful in determining the precision and the value of data, after upscaling. The goal of upscaling is to reduce the volume of data by fusing the adjacent well-log records. So, the destructive effects of both vertical resolution and sampling rate have to be considered simultaneously.
- The regression-based deconvolution relations are developed for GR, RHOB and NPHI well-logs (based on geometric method). These relations are effective when the thickness of the bed is less than 30 cm, and underlying and overlying beds have relatively the same petrophysical properties. The difference of the petrophysical values of the thin-bed and the surrounding beds have to be less than 30 API,  $0.15 \text{ g.cm}^{-3}$  and 30% for GR, RHOB and NPHI, respectively.
- The thickness estimation after applying deconvolution relations is from 40 to 80 times more accurate than before deconvolution. The standard deviation of thickness estimation is 4.4 cm, which is a very small error, when comparing with the vertical dimension of volume of investigation, which is more than 60 cm. In addition, petrophysical characterization of thin-bed is now more accurate. RMSE of GR, RHOB and NPHI of thin-bed is reduced from 42.25 to 20.20, from 0.003 to 0.001 and from 139.61 to 39.99, respectively.
- The corrected NPHI (after deconvolution) is compared to the core porosity. NPHI before deconvolution was 3.8%, and after being deconvolved, it became 11.7%. Core porosity, representing the effective porosity, was 8.4%. So, the deconvolved NPHI is higher than the core porosity. It is thus more accurate than the original NPHI, since the total porosity (NPHI) have to be more than the effective porosity (core porosity).
- The estimated thickness of the same thin-bed by geometric method is  $13 \pm 7.5$  cm, which is smaller than thickness of thin-bed in the core box ( $< 25 \text{ cm}$ ). The estimated thickness seems to

be reasonable, because the cores at the surface become expanded (removing overburden and crushing).

- The advantages of geometric method: **(i)** estimation of the thin-bed thickness, **(ii)** correction (deconvolution) of well-log at the depth of thin-bed, and **(iii)** theoretical basis of the algorithm is simple. The disadvantages of geometric method: **(i)** It does not provide a complete curve of corrected well-log. **(ii)** Applying the algorithm is time consuming and not automated.
- The body of evidences is designed for the well-logs in order to calculate belief and plausibility values (vertical resolution of volume of investigation is more than 60 cm). Four simulators are then designed to scan the uncertainty range (between belief and plausibility) to enhance the vertical resolution of well-logs (15 cm) (Figure 5-5).
- Constraint-based error is designed for selecting the best realization (output of simulator or corrected well-log). It is based on the volumetric nature of well-logs, and compares the acquired well-log (larger volume of investigation) with corrected log (smaller volume of investigation). Constraint-based error provides an error for each well-log record. This error is useful in comparing the realizations, and selecting the realization with the least error. Ideal-based error is used to validate constraint-based error (correlation coefficient of 0.89 in Figure 5-9).
- DST-based algorithm is automated, and provides a continuous corrected-log. Compared to geometry-based algorithm, DST-based algorithm characterizes the thin-bed more accurately. Characterization of a thin-bed in well#1 is improved by 100%, 71% and 66% for GR, RHOB and NPHI well-logs, respectively. But DST-based algorithm does not provide thin-bed estimation.
- Clustering-based porosity estimation was at least 33% more accurate than the common porosity estimation methods. In addition, it provides an uncertainty range for each cluster.
- By checking the generalization ability of porosity estimation method, homogeneous zone of porosity is identified, consisting of wells #1, #3 and #5. Generalization of porosity estimators is possible in this zone.
- Using fuzzy arithmetic, the input uncertainty (well-logs) is projected into the output uncertainty (irreducible water saturation and permeability). Comparing to the probabilistic method of VLSA for evaluating the porosity, the proposed method, based on the possibilistic approach, is about 200% (in average) more accurate. In addition, the fuzzy uncertainty range

of irreducible water saturation is closer to the core values, compared to the crisp evaluation. For studying permeability, the fuzzy results of well#5 were promising.

## 7.2 Recommendations

### 7.2.1 Recommendations for industrial applications

- Applying DST-based algorithm for improving the vertical resolution of well-logs.
- Using volumetric Nyquist frequency in identifying the least thickness that could be characterized by well-logs or other geophysical data. In addition, the up-scaled well-logs must have relatively the same accuracy as the seismic data. For checking the compatibility of the accuracies, volumetric Nyquist frequency could be used as well.
- It is suggested to carry out fracture study in the intervals that NPHI is higher than core porosity, while the gamma ray (shale content) is low. So, in the development phases of the oil field, it is necessary to do fracture studies within the Sarvak interval of well#4, by running image logs.
- In addition, drilling new exploratory wells is necessary in the heterogeneous (around wells #4 and #6) and transmission (around well#2) zones.
- Developing the software of “Characterizing Thin-beds”, using geometry- and DST-based algorithm.

### 7.2.2 Recommendations for further researches (perspectives)

- In order to further verify the proposed algorithms, they should be **(a)** applied to the surface logging data, **(b)** used in other formations and other oil fields.
- Geometric thin-bed simulator could be developed on non-triangular membership functions. Thin-bed thickness could also pass  $\frac{1}{2}VRmf$ . So, two (out of five) limiting conditions of geometric thin-bed simulator could be removed.
- A geometric simulator is developed for a situation with a single thin-bed. The next steps in improving it are **(i)** to develop it on two close thin-beds, which are not adjacent; **(ii)** to lift off

the limitation of  $q_1=q_3$ , i.e. three adjacent thin-beds. Therefore, we will have different realizations for thin-bed conditions, and will be able in doing risk assessment.

- The geometric thin-bed simulator could be developed on the other well-log data to further study the behaviour of fluids, pore pressure, etc.
- The epsilon in DST-based algorithm is found by trial-and-error. It could be replaced by an automated function, e.g. using the theoretical functions of belief (very small) and plausibility (very large), or the uncertainty interval of the adjacent data.
- The development of an evidence-based software seems necessary for applying DST algorithm. The software should be able in defining focal elements and related properties. It should also have graphical facilities for demonstrating outputs.
- The clustering methods could be further applied to saturation analysis, permeability analysis, net pay studies, etc. A similar study has also been recently applied ([Masoudi \*et al.\*, 2016](#)).
- Fuzzy arithmetic should be applied to other experimental permeability models.
- The developed methodologies should be verified in other formations and oil-fields to be sure about the generalization ability of methods.



## References

- AbdollahieFard, I., Braathen, A., Mokhtari, M., Alavi, S.A., 2006. Interaction of the Zagros Fold–Thrust Belt and the Arabian-type, deep-seated folds in the Abadan Plain and the Dezful Embayment, SW Iran. *Petroleum Geoscience* 12(4), 347-362.
- Anderson, D.T., Bezdek, J.C., Popescu, M., Keller, J.M., 2010. Comparing fuzzy, probabilistic, and possibilistic partitions. *Fuzzy Systems, IEEE Transactions on* 18, 906-918.
- Babuka, R., Van der Veen, P., Kaymak, U., 2002. Improved covariance estimation for Gustafson-Kessel clustering, *Fuzzy Systems, 2002. FUZZ-IEEE'02. Proceedings of the 2002 IEEE International Conference on*. IEEE, pp. 1081-1085.
- Baraldi, A., Blonda, P., 1999. A survey of fuzzy clustering algorithms for pattern recognition. I. Systems, Man, and Cybernetics, Part B: Cybernetics, *IEEE Transactions on* 29, 778-785.
- Bardy, G., 2015. Intégration de modèles approchés pour mieux transmettre l'impact des incertitudes statiques sur les courbes de réponse des simulateurs d'écoulements, UMR7359-GéoRessources (Ecole doctorale RP2E). Université de Lorraine, France, 101p.
- Bayless, J.W., Brigham, E.O., 1970. Application of the Kalman filter to continuous signal restoration. *Geophysics* 35, 2-23.
- Bezdek, J.C., 1993. A review of probabilistic, fuzzy, and neural models for pattern recognition. *Journal of Intelligent and Fuzzy Systems* 1, 1-25.
- Buckles, R.S., 1965. Correlating and averaging connate water saturation data. *Journal of Canadian Petroleum Technology* 4.
- Busch, P., Heinonen, T., Lahti, P., 2007. Heisenberg's uncertainty principle. *Physics Reports* 452, 155-176.
- Caers, J., 2011. Modeling uncertainty in earth sciences. Wiley-Blackwell.
- Campbell, C.V., 1967. Lamina, lamina set, bed, and bedset. *Sedimentology* 8, 7-26.
- Chen, H.-C., Fang, J.-H., 1993. A new method for prospect appraisal. *AAPG Bulletin* 77, 9-18.
- Chen, Z., Osadetz, K.G., 2006. Geological risk mapping and prospect evaluation using multivariate and Bayesian statistical methods, western Sverdrup Basin of Canada. *AAPG Bulletin* 90, 859-872.
- Close, D., Cho, D., Horn, F., Edmundson, H., 2009. The sound of sonic: a historical perspective and introduction to acoustic logging. *CSEG Recorder* 34, 35-44.
- Coates, G.R., Dumanoir, J.L., 1974. A new approach to improved log derived permeability. *The Log Analyst*, XV(1), 17-29.
- Crain, E., 2000. Crain's petrophysical handbook. Spectrum.
- Dashtban, H., 2002. Complementary geology report of the well#3. Exploration Directorate of NIOC, Tehran, p. 35.
- Demicco, R.V., Klir, G.J., 2004. Fuzzy logic in geology. Academic Press, Burlington.
- Dempster, A.P., 1967. Upper and lower probabilities induced by a multivalued mapping. *The annals of mathematical statistics* 38, 325-339.
- Dempster, A.P., 1968. A Generalization of Bayesian Inference. *Journal of the Royal Statistical Society. Series B (Methodological)* 30, 205-247.
- Desvignes, G., Barthes, V., Tabbagh, A., 1992. Direct determination of the natural remanent magnetization effect in a hole drilled in layered ground from magnetic field and susceptibility logs. *Geophysics* 57, 872-884.
- Dewan, J., 1983. Essentials of modern open-hole log interpretation. PennWell Books, Tulsa, 361 pp.
- Dromgoole, P., Speers, R., 1997. Geoscore; a method for quantifying uncertainty in field reserve estimates. *Petroleum Geoscience* 3, 1-12.
- Durant, W.J., 1953. The pleasures of philosophy: a survey of human life and destiny, 23th edn. Elmi Farhangi Publication Company, Tehran.
- Ellis, D.V., Singer, J. M., 2007. Well logging for earth scientists, 2nd ed. Springer, Dordrecht.
- Fang, J., Chen, H., 1990. Uncertainties are better handled by fuzzy arithmetic. *AAPG Bulletin* 74, 1228-1233.
- Finol, J.J., Guo, Y.K., Jing, X.D., 2001. Fuzzy partitioning systems for electrofacies classification: a case study from the Maracaibo basin. *Journal of Petroleum Geology* 24, 441-458.

- Flaum, C., 1990. Enhancing geochemical interpretation using high vertical resolution data. *Nuclear Science, IEEE Transactions on* 37, 948-953.
- Flaum, C., Galford, J., Hastings, A., 1989. Enhanced vertical resolution processing of dual detector gamma-gamma density logs. *The Log Analyst* 30, 139-149.
- Foley, L., Ball, L., Hurst, A., Davis, J., Blockley, D., 1997. Fuzziness, incompleteness and randomness; classification of uncertainty in reservoir appraisal. *Petroleum Geoscience* 3, 203-209.
- Foster, M.R., Hicks, W.G., Nipper, J.T., 1962. Optimum inverse filters which shorten the spacing of velocity logs. *Geophysics* 27, 317-326.
- Galford, J.E., Flaum, C., Gilchrist, W.A., Jr., Duckett, S.W., 1989. Enhanced resolution processing of compensated neutron logs. *SPE Formation Evaluation* 4, 131-137.
- Gallet, Y., Courtillot, V., 1989. Modeling magnetostratigraphy in a borehole. *Geophysics* 54, 973-983.
- Gartner, M.L., 1989. A new resolution enhancement method for neutron porosity tools. *Nuclear Science, IEEE Transactions on* 36, 1237-1242.
- Gath, I., Geva, A.B., 1989. Unsupervised optimal fuzzy clustering. *Pattern Analysis and Machine Intelligence, IEEE Transactions on* 11, 773-780.
- Ghabeishavi, A., Vaziri-Moghaddam, H., Taheri, A., Taati, F., 2010. Microfacies and depositional environment of the Cenomanian of the Bangestan anticline, SW Iran. *Journal of Asian Earth Sciences* 37, 275-285.
- Ghazban, F., 2009. *Petroleum geology of the Persian Gulf*, 1 edn. University of Tehran, Tehran.
- Gimbe, M., 2015. Formation evaluation and uncertainty analysis of the Ormen Lange Field, Norwegian sea offshore Norway, Department of Geology and Mineral Resources Engineering. Norwegian University of Science and Technology, Trondheim, p. 69.
- Gluyas, J., Swarbrick, R., 2009. *Petroleum geoscience*. Blackwell Publishing.
- Grandjean, G., Hibert, C., Bitri, A., Travelletti, J., Malet, J., 2009a. Geophysical data fusion applied to the characterization of the La Valette landslide, Proceedings of the International Conference on Landslide Processes: from geomorphologic mapping to dynamic modelling, Strasbourg, CERG Editions, pp. 119-124.
- Grandjean, G., Hibert, C., Mathieu, F., Garel, E., Malet, J.-P., 2009b. Monitoring water flow in a clay-shale hillslope from geophysical data fusion based on a fuzzy logic approach. *Comptes Rendus Geoscience* 341, 937-948.
- Grandjean, G., Malet, J.P., Bitri, A., Meric, O., 2007. Geophysical data fusion by fuzzy logic for imaging the mechanical behaviour of mudslides. *Bulletin de la Societe Geologique de France* 178, 127-136.
- Gray, R.M., Lee, D.D., 2007. *An introduction to statistical signal processing*. Cambridge University Press.
- Gringarten, E., Deutsch, C.V., 2001. Teacher's aide variogram interpretation and modeling. *Mathematical Geology* 33, 507-534.
- Gustafson, D.E., Kessel, W.C., 1978. Fuzzy clustering with a fuzzy covariance matrix, Decision and Control including the 17th Symposium on Adaptive Processes, IEEE Conference on. IEEE, pp. 761-766.
- Hartigan, J.A., Wong, M.A., 1979. Algorithm AS 136: a k-means clustering algorithm. *Applied statistics*, 100-108.
- Heidari, Z., Torres-Verdin, C., Preeg, W.E., 2012. Improved estimation of mineral and fluid volumetric concentrations from well logs in thinly bedded and invaded formations. *Geophysics* 77, WA79-WA98.
- Hibert, C., Grandjean, G., Bitri, A., Travelletti, J., Malet, J.-P., 2012. Characterizing landslides through geophysical data fusion: example of the La Valette landslide (France). *Engineering Geology* 128, 23-29.
- Hurst, A., Brown, G., Swanson, R., 2000. Swanson's 30-40-30 rule. *AAPG Bulletin* 84, 1883-1891.
- Hurst, A., Verstralen, I., Cronin, B., Hartley, A., 1999. Sand-rich fairways in deep-water clastic reservoirs: genetic units, capturing uncertainty, and a new approach to reservoir modeling. *AAPG Bulletin* 83, 1096-1118.
- James, G.A., Wynd, J.G., 1965. Stratigraphic nomenclature of Iranian Oil Consortium Agreement Area. *AAPG Bulletin* 49, 2182-2245.
- Johnson, D.E., Pile, K.E., 2002. *Well logging In nontechnical language*, 2nd edn. Penn Well Publishing Company, Tulsa.
- Kitts, D.B., 1976. Certainty and uncertainty in geology. *American Journal of Science* 276, 29-46.
- Klir, G.J., 1997. Fuzzy arithmetic with requisite constraints. *Fuzzy Sets and Systems* 91, 165-175.
- Klir, G.J., Yuan, B., 1995. *Fuzzy sets and fuzzy logic, theory and applications*. Prentice Hall New Jersey, 574 pp.
- Krishnapuram, R., Keller, J.M., 1993. A possibilistic approach to clustering. *Fuzzy Systems, IEEE Transactions on* 1, 98-110.

- Lia, O., Omre, H., Tjelmeland, H., Holden, L., Egeland, T., 1997. Uncertainties in reservoir production forecasts. *AAPG Bulletin* 81, 775-802.
- Liu, L., Yager, R.R., 2008. Classic works of the Dempster-Shafer Theory of belief functions. Springer Berlin Heidelberg, 806 pp.
- Lucia, F. J., 1983. Petrophysical parameters estimated from visual descriptions of carbonate rocks: a field classification of carbonate pore space. *Journal of Petroleum Technology* 35(3), 629-637.
- Lucia, F. J., 1995. Rock-fabric/petrophysical classification of carbonate pore space for reservoir characterization. *AAPG bulletin* 79(9), 1275-1300.
- Lyle, W.D., Williams, D.M., 1987. Deconvolution of well log data - an innovations approach. *The Log Analyst* 28, 321-328.
- MacQueen, J., 1967. Some methods for classification and analysis of multivariate observations, *Proceedings of the fifth Berkeley symposium on mathematical statistics and probability*, pp. 281-297.
- Majid, A.A., Worthington, P.F., 2012. Definitive petrophysical evaluation of thin hydrocarbon reservoir sequences. *SPE Reservoir Evaluation & Engineering* 15, 584-595.
- Masoudi, P., Arbab, B., Mohammadrezaei, H., 2014. Net pay determination by Dempster rule of combination, case study on Iranian offshore oil fields. *Journal of Petroleum Science and Engineering* 123, pp. 78-83.
- Masoudi, P., Asgarinezhad, Y., Tokhmechi, B., 2015. Feature selection for reservoir characterisation by Bayesian network. *Arabian Journal of Geosciences* 8, 3031-3043.
- Masoudi, P., Memarian, H., Aïfa, T., Tokhmechi, B., 2017. Geometric modelling of the volume of investigation of well logs for thin-bed characterization. *Journal of Geophysics and Engineering* 14(2), 426-444.
- Masoudi, P., Nadjar Araabi, B., Aïfa, T., Memarian, H., 2016. Clustering as an efficient tool for assessing fluid content and movability by resistivity logs. In: *Numerical Proceedings of the 4th International Mine and Mining Industries Congress and Exposition*, Tehran, 9p.
- Masoudi, P., Zahedi, A., Moradzadeh, A., Alirezaei, F., Zamanzadeh, S.M., 2011. Estimation of in place hydrocarbon volume in multilayered reservoirs using deterministic and probabilistic approaches. *Energy Exploration and Exploitation* 29, 543-557.
- Matsakis, P., Andréfouët, S., Capolsini, P., 2000. Evaluation of fuzzy partitions. *Remote Sensing of Environment* 74, 516-533.
- Mazaheri, A., Memarian, H., Tokhmechi, B., Araabi, B.N., 2015. Developing fracture measure as an index of fracture impact on well-logs. *Energy Exploration and Exploitation* 33, 555-574.
- Mendoza, A., Torres-Verdin, C., Preeg, W., 2006. Environmental and petrophysical effects on density and neutron porosity logs acquired in highly deviated wells, SPWLA 47th Annual Logging Symposium, Society of Petrophysicists and Well-Log Analysts.
- McCall, D.C., Allen, D.F., Culbertson, J.S., 1987. High-resolution logging: the key to accurate formation evaluation, *SPE Annual Technical Conference and Exhibition*. Society of Petroleum Engineers, Dallas, Texas, pp. 283-298.
- McLane, M., Gouveia, J., Citron, G.P., MacKay, J., Rose, P.R., 2008. Responsible reporting of uncertain petroleum reserves. *AAPG Bulletin* 92, 1431-1452.
- Megill, 1979. *An introduction to exploration economics*, 2nd edn. PennWell Books, Tulsa.
- Mehrabi, H., Rahimpour-Bonab, H., Hajkazemi, E., Jamalian, A., 2015. Controls on depositional facies in Upper Cretaceous carbonate reservoirs in the Zagros area and the Persian Gulf, Iran. *Facies* 61, 1-24.
- Meshkani, S.A., Mehrabi, B., Yaghubpur, A., Alghalandis, Y.F., 2011. The application of geochemical pattern recognition to regional prospecting: A case study of the Sanandaj-Sirjan metallogenic zone, Iran. *Journal of Geochemical Exploration* 108, 183-195.
- Moore, W., Ma, Z., Urdea, J., Bratton, T., 2011. Uncertainty analysis in well log and petrophysical interpretations, In: Ma, Y.Z., LaPointe, P. (Eds.), *Uncertainty analysis and reservoir modeling*. AAPG Memoir, pp. 17-28.
- Moradi, M., Tokhmechi, B., Masoudi, P., Ramezani, O., 2015. Evaluation of production capability of the reservoir using clustering techniques, 33rd National Geosciences Symposium. Geological Survey of Iran.
- Morris, R.L., Biggs, W.P., 1967. Using log-derived values of water saturation and porosity, *SPWLA 8th Annual Logging Symposium*. Society of Petrophysicists and Well-Log Analysts, Denver, Colorado.
- Mukaka, M.M., 2012. A guide to appropriate use of Correlation coefficient in medical research. *Malawi Medical Journal : The Journal of Medical Association of Malawi* 24, 69-71.
- Nelson, R., Lenox, L., Ward Jr, B., 1987. Oriented core: its use, error, and uncertainty. *AAPG Bulletin* 71, 357-367.

- NikTab, M., 2003. Complementary geology report of the well#5. Exploration Directorate of NIOC, Tehran, p. 18.
- Nyquist, H., 1924. Certain factors affecting telegraph speed. *Bell System technical journal* 3, 324–346.
- De Oliveira, J.V., Pedrycz, W., 2007. Advances in fuzzy clustering and its applications. John Wiley & Sons, Ltd.
- Ortet, S., Vidal, O., Fournier, F., Guillemot, D., Hayet, M., Yven, B., 2012. Estimation of uncertainties associated to porosity prediction from inversion, 2012 SEG Annual Meeting. Society of Exploration Geophysicists.
- Pal, N.R., Pal, K., Keller, J.M., Bezdek, J.C., 2005. A possibilistic fuzzy c-means clustering algorithm. *Fuzzy Systems, IEEE Transactions on* 13, 517-530.
- Passey, Q.R., Dahlberg, K.E., Sullivan, K.B., Yin, H., Brackett, B., Xiao, Y.H., Guzmán-Garcia, A.G., Brackett, R.A., 2006. Petrophysical evaluation of hydrocarbon pore-thickness in thinly bedded clastic reservoirs. AAPG
- Passey, Q.R., Dahlberg, K.E., Sullivan, K.B., Yin, H., Xiao, Y.H., Guzmán-Garcia, A.G., Brackett, R.A., 2004. A systematic approach to evaluate hydrocarbons in thinly bedded reservoirs, SPWLA 45th Annual Logging Symposium. Society of Petrophysicists and Well-Log Analysts.
- Petler, J.S., 1990. Modelling the spatial response of a compensated density tool. *Nuclear Science, IEEE Transactions on* 37, 954-958.
- Qi, L., Carr, T.R., 2006. Neural network prediction of carbonate lithofacies from well logs, Big Bow and Sand Arroyo Creek fields, southwest Kansas. *Computers and Geosciences* 32, 947-964.
- Rajabi, M., Sherkati, S., Bohloli, B., Tingay, M., 2010. Subsurface fracture analysis and determination of in-situ stress direction using FMI logs: an example from the Santonian carbonates (Ilam Formation) in the Abadan Plain, Iran. *Tectonophysics* 492, 192–200.
- Razin, P., Taati, F., van Buchem, F.S.P., 2010. Sequence stratigraphy of Cenomanian–Turonian carbonate platform margins (Sarvak Formation) in the High Zagros, SW Iran: an outcrop reference model for the Arabian Plate. *Geological Society, London, Special Publications* 329, 187-218.
- Read, J.F., 1985. Carbonate platform facies models. *AAPG Bulletin* 69, 1-21.
- Rose, P.R., 1987. Dealing with risk and uncertainty in exploration: how can we improve? *AAPG Bulletin* 71, 1-16.
- Saggaf, M., Nebrija, L., 2003. A fuzzy logic approach for the estimation of facies from wire-line logs. *AAPG Bulletin* 87, 1223-1240.
- Sams, M., Saussus, D., 2008. Comparison of uncertainty estimates from deterministic and geostatistical inversion, 70th EAGE Conference & Exhibition.
- Schlumberger, 2015. Wireline services catalog. Well Services of Iran [Schlumberger Methods], p. 81.
- Seiler, A., Rivenæs, J.C., Aanonsen, S.I., Evensen, G., 2009. Structural uncertainty modelling and updating by production data integration, SPE/EAGE Reservoir Characterization & Simulation Conference.
- Sengupta, M.K., 1987. Time-offset-frequency-amplitude panels for seismic identification of hydrocarbons. United States Patent, United States.
- Sengupta, M.K., Lange, J.N., Almoghrabi, H.A., 1989. Lithology discrimination for thin layers using wavelet signal parameters; discussion and reply. *Geophysics* 54, 789-789.
- Sfidari, E., Kadkhodaie-Ilkhchi, A., Rahimpour-Bbonab, H., Soltani, B., 2014. A hybrid approach for litho-facies characterization in the framework of sequence stratigraphy: a case study from the South Pars gas field, the Persian Gulf basin. *Journal of Petroleum Science and Engineering* 121, 87-102.
- Shafer, G., 1976. A mathematical theory of evidence. Princeton University press, Princeton, 314 pp.
- Shafer, G., 1990. Perspectives on the theory and practice of belief functions. *International Journal of Approximate Reasoning* 4, 323-362.
- Shannon, 1948. A mathematical theory of communication. *The Bell System Technical Journal* 27, 379–423.
- Sherkati, S., Letouzey, J., 2004. Variation of structural style and basin evolution in the central Zagros (Izeh zone and Dezful Embayment), Iran. *Marine Petroleum Geology* 21, 535–554.
- Smalley, P.C., Begg, S.H., Naylor, M., Johnsen, S., Godi, A., 2008. Handling risk and uncertainty in petroleum exploration and asset management: An overview. *AAPG Bulletin* 92, 1251-1261.
- Templ, M., Filzmoser, P., Reimann, C., 2008. Cluster analysis applied to regional geochemical data: problems and possibilities. *Applied Geochemistry* 23, 2198-2213.
- Thore, P., Shtuka, A., Lecour, M., Ait-Ettajer, T., Cognot, R., 2002. Structural uncertainties: determination, management, and applications. *Geophysics* 67, 840-852.
- Tiab, D., Donaldson, E. C., 2004. Petrophysics: theory and practice of measuring reservoir rock and fluid transport properties, 2<sup>nd</sup> edition, Gulf Professional Publishing, 899 pp.

- Timur, A., 1968. An investigation of permeability, porosity, and residual water saturation relationships for sandstone reservoirs, SPWA 9th Annual Logging Symposium, New Orleans, Louisiana.
- Vincent, B., van Buchem, F.S.P., Bulot, L.G., Jalali, M., Swennen, R., Hosseini, A.S., Baghbani, D., 2015. Depositional sequences, diagenesis and structural control of the Albian to Turonian carbonate platform systems in coastal Fars (SW Iran). *Marine and Petroleum Geology* 63, 46-67.
- Wessling, S., Bartetzko, A., Tesch, P., 2013. Quantification of uncertainty in a multistage/multiparameter modeling workflow: Pore pressure from geophysical well logs. *Geophysics* 78, WB101-WB112.
- Wyllie, M.R.J., Rose, W.D., 1950. Some Theoretical Considerations Related to the Quantitative Evaluation of the Physical Characteristics of Reservoir Rocks from Electrical Log Data. *Petroleum Transactions of AIME*, 189, 105-118.
- Wong, P.M., 2003. A novel technique for modeling fracture intensity: A case study from the Pinedale anticline in Wyoming. *AAPG Bulletin* 87, 1717-1727.
- Yang, W., Howley, E., Leahy, G.M., 2013. Quantifying uncertainty in seismic interpretation, 2013 SEG Annual Meeting. Society of Exploration Geophysicists.
- Yeh, T.-H., Jimenez, E., Van Essen, G., Chen, C., Jin, L., Girardi, A., Gelderblom, P., Horesh, L., Conn, A.R., 2014. Reservoir uncertainty quantification using probabilistic history matching workflow, SPE Annual Technical Conference and Exhibition. Society of Petroleum Engineers.
- Zadeh, L.A., 1965. Fuzzy sets. *Information and Control* 8, 338-353.
- Zadeh, L.A., 1971. Similarity relations and fuzzy orderings. *Information Sciences* 3, 177-200.
- Zadeh, L.A., 1975a. The concept of a linguistic variable and its application to approximate reasoning-I. *Information Sciences* 8, 199-249.
- Zadeh, L.A., 1975b. The concept of a linguistic variable and its application to approximate reasoning-II. *Information Sciences* 8, 301-357.
- Zadeh, L.A., 1975c. The concept of a linguistic variable and its application to approximate reasoning-III. *Information Sciences* 9, 43-80.
- Zadeh, L.A., 1996. Fuzzy logic = computing with words. *IEEE Transactions on Fuzzy Systems* 4, 103-111.
- Zarasvandi, A., Charchi, A., Carranza, E.J.M., Alizadeh, B., 2008. Karst bauxite deposits in the Zagros Mountain Belt, Iran. *Ore Geology Reviews* 34, 521-532.
- Zheng, S.-Y., Corbett, P.W., Ryseth, A., Stewart, G., 2000. Uncertainty in well test and core permeability analysis: a case study in fluvial channel reservoirs, northern North Sea, Norway. *AAPG Bulletin* 84, 1929-1954.

# Appendices

## Appendix A: Convolution form of Relation 4-2

In order to reach the convolution form of [Relation 4-2](#), the domain of functions  $MF(x)$  and  $q(x)$  must be extended from  $-\infty$  to  $+\infty$  ([Relations A1](#) and [A2](#)). Considering [Relation A3](#) the final convolution form could be achieved ([Relation A4](#)).

$$MF_e(x) = \begin{cases} MF(x); & 0 \leq x \leq VRmf \\ 0; & x < 0 \text{ or } VRmf < x \end{cases} \quad (A1)$$

$$q_e(x) = \begin{cases} q(x); & 0 \leq x \leq \text{Max}\{z\} \\ 0; & x < 0 \text{ or } \text{Max}\{z\} < x \end{cases} \quad (A2)$$

$$g(z - x) = MF_e(x) \quad (A3)$$

$$\begin{aligned} slog(z) &= \int_{\frac{z-VRmf}{2}}^{\frac{z+VRmf}{2}} q(x).MF(x).dx = \int_{-\infty}^{+\infty} q_e(x).MF_e(x).dx \\ &= \int_{-\infty}^{+\infty} q_e(x).g(z - x).dx \end{aligned} \quad (A4)$$

## Appendix B: Application check of DST-based simulators on synthetic-logs

Outputs, error profiles, total errors and interpretation of DST-based simulators on cases 2-5 and 7 ([Table 1-2](#)) are provided.

### Case 2: Deepening (fining) upward of GR

None of simulators reproduce exact shape of the ideal-log, however they were able to generate very similar shapes, especially random-optimization and recursive-optimization simulators ([Figure A 1a](#)). The reason is the incompatibility of depths of ideal- and simulated-

log. This deficiency exists when the  $FE^t$  is the integration of even number of  $FE^r$ . Due to the formulas, when  $n_{fuse}$  is odd, there is no problem. So, this deficiency exists in GR and DT ( $n_{fuse} = 4$ ) and not in RHOB and NPHI ( $n_{fuse} = 5$ ).

Due to ideal-based error, recursive-optimization is the most accurate simulator, while due to constraint-based error, random-optimization should be used (Figure A 1b,c). Though the errors do not have the same decisions in this example, they are matched highly (Figure 5-9).

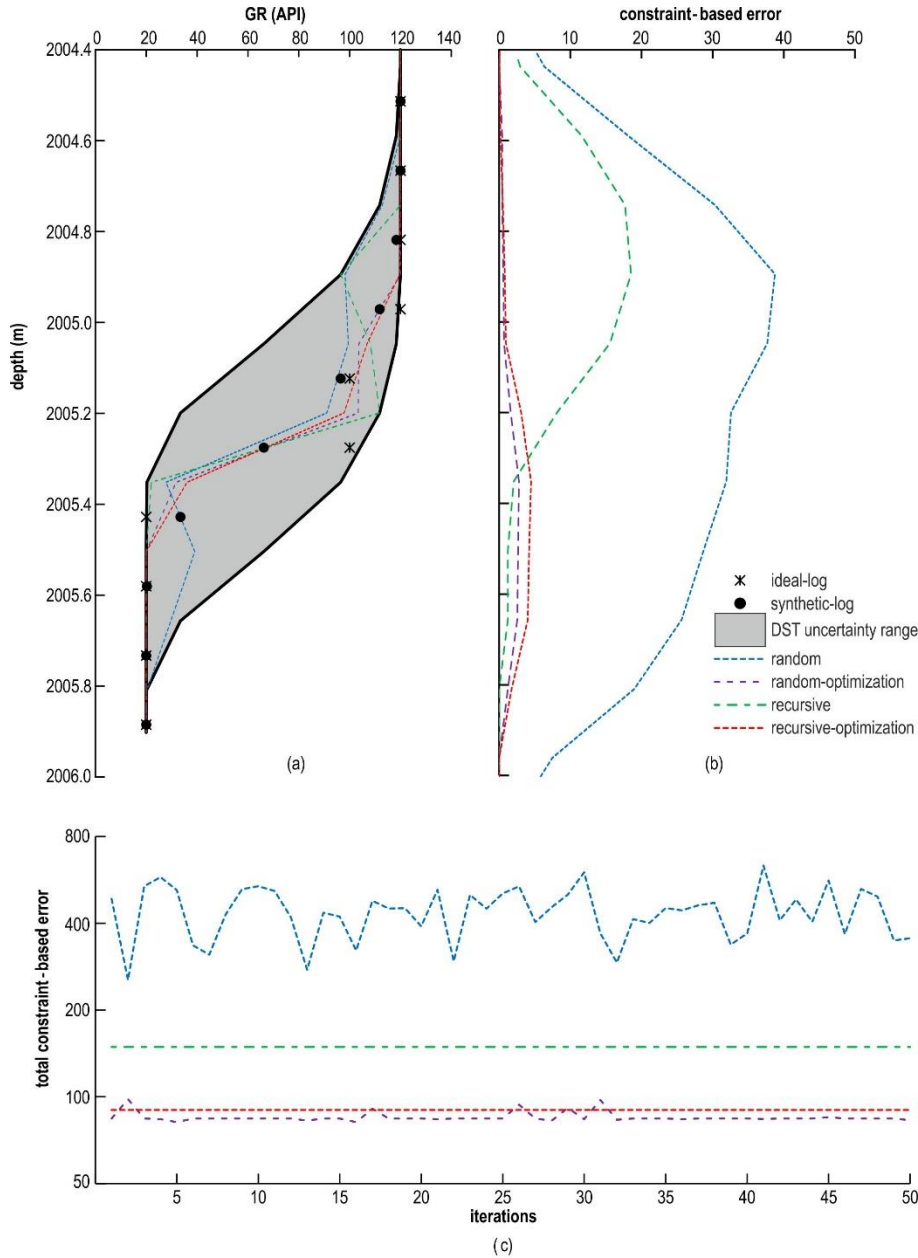


Figure A 1. a) Ideal-log, synthetic-log, uncertainty range, simulations (realizations) and the best realization of each simulator in case 2. Error comparison between the simulators: b) error profiles, and c) total error of 50 iterations.

### Case 3: Trough in RHOB

In case 3, because of misspeak of the synthetic-log, none of the simulators were able in well-detecting the exact place of the thin-bed. However, random-optimization, recursive and recursive-optimization simulators reduced shoulder-bed effect to some extent (Figure A 2). In brief, skewness of the measured well-log or synthetic-log will result in misplacing the anomaly. So, the developed methodology is more accurate in symmetric cases.

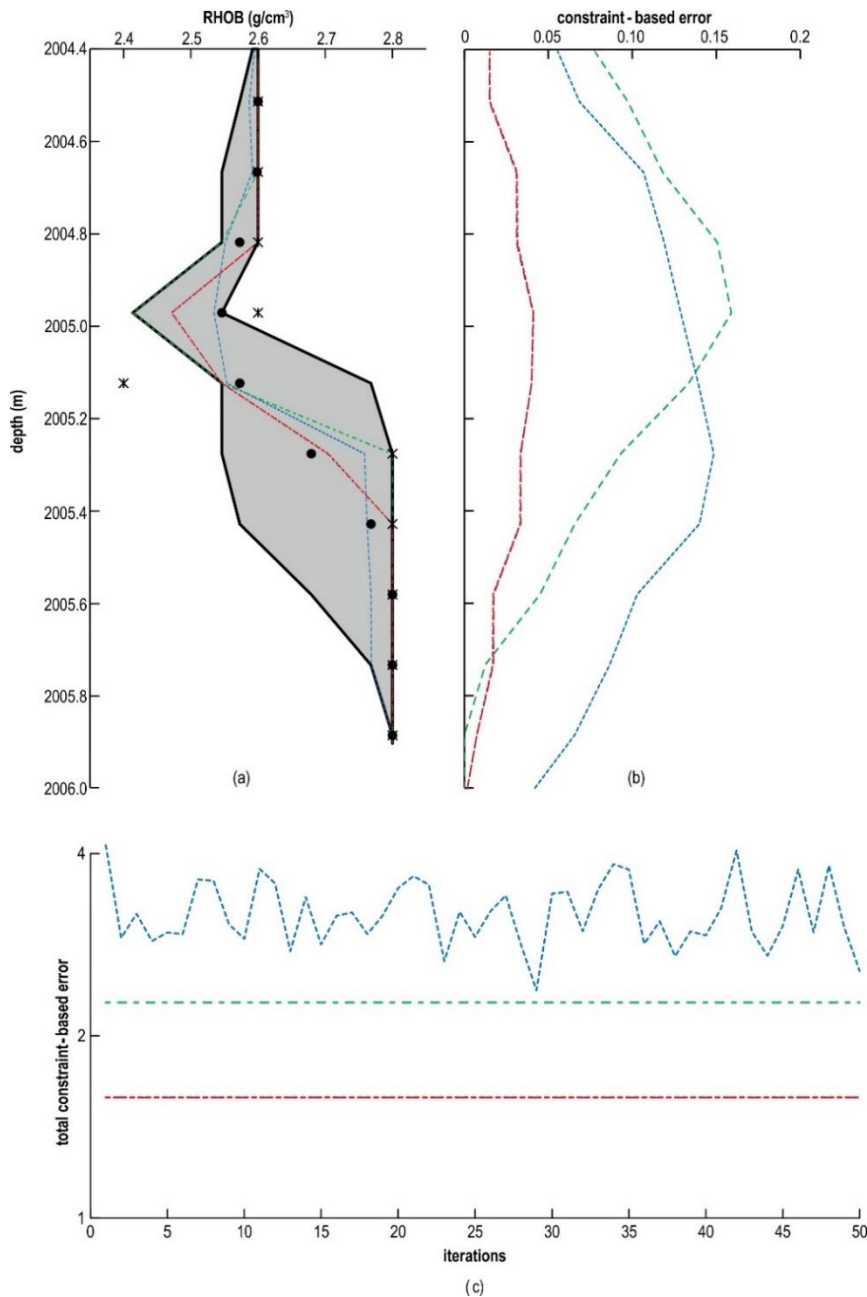


Figure A 2. Same legend as in Figure A 1, case 3.



#### Case 4: Increasing upward of NPHI

This is an exceptional case that random simulator provides the best realization (Figure A 3a) even though the error profile supports random- and recursive-simulators (Figure A 3b). In this specific example, random- and recursive-optimization simulators regenerated high-frequencies, while honouring the volumetric constraint of well-log records. However, the realizations are not satisfactory (Figure A 3a). It shows the importance of qualitative (visual) assessment to avoid quantitative mistakes.

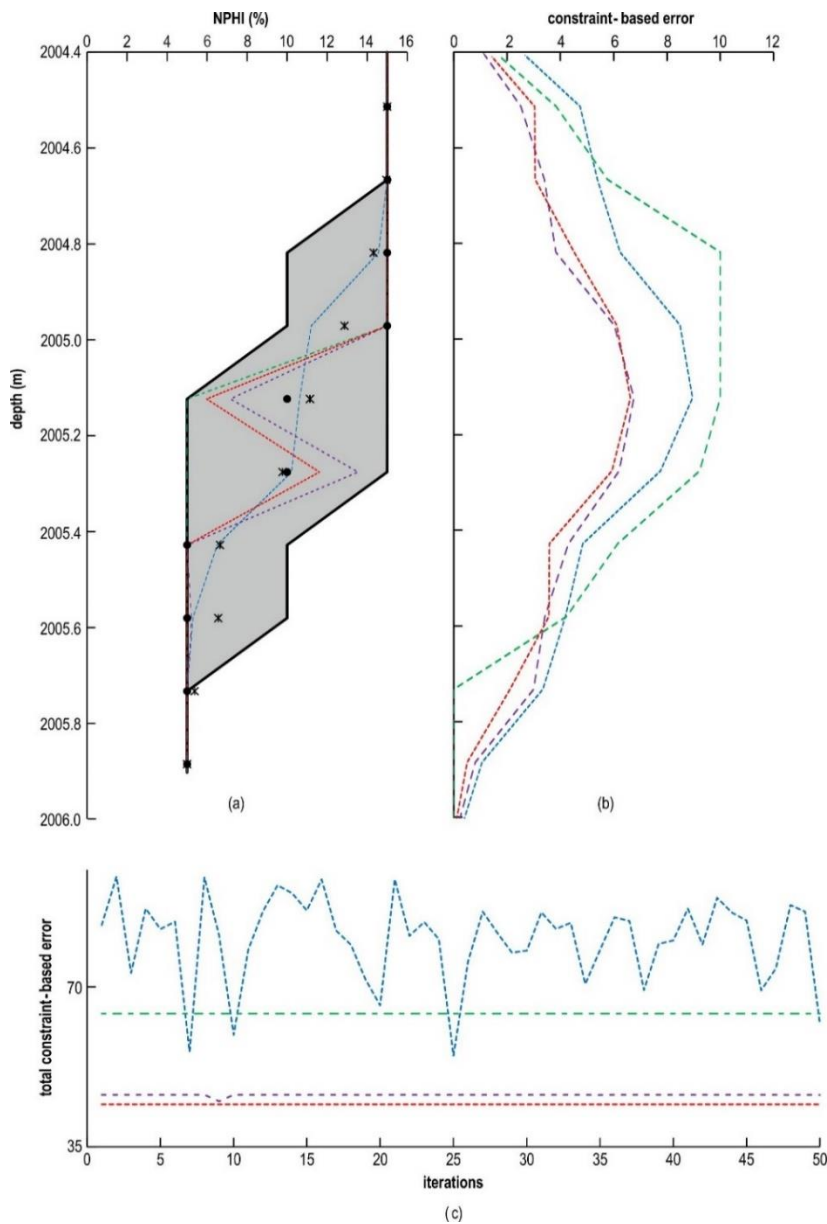


Figure A 3. Same legend as in Figure A 1, case 4.

## Case 5: Peak in NPHI

In this case, recursive-optimization simulator is considerably more accurate than the others. Although outputs of recursive and recursive-optimization simulators are the same qualitatively (Figure A 4a), the quantitative assessment (Figure A 4b,c) votes for the latter.

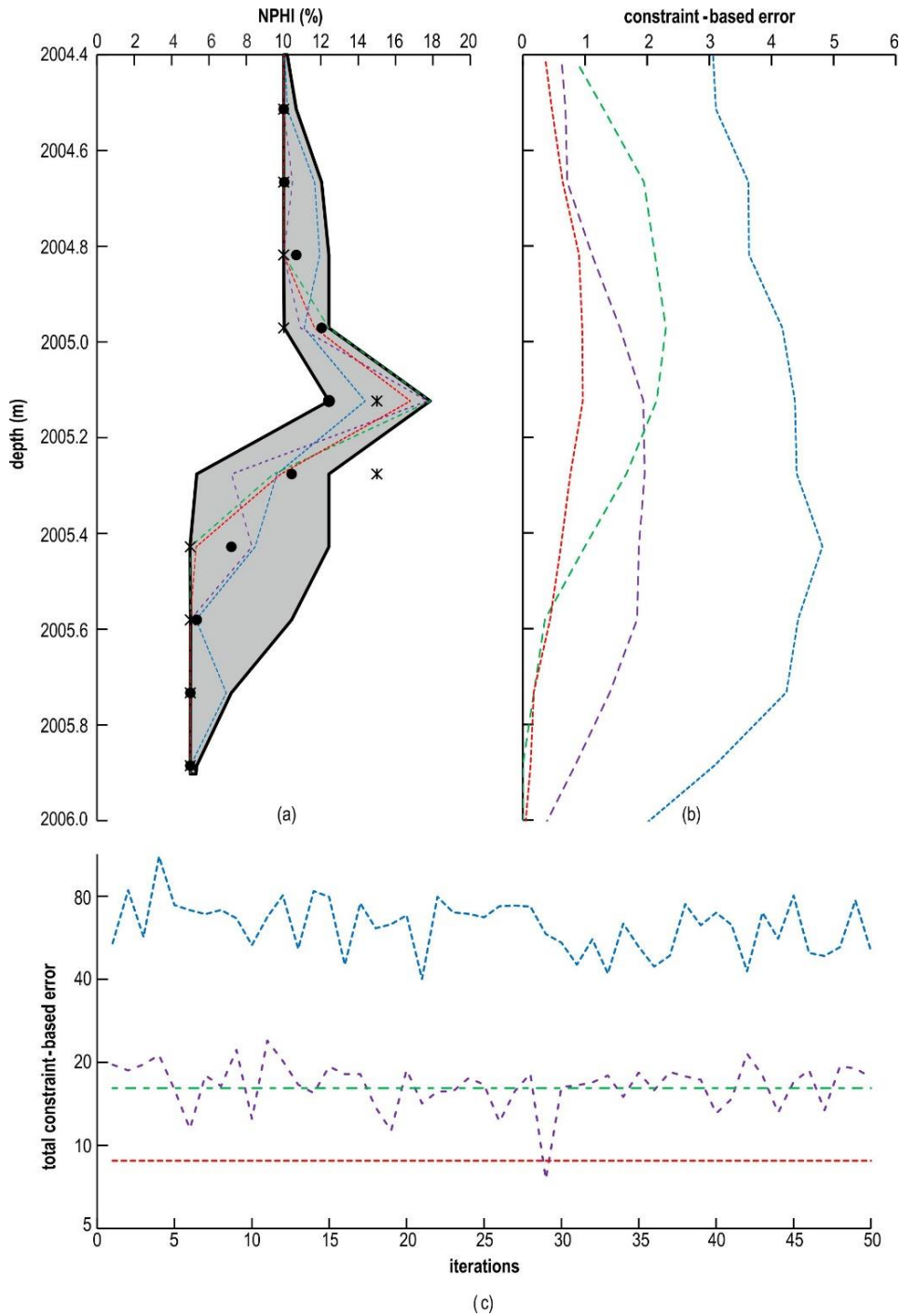


Figure A 4. Same legend as in Figure A 1, case 5.

## Case 7: Fractured horizon in DT

This is another counterexample of application of constraint-based error as validation. Ideal-based error selects random-optimization simulator (Figure A 5a) while constraint-based error chooses recursive-optimization simulator (Figure A 5b,c).

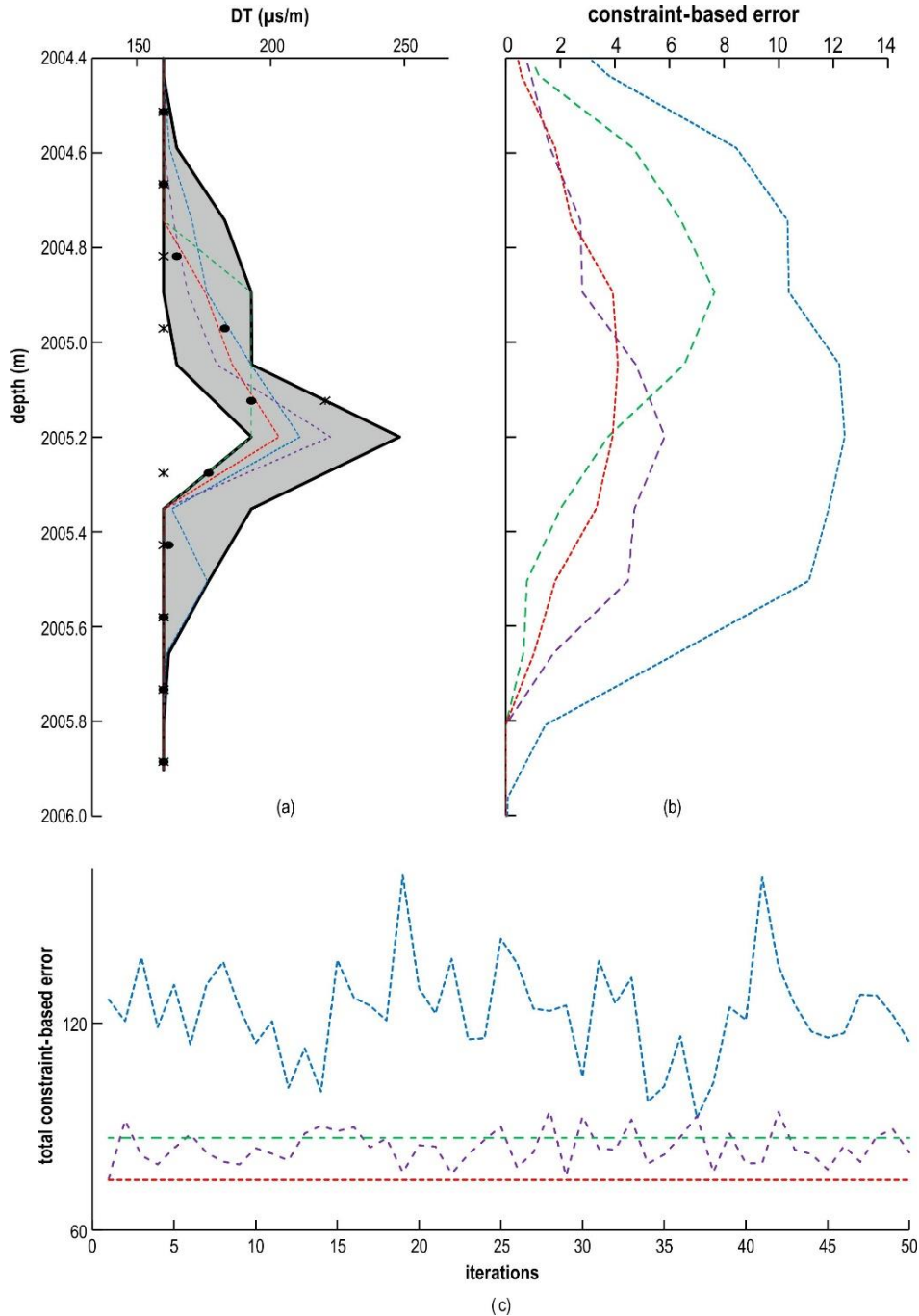


Figure A 5. Same legend as in Figure A 1, case 7.

## Appendix C: Application check of random-optimization simulator on real well-logs

The realizations and errors of random-optimization simulator on real data (GR, RHOB, NPHI and DT well-logs) of wells #2 to #5 are provided here. The intervals belong to the upper Sarvak Formation, a well-known high-quality carbonate reservoir. The best perforation point within the illustrated intervals is further recommended. The perforation interval should have the best reservoir quality for a successful production, i.e. simultaneous with less heterogeneity and uncertainty to avoid decreasing the operational risk.

### Well#2: 2766 – 2770 m

The lower part (2767.5- 2770 m) of well#2 (Figure A 6) shows higher quality, compared to its upper part (2766.0 - 2767.5 m). Due to DST uncertainty range, the lower part is relatively a certain part, however GR log shows more variations. GR records the depositional changes very well. Because of its sensitivity, it can provide a prioritization in homogeneous parts, like in the lower part of well#2 (Figure A 6). The simulation reduced shoulder-bed effect at the horizon of 2768.55 m, so that it is sharpened to be selected as the best pay zone for perforation and production within the interval of 2766 - 2770 m.

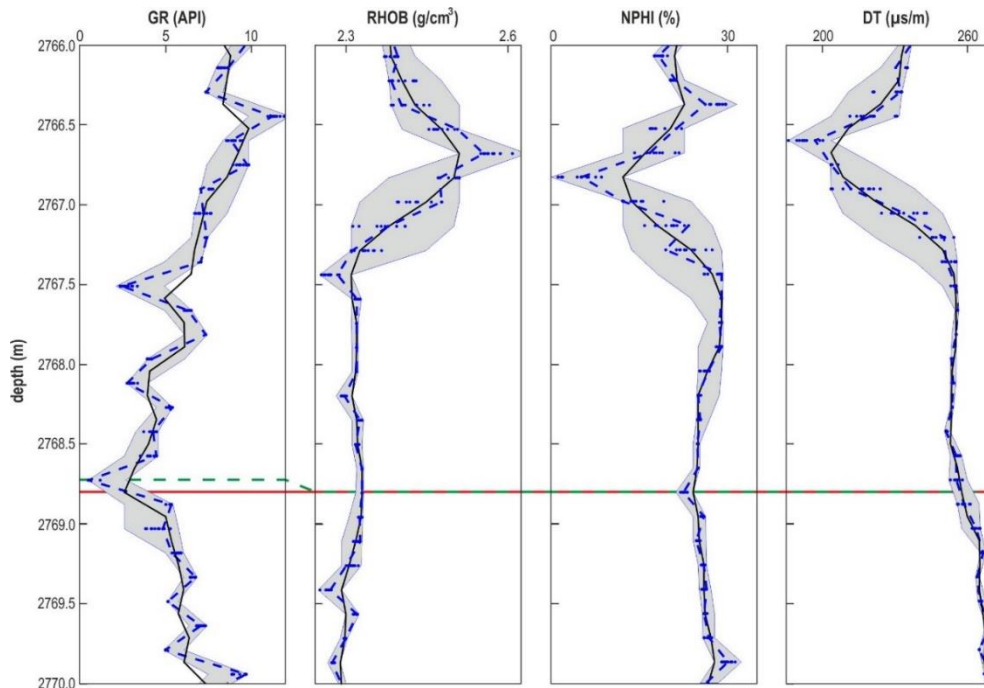


Figure A 6. Well-log (solid line), uncertainty range, simulations (realizations, dots), and best realization (dashed line) in well#2. Correlation of well- and simulated-logs for perforation is marked by solid red and dashed green line, respectively.

### Well#3: 2809 – 2813 m

The depth of 2809.5 m could be recommended for perforation. A slight GR trough and an amplified NPHI peak were indicators for suggesting this depth. Relatively low RHOB, less than  $2.4 \text{ g.cm}^{-3}$  and high DT confirm the decision made. High heterogeneities within the interval of 2810 – 2813 m increases the operational risk (Figure A 7).

### Well#4: 2662 – 2666 m

The peak of NPHI at 2664.1 m is an indicator of a high porous thin-bed. The shoulder-bed effect is removed within all the four well-logs (Figure A 8).

### Well#5: 2840 – 2844 m

GR at about 2842 m represents low shale, which is confirmed by a peak in NPHI log, i.e. effective porosity. Relatively low DT confirms that the increase of porosity is only due to primary porosity, and is not related to fractures or vugs. RHOB reconfirms an event at about 2842 m (Figure A 9).

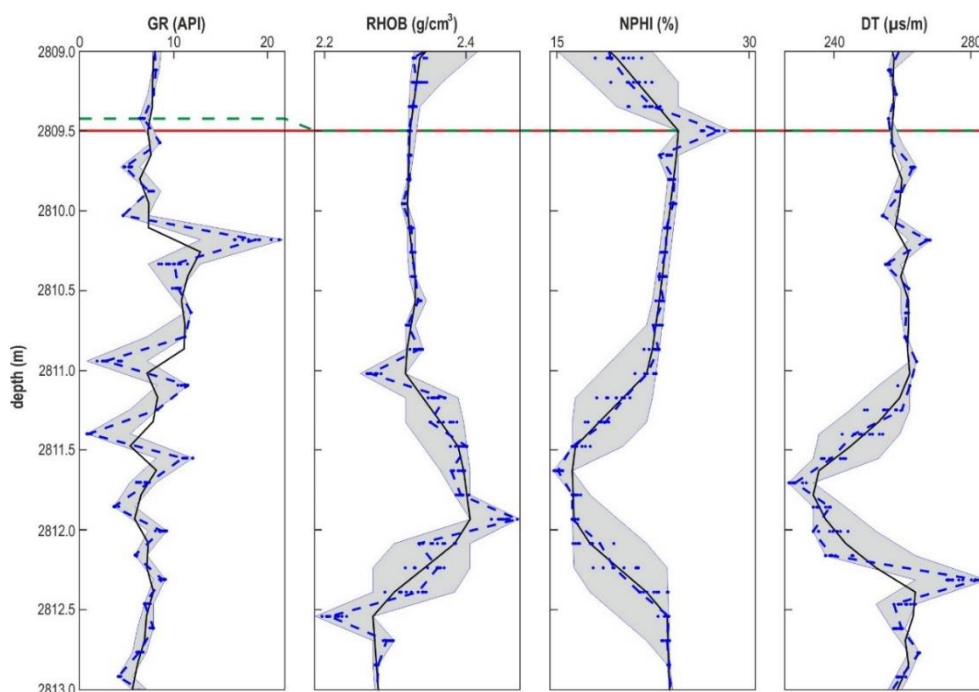


Figure A 7. Well#3. Same descriptions as in Figure A 6.

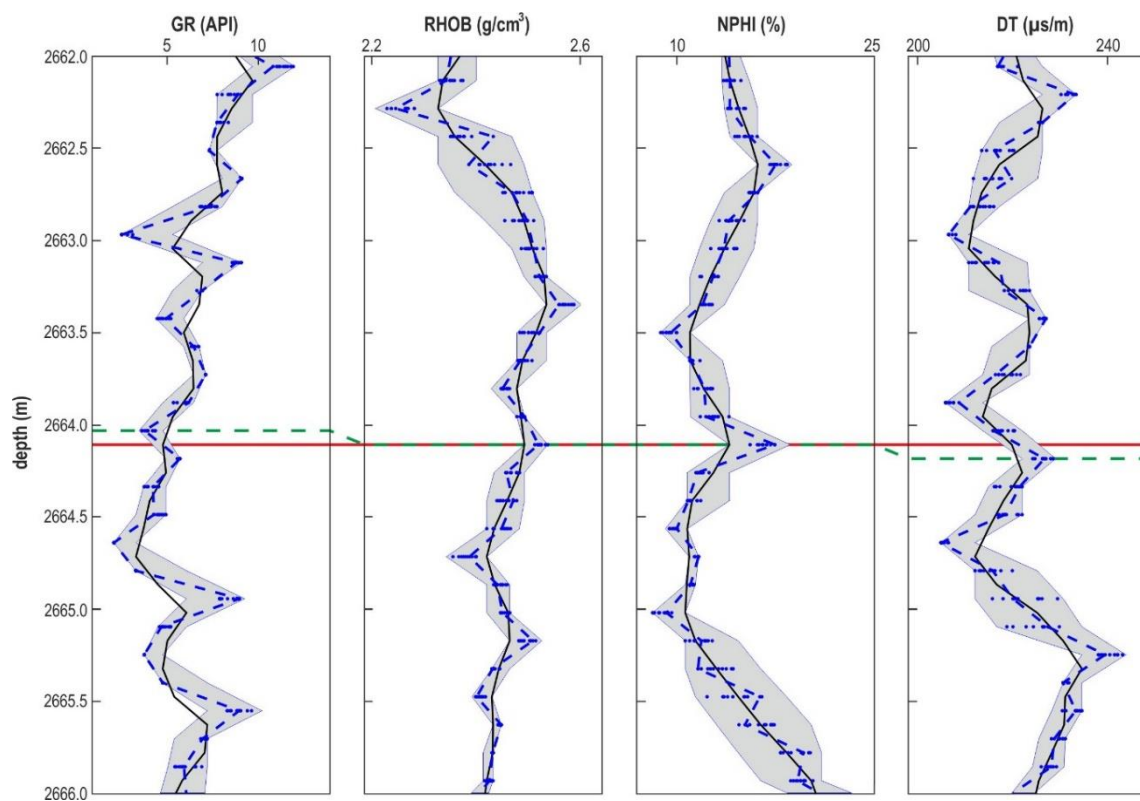


Figure A 8. Well#4. Same descriptions as in [Figure A 6](#).

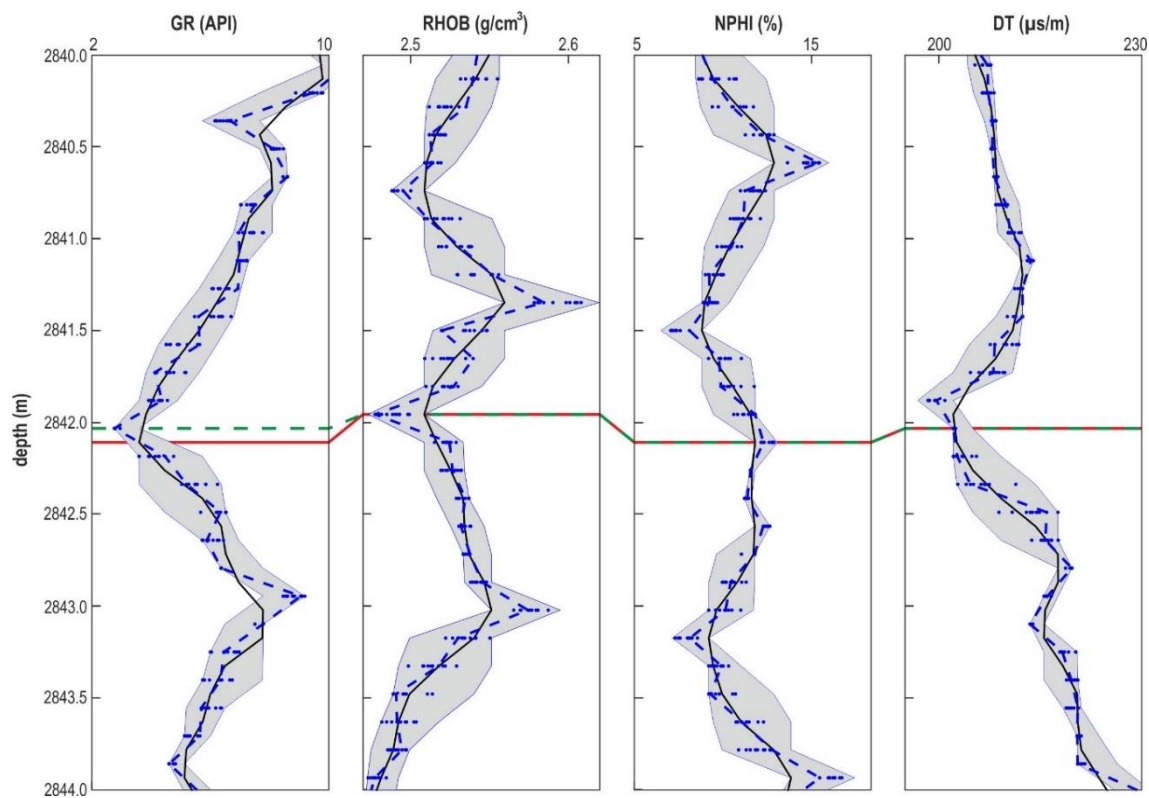


Figure A 9. Well#5. Same descriptions as in [Figure A 6](#).



## Appendix D: Publications and presentations of the thesis

- The results of [chapters 3](#), [4](#) and [5](#) are presented (poster) in the event of *Journée des Doctorants* (January 2016, Rennes):

**Journal of Doctorors (13 janvier 2016), Ecole Doctorale Sciences de la Matière (SDM), Rennes, France**

# Shoulder-bed Effect Removal for Thin-bed Characterization by Well-logs

P. Masoudi<sup>1,\*</sup>, T. Afifi<sup>2</sup>, H. Memarian<sup>3</sup> and B. Takhmechi<sup>4</sup>

<sup>1</sup> *Geosciences Rennes, CNRS UMR1181, Univ. de Rennes 1, Campus de Beaulieu, 35042 Rennes cedex, France*  
<sup>2</sup> *School of Mining Eng., Univ. of Tabriz, North Kampar 141914176 Tabriz, Iran*  
<sup>3</sup> *School of Mining, Petroleum and Geophysics Eng., Univ. of Shahrud, Shahrud, Iran*  
<sup>4</sup> *petroleum.masoudi@univ-rennes1.fr*

**Abstract:** Subsurface geological measurements are not fully representative of all geological and sedimentological aspects of the beds. The electrofacies, interpretable through well logs, are only simplified quantitative images of the petrophysical properties of the deposits. But the reality of geological phenomena is much more complex. The incompatibility of surface and sub-surface information could be addressed to different levels, shoulder-bed effect as well.

When a thin-bed is sandwiched between two thick beds, its petrophysical effect would be highly attenuated [1] because of the volumetric nature of well-logs. The first outcome of the study was developing volumetric Nyquist frequency for assessing well-log data. Two methodologies were thus developed to reduce the unwanted effect of shoulder-bed: geometry- and Dempster-Shafer Theory (DST)-based algorithms.

**Volumetric Nyquist frequency**

The volumetric nature of well-logs, inspired the idea of developing volumetric Nyquist frequency (the inverse of summation of sampling rate and vertical resolution of the bed). Nyquist frequency inverse of sampling rate is developed in communications, where the pulses of the signals are not volumetric [2]. Whereas in the geosciences, including well-logging, the measurements are volumetric (in contrast to electric pulses). The other outcome of volumetric viewpoint is to provide extra inferences for the intervention of volumes of investigations of the recordings (state III).

$$f_{Nyq} = \frac{1}{SR} \Rightarrow f_{Nyq,vol} = \frac{1}{SR + VR}$$

where SR and VR represent Sampling Rate and Vertical Resolution, respectively. In fact, volumetric Nyquist frequency is a constraint to the conventional Nyquist frequency, in a context of VR (no volume of resolution for electric pulses), the volumetric Nyquist frequency would turn into conventional Nyquist frequency.

The physical meaning of the volumetric Nyquist frequency "in order to have at least one fully representative record of a homogeneous bed, the thickness of the bed have to be at least SR-VR". In this sentence, the term "fully representative" means that the logging sensors are affected by the homogeneous bed at 100%, i.e. the volume of investigation of the logging tool is completely overlapping the homogeneous bed for at least one recording.

**Geometry-based algorithm**

For geometry-based algorithm, a well-log simulator is first designed to simulate well-logs based on (B) predefined ideal-log (for a single thin-bed), (C) sampling of the vertical resolution of the measuring tool, (D) thickness of the thin-bed, and petrophysical values, forming synthetic ideal-log are defined and corresponding synthetic logs are generated by simulation. (E) Ideal-log and synthetic logs are created for gamma ray (GR) and neutron porosity (NPH) logs, and 42 cases for density (RHOB) log. Finally, geometric models are developed to find the ideal-log value (GR, RHOB and NPH) and the thickness of the thin-bed. Each of these models is based on the apparent well-log value and the apparent thickness of the thin-bed, read from the well-log and one output (either the ideal-log value or the ideal thickness). The advantage of this algorithm is a more precise thickness estimation, using decision-level features of the different elements. Its drawback is to require time-consuming because extraction of the models is a complex manual process.

**DST-based algorithm**

In DST-based algorithm, the upper (plausibility) and lower (belief) limits of the petrophysical values are determined, using multiple simulations. For each horizon, the evidences are intersecting well-log recordings (4 for GR, 3 for the horizon) in place at the intersection of volumes of investigation of neighborhood horizons. The mass function in DST is the probability measure in Bayesian inference. So, the mass function is the core of calculations, and probability bounds (belief and plausibility functions) would be calculated by mass value [3]. We defined mass function by scaling well-log value.

An axiomatic structure is defined to calculate the probability bounds. This structure imposes geological and DST-based constraints to the results of the DST-based algorithm. (i) volumetric constraint of the well-logs: for each horizon, the belief (plausibility) is the minimum (maximum) well-log value within the interval of a vertical resolution, centered at the location of recording. (ii) mass function conditions: if a well-log value is constant in an interval of at least vertical resolution, then it is uncertainty range in the middle of the horizon, i.e. belief (plausibility) and mass functions will be equal. (iii) DST peaks and troughs: the shoulder-bed effect which has to be compensated. So, peaks (troughs) should be compensated by the belief (plausibility) value to be equal to the mass function.

Defining a factor for compensating the shoulder-bed effect is the only parameter in this algorithm, which requires manual optimization. The success of the compensating procedure is likely what Faum et al. [4] suggested.

**Volumetric constraint of well-logs**

Although a well-log value is a recording over a volume of investigation, it is assigned to a single depth. In fact, small dimension heterogeneities at the scale of the well-log value are ignored by the well-log. In mathematical language, the recorded value is the integral of petrophysical values over geologic bed (continuous and discrete forms are provided).

$$w(t) = \int_{t-\frac{VR}{2}}^{t+\frac{VR}{2}} p(x) * w(t-x) * dx$$

$$w(t) = \int_{t-\frac{VR}{2}}^{t+\frac{VR}{2}} \sin(x) * w(t-x) * dx$$

where  $w(t)$ : well-log value at depth "t",  $p(x)$ : the real petrophysical value of the formation at depth "x",  $\sin(x)$ : discrete simulation value, equivalent to  $\exp(i\pi x)$ ,  $w(t-x)$ : weight for increasing the relative impact of petrophysical values, closer to the centre of volume of investigation. FE: focal element or simply vertical resolution. The superposition of "VR" shows that FE belongs to the well-log recording. SR: sampling rate.

In the "volumetric constraint of well-logs", "FE" is a known mass value, "VR" and "SR" are known specifications of the beds. The weight "w" is considered as a linear function of the depth. So, the only unknown function is "p" or "sin" that could be found by an inverse procedure. This concept is an important technical trick that is used here as a factor for optimizing the simulations, also for validating and generalizing realizations.

**Validation criteria**

Several realizations could be generated by the simulation. It is necessary to have a measure to validate and prioritize the realizations. The ideal criterion is to compare the simulated-log with the ideal-log. Both ideal- and simulated-logs are functions of the depth up to the depth maximum of the two logs, the simulations have to be interpreted to the exact place of ideal-log logs.

Evidently in subsurface geology, we do not have ideal-logs, so the ideal error is practical only in synthetic cases. In real data, instead of ideal logs, the constraint-based error is developed, which is based on volumetric constraint of well-logs. In fact, the constraint-based error measures the validity of volumetric constraint of well-logs on the simulated-log. Since the volumetric constraint of well-logs is a priori pre-assumption of this research, hence, implemented logs have to honor to be considered as valid logs. Both ideal- and constraint-based errors (respectively indicated by id and cv) are applied on synthetic data and it is found that they are highly correlated ( $R^2 \sim 80\%$ ).

**The advantages of constraint**

The advantages of constraint are (i) providing a quality profile for each horizon, (ii) bulk error reduction through the simulated well, (iii) applicability by well-log and no need to use other well-logs, and (iv) highly correlated with the realizations.

The parameters of the formulas are previously defined:  $n_{sim}$ : number of realizations that can be found.

**Concluding remarks**

- Volumetric constraint of well-logs is used as a pre-assumption of the research. Based on this constraint, a validation criteria, the simulation of geometry- and DST-based algorithms are developed. The advantage of the constraint-based error is in prioritizing (and validating) realizations, due to the original well-logs. So, oriented to real data for validating enhanced well-logs.
- Geometry-based algorithm is developed to characterize thin-bed: decreasing shoulder-bed effect and bed thickness estimation. Its unique advantage is in DST-based evaluation of thin-bed. The theory of this methodology is relatively simple, however time consuming.
- DST-based algorithm is developed to enhance the real resolution of well-logs. The advantages of the developed DST-based algorithm could be summarized as: (i) providing uncertainty assessment measures for each record of the well-logs, (ii) Simulating an alternative well-log with a vertical resolution of about 15 cm, and (iii) the real resolution (vertical resolution of 0.91 cm).
- Representing high petrophysical variations in well-logs that were filtered during the logging measurements. (iv) Automating an algorithm (v) Relative to geometry-based algorithm, the DST-based algorithm reduced the uncertainty of GR, RHOB and NPH logs by 70%, 11% and 60%, respectively. However the DST-based algorithm cannot provide thickness of thin-beds.

**References**

1. A. S. Masoudi, P. T. Afifi, H. Memarian, B. Takhmechi, "Shoulder-bed Effect Removal for Thin-bed Characterization by Well-logs", *Journal of Doctorors*, vol. 1, no. 1, pp. 1-10, 2016.
2. P. T. Afifi, H. Memarian, B. Takhmechi, "Shoulder-bed Effect Removal for Thin-bed Characterization by Well-logs", *Journal of Doctorors*, vol. 1, no. 1, pp. 1-10, 2016.
3. P. T. Afifi, H. Memarian, B. Takhmechi, "Shoulder-bed Effect Removal for Thin-bed Characterization by Well-logs", *Journal of Doctorors*, vol. 1, no. 1, pp. 1-10, 2016.
4. P. T. Afifi, H. Memarian, B. Takhmechi, "Shoulder-bed Effect Removal for Thin-bed Characterization by Well-logs", *Journal of Doctorors*, vol. 1, no. 1, pp. 1-10, 2016.


- Detailed results of [chapters 3](#) and [4](#) are published in:

<b>IOP Publishing</b> J. Geophys. Eng. <b>14</b> (2017) 426–444 (19pp)	Journal of Geophysics and Engineering <a href="https://doi.org/10.1088/1742-2140/aa59d4">https://doi.org/10.1088/1742-2140/aa59d4</a>
<h1 style="margin: 0;">Geometric modelling of the volume of investigation of well logs for thin-bed characterization</h1>	
<p><b>Pedram Masoudi<sup>1,2</sup>, Hossein Memarian<sup>2,4</sup>, Tahar Aïfa<sup>1,4</sup> and Behzad Tokhmechi<sup>3</sup></b></p>	
<p><sup>1</sup> Geosciences-Rennes, CNRS UMR6118, Université de Rennes 1, Bat 15, Campus de Beaulieu, F-35042 Rennes cedex, France</p> <p><sup>2</sup> School of Mining Engineering, College of Engineering, University of Tehran, North Kargar, 1431954378 Tehran, Iran</p> <p><sup>3</sup> Department of Petroleum Engineering, University of North Dakota, 243 Centennial Drive Stop 8154, Grand Forks, ND 58202-8154, USA</p> <p>E-mail: <a href="mailto:memarian@ut.ac.ir">memarian@ut.ac.ir</a> and <a href="mailto:tahar.aifa@univ-rennes1.fr">tahar.aifa@univ-rennes1.fr</a></p>	
<p>Received 10 June 2016, revised 8 January 2017          Accepted for publication 17 January 2017          Published 10 March 2017</p>	
 CrossMark	
<p><b>Abstract</b></p> <p>The fuzzy membership function is used to model the volume of investigation of well logs geometrically. We discuss the fact that the spacing of a transmitter–receiver is not a precise parameter for addressing the vertical resolution of well logs. Instead, the vertical resolution of membership function (VRmf) is developed and estimated by variography analysis. In the five studied wells, the vertical resolution of gamma ray (GR), bulk density (RHOB), neutron porosity (NPHI) and sonic (DT) logs are estimated to be 61, 76, 76 and 61 cm, respectively. The simplest membership function for describing the volume of investigation of the GR, RHOB and NPHI is the triangle. For DT it is a complex shape. Being compatible with volumetric records in the well logs, the volumetric Nyquist frequency is introduced while considering the VRmf. Based on triangular membership functions, a thin-bed geometric simulator is designed. Regression models, i.e. deconvolution relations, are developed between the real thickness and the real petrophysical variation of a thin bed as outputs, and the same log-derived parameters are used as inputs. The shoulder-bed effect in GR, RHOB and NPHI is reduced by two to three times due to the mean squared error (MSE). To check the applicability of the deconvolution relations for the real data, ten thin beds are chosen within a well at the interval of the Sarvak Formation. In all the observations, the shoulder-bed effect is reduced after deconvolution. The thickness of the thin beds is estimated with a standard deviation of 4.4 cm, which is a precise value. The method is applied to the cored interval of the Sarvak Formation in a nearby well to characterize a porous carbonate thin bed sandwiched between dense carbonates. The estimated thin-bed thickness (<math>13 \pm 7.5</math> cm) is close to the <i>in situ</i> thin-bed thickness (<math>&lt;25</math> cm). Furthermore, the NPHI (total porosity) of the thin bed is estimated to be 11.7%, which is compatible with the core porosity (effective porosity), which is 8%, since the effective porosity should be less than the total porosity.</p> <p><b>Keywords:</b> volumetric Nyquist frequency, well log deconvolution, shoulder-bed effect, thin-bed simulator, thin-bed characterization</p> <p>(Some figures may appear in colour only in the online journal)</p>	
<hr/> <p><sup>4</sup> Authors to whom any correspondence should be addressed.</p>	
<div style="display: flex; justify-content: space-between; font-size: small;"> <span>1742-2132/17/020426+19\$33.00</span> <span>426</span> <span>© 2017 Sinopec Geophysical Research Institute Printed in the UK</span> </div>	



- The results of Chapter 5 is published in:

Journal of Petroleum Science and Engineering 154 (2017) 252–276




**ELSEVIER**

Contents lists available at ScienceDirect

**Journal of Petroleum Science and Engineering**

journal homepage: [www.elsevier.com/locate/petrol](http://www.elsevier.com/locate/petrol)



---


## Uncertainty assessment of volumes of investigation to enhance the vertical resolution of well-logs

Pedram Masoudi<sup>a,b</sup>, Tahar Aïfa<sup>a,\*</sup>, Hossein Memarian<sup>b</sup>, Behzad Tokhmechi<sup>c</sup>

<sup>a</sup> Géosciences-Rennes, CNRS UMR6118, Université de Rennes 1, Bat.15, Campus de Beaulieu, 35042 Rennes cedex, France

<sup>b</sup> School of Mining Eng., College of Eng., University of Tehran, North Kargar, 1431954378 Tehran, Iran

<sup>c</sup> Department of Petroleum Engineering, University of North Dakota, 243 Centennial Drive Stop 8154, Grand Forks, ND 58202-8154, USA

 CrossMark

---

### ARTICLE INFO

**Keywords:**  
Shoulder-bed effect  
Volumetric measurement  
Vertical resolution  
Thin-bed  
Depth uncertainty  
Realization prioritizing

### ABSTRACT

Whereas well-log data are dense recordings, i.e. low sampling rate, there is a high depth uncertainty. The depth uncertainty originates from the volumetric nature of well-logging that each record belongs to a volume of investigation, around the logging tool. The developed algorithm in this work consists of two parts: (i) uncertainty assessment using Dempster-Shafer Theory (DST). The lower (upper) uncertainty boundary of each well-log is calculated by belief (plausibility) function. (ii) Four simulators are designed for scanning the uncertainty range in order to enhance the vertical resolution of well-logs (~60 cm) by generating simulated-logs (vertical resolution of ~15 cm). Shoulder-bed effect is reduced simultaneously with resolution improvement, resulting in more accurate thin-bed characterization. In order to validate functionality of the simulators, two error criteria are considered: ideal- and constraint-based errors. Ideal-based error is applicable in synthetic-logs where the rock specifications are completely known through ideal-logs. However, constraint-based error does not need ideal-log. It measures the error due to the volumetric nature of the well-logs, hence applicable in the real cases. The high correlation ( $R^2=0.89$ ) between both the errors indicates that the second criterion is precise for validation. Step-by-step procedure of the algorithm is shown in detail on synthetic and real data (a cored interval). Finally, DST-based algorithm is not only automated but also more accurate than geometry-based thin-bed characterization method. The error bars of characterizing gamma, density and neutron porosity of thin-beds are lower in DST-based algorithm by 100%, 71% and 66%, respectively.

---

### 1. Introduction

Vertical resolution of logging tools is reported from some centimetres, e.g. Micro Spherically Focused Log (MSFL), to about 100 cm, e.g. Spontaneous Potential (SP). So characterizing geological beds thinner than the vertical resolution is imprecise even if the sampling rate is precise enough (McCall et al., 1987; Passey et al., 2006; Masoudi et al., 2017). Acquired petrophysical data belong to a three dimensional space namely volume of investigation. Projection of this 3D volume on the 1D well axis is called vertical resolution.

Geological and technical aspects of well-logging were overwhelmed in the first publications concerning resolution enhancement. Only signal-processing theories, Weiner and Kalman filter, were developed for the purpose of increasing frequency of the well-logs (Foster et al.,

1962; Bayless and Brigham, 1970). The other practical issue of signal processing algorithms is lack of knowledge about the theoretical parameters since there was no confidence about the used parameters (Lyle and Williams, 1987).

Until 1987, the studies were totally theoretical, however practical improvement of vertical resolution of well-logs was basically done within the years 1989–1990, when industrial researchers of Schlumberger, Halliburton and British Petroleum played part. They used geometrical and numerical analysis for developing easy-to-apply procedures to improve well-log resolution.

The beds thinner than 2 feet (60.96 cm) cannot be properly evaluated by (far) density log. Based on geometrical reasoning, a wise correction to enhance density log for characterizing thin-beds (less than 6 in. or 15.24 cm) is developed. The main idea was inferring the

---

**Abbreviations:** Bel, belief function; BOE, body of evidence; dist, distance; DST, Dempster-Shafer theory; DT, sonic log (slowness log); FE, focal element; FE', focal element of recording; FE'', focal element of target; fr, fraction; GR, gamma ray log; id, ideal; int, interpolation; m, mass function; MSE, mean square error; NPHI, neutron porosity log; PDF, probability distribution function; Pls, plausibility function; pv, petrophysical value; rec, recording; RHOB, bulk density log; RMSE, root mean square error; sim, simulation; SE, shoulder-bed effect; SR, sampling rate; std, standard deviation; UNC, uncertainty; VR, vertical resolution; wl, well-log

\* Corresponding author.  
E-mail address: [tahar.aifa@univ-rennes1.fr](mailto:tahar.aifa@univ-rennes1.fr) (T. Aïfa).


<http://dx.doi.org/10.1016/j.petrol.2017.04.026>

Received 14 December 2016; Received in revised form 13 April 2017; Accepted 19 April 2017

Available online 20 April 2017

0920-4105/© 2017 Elsevier B.V. All rights reserved.


- *Mi-parcours* of the thesis was defended in Rennes, April 13<sup>th</sup> 2016:

	
<b>ECOLE DOCTORALE</b> « Sciences de la Matière » de Rennes	
<b>RAPPORT DU JURY</b>	
<b>Prénom - Nom du doctorant</b>  <b>Pedram MASOUDI</b>	<b>Laboratoire - Etablissement d'inscription - e. mail</b>  Equipe systèmes tectoniques- Géosciences-Rennes, CNRS-UMR6118, UR1 pedram.masoudi@univ-rennes1.fr
<b>Date de la soutenance à mi-parcours - salle</b>  <b>13.04.2016</b>	
<b>Membres du Jury</b>  <b>Aline Dia</b>  <b>Jean-Noël Proust</b>  <b>Jean-Laurent Monnier</b>  <b>Tahar Aïfa</b>	<b>Laboratoire - Laboratoire / Etablissement de rattachement - e. mail</b>  Equipe Géochimie des Eaux et des Interfaces - Géosciences-Rennes, CNRS UMR6118, UR1, aline.dia@univ-rennes1.fr Equipe Dynamique des Bassins - Géosciences-Rennes, CNRS UMR6118, UR1, jean-noel.proust@univ-rennes1.fr Equipe Archéologie - CreAAH, CNRS UMR6566, UR1, jean-laurent.monnier@univ-rennes1.fr Equipe Systèmes tectoniques - Géosciences-Rennes, CNRS UMR6118, UR1, tahar.aifa@univ-rennes1.fr
<b>Directeur(s) de thèse</b> <b>Prénom - Nom</b> <b>Tahar Aïfa</b>	<b>Laboratoire - Laboratoire / Etablissement de rattachement - e. mail</b>  Equipe systèmes tectoniques - Géosciences-Rennes, CNRS UMR6118, UR1, tahar.aifa@univ-rennes1.fr
<b>Titre de la thèse</b>  <b>Application of Hybrid Uncertainty-clustering Approach in Preprocessing Well-logs</b>	


**RAPPORT DU JURY**


☒ Si la soutenance à mi-parcours s'est bien déroulée et que le parcours du (de la) doctorant(e) se déroule conformément, veuillez cocher la case et transmettre avec votre signature.

☐ Si vous jugez qu'un complément d'information doit être signalé au Directeur de l'ED « SDLM » vous pouvez rédiger votre rapport ci-dessous.

  
**Aline DIA**  
 Directrice Adjointe  
 Rennes UMR 6118

  
**Jean-Noël Proust**

  
**Jean-Laurent Monnier**

  
**Tahar Aïfa**

**Date :** 13 April 2016

**Signatures des membres du Jury**

Université de Rennes 1 - Campus de Beaulieu - Ecole Doctorale "Sciences de la Matière" de Rennes  
 Avenue du Général Leclerc 35042 Rennes Cedex -  
 Directeur : Bât. 11 - Tél. 02 23 23 59 50  
 Secrétariat : Bât. 1 - Tél. 02 23 23 64 45  
 e.mail : sdlm@univ-rennes1.fr



- The *final defense* is presented in Tehran, 16/05/2017, Tehran.
- Other publications:






October 2016 - Tehran

## Clustering as an efficient tool for assessing fluid content and movability by resistivity logs

**Pedram Masoudi<sup>1,3</sup>, Babak Nadjari Araabi<sup>2</sup>, Tahar Aïfa<sup>1\*</sup>, Hossein Memarian<sup>3\*</sup>**

1\* : Géosciences-Rennes, CNRS UMR6118, Université de Rennes 1, Bat.15, Campus de Beaulieu, 35042 Rennes cedex, France, tahar.aifa@univ-rennes1.fr and pedram.masoudi@univ-rennes1.fr

2 : School of Electrical and Computer Eng., Univ. of Tehran, Tehran, Iran, araabi@ut.ac.ir

3 : School of Mining Eng., Univ. of Tehran, Tehran, Iran, memarian@ut.ac.ir and masoudip@ut.ac.ir

**Abstract**

Neither core measurements nor well tests provide precise measurement of fluid contents; so, at the moment there is no validated saturation measurement in the oil industry. However, resistivity logs contain some valuable information about reservoir fluids, and classes of saturation based on the behaviour of resistivity data. In order to extract saturation value, clustering algorithms are proposed and tested here. Clustering is an unsupervised categorization method, which relies on natural groupings of real data, instead of predefined labels. Distance or dissimilarity plays an important role in the formation of clusters in an algorithm. The application of three clustering algorithms on prediction of water saturation is discussed here. It is shown that Fuzzy C-Means clustering divides data only according to saturation property; while the Gustafson-Kessel algorithm considers not only saturation but also permeability. The reason is that Gustafson-Kessel can detect linear patterns. This algorithm is introduced as the most appropriate clustering method for predicting permeability, and for understanding the reservoir quality of the formation under examination. Gath-Geva clustering did not provide as much information as Gustafson-Kessel. In addition to these three clustering algorithms, two other methods were likewise checked, but they did not provide acceptable interpretations, so not reported. Another achievement of this study is the introduction of a cluster label instead of a single value which is very unreliable for expressing saturation and permeability simultaneously. Predictions of these two petrophysical properties are provided merely by two conventional resistivity well-logs: deep and shallow. The output of cluster analysis is much closer to well-scale reservoir properties as compared with that of core-scale properties, since clustering algorithms are applied to logs that are volumetric recordings. The applicability and efficiency of the proposed methods are examined and verified through the use of well-logs of Sarvak Formation in an anticlinal oil field in the Abadan Plain, Iran.

**Keywords:** water saturation in carbonate reservoirs; clustering permeable zones; clustering saturated zone; application of unsupervised learning; Gustafson-Kessel clustering

### 1. INTRODUCTION

The importance of evaluating water saturation in petroleum exploration is taken for granted by petroleum geoscientists. The widest usage of water saturation is in net pay detection. Petrophysicists apply cut-off values to water saturation logs, to distinguish oil-bearing intervals in both horizontally [1] and vertically drilled wells [2, 3, 4 and 5]. Due to the effect of water saturation on the plasto-elastic properties of rocks, accurate determination of this property is essential in geomechanics [6]. In addition, Tokhmechi et al. (2009) have used water saturation log in the process of fracture detection within wells [7]. Production planning is another criterion which water saturation is essential for [8].

Still, empirical relations for estimating water saturation are the most widely used methodologies. Among them, Archie relations, developed by early Archie works [9, 10, 11 and 12] are the best-known. There are so many other empirical relations which have also been developed, such as Carman [13] and Timur [14]. For the comprehensive study of empirical methods in estimating water saturation, please refer to [15]. Worthington (2004) offered a wise fit-for-purpose usage of Archie and non-Archie relations due to rock type and our purpose of estimating water saturation [16].

There are some other methodologies, based on supervised methods and trainable machines, which have recently been developed. To use these supervised methods, a reference criterion is required to train a machine. For example, Kadkhodaie-Ilkhchi et al. (2009) proposed a Committee Machine with Training Algorithm (CMTA), utilizing a combination of Levenberg-Marquardt, Bayesian regularization, gradient descent, one step secant and resilient back-propagation to train a neural network for predicting Normalized Oil Content (NOC) [17].

The Bayesian classifier can be applied, while using Gassmann equation as labels [18]. Also, Radial Basis Function Neural Networks [19] and support vector

\* Corresponding author





## Methodology-selection by Fuzzy Analytic Hierarchy Process for Studying Net Pays

Pedram Masoudi<sup>1,3</sup>, Mohammad Ataei<sup>2</sup>, Tahar Aïfa<sup>1\*</sup>, Hossein Memarian<sup>3\*</sup>

1\* : Géosciences-Rennes, CNRS UMR6118, Université de Rennes 1, Bat.15, Campus de Beaulieu, 35042 Rennes cedex, France, tahar.aifa@univ-rennes1.fr and pedram.masoudi@univ-rennes1.fr

2 : School of Mining, Petroleum and Geophysics Eng., Shahrood Univ. of Technology, Iran.

3 : School of Mining Eng., Univ. of Tehran, Tehran, Iran, memarian@ut.ac.ir and masoudip@ut.ac.ir

### Abstract

Net pay intervals are conventionally determined, applying cut-off values on geological well-logs. Recently developed methodologies utilize more complicated algorithms: Bayesian classifier, artificial neural network and Dempster-Shafer theory. The outputs of these methodologies are not completely compatible. It rises this question that which method should be recommended in each situation: (i) industrial use, (ii) research goal and (iii) general situations.

Fuzzy analytical hierarchy process is used here to compare effectiveness of the four net pay determination methods in each three situations. Six criteria were defined: precision, generalization ability, fuzziness, simplicity of methodological concepts, user-friendly and speed of the algorithm. For the precision and generalization ability, mean squared error of training and generalization data are used, respectively. Mean squared error and speed (inverse of time) of the algorithm are continuous variables, and provide quantitative comparison. While qualitative comparison is done for the criteria of simplicity and user-friendly. For the criterion of the fuzziness, a ranking, i.e. categorical variable, is used based on the number of classes that the classifier could provide. The comparison is done based on the results of net pay determination (the four methods) on sandy Burgan and carbonated Mishrif reservoirs, Iranian offshore oil-fields.

The results show that from viewpoint of general situation, Bayesian and Dempster-Shafer-based methods are the best. Artificial neural network and Dempster-Shafer are the most suitable methods for industrial mode, and Bayesian and artificial neural network are the best methods for research applications. Finally, cut-off methodology is never prioritized.

**Keywords:** net pay methodologies; fuzzy AHP for net pay; purposes of net pay determination; solution-selection for net pays; intelligent net pay determination

### 1. INTRODUCTION

In cases that there are multiple solutions for a problem, how to select the most optimum methodology is an important question. Recently, novel net pay determination methods have been proposed that let user decide the process of evaluating productive zones by his own. Conventionally, pay zone identification methodologies were based on cut-off approaches, which simply applies two to three cut-offs on petrophysical parameters of shale percent, porosity and water saturation [1, 2 and 3]. However, it is also possible to study productive zones from other perspectives: reservoir engineering [4], probabilistic view of Bayesian classifier [5], using fuzzy aggregation for merging outputs of other net pay identification procedures [6] or by the means of other intelligent methods as Dempster's rule of combination [7] or Artificial Neural Networks (ANN) [8, 9 and 10].

Resolving a question by multiple approaches might be considered as a repetitive job, e.g. in above literature, net

pay detection is addressed using six different methodologies. However, we believe that multiple approaches can provide options in different conditions. Here, fuzzy Analytic Hierarchy Process (fuzzy AHP) is used as a decision making tool to prioritize introduced methodologies in three cases: general situation, industrial use and research divisions.

AHP is a powerful and well-known process for ranking options/choices due to predefined criteria and goals; meanwhile, considering hierarchy of goals- criteria- options. From managerial viewpoint, AHP provides a link between "human's thoughts" and "decision making", through the tunnel of pairwise comparison process. If we use fuzzy numbers instead of crisp numbers for comparing options or criteria, this methodology is called fuzzy AHP. Using fuzzy numbers means that the process of pairwise comparison contains uncertainty. In another word, there is a vagueness or gloominess in our comparison procedure. Here, the aim of using AHP is to prioritize different net pay methodologies due to multiple goals (research, industry and general usage of methods).

\* Corresponding author

## Appendix E: Publication list

### Peer-reviewed journals:

- Masoudi P., Aifa T., Memarian H., Tokhmechi B., (ready for submission). Uncertainty assessment of porperm by clustering algorithm and fuzzy arithmetic.
- Moradi M., Tokhmechi B., Masoudi P., (minor revision). Inversion of well logs into rock types, lithofacies and environmental facies, using pattern recognition, a case-study of carbonate Sarvak Formation. *Carbonates & Evaporates*
- Masoudi P., Aifa T., Memarian H., Tokhmechi B., 2017. Uncertainty assessment of volumes of investigation to enhance the vertical resolution of well-logs. *J. Petrol. Sci. Eng.* 154: 252-276
- Masoudi P., Memarian H., Aifa T., Tokhmechi B., 2017. Geometric modelling of volume of investigation of well-logs for thin-bed characterization. *J. Geophysics & Eng.* (IOP) 14(2): 426-444
- Masoudi P., Asgarinezhad Y., Tokhmechi B., 2015. Feature selection for reservoir characterisation by Bayesian Network. *Arabian J. Geosciences* 8(5): 3031-3043
- Masoudi P., Arbab B., Mohammadrezaei H., 2014. Net pay determination by Dempster rule of combination, case study on Iranian offshore oil fields. *J. Petrol. Sci. Eng.* 123: 78-83
- Masoudi P., Arbab B., Mohammadrezaei H., 2014. Net pay determination by artificial neural network, case study on Iranian offshore oil fields. *J. Petrol. Sci. Eng.* 123: 72-77
- Masoudi P., Tokhmechi T., Ansari Jafari M., Zamanzadeh S.M., Sherkati S., 2012. Application of Bayesian technique in determining net pay zones. *J. Petrol. Sci. Eng.* 94: 47-54
- Masoudi P., Tokhmechi B., Ansari Jafari M., Moshiri B., 2012. Application of fuzzy classifier fusion in determining productive zones in oil wells. *J. Energy Exploration & Exploitation* 30(3): 403-416
- Masoudi P., Tokhmechi B., Bashari A., Ansari Jafari M., 2012. Identifying productive zones of Sarvak Formation by integrating outputs of different classification methods. *J. Geophysics & Eng.* (IOP) 9(3): 282-290
- Masoudi P., Zahedi A., Moradzadeh A., Alirezaei F., Zamanzadeh S.M., 2011. Estimation of in place gas volume in multilayered reservoirs using deterministic and probabilistic approaches. *J. Energy Exploration & Exploitation* 29(5): 543-557
- Masoudi P., Tokhmechi B., Zahedi A., Ansari Jafari M., 2011. Developing a new method for identification of net zones using log data and diffusivity equation. *J. Mining & Environment* 2(1): 53-60

### Conferences:

- Masoudi P., Ataei M., Aifa T., Memarian H., 2016. Methodology-selection by fuzzy analytic hierarchy process for studying net pays. *4th International Mine and Mining Industries Congress*, Tehran, Iran
- Masoudi P., Nadjar Araabi B., Aifa T., Memarian H., 2016. Clustering as an efficient tool for assessing fluid content and movability by resistivity logs. *4th International Mine and Mining Industries Congress*, Tehran, Iran
- Tavanaei F., Mohammadian R., Masoudi P., 2015. Structural zonation of Ahwaz oil field. *Petroleum Geomechanics Conf.*, Tehran, Iran
- Moradi M., Tokhmechi B., Masoudi P., Ramezani O., 2015. Evaluation of production capability of the reservoir using clustering techniques. *The 33rd National Geosciences Symp.*, Tehran, Iran
- Moradi M., Tokhmechi B., Masoudi P., 2015. A discussion about validity and adaptation between electrofacies and geological facies. *The 33rd National Geosciences Symp.*, Tehran, Iran
- Moradi M., Tokhmechi B., Masoudi P., 2014. Using knn classifier in identifying reservoir facies. *The 2nd National Iranian Petroleum Conf.*, Kerman, Iran
- Masoudi P., Tokhmechi B., Memarian H., Ghiasi-Nasab M., 2014. Development of scale-based categorization of geoscience projects in Iran. *The 32nd National Geosciences Symp.*, Tehran, Iran
- Masoudi P., Tokhmechi B., Memarian H., Ghiasi-Nasab M., 2013. Scale-based categorization of geoscience projects in Iran. Presented in *National Conf. on Exploration Eng.*, Shahrood, Iran
- Masoudi P., Mazaheri A., Tokhmechi B., Memarian H., 2012. The application of Sugeno discrete integral for determining net pay zones. *The 3rd Iranian Petroleum Conf.*, Tehran, Iran
- Masoudi P., Hourfar F., Mazaheri A., 2011. An improvement in estimating petrophysical parameters by utilizing normalizing mapping on inputs of artificial neural networks. *The 8th Iranian Student Mining Eng. Conf.*, Tehran, Iran
- Masoudi P., Tokhmechi B., Ansari Jafari M., Zamanzadeh S.M., Tohidinia A., 2011. Selecting the best horizon for operation of gas injection and storage in depleted oil fields. *Iranian Conf. on Underground Storage of Hydrocarbons*, Shahrood, Iran

## **ANNEXE 2**

VU :

**Le Directeur de Thèse**

Tahar AÏFA



VU :

**Le Responsable de l'École Doctorale**

**VU pour autorisation de soutenance**

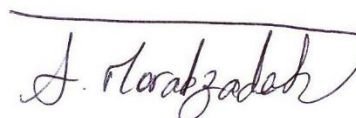
**Rennes, le**

**Le Président de l'Université de Rennes 1**

David ALIS

**VU après soutenance pour autorisation de publication :**

**Le Président de Jury,**



## ***Abstract***

In the subsurface geology, characterization of geological beds by well-logs is an uncertain task. The thesis mainly concerns studying vertical resolution of well-logs (question 1). In addition, fuzzy arithmetic is applied to experimental petrophysical relations to project the uncertainty range of the inputs to the outputs, here irreducible water saturation and permeability (question 2). Regarding the first question, the logging mechanism is modelled by fuzzy membership functions. Vertical resolution of membership function (VRmf) is larger than spacing and sampling rate. Due to volumetric mechanism of logging, volumetric Nyquist frequency is proposed.

Developing a geometric simulator for generating synthetic-logs of a single thin-bed enabled us analysing sensitivity of the well-logs to the presence of a thin-bed. Regression-based relations between ideal-logs (simulator inputs) and synthetic-logs (simulator outputs) are used as deconvolution relations for removing shoulder-bed effect of thin-beds from GR, RHOB and NPHI well-logs. NPHI deconvolution relation is applied to a real case where the core porosity of a thin-bed is 8.4%. The NPHI well-log is 3.8%, and the deconvolved NPHI is 11.7%. Since it is not reasonable that the core porosity (effective porosity) be higher than the NPHI (total porosity), the deconvolved NPHI is more accurate than the NPHI well-log. It reveals that the shoulder-bed effect is reduced in this case. The thickness of the same thin-bed was also estimated to be  $13 \pm 7.5$  cm, which is compatible with the thickness of the thin-bed in the core box ( $< 25$  cm). Usually, in situ thickness is less than the thickness of the core boxes, since at the earth surface, there is no overburden pressure, also the cores are crushed.

Dempster-Shafer Theory (DST) was used to create well-log uncertainty range. While the VRmf of the well-logs is more than 60 cm, the VRmf of the belief and plausibility functions (boundaries of the uncertainty range) would be about 15 cm. So, the VRmf is improved, while the certainty of the well-log value is reduced. In comparison with geometric method, DST-based algorithm resulted in a smaller uncertainty range of GR, RHOB and NPHI logs by 100%, 71% and 66%, respectively.

In the next step, cluster analysis is applied to NPHI, RHOB and DT for the purpose of providing cluster-based uncertainty range. Then, NPHI is calibrated by core porosity value in each cluster, showing low RMSE compared to the five conventional porosity estimation models (at least 33% of improvement in RMSE). Then, fuzzy arithmetic is applied to calculate fuzzy numbers of irreducible water saturation and permeability. Fuzzy number of irreducible water saturation provides better (less overestimation) results than the crisp estimation. It is found that when the cluster interval of porosity is not compatible with the core porosity, the permeability fuzzy numbers are not valid, e.g. in well#4. Finally, in the possibilistic approach (the fuzzy theory), by calibrating  $\alpha$ -cut, the right uncertainty interval could be achieved, concerning the scale of the study.

**Keywords:** well-log uncertainty, vertical resolution, volumetric Nyquist frequency, thin-bed characterization, Dempster-Shafer, fuzzy arithmetic